Physical and Structural Improvements in the Stellar Evolutionary Code ATON2.3

Natália Rezende Landin

August 2006

NATÁLIA REZENDE LANDIN

Physical and Structural Improvements in the Stellar Evolutionary Code ATON2.3

Thesis submitted to UNIVERSIDADE FEDERAL DE MINAS GERAIS as a partial requirement for obtaining the Ph.D. degree in Physics

Concentration Area: ASTROPHYSICS

Advisor: Dr. Luiz Paulo Ribeiro Vaz (UFMG)

Co-Advisor: Dr. Luiz Themystokliz Sanctos Mendes (UFMG)

International Collaboration: Drs. Francesca D'Antona and Paolo Ventura (Osservatorio Astronomico di Roma, Italy)

Departamento de Física - ICEx - UFMG

2006

Agradecimentos

Agradeço sinceramente às seguintes pessoas e instituições que contribuiram para a realização deste trabalho:

- a Deus pela oportunidade de trabalhar fazendo o que gosto;

- aos meus pais, Eustáquio e Lia, pelo amor, carinho, dedicação e por desempenharem tão bem o difícil papel de pais;

- aos meus irmãos Rodrigo, Randal e Nardelle pelo apoio, companheirismo e amizade;

- às minhas sobrinhas Isabela e Ana Flávia por preencherem nossa casa e nossas vidas com suas alegrias;

- ao Dr. Luiz Paulo (UFMG) pela orientação, incentivo e amizade durante todo o curso;

- ao Dr. Luiz Themystokliz (CPDEE) pela co-orientação e colaboração ao longo de todo o trabalho;

- aos meus co-orientadores italianos, Dra. Francesca D'Antona e Dr. Paolo Ventura *Osservatorio Astronomico di Roma*), não somente pela enorme contribuição ao trabalho, mas também pela hospitalidade durante minha estadia na Itália;

- aos professores e amigos do Laboratório de Astrofísica;

- a todos os meus amigos;

- aos membros da banca examinadora pelas críticas construtivas feitas a este trabalho.

- aos funcionários do Departamento de Física da UFMG, pela contribuição anônima;

- à CAPES, pelo apoio financeiro dado através de bolsas de estudos tanto no Brasil quanto no exterior;

- à FAPEMIG e ao CNPq (Instituto do Milênio e adicional de bolsa de pesquisa) pelo suporte financeiro dado para aquisição de computadores.

Acknowledgements

I thank sincerely the following persons and institutions that contributed to the accomplishment of this work:

- God for the opportunity to work doing what I like to do;

- my parents, Eustáquio e Lia, for their love, care, dedication and for performing so well the hard role of being parents;

- my brothers Rodrigo, Randal and my sister Nardelle for their constant support, company and friendship;

- my nieces, Isabela and Ana Flávia, for filling our home and lives with their joy;

- Dr. Luiz Paulo (UFMG) for the orientation, support and friendship during all the course;

- Dr. Luiz Themystokliz Sanctos Mendes (CPDEE) for the co-orientation and collaboration during all these years;

- my italian co-advisors, Dr. Francesca D'Antona and Dr. Paolo Ventura (*Osservatorio Astronomico di Roma*) not only for the enourmous contribution to the work, but also for their hospitality during my stay in Italy;

- my friends and teachers of the Astrophysics Lab;

- all my friends;

- the judging committee for the constructive critic given to this work;

- the staff of Physics Department - UFMG - for their anonymous contributions;

- CAPES for the financial support through scholarships during the whole course, including my stage in Italy;

- FAPEMIG and CNPq (Instituto do Milênio and research grants) for financial support given to acquisition of computers.

Contents

List of Figures

List of Tables

Resumo

No presente trabalho investigamos alguns efeitos físicos que acontecem na estrutura e evolução estelar. Focalizamos nossa atenção em estrelas de baixa massa na pré-sequência principal. Incluimos alguns efeitos físicos no código de estrutura e evolução estelar `ATON2.3`, escrito pelo Dr. Italo Mazzitelli (1989) e posteriormente modificado pelo Dr. Luiz Themystokliz Sanctos Mendes (1999b) para adicionar os efeitos de rotação e redistribuição interna de momentum angular. Com o objetivo de economizar tempo computacional, introduzimos o mecanismo de parada de controle (*checkpoint*), que permite iniciar uma dada execução em um estágio de evolução intermediário, desde que os passos iniciais tenham sido devidamente registrados. Essas modificações foram feitas juntamente com um controle completo de variáveis não inicializadas, precisão e reestruturação do programa, visando futuramente paralelizar o código. Introduzimos efeitos combinados de rotação e forças de maré na configuração de equilíbrio das estrelas. Esses efeitos perturbadores, contidos na função potencial total, desviam a forma da estrela da aproximação esfericamente simétrica. Usamos o método de Kippenhahn & Thomas (1970), posteriormente aperfeiçoado por Endal & Sofia (1976). À função potencial obtida por esses autores, adicionamos termos relacionados a forças de maré e outros relacionados à parte não simétrica do potencial gravitacional devido à distorção que tais forças causam na figura da estrela. Seguindo essa aproximação, corrigimos as equações constitutivas a fim de obter uma configuração estrutural de uma estrela distorcida. Derivamos uma nova expressão para a inércia rotacional de estrelas sob a ação de potenciais perturbativos devido à rotação e forças de maré. Cálculos de constantes de estrutura interna e raios de giração foram incluídos no código tanto para para o caso os modelos sem distorção quanto para os distorcidos. Apresentamos, pela primeira vez na literatura, cálculos de constantes de estrutura interna que se extendam até a pré-sequência principal. Várias trilhas evolutivas foram geradas com os novos modelos, incluindo as grandezas mencionadas acima. Os novos modelos foram testados através de dados observacionais das dimensões absolutas, taxa de movimento apsidal e abundância de lítio das componentes do sistema binário eclipsante EK Cephei. No presente trabalho, também apresentamos estimativas teóricas do "convective turnover time", τ_c, e Números de Rossby, *Ro*, para estrelas com massas semelhantes à massa solar, com rotação e na pré-sequência principal. *Ro* está relacionado com a força magnética na teoria do dínamo estelar e, pelo menos para estrelas na sequência principal, observa-se uma correlação entre rotação e atividade estelar. Incluimos também a possibilidade de utilizar modelos de atmosferas não cinza, com o objetivo de seguir a evolução estelar de estrelas de baixa massa desde estágios bem iniciais, caracterizados por baixa gravidade. Adotamos os modelos NextGen e ATLAS9 de atmosferas estelares. Usando os nossos novos modelos não-cinza, geramos vários conjuntos de trilhas evolutivas, partindo da pré-sequência principal. Tais trilhas foram usadas para investigar algumas propriedades físicas e rotacionais de estrelas jovens na Nebulosa de Orion. Comparações entre resultados teóricos e dados observacionais, permitiram-nos obter informações sobre esta classe de objetos, principalmente no que diz respeito à distribuição inicial de momentum angular. A interpretação dos dados depende fortemente das considerações físicas feitas no modelos, sendo a eficiência da convecção a mais importante. Nossa análise indica que um segundo parâmetro é necessário para descrever a convecção na pré-sequência principal. Tal parâmetro está possivelmente relacionado ao efeito estrutural de um campo magnético gerado por efeito dínamo.

Abstract

We have investigated some physical phenomena that take place in the stellar structure and evolution. Special attention was given to low-mass pre-main sequence stars. We have included the possibility of using non-gray atmosphere models in the boundary conditions, as well as the possibility of extracting information of some physical effects (like the internal structure constant and the Rossby number) in the stellar evolutionary code `ATON2.3`. The code was originally written by Dr. Italo Mazzitelli (1989) and further improved by Dr. Luiz Themyztokliz Sanctos Mendes (1999b) to take into account the effects of rotation and redistribution of angular momentum. In order to save computing time, we have introduced a *checkpoint* mechanism that allow starting the run in any step of evolution since previous computations had been registered. This modification was done together with a complete control for non-initialized variables, machine precision and restructuring, aiming a later implementation of parallel computation. We have introduced the effects of tidal forces combined with the rotational ones on the equilibrium configuration of the stars. These disturbing effects, all included in the total potential function, deviate the stellar configuration from sphericity. We have used the Kippenhahn & Thomas (1970) approximation, which was further improved by Endal & Sofia (1976). To the potential function obtained by the latter authors, we added both the terms related to the tidal potentials and those related to the non-symmetrical part of the gravitational potential due to the distortion of the star figure due to tidal forces. Following this approach, we correct the constitutive equations in order to obtain a stellar structure configuration of a distorted star. We dereived a new expression for the rotational inertia of tidally and rotationally distorted star. We included also calculations of internal structure constants and gyration radii, tabulating them for a serie of models. We presented, for the first time in the literature, calculations of the internal structure constant extended to the pre-main sequence. Our new models were tested against observations through the analysis of the evolutionary status of EK Cephei. We also present theoretical estimates of the convective turnover time, τ_c, and Rossby numbers, Ro, for rotating pre-main sequence solar-type stars. Ro is related to the magnetic strength in dynamo theories and, at least for main sequence stars, shows an observational correlation with stellar activity. We have included the possibility of using non-gray atmosphere models in order to follow the evolution of low mass stars starting from early, low-gravity stages. NextGen and ATLAS9 atmosphere models were adopted. By using our new non-gray models we generated sets of pre-main sequence evolutionary tracks that were used to investigate some physical and rotational properties of young stars in the Orion Nebular Cluster (ONC). The comparison between theoretical results and observational data allows us to otain some information about this class of objects, mainly those related to the initial distribution of angular momentum. The data interpretation was found to depend strongly on the physical inputs, being the convection efficiency the most significant one. The comparisons made indicate that a second parameter is needed to describe convection in the pre-main sequence, possibly related to the structural effect of a dynamo-generated magnetic field.

Chapter 1

Introduction

The physical processes occuring in the stellar interiors cannot be directly observed, except, perhaps, through the elusive neutrinos. The vast majority of the information we have about the conditions existing inside a star, comes from the light emitted by its atmosphere, what indirectly reflects the internal environment.

The stellar interior properties must be deduced from the observed features and from the laws that govern the stellar structure and evolution. Through a suitable combination of these laws in theoretical models, one can have an insight of the equilibrium configuration and of the temporal evolution of the stars.

There exist only few stellar features that can be directly observed. For a large number of stars, we have measurements of magnitudes (apparent and absolute) and color indexes. For the Sun and a relatively small number of components of binary systems, we have good determination of masses, radii and luminosities. Additional verifications in theories are provided by data obtained from asteroseismology, the study of the internal structure of stars through the interpretation of their pulsation periods, and from binary systems in which the line of apsides (the major axis of the orbit) presents a small rotation velocity. This phenomenon depends on the stellar internal conditions and, therefore, provides information that can be used to control the stellar interior theories. Information about the chemical composition of the stellar surface can be achieved spectroscopically, and one can assume that the composition of the major part of the stellar interior is similar to that of the outer layers, at least for main sequence (MS) stars. On the other hand, giant stars have already processed part of the elements originally present in their interior, and the spectroscopic data can only provide reliable information about the surface chemical composition.

When we try to understand the life of a star, we face a hard problem: stars last much more than a human life. A human could never watch a star go through its complete life cycle. We need a special approach. We use the laws of physics and a few observable quantities to understand the lives of stars. In order to learn about the life cycles of a star, we look at a large number of stars. We can see them in various stages of development. If we look at enough stars of various ages, we can put together a complete picture of stellar evolution. The tool we use to study stars is called the Hertzsprung-Russell diagram

(usually referred to by the abbreviation H-R diagram or HRD; another form of it is also known as a Colour-Magnitude diagram, or CMD). It shows the relationship between absolute magnitude, luminosity, spectral classification, and surface temperature of stars. The diagram was developed independently by Ejnar Hertzsprung in 1911 and Henry Norris Russell in 1913 and represented a huge leap forward in understanding stellar evolution, or the "lives of stars". From it, most of the peculiarities of stellar behavior can be studied. One of these, in particular, is that the stars are sitting along a well-defined band called MS, where the majority of stars are clustered in a region from the bottom right to the top left (see Fig. 1.1). The H-R diagram is the fundamental tool astronomers use to explore the birth and the death of stars. Although it began as a way to group information concerning the intrinsic characteristics of stars, it quickily became a tool to explore changes in stars as they age. It is used to define different types of stars and to match theoretical predictions of stellar evolution using computer models with observations of actual stars. It is then necessary to convert either the calculated quantities to observables, or the other way around, thus introducing an extra uncertainty.

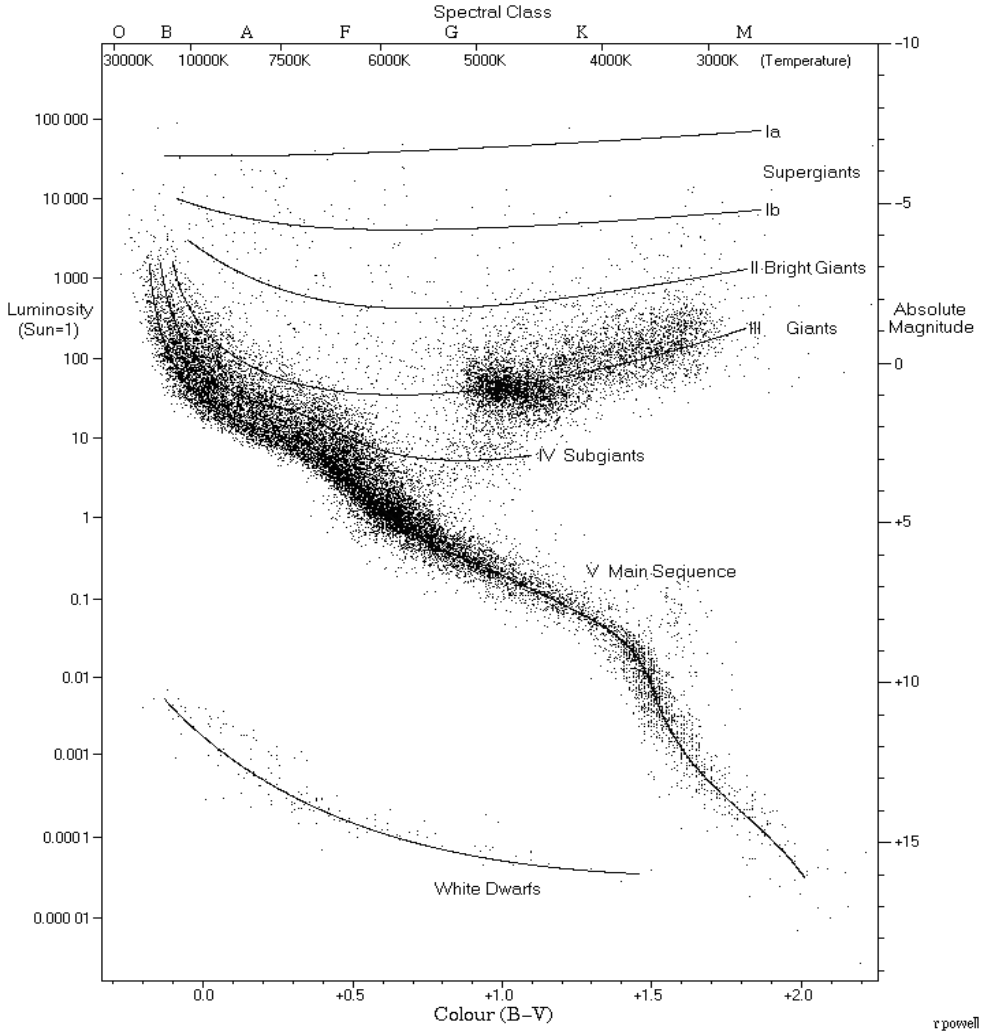

Figure 1.1: Hertzsprung-Russell diagram with 22,000 stars plotted from the Hipparcos catalog and 1000 from the Gliese catalog of nearby stars.

The theoretical studies about the stellar interior are based in a set of equations that must be solved simultaneously, aiming to reproduce the observed stellar properties and to explain the internal structure of the stars. Such models treat the physical phenomena taking place inside a star by describing them through basic equations that govern the internal physical properties. The basis of the stellar structure theory was developed in the first part of the past century, when several important works were published, among which those of Chandrasekhar (1939) and Schwarzschild (1958) can be considered the fundamental ones.

The structure of a star can be described by a set of differential equations containing variables like pressure, density, temperature, luminosity, etc. They are the so-called "constitutive equations":

$$\frac{dP}{dM} = -\frac{GM}{4\pi r^4} \tag{1.1a}$$

$$\frac{dr}{dM} = \frac{1}{4\pi r^2 \rho} \tag{1.1b}$$

$$\frac{dL}{dM} = \epsilon - T\frac{\partial S}{\partial t} \tag{1.1c}$$

$$\frac{dT}{dM} = -\frac{GMT}{4\pi r^4 P}\nabla, \qquad \nabla = \{\nabla_{\rm rad}, \nabla_{\rm conv}\}\,. \tag{1.1d}$$

This equations are respectively named equation of hydrostatic equilibrium, equation of continuity of mass, equation of conservation of energy and equation of transport of energy. Besides the set of Eqs. (1.1), it is also necessary to assume an equation of state of the material that form the star, an opacity law and an equation of energy generation to describe the stellar structure. Furthermore, some boundary conditions must be defined in order to match interior and atmosphere integrations. The theoretical models are built aiming the self consistent solution of these equations throughout the stellar radius, having the stellar mass and the initial chemical composition (and, eventually, some amount of rotation) as input parameters. A sequence of models of stellar structure in successive time intervals define a stellar "evolutionary track" in the HRD.

In the 1960's, the construction of evolutionary models was stimulated by the introduction of the *relaxation method* for the numerical solution of the differential equations that describe the stellar structure (Henyey, Forbes & Gould 1964). This method replaces the differential equations with a set of finite difference equations whose solution is carried out globaly and enables one to include time-dependent phenomena in a natural way. Also, the appearing of faster computers speeded up the improvement process of the models. Besides that, the knowledge of several other aspects of the stellar interiors, such as nucleosynthesis of elements (Clayton 1968) and more realistic opacity tables calculations (Cox & Stewart 1970), were important in bringing the models to a very well succeeded interpretation of a large part of intermediate mass stars in the MS phase.

The physical processes happening inside a star are rather complex to be completely reproduced by the models. The models are necessarily an idealized scenario of this complicated environment and, consequently, cannot reproduce, with the desirable accuracy, the large quantity of observational data obtained from real stars. Since the first models became available, researchers have made efforts to improve the quality of the achieved results by developing new numerical tools and/or by introducing in the codes improved

approximations for the underlying physical phenomena. It is important to emphasize that, although some of the physical processes involved in the stellar theories have solid theoretical basis, the corresponding implementation in the models is, most of the times, a hard task. This is due to a series of problems, such as numerical accuracy and instability, mathematical complexity, computational time, and so on. A significant number of important questions related to stellar structure and evolution is still under debate. A good example is turbulence, that is not well understood, yet. Many of these several open issues are discussed in some reference works. For example, the problem of the chemical mixing of elements was addressed by Goulpil & Zahn (1989); D'Antona & Mazzitelli (1984) discuss the lithium and berilium burning, Mihalas et al. (1988) treat the stellar equation of state; Canuto & Mazzitelli (1991) give some insight on the turbulent convection, and Kippenhahn & Thomas (1970) investigated the influence of rotation in the stellar evolution. Some of these subjects, like rotation and turbulent convection, have already been implemented in the evolutionary models and presented promising results.

Regarding the star formation process, one believes that the stars are formed from clouds made up by the interstellar material. The chemical composition of a newborn star is similar to that of the cloud from which the star in question was formed. The total stellar mass is primarily determined in the formation process, although it can undergo some changes due to the residual accretion after the protostellar phase (Basri & Bertout 1989) and to outflows, which are mass loss processes due to magneto-rotationally driven winds (Hartmann & MacGregor 1982).

Star formation occurs as a result of the action of gravity on a wide range of scales, and different mechanisms may be important on different scales, depending on the forces opposing gravity. On galactic scales, the tendency of interstellar matter to condense under gravity into star-forming clouds is counteracted by galatic tidal forces, and star formation can occur only where the gas becomes dense enough for its self-gravity to overcome these tidal forces, for example in spiral arms (Larson 2003). On intermediate scales, turbulence and magnetic fields may be the most important effects opposing gravity, while on the small scales of individual prestellar cloud cores, thermal pressure becomes the most important force resisting gravitation. When the cloud core begins contracting, the centrifugal force associated with its angular momentum may eventually interrupt the collapse, leading to the formation of a binary or multiple star system. When a very small central region attains stellar density, the contraction is halted by the thermal pressure and a protostar forms and continues growing in mass by accretion. In this final stage of star formation, magnetic fields can become important by controlling gas accretion and outflows. These events characterize the pre-main sequence (pre-MS) evolutionary phase. As the thermodynamic conditions within a star become close to those suitable for the nuclear reactions ignition, these phenomena finish and the star approaches a far more stable configuration, called MS.

After deutherium, lithium and berilium burning phases, which take place in early phases of evolution, the first element to be processed within the star is the Hydrogen. When the star has hydrogen burning as its main energy source, the latter can be considered in the MS. Iben (1965) defines the Zero-Age Main Sequence (ZAMS) the time at which 90% of the total stellar energy comes from the Hydrogen burning. The stars spend the major part of their lives burning Hydrogen. This is a long, quiet and stable phase of their evolution. During the MS, the changes in radius, luminosity, temperature, density, and other quantities, are negligible. It will last until the available supply of Hydrogen for

"burning" is almost completely consumed. As the more massive stars have higher central temperature, pressure and density, they process their nuclear Hydrogen faster than the lower mass stars, remaining less time in the MS. Therefore, the time spent by a given star in the MS phase, and, in general, in its evolution after that, is determined by its initial mass.

Depending on the stellar mass, other chemical elements can be processed in the stellar nucleus. The production of new elements, other than Helium (from H-burning), by nuclear reactions is called "nucleosynthesis". Again, the stellar mass will determine what kind of reactions will take place in the central core of a star. Objects with less than $0.08 M_\odot$, the so-called brown dwarfs, are not real stars because they never develop a central temperature which is high enough to ignite Hydrogen burning. Instead, they release energy by gravitational contraction. The very low mass stars (between about 0.25 and 0.08 $M_\odot$) are real fully convective stars that burn Hydrogen in their cores, via p-p chain, so slowly that they will stay on the MS for a very long time (about 10^{12} years). Once Hydrogen is burned out, the core collapes, but never reaches temperatures high enough to ignite Helium-burning. Such stars evolve directly to white dwarfs. One believes that the universe is so young that no very low-mass stars has had time to evolve off the MS, so this prediction is not really testable. Low mass stars ($0.25<M/M_\odot<1.2$) have radiative cores, so that the surrounding Hydrogen cannot be transported into the core where it can be burned. Instead, only the Hydrogen inilially present in the inner core, where the temperature is high enough, will be processed via p-p chain. When the Hydrogen is used up, the central core contracts gravitationally until the degeneracy halts the contraction. Eventually, the core will heat up until Helium can be ignited and, when this occurs, the star is in a giant phase. He-burning in degenerate core takes place explosively, in a process called "Helium Flash". The changes produced by this process are very rapid and the physics involved becomes very difficult to be described approximately. Despite the difficulties involved in calculations of the He flash, the star certainly ends up in a stable configuration, where it burns Helium in the core and Hydrogen in a shell around it. This phase is called the "Horizontal Branch". After Helium is used up in the core, He-burning shell takes place, but the star will not be able to burn any further element because it cannot get hot enough in the core, and it will move to the white dwarf region.

High mass stars ($M>1.2\,M_\odot$) have convective cores and, for this reason, a large amount of Hydrogen can be transported to the central regions, where it can be burned into He by the CNO cycle. In this way, a considerable fraction of the Hydrogen is processed and the following gravitational collapse phase may be relatively short. In the Hertzprung-Russel diagram, the stars in this phase are supposed to be in a region called "Hertzsprung gap", that lies between the MS and the giant branch. In fact, only a few stars observed in open clusters are found in this region. After Hydrogen is consumed in the core, the central regions of the star begin collapsing, and the Hydrogen burning can continue in a shell outside the core. When the temperature becomes high enough, Helium begins burning in the core, building Carbon. Even when the Helium in the core is finished, Helium can continue being processed into Carbon in a shell outside the core, while still further out the Hydrogen burning shell continues producing Helium. The core contracts again, the outer layers expand, and the star increases in luminosity. Then, the ignition of Carbon takes place in the core building other elements like Mg, Ne and Na. After Carbon burning, and depending on the mass of the star, further elements can be processed all the way to Fe, beyond which no further energy can be extracted by fusion because the production of any

heavier nucleus by direct fusion is endothermic. Massive stars can reach a stage where they consist of shells of nuclear burning, with Fe production in the core, surrounded by shells of Si, C and O, He and H. Eventually, the fuel sources will finish and the star (if the mass is high enough) will undergo a core collapse, resulting in a supernova. In this process, a small amount of elements beyond Fe can be produced. The result of such a collapse can be a neutron star or a black Hole (for very high mass stars).

The main goal in building evolutionary tracks is to explain the processes described above, following the structural changes that a given star undergoes throughout its evolution. Most of the current evolutionary models start the stellar evolution from the ZAMS and follow the evolution of the stars until their post-main sequence (post-MS) phase, without considering the processes that can take place on the pre-MS evolution that, consequently, affect the MS configuration. Since the works by Henyey et al. (1955) and Hayashi (1961), it is commonly accepted that pre-MS stars derive their energy by gravitational contraction, with exception of a short D-burning phase. In general, the definition of the zero point of ages for pre-MS evolution is connected to the location in luminosity of the *starting model*, i.e., the internal thermodynamic conditions within the star, for which, the stellar structure equations can be numerically solved. An extensivelly used approximation when modeling pre-mais sequence evolution, is to consider that the mass accretion proccess does not continue further the zero age point.

The first models, the so-called "standard models", considered the star as an homogeneous gas sphere, in complete hydrostatic equilibrium (balance between pressure and gravity). Besides, they did not include more complicated effects such as rotation, magnetic fields, etc. These models were capable to reproduce the basic global characteristics of the stars available by that time, but as the quantity and accuracy of observational data increased, the standard models showed to be inefficient and with many limitations. They failed in reproducing the abundances of light elements like Lithium and Berilium in low mass stars and in fitting the position in the HR diagram of some pre-MS components of binary systems. Another inconsistency between observations and standard models is the anomalous surface abundances in evolved stars, suggesting that the elements may be mixed in deeper layers (Langer et al. 1993). Rotation is a feature found in all stars and, even if its intensity is low, it is nowadays considered an important causing agent of mixture.

In order to explain the new and more accurate observational stellar data, the modelists improved the evolutionary models with some non-standard effects. The first attempts to include rotation effects in the evolutionary codes date from the 1960's and are in use still today (Faulkner et al. 1968, Sackmann & Anand 1969, Kippenhahn & Thomas 1970, Papaloizou & Thomas 1972).

As already mentioned, magnetic fields can play an important role in the last stages of pre-MS evolution. However, the existing evolutionary models do not take their effects into account, although the subject is treated in some exploratory ways. According to D'Antona et al. (2000), the inclusion of magnetic fields in the models, considering the hypothesis that they are produced by rotation, changes the Schwarzschild's stability criterion, so that the convection is established for a temperature gradient higher than in non-magnetic cases. This gradient is inversely proportional to the effective temperature, so the magnetic fields seems to have a thermal effect in the pre-MS stars, leading to cooler models. In a series of works, Maeder & Meynet (2003, 2004, 2005) and Eggenberger et al. (2005) studied the relative importance of rotational and magnetic effects in high mass stars, by

calculating the magnetic instabilities that may rise in differentially rotating stars and create magnetic fields.

While models with magnetic fields are not available, one can have some insight about the stellar magnetic fields through the stellar magnetic activity, that can be observed in a broad range of phenomena (sunspots, flares, chromospheric emission lines). In solar-type stars, the driving mechanism for stellar magnetic activity is the magnetic field that is presumably generated by a dynamo in the deep layers of the convection zone and in the overshoot region just below the convection zone itself (Montesinos et al. 2001). For fully convective stars the driving mechanism for stellar magnetic activity is thought to be a distributed dynamo, which depends on the turbulent velocity field. It is also possible that the dominant source of magnetic flux in the T Tauri stars are "fossil fields" inherited from the star formation process (Mestel 1999). From the theoretical point of view, researchers try to understand the observed correlations between activity-related parameters and stellar parameters such as mass, temperature, gravity, rotation velocity, and quantities related to the internal structure of the star. Semi-empirical calculations of an activity indicator, such as the Rossby number, have been a way for this kind of investigation (see Feigelson 2003). More recently, self-consistent values of th Rossby number, calculated theoretically by rotating models, became available (Kim & Demarque 1996 and Landin et al. 2005).

As it is emphasized by Mihalas (2001), the atmosphere of a star is what we can see, measure and diagnose. So, the treatment given to the stellar atmosphere directly influences the results obtained by the evolutionary models. Chabrier & Baraffe (1997) pointed out that the use of $T(\tau)$ relations or the gray atmosphere (widely used in the first models) is invalid when molecules form near the photosphere. For stars with effective temperature below about 4000 K, the atmosphere must be modeled by using more realistic treatments, such as the non-gray approximation. Non-gray atmosphere boundary conditions can be obtained from the atmospheric models for a wide range of metallicities, effective temperatures and gravities. As good examples, we can cite the NextGen (Allard et al. 1997) and ATLAS9 (Heiter et al. 2002) atmosphere models.

Because of the fact that binary stars are the most reliable source of accurate information about the most basic stellar parameters, they are largely used to compare theory and observations. They provide also important information about stellar phenomena like tidal and rotational distortions, limb darkening, mutual irradiation, etc., which, although sometimes neglected, may be the responsible for some differences between stellar evolution in binary and single stars (Claret 1993). It is well known that tidal and rotational distortions of the stellar configuration are related to the internal structure constants of the component stars (Kopal 1978). An important consequence of such distortions in eccentric binary systems is the secular change in the position of the periastron, that can be accurately measured by monitoring times of minimum light in eclipsing binaries. From this kind of data, we can derive empirical values of the internal structure constants in order to compare them with theoretical predictions.

All the effects cited above are important in the stellar structure and evolution. The inclusion of new physical phenomena in stellar evolution models greatly improves the comparisons with observations. This is the reason why modelists concentrate efforts in continuously introducing new and more realistic physical inputs in the evolutionary codes.

The evolutionary code used in this study is the `ATON2.3`, originally writen by Dr. Italo Mazzitelli (Mazzitelli 1989, Mazzitelli et al. 1995 and D'Antona & Mazzitelli 1997)

and further updated by Dr. Luiz Themystokliz Sanctos Mendes (Electronic Engineering Department of Universidade Federal de Minas Gerais), my co-advisor, in his Ph.D thesis, for including rotation and angular momentum redistribution (Mendes 1999b). This work was coordinated by Dr. Luiz Paulo Ribeiro Vaz (Physics Department of Universidade Federal de Minas Gerais), also my Ph.D advisor, who started a scientific collaboration with Dr. Francesca D'Antona (Osservatorio Astronomico di Roma, Italy) and Dr. Italo Mazzitelli allowing our access to their evolutionary code. The present Ph.D work was carried through the international collaboration with the italian researchers, including a year of activities in Italy, having Dr. D'Antona as foreign co-advisor. During this time, Dr. Paolo Ventura (Osservatorio Astronomico di Roma) participated of the collaboration work, also.

In this work, we investigate some physical phenomena that take place in the stellar structure and evolution, like stellar activity, rotation, tidal interaction and non-gray effects of radiative process. Special attention is given to low mass pre-MS stars.

In general, inclusion of new physical processes in evolutionary codes is a work that demands a long time to be completed, mainly due to the many debuging steps in testing the changes. Aiming to save computing time, we decided to change the computational structure of the `ATON2.3` code, introducing a mechanism that allows starting the run in an intermediate step of the evolution, since the initial steps have been registered in a previous run. This mechanism is known as *checkpoint*. After that, we introduced in the code some important modifications to test theoretical predictions. The first one was the theoretical computations of convective turnover times and Rossby numbers. Further, we implemented the computation of the internal structure constants, in the `ATON2.3`, fundamental in apsidal motion tests. Finally, we included in the code more realistic boundary conditions by using the NextGen and ATLAS9 atmosphere models.

In Chap. 2 we present the changes we made in the computational structure of the code concerning the checkpoint. The changes to consider the stellar equilibrium configuration modifications due to tidal and rotational distortions, and the internal structure constant calculations, are shown in Chap. 3. Chap. 4 presents the theoretical estimates of the Rossby number with our modified model. In Chap. 5 we describe the implementation of non-gray boundary conditions. Chap. 6 gives the general conclutions and suggests some future improvements of the work already done. And, finally, in Chap. 7 we bring a synopsis of the work in Portuguese.

Chapter 2

Structural Changes in the Stellar Evolutionary Code ATON 2.3

The modeling of physical processes describing both the structure and the evolution of stars is usually very complex. Some processes have well founded theoretical basis, but are implemented in stellar models with several degrees of simplifications. Often, these difficulties of implementation are due to mathematical complexity, numerical accuracy, long computing time, etc. On the other hand, there are some physical processes that remain still very poorly understood and, for this reason, they are completely ignored in the stellar models or taken into account in a very idealized approach.

In general, implementation of physical improvements in stellar evolutionary codes is a work that demands a long time to be completed, mainly when we are testing them, because the same calculation steps must be repeated several times. However, test phases are a fundamental part of the model development and very efficient at locating certain types of faults in the program.

Aiming to save computing time, we changed the computational structure of the ATON 2.3 code, in order to introduce a mechanism that allow starting the run in an intermediate step of the evolution, once the initial steps have been registered in a previous run. This is the mechanism of *checkpoint*. In this chapter we will explain how we have introduced it in the code and how it works.

2.1 Implementation of the structural changes

In order to improve the performance and to make easier the testing and debugging of the physical changes introduced in the ATON2.3 code, it became evident, after an accurate analysis, that its structure should undergo some changes. Since the code has been evolving through the contribution of many different authors, it is written in many different "dialects" of FORTRAN, making necessary an uniformization of the code in numerical precision, "common blocks" alignment, declaration of variables, etc. These structural improvements were made by using some analyzing and transforming tools for FORTRAN

77 from `NagWare FORTRAN Tools`, Release 4.0, 1990 (The Numerical Algorithms Group Limited). The transformers carry out automatic transformations on FORTRAN 77 codes. These can be used to make repetitive changes to code easy, eliminating errors introduced by "hand editing". The principal analyzer gives a more rigorous approach to verification of FORTRAN 77 code against the ANSI (American National Standards Institute) standard than, in general, compilers do. This analysis is also extended to highlight non-portable usage of FORTRAN 77 features.

With NagWare's tools, we have checked for non-initialized variables and converted the whole code to double precision. Besides, we standardized the layout of the code, changed the spacing within and between the lines, byte aligned all COMMON structures, etc. These procedures must be done before the step of controlling the memory use for the implementation of a working mechanism for check-points. Checkpointing facility consists in saving all necessary variables in one or more binary files at some given stages during the code execution, so that a given run can be resumed from one of such stages. In this way, in a further execution one can read the recorded binary file and continue the computations of the previous model from the intermediate stage memorized and continue to evolve the star. In the Fig. 2.1 we show how the checkpoint works, schematically.

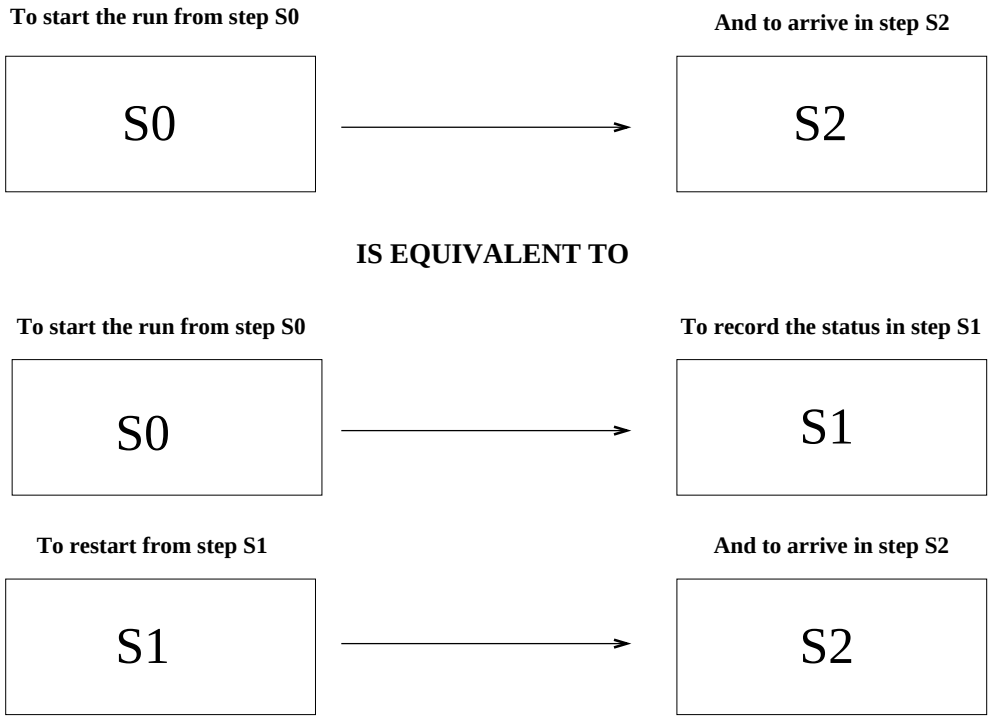

Figure 2.1: Diagram showing the functioning of the checkpoint mechanism.

In order to introduce this procedure in the code, we created two new routines and modified some of the previously existing ones, adjusting them in the new structure of the code. The first of the new routines is responsible for saving in a binary file (of about 9MB), at a given step of the code execution, all global variables needed to go ahead with the calculations from that intermediate step on. When it is necessary to restore the memory of a given model in an already registered point of the execution, the program

makes use of the second new routine, especially designed for reading all this set of data from the corresponding binary file. With these variables restored in its memory, the code can continue to run and produce, upon its termination, the same results generated if it had started from the initial point, with an evident gain in computing time and. equally important, without any loss of numerical accuracy.

2.2 The importance of the checkpoint mechanism

The checkpoint mechanism is a fundamental tool when modifying computational models, mainly in cases where the program in question is complex and takes a long time to be executed. In order to illustrate how the computing time varies with the complexity of the program, let us consider the execution time spent by earlier versions of the `ATON` code for reproducing some characteristics of a star with the same mass and metallicity as the sun, running in a XEON 1.8 GHz processor. The 2.0 version of the code is relatively simple and spends 3 (three) minutes to perform the calculations for such a star without considering rotation, starting from the pre-MS and arriving in the MS configuration, what is equivalent to an age of 9.6 billion years. But this computing time increases by a factor of 7 (seven) if we let this star evolve until 13 billion years, when it will be a red giant. In the post-MS phase, the time scale of the processes are much shorter than in MS, so an evolution of an interval of Δt requires more computing time in the evolved phases than in the previous MS ones.

The `ATON2.3` code is a more realistic version of the stellar evolutionary model in question, in the sense that it takes into account the non-standard effects of rotation, ignored by the previous versions. We can choose among three different schemes of rotation: rigid body rotation or differential rotation over the whole star, or rigid body rotation in the convective zones plus differential rotation in radiative regions. In the first two cases, the code spends about 13 (thirteen) minutes to evolve the star from the pre-MS to the MS configuration. In the third case, the same evolution is done in 25 (twenty five) minutes. The computing time for evolving a solar-like rotating stars from the pre-MS to the post-MS will certainly increase considerably, but we do not quantify it, yet, because the rotating version of the code is not suitably tested beyond the MS phase.

The higher the consistency in the physical processes inserted in the evolutionary code, the greater will be the computing time needed to accomplish the computational task. So, the importance of a checkpoint mechanism is clear, not only during implementation and test phases of aimed improvements, but also in the studies of the model properties, after the implementations have been tested. When some aimed improvement is activated in a more evolved phase of the stellar evolution, such as mass transfer in binary systems, mass loss in evolved phases, etc., the checkpoint mechanism is even more efficient. It allows to evolve a model until a given stage, before the physical process in question is activated, and store all necessary variables to continue the evolution. After that, we can study our modifications regarding this process, just by restarting the computation from the relevant point. In this mode of execution, all computing time spent to run the initial part of calculations will be saved, without loss of information, accuracy or precision.

This mechanism was already successfully used in the present work to implement the self-consistent calculation of both local and global "convective turn over time", and in the studies about the internal redistribution of angular momentum.

Chapter 3

Internal Structure Constants

The internal structure constants, namely, k_2, k_3 and k_4, also known as apsidal motion constants, are important parameters in stellar astrophysics. They are mass concentration parameters and depend on the mass distribution throughout the star. There is, also, a direct relation between the gravitational field of a non-spherical body and the internal density concentration in that body (Sahade & Wood 1978).

From the theoretical point of view, the values of k_j (j=2, 3, 4) depend on the model used. For the Roche model, in which the whole stellar mass is concentrated in its center, the k_j's values are all equal to zero, while for a homogeneous model k_2=3/4, k_3=3/8 and k_4=1/4. The values of the internal structure constants are essential to compute the theoretical apsidal motion rates in close binaries, and the comparison with the observations constitutes an important test for evolutionary models. The most centrally concentrated stars have the lowest values of k_j and the longest values of apsidal periods (Eq. 3.6).

From the observational point of view, it can be shown that the apsidal rate $\dot{\omega}$, in radians per cycle, in terms of the internal structure constants is given by (Martynov 1973, Hejlesen 1987):

$$\frac{\dot{\omega}}{2\pi} = \sum_{i=1}^{2} \sum_{j=2}^{4} c_{ji} k_{ji}, \tag{3.1}$$

where the index i denotes the component star (1=primary, 2=secondary) and j the harmonic order. Generally, the terms of orders higher than j=2 are very small and the equation above gives the empirical weighted mean k_2 values for comparison with theoretical coefficients (Eq. 3.18). Although not directly comparable with observational data, the apsidal motion constant, k_2, is important in other astrophysics aspects, since synchronization and circularization time scales in close binaries are functions of k_2 (Zahn 1977). Other applications of the internal structure constants are the computation of rotational angular momenta (as can be seen in the Sect. 3.5.4), where gyration radii (defined in the Eq. 3.83) can be expressed as a linear function of the apsidal motion constants (Ureche 1976), and the determination of the effect of binarity in the geometry of the stellar surfaces due to rotation and tides (Ruciński 1969, Kopal 1978).

Russell (1928) was the first one to find an analytical expression for the apsidal motion

period in close binaries (later improved by Cowling 1938), in terms of the stellar masses, relative radii and internal structure constants of the component stars. Meanwhile, Chandrasekhar (1933) used polytropic models to predict internal structure constants for main sequence stars. At that time the large uncertainties involved, in obtaining observational data as well as the use of polytropic models with an arbitrary index n, were responsible for the apparently good agreement obtained between observed and predicted values of $\log k_2$. By using more realistic stellar models, a more elaborated expression for the apsidal motion period, separating rotational and tidal contributions to the total apsidal motion rate, was derived by different authors. Apsidal motion test was also applied to polytropic stellar models by Sterne (1939), Brooker & Olle (1955) and later to early theoretical stellar models at the ZAMS by Schwarzschild (1958) and Kushawa (1957), both using the old Keller & Meyerott (1955) opacities. Since then, comparisons between theory and observations have systematically shown that real stars are more centrally condensed than predicted by theoretical models. After that, Jeffery (1984) and Hejlesen (1987) computed more recent internal structure constants for stars within the main sequence. The former author used Carson (1976) opacities while Hejlesen used opacity tables by Cox & Stewart (1969). The most recent internal structure constants for main sequence stars are those by Claret & Giménez (1989a, 1991, 1992).

In this work, we present new calculations of internal structure constants extended, for the first time, to the pre-main sequence phase. We calculated internal structure constants for spherically symmetric stars by using a standard version of the `ATON` code (without a disturbing potential). By using our new version of the `ATON` code, described in the Sec. (3.5), we calculated new internal structure constants for rotating stars, stars in binary systems, and rotating stars in binary systems. As a by-product of our calculations, we also derived a new expression for the rotational inertia of a star distorted by rotation and tidal forces (see Sec. 3.5.4). The results are presented in the Sec. (3.6). Discussion and comparisons with observed apsidal motion rates are given in Sect. (3.7).

3.1 Apsidal motion

The longitude of periastron of a binary orbit, denoted by ω, defines the direction of the line of apsides in the orbital plane. It is an element of the orbit, which is constant if all the following conditions, in a system consisting of two gravitating bodies, are valid:

- the bodies can be regarded as point masses,
- they move in accordance with Newton's law of gravitation (r^{-2}), and
- the two bodies form a gravitationally isolated system.

However, if any of these assumptions are not satisfied, the size, the form, and the spatial position of the orbit will vary. The most readily detected departure of the observed motion from the prediction of the simple theory is a variation in the value of ω with time, what is referred to as rotation (advance or recession) of the line of apsides. For a more detailed discussion on this subject, the reader is addressed, for instance, to the works of Batten (1973) or Claret & Giménez (2001).

There exist several types of perturbations that can lead to rotation of apsides, namely mutual tidal distortion of the components, distortion of the components due to axial

rotation, relativistic effects, presence of a third body, and recession due to a resisting circumstellar medium.

In close binary systems, the axial rotation and the mutual tidal forces of the component stars will deform each other and destroy their spherical symmetry, by means of the respective disturbing potentials. Besides the changes in the stellar structure described in Sect. 3.5, these disturbing potentials produce an observed variation in ω which is the sum of the variations produced by each component (Batten 1973). The final resultant variation of ω produced by the disturbing potentials, Eq. (3.72), i.e., the rate of apsidal advance, $\dot{\omega}$ per orbital revolution, is given by

$$\frac{\dot{\omega}}{2\pi} = \frac{P}{U} = k_{21}c_{21} + k_{22}c_{22}, \tag{3.2}$$

where P is the anomalistic orbital period and U is the apsidal motion period, and

$$c_{2i} = \left[\left(\frac{\Omega_i}{\omega_K}\right)^2\left(1+\frac{M_{3-i}}{M_i}\right)f(e) + \frac{15M_{3-i}}{M_i}g(e)\right]\left(\frac{R_i}{A}\right)^5. \tag{3.3}$$

In Eq. (3.3), the subscript i=1,2 stands for star 1 and star 2 respectively, M_i and R_i are stellar mass and radius of component i, A is the semi-major axis, e is the orbital eccentricity, and functions $f(e)$ and $g(e)$ are defined as

$$f(e) = (1-e^2)^{-2} \quad \text{and} \tag{3.4}$$

$$g(e) = \frac{(8+12e^2+e^4)f(e)^{2.5}}{8}, \tag{3.5}$$

(Ω_i/ω_K) being the ratio between the actual angular rotational velocity of the stars and that corresponding to synchronization with the average orbital velocity. Note that Eq. (3.2) is a special case of Eq. (3.1), in which only the second order harmonics are taken into account. The first term in Eq. (3.3) represents the contribution to the total apsidal motion given by rotational distortions and the second term corresponds to the tidal contributions.

With the exception of the k_{2i}'s, all parameters in the above equation can be independently measured and thus the weighted average of the internal structure constants can be empirically derived for individual systems. The observational average value of the apsidal motion constant of the component stars is moreover given by

$$\bar{k}_{2obs} = \frac{1}{c_{21}+c_{22}}\frac{P}{U} = \frac{1}{c_{21}+c_{22}}\frac{\dot{\omega}}{2\pi}. \tag{3.6}$$

From Eqs. (3.3) and (3.6), we can see that the derived average values of $\log k_2$ depend on our knowledge of the rotation velocities of the component stars. In most binaries with good absolute dimensions, the rotation velocities of the individual components are known through spectroscopic analysis. Since the average orbital rotation, or Keplerian velocity, is a function of the orbital period, the ratio of rotational velocities in Eq. (3.3), namely, Ω_i/ω_K, is well determined in these binaries (Claret & Giménez 1993). For some systems the observational values are not available. In these cases, the best approximation is given by assuming that the component stars are synchronized with the orbital velocity at periastron, where the tidal forces are at maximum. In this case, the mentioned rotation velocities ratio is given by (Kopal 1978)

$$\omega_P^2 = \frac{(1+e)}{(1-e)^3}\,\omega_K^2, \tag{3.7}$$

where ω_P is the angular velocity at periastron, e, as in Eq. (3.3), denotes the orbital eccentricity, and ω_K is the Keplerian angular velocity, given in Eq. (3.15). Claret & Giménez (1993) have checked the validity of this approximation and they achieved a good agreement between the observed and the predicted rotational velocities assuming synchronization at periastron (see their Fig. 6).

The mean values of k_{2i}, calculated by Eq. (3.6), can be compared with those derived from theoretical models, Eq. (3.18). However, the observed mean value of k_{2obs} should be corrected first from non-distortional effects, like relativistic, third body, and interstellar medium contributions.

3.1.1 Relativistic Effects

In cases where Newton's law of Gravitation is not valid, where the relativistic effects are important, the observed apsidal motion rate has to be corrected from the relativistic contribution (Levi-Civita 1937; Kopal 1978; Giménez 1985). Einstein's theory of relativity predicts an advance of the line of apsides, even if the two stars can be considered as point masses, due to the different time metrics in different points of the eccentric orbit. In this case, the displacement does not depend on rotational and tidal distortions and should be added to the classical Newtonian term. In fact, it is found that the change in position of the periastron per orbit is given by (Levi-Civita 1937)

$$\delta\omega = \frac{6\pi GM}{Ac^2(1-e^2)}, \tag{3.8}$$

where M denotes the total mass of the system and, if U' denotes the period of revolution of the line of the apsides, we have

$$\frac{P}{U'} = 6.35 \times 10^{-6} \frac{M_1 + M_2}{A(1-e^2)}, \tag{3.9}$$

provided that the semi-major axis and the masses are given in solar units.

3.1.2 Effects of a third body

Other possible correction comes from the fact that the binary system may not be completely isolated. The presence of a third component with period P' perturbs the orbit of a close binary system with period P, and one of the affected orbital elements is the longitude of the periastron. The induced apsidal motion, U'', for coplanar orbits and small eccentricities can be approximated by (Martynov 1948)

$$\frac{P}{U''} = \frac{3}{8}\frac{M_3}{M_1+M_2+M_3}\left(\frac{P}{P'}\right)^2 + \frac{225}{32}\frac{M_3^2}{(M_1+M_2+M_3)^2}\left(\frac{P}{P'}\right)^3. \tag{3.10}$$

In general, if we consider that the two orbits are eccentric and not coplanar, we have

$$\frac{P}{U''} = 2a\left(1 - \frac{e^2}{2} + \frac{3}{2}e'^2 - 2\tan^2 I\right) + 50a^2 \tag{3.11}$$

where

$$a = \frac{3}{8}\frac{M_3}{M_1+M_2+M_3}\left(\frac{P}{P'}\right)^2 (1-e^2)^{-3/2}, \tag{3.12}$$

in which e is the eccentricity of the orbit of the close pair, e' is the eccentricity of the orbit of the wide system, and I is the inclination angle between the close and the wide orbits.

Besides that, the line of the nodes also precesses with a period U''

$$\frac{P}{U''} = 2a\left(1 + 2e^2 + \frac{3}{2}e'^2 - \frac{1}{2}\tan^2 I\right) - 2a^2. \tag{3.13}$$

3.1.3 Effects of interstellar medium

Another effect that may change the rate of advance of periastron is that of a viscous medium. The resistance itself has no influence on that rate but the mutual attraction is changed. Indeed, there appears a recession of the apsidal motion given by (Hadjidemetriou 1967)

$$\frac{P}{U'''} = -\frac{GP^2\sigma}{2\pi} \tag{3.14}$$

where U''' is the period of revolution of the line of the apsides due to this effect and σ stands for the density of the medium. Average interstellar densities, though, imply that this effect should be in general a negligible contribution.

3.2 Equilibrium configuration of stars

A binary system consists of two stars that rotate around their own axis and, at the same time, revolve around the center of mass of the system. Sometimes, the intrinsic rotation axis and the orbital one are aligned since the beginning of the formation process. Usually, the orbit begins with a considerable eccentricity and the component stars are not synchronized with the orbital velocity. However, due to the inertial forces that take place, the system tends to align its axes, to synchronize rotational velocity of the components with the orbital speed by occasion of the periastron passage and, finally, to circularize the orbit. When both the rotation and the orbital periods are equal, the system is called a synchronized binary system. Extensive spectroscopic evidence reveals that the components of close binary systems do rotate with an angular velocity Ω which is generally equal to the Keplerian angular velocity, ω_K, of the orbital motion around a common center of mass, so that

$$\Omega \cong \omega_K = \sqrt{G\frac{M_1 + M_2}{R^3}}. \tag{3.15}$$

However, occasionally Ω is much larger the ω_K – the sense of rotation being direct in every known case. In systems exhibiting circular orbits, synchronism between rotation and revolution may usually (though not always) be expected to exist, while components describing eccentric orbits rotate, as a rule, faster than their mean orbital angular velocity.

Generally, one of these stars, called primary, is larger (in size and mass) and hotter than its companion (called secondary). It is a common situation, in certain evolutionary stages of the components, that the more massive star of the system is not the larger one or the one of higher effective temperature. In these cases, it is necessary to specify what is to be understood by "primary component". When we are dealing with spectroscopic binary systems, the primary is usually the more massive one, but in eclipsing binary systems the star that has the higher effective temperature is normally designed as the primary one.

One important aspect of the evolution of close binaries is the dynamical evolution due to tidal interaction, which is reflected in the rotation of the stars and in the eccentricity of their orbits.

Tidal deformation due to the companion would be symmetric about the line joining their centers, if there were no dissipation of kinetic energy into heat. It is this dissipation that induces a phase shift in the tidal bulge, and the tilted mass distribution, then, exerts a torque on the star, leading to an exchange of angular momentum between its spin and the orbital motion. Theory distinguishes two components in the tide, namely, equilibrium tide and dynamical tide (Zahn 1989):

- Equilibrium tide is the hydrostatic adjustment of the structure of the star to the perturbing force exerted by the companion. The dissipation mechanism acting on this tide is the interaction between the convective motions and the tidal flow (Zahn 1966).
- Dynamical tide is the dynamical response to the tidal force exerted by the companion; it takes into account the elastic properties of the star, and the possibilities of resonances with its free modes of oscillation. The dissipation mechanism acting on this tide is the departure from adiabaticity of the forced oscillation, due to the radiative damping (Zahn 1975).

In standard models, the stars are assumed to be spherically symmetric. However, we know that the spherically symmetric configuration can be destroyed if a disturbing potential exists. For example, rotating stars and stars in binary systems do not have spherical symmetries. Their equilibrium structures are distorted by rotational and tidal forces. While rotational forces distort the spherically symmetric configuration of a rotating star, relative to the original spherically symmetric shape of a non-rotating star, tidal forces (caused by the gravitational pull of the companion star) distort the spherically symmetric configuration of a star in a binary system (see Fig. 3.1).

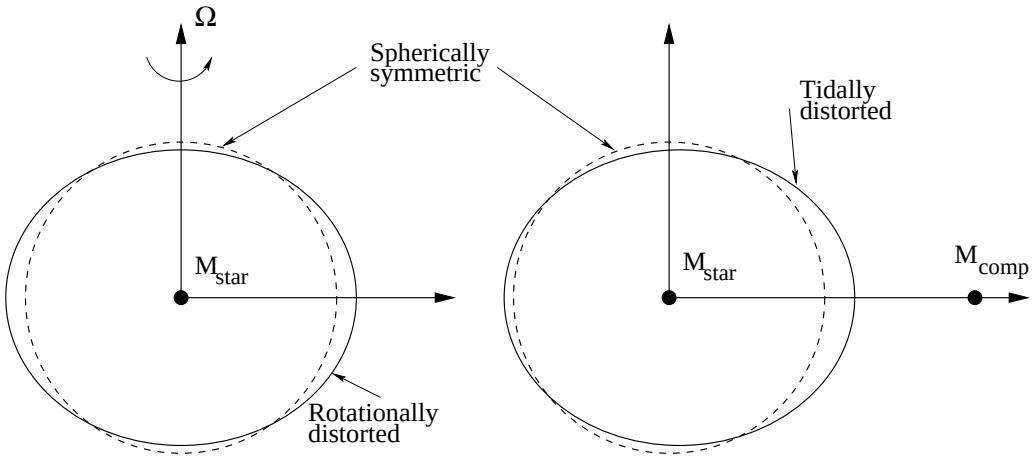

Figure 3.1: Distortions in the figure of the star relative to a spherically symmetric shape, shown schematically. On the left are shown the distortions due to rotation. On the right are shown the distortions due to tidal forces caused by a companion (in this case, the distortions effects are amplified to better understanding).

In the case of a rotating star in a binary system, both rotational and tidal forces distort its shape from the spherical symmetry. In cases in which tidal and/or rotational forces are present, the analytic determination of these combined effects is quite complex and some approximative methods have been used in the literature. In such methods one of these distortional forces (generally rotation) is analyzed in approximate ways (Mohan *et al.* 1990). Chandrasekhar (1933) developed the theory of distorted polytropes and Kopal (1972, 1974) developed the concept of Roche equipotentials and Roche coordinates to study the combined effects of a tidally and rotationally distorted star. Kippenhahn & Thomas (1970) proposed a method for determining the equilibrium structures of rotationally and tidally distorted stellar models. This method has an advantage that the non-spherical stellar equations can be easily obtained from the spherical ones. In Sect. (3.4), we will describe the method of Kippenhahn & Thomas (1970).

3.3 Internal structure constants for spherically symmetric configurations

Here we show how we computed the internal structure constants (k_js) based on the simple (and unrealistic) assumption that stars can be described by spherically symmetric models. The k_js have been computed to permit the comparison with observed rates of apsidal motion.

The Radau's differential equation (Kopal, 1959) is numerically integrated throughout all the structure through a 4th-order Runge Kutta method (Press et al. 1992):

$$r\frac{d\eta_j}{dr} + 6\frac{\rho(r)}{\bar{\rho}(r)}(\eta_j + 1) + \eta_j(\eta_j - 1) = j(j+1), \tag{3.16}$$

where $\eta_j(0) = j - 2$ (j=2, 3, 4), $\rho(r)$ is the local density at a distance r from the center, and $\bar{\rho}(r)$ is the mean density within the inner sphere of radius r. The resulting value of the function $\eta_j(R)$, which satisfies Radau's equation with R being the radius of the configuration, is used to obtain the internal structure constants k_js:

$$k_j = \frac{j + 1 - \eta_j(R)}{2(j + \eta_j(R))}, \tag{3.17}$$

Because the observed motion of apsides is the sum of the motion produced by both stars, the quantities k_{2i} (where i=1,2 for the primary and the secondary star, respectively) cannot be determined separately. Only a weighted mean value of the apsidal motion constant can be computed using

$$\bar{k}_{2theo} = \frac{c_{21}k_{21theo} + c_{22}k_{22theo}}{c_{21} + c_{22}}, \tag{3.18}$$

where c_{21} and c_{22} are given by Eq. (3.3), k_{21theo} and k_{22theo} are the theoretical apsidal motion constants for the primary and the secondary, respectively, computed from the models, Eq. (3.17), for the corresponding mass and radius of each individual component star. Such values are inferred from a previous comparison with the absolute dimensions. Before performing the apsidal motion comparison, one has to check if the models are able to reproduce some basic stellar parameters, such as effective temperatures, and to predict a common age for the two components. A good discussion in this subject is given by

Claret & Giménez (1993). The apsidal motion constant can be directly compared with observational values as we will show in Sect. (3.1).

3.4 The Kippenhahn & Thomas's formulation

The Kippenhahn & Thomas (1970) method (from now on simply KT70) is a strategy for introducing disturbing potentials in evolutionary stellar models, in which the distortion produced by a given disturbing potential is entirely included in the total potential function. In order to describe the distortions yielded by the combination of rotation and tidal forces effects, KT70 used a Roche-like potential function ψ_R of the form

$$\psi_R = G\frac{M_1}{R_1} + G\frac{M_2}{R_2} + \frac{1}{2}\Omega^2\left[\left(x - \frac{M_1 R}{M_1 + M_2}\right)^2 + y^2\right]. \tag{3.19}$$

This is the total potential of the gravitational, rotational and tidal disturbing forces acting at point P, which is outside of the two gaseous sphere stars. M_1 and M_2 are, respectively, the primary and secondary stellar masses, R_1 e R_2 are the distances of P from their centers. R is the mutual separation between the centers of their masses, G is the constant of gravitation and Ω is the angular velocity about a fixed axis which is perpendicular to the orbital x-y plane (as can be seen in the Fig. 3.2).

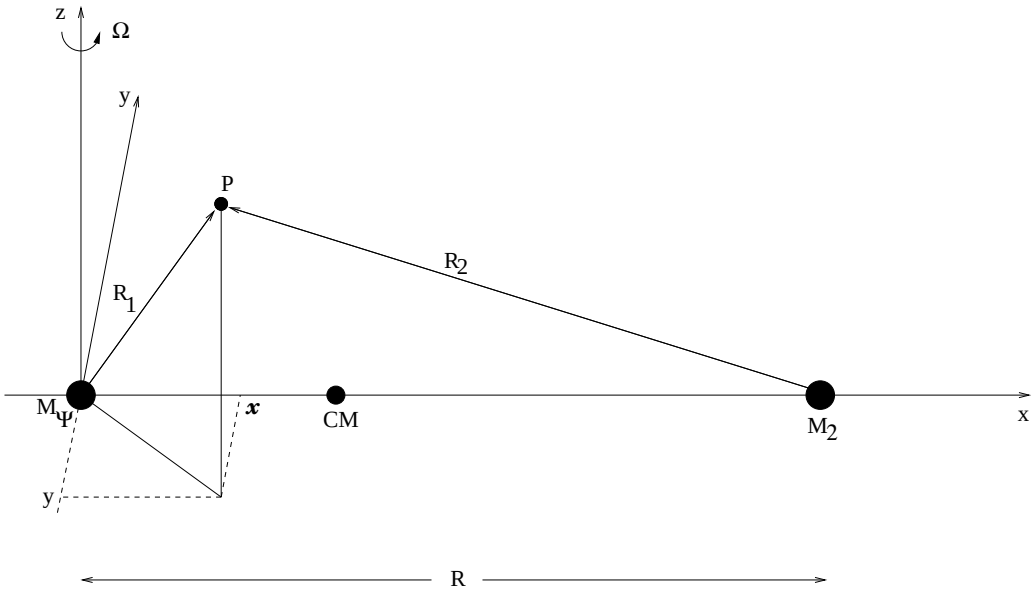

Figure 3.2: Geometric configuration for the Roche potential of Eq. (3.19), which calculates the gravitational pseudo-potential of a point P in a binary system in which the primary is a rotating star.

In order to clarify how these disturbing effects were taken into account in the KT70 method, the equations are re-derived here. In this formulation, the spherically symmetric surfaces, normally used in standard stellar models, are replaced by suitable non-spherical equipotential surfaces characterized by the total potential ψ, the mass M_ψ enclosed by the corresponding equipotential surface whose surface area is S_ψ and encloses a volume

V_ψ, and r_ψ, the radius of the topologically equivalent sphere with the same volume V_ψ, enclosed by the equipotential surface.

For any quantity f that varies over an equipotential surface, we can define its mean value as

$$\langle f \rangle = \frac{1}{S_\psi} \int_{\psi=\text{const.}} f d\sigma, \tag{3.20}$$

where S_ψ is the surface area of the equipotential surface, defined as

$$S_\psi = \int_{\psi=\text{const.}} d\sigma, \tag{3.21}$$

and $d\sigma$ is the surface element.

The local effective gravity, given by

$$g = \frac{d\psi}{dn}, \tag{3.22}$$

where dn is the (non-constant) separation between two successive equipotential ψ and $\psi + d\psi$, so that we have

$$\langle g \rangle = \frac{1}{S_\psi} \int_{\psi=\text{const.}} \frac{d\psi}{dn} d\sigma, \tag{3.23}$$

$$\langle g^{-1} \rangle = \frac{1}{S_\psi} \int_{\psi=\text{const.}} \left(\frac{d\psi}{dn} \right)^{-1} d\sigma. \tag{3.24}$$

The volume between the surfaces ψ and $\psi + d\psi$ is given by

$$\begin{aligned} dV_\psi &= \int_{\psi=\text{const}} dn d\sigma \\ &= d\psi \int_{\psi=\text{const}} \left(\frac{dn}{d\psi} \right) d\sigma \\ &= d\psi S_\psi \langle g^{-1} \rangle, \end{aligned} \tag{3.25}$$

from which we obtain

$$\begin{aligned} d\psi &= \frac{1}{S_\psi \langle g^{-1} \rangle} dV_\psi \\ &= \frac{1}{S_\psi \langle g^{-1} \rangle} \frac{dM_\psi}{\rho(\psi)}. \end{aligned} \tag{3.26}$$

and the volume of the topologically equivalent sphere is given by

$$V_\psi = \frac{4\pi}{3} r_\psi^3. \tag{3.27}$$

Eq. (3.26) can be combined with the general form of the hydrostatic equilibrium equation,

$$\frac{dP}{d\psi} = -\rho, \tag{3.28}$$

to give

$$\frac{dP}{dM_\psi} = -\frac{GM_\psi}{4\pi r_\psi^4} f_p, \tag{3.29}$$

where f_p is given by

$$f_p = \frac{4\pi r_\psi^4}{GM_\psi} \frac{1}{S_\psi \langle g^{-1} \rangle}. \tag{3.30}$$

With these corrections, the four stellar structure equations become, with M_ψ as the independent variable,

$$\frac{dP}{dM_\psi} = -\frac{GM_\psi}{4\pi r_\psi^4} f_p \tag{3.31a}$$

$$\frac{dr_\psi}{dM_\psi} = \frac{1}{4\pi r_\psi^2 \rho} f_p \tag{3.31b}$$

$$\frac{dL_\psi}{dM_\psi} = \epsilon - T\frac{\partial S}{\partial t} \tag{3.31c}$$

$$\frac{dT_\psi}{dM_\psi} = -\frac{GM_\psi T}{4\pi r_\psi^4 P}\nabla, \qquad \nabla = \left\{ \nabla_{\rm rad}, \frac{f_{\rm t}}{f_{\rm p}} \nabla_{\rm conv} \right\}. \tag{3.31d}$$

where f_p is given by Eq. (3.30) and

$$f_t = \left(\frac{4\pi r_\psi^2}{S_\psi} \right)^2 \frac{1}{\langle g \rangle \langle g^{-1} \rangle}. \tag{3.32}$$

In the case of isolated and non-rotating stars, $f_p = f_t = 1$, and the original stellar structure equations are recovered. In order to obtain the internal structure of a distorted gas sphere, the set of Eqs. (3.31) must be numerically integrated under the suitable boundary conditions (see Chap. 5 for a discussion on non-gray boundary conditions).

This formulation was largely used in the literature mainly due to the easiness of its implementation in existing evolutionary codes (e.g. Endal & Sofia 1976, Law 1980, Pinsonneault 1988, Martín & Claret 1996).

3.5 Tidal and/or rotational distortions on the equilibrium structure of stars

The treatment we used to implement the tidal and rotational effects in stellar models has been derived by Kippenhahn & Thomas (1970) and modified by Endal & Sofia (1976). Instead of using a Roche potential, we use a more refined function to take into account the terms related to the distortion of the figure of the star. In order to accomplish this goal, we used the Clairaut-Legendre expansion for the gravitational potential of a self-gravitating body (Kopal 1959). This implementation was introduced in the `ATON` stellar evolutionary code, first for including effects of rotation (Mendes 1999b). The effects of tidal forces, as well as the combined effects of tidal forces and rotation on the structure of the star, are introduced in the present work.

The calculations presented here are derived within the framework of static tides. In the case of dynamic tides, a more refined treatment is required (see Claret & Willems 2002, and Willems & Claret 2003).

In our model, tides and axial rotation are the two physical causes of the stellar configuration departuring from a spherical form. We treat three different situations: 1) rotation

acting alone, 2) tidal forces acting alone and 3) a combination of both effects distorting the star. We consider the special case in which we follow the evolution of only one of the binary system's component, assuming that it rotates about a fixed axis perpendicular to the orbital plane. The disturbing star is considered to be a mass point located at a sufficiently large distance from its companion in comparison to the radius of the distorted star in question. Particularly, at this work, the ratio between the mutual separation and the radius of the evolving (distorted) star is supposed to be constant, which imply in a circular orbit. The value of this ratio is established as an input parameter which depends on the system to be reproduced. In close binary systems, the separation of the stars is often less than 10 times their radii. The assumptions made about the stellar separation do not describe a real situation. They were used as an attempt to introduce the structural effects of tidal distortions in the `ATON2.3` code, preserving its numerical convergence. We have also tried to use a fixed separation between the stars, but for typical separations of close binary systems the stars evolve to a non physical configuration, in which the equipotential surfaces cross each other making the derivatives undefined in the crossing points.

Following Kopal (1959), we assume that the equipotential surfaces can be written as an expansion of the tesseral harmonics, Y_j, of the form

$$r = r_0\left[1 + \sum_j Y_j(r_0, \theta, \phi)\right]. \tag{3.33}$$

where r_0 is the mean radius of the corresponding equipotential. In this work, we assume that the distortions of our configurations is so small that quantities of the order of squares and higher powers of the individual harmonics Y_j may be negleted. The tesseral harmonics $Y_j(r_0, \theta, \phi)$ can be fatorized in the form

$$Y_j(r_0, \theta, \phi) = K(r_0)P_j(\theta, \phi), \tag{3.34}$$

where $K(r_0)$ is the radial part of the tesseral harmonics and P_j's are the Legendre polynomials.

3.5.1 Rotational distortion

Rotation alone would render the star a rotational spheroid flattened at the poles (see left panel of Fig. 3.1). The total potential is divided in three parts according to Eq. (3.35). ψ_s is the spherically symmetric part of the gravitational potential, ψ_r is the cylindrically symmetric potential due to rotation and ψ_d is the cilindrically symmetric part of the gravitational potential due to distortion of the figure of the star caused by rotation. If the coordinates of the point P are the radius r and the polar angle θ the components of the potential at P can be written as (Kopal 1959):

$$\begin{aligned}
\psi &= \psi_s + \psi_r + \psi_d \\
\psi_s &= \frac{GM_\psi}{r} \\
\psi_r &= \frac{1}{2}\Omega^2 \sin^2\theta \\
\psi_d &= -\frac{4\pi}{3r^3}P_2(\cos\theta)\int_0^{r_0} \rho \frac{r_0'^7}{M_\psi}\Omega^2 \frac{5+\eta_2}{2+\eta_2} dr_0'
\end{aligned} \tag{3.35}$$

In Eq. (3.35), Ω is the rotation angular velocity of the distorted star, r_0 is the radius of the equipotential surface at θ_0, which is defined such that $P_2(\cos\theta_0) = 0$, P_2 is the 2nd order Legendre polynomial. Here, the shape of rotating configurations is described by following the expansion given in Eq. (3.33). We note that terms further than the second-harmonic (Y_2) have amplitudes as small as $(Y_2)^2$. By limiting ourselves to consider terms in Y of no higher than the second order, we can simplify our notation replacing Y_2 due to rotation by $Y_{\rm rot}$. In this way, the equipotential surface is given by

$$r(r_0, \theta) = r_0\Big[1 + Y_{\rm rot}\Big]. \tag{3.36}$$

In their turn, the $Y_{\rm rot}$'s are given by:

$$Y_{\rm rot} = -\frac{\Omega^2 r_0^3}{3GM_\psi}\frac{5}{2+\eta_2(r_0)}P_2(\cos\theta). \tag{3.37}$$

The quantity η_2 is of particular interest to our study, because we can derive from it the theoretical apsidal motion constants (see Sect. 3.1). The evaluation of η_2 can be done by numerically integrating the Radau's equation:

$$r_0\frac{d\eta_2}{dr_0} + 6\frac{\rho(r_0)}{\bar{\rho}(r_0)}(\eta_2+1) + \eta_2(\eta_2-1) = 6. \tag{3.38}$$

This equation is slightly different form Eq. (3.16). Here, we use j=2 and the spherical radius, r, which appears in Eq. (3.16), was replaced by r_0, the mean radius of the distorted configuration. η_2 can also be associated to the logarithmic derivative of the tesseral harmonic, $Y_{\rm rot}$, with respect to r_0:

$$\eta_2 = \frac{r_0}{Y_{\rm rot}}\frac{\partial Y_{\rm rot}}{\partial r_0}. \tag{3.39}$$

$Y_{\rm rot}$ is a measure of the deviation from the sphericity caused by rotation.

If we define the radial part of the axisymmetric tesseral harmonic, $A(r_0)$, as

$$A(r_0) = \frac{\Omega^2 r_0^3}{3GM_\psi}\frac{5}{2+\eta_2}, \tag{3.40}$$

the equipotential surface, Eq. (3.36), can be rewritten as

$$r(r_0, \theta) = r_0\Big[1 - A(r_0)P_2(\cos\theta)\Big]. \tag{3.41}$$

In order to relate r_0 to r_ψ, we evaluate the volume integral from $r = 0$ to r given by Eq. (3.41) and the resulting expression is

$$V_\psi = \frac{4\pi r_0^3}{3}\left[1 + \frac{3}{5}A^2 - \frac{2}{35}A^3\right]. \tag{3.42}$$

For simplicity, the arguments of the constant $A(r_0)$ were suppressed. From the equation above, r_ψ is given by

$$r_\psi = r_0\left[1 + \frac{3}{5}A^2 - \frac{2}{35}A^3\right]^{1/3}. \tag{3.43}$$

Usually, one has that r_ψ and r_0 can be calculated through Eq. (3.43) by means of an iterative procedure.

Since the local effective gravity is given by

$$g = \frac{\partial \psi}{\partial n} = \left[\left(\frac{\partial \psi}{\partial r} \right)^2 + \left(\frac{1}{r} \frac{\partial \psi}{\partial \theta} \right)^2 \right]^{1/2}, \tag{3.44}$$

g can be found by differentiation of Eq. (3.35). The integrals in Eq. (3.35) and its derivatives must be evaluated numerically. Once the values of $\langle g \rangle$ and $\langle g^{-1} \rangle$ are known for a set of points on an equipotential surfaces, $S_\psi \langle g \rangle$ and $S_\psi \langle g^{-1} \rangle$ can be found, respectively, from Eqs. (3.23) and (3.24) by numerically integrating over θ, as follows:

$$\begin{aligned} S_\psi \langle g \rangle &= \int_0^{2\pi} \int_0^{\pi} \left\{ \left[\left(-\frac{GM_\psi}{r'^2} + \frac{4\pi}{r'^4} P_2(\cos\theta) \int_0^{r_0} \rho \frac{r_0'^7}{M_\psi} \Omega^2 \frac{5+\eta_2}{2+\eta_2} dr_0' + \Omega^2 r' \sin\theta \right. \right. \right. \\ &\quad \left. \left. \left. - \frac{4\pi}{3r'^3} P_2(\cos\theta) \rho \frac{r_0^7}{M_\psi} \Omega^2 \frac{5+\eta_2}{2+\eta_2} \frac{\partial r_0}{\partial r'} + \Omega r'^2 \sin^2\theta \frac{\partial \Omega}{\partial r'} \right)_{r'=r} \right]^2 \right\}^{1/2} d\sigma \end{aligned} \tag{3.45}$$

where r_0 is given by Eq. (3.41) and $d\sigma$, the surface element of a rotationally distorted gas sphere, is given by

$$d\sigma = r' \sin\theta \left[r'^2 + r_0^2 A^2 \left(\frac{\partial P_2(\cos(\theta))}{\partial \theta} \right)^2 \right]^{1/2} d\theta d\phi. \tag{3.46}$$

$S_\psi \langle g^{-1} \rangle$ is obtained by exchanging the expression for $\frac{\partial \psi}{\partial n}$ in Eq. (3.45) by that for $\left(\frac{\partial \psi}{\partial n} \right)^{-1}$. In the equations above, $P_2(\cos\theta)$ are the Legendre polynomial of order 2, given by

$$P_2(\cos\theta) = \frac{1}{2}(3\cos^2\theta - 1) \tag{3.47}$$

and its derivative with respect to θ, $\partial P_2(\cos\theta)/\partial\theta$, is given by

$$\frac{\partial P_2(\cos\theta)}{\partial \theta} = -3 \sin\theta \cos\theta, \tag{3.49}$$

The expressions for $\partial r_0/\partial r$ and $\partial r_0/\partial\theta$ are:

$$\frac{\partial r_0}{\partial r} = \frac{r_0}{r + r_0^2 \left[- P_2(\cos\theta) \frac{\partial A}{\partial r_0} \right]} \tag{3.50}$$

$$\frac{\partial r_0}{\partial \theta} = \frac{r_0^2 \left[- A \frac{\partial P_2(\cos\theta)}{\partial \theta} \right]}{r + r_0^2 \left[- P_2(\cos\theta) \frac{\partial A}{\partial r_0} \right]} \tag{3.51}$$

where

$$\frac{\partial A}{\partial r_0} = \frac{A}{r_0} \left(\frac{3(2+\eta_2) - r_0 \partial \eta_2 / \partial r_0}{2+\eta_2} \right), \tag{3.52}$$

and the derivatives of η_2 with respect to r_0 are obtained from Eq. (3.38).

3.5.2 Tidal distortion

Tidal distortion acting alone would tend to elongate the star in the direction of the other component (see right panel of Fig. 3.1). The total potential is divided in three parts according to Eq. (3.53). ψ_s is the spherically symmetric part of the gravitational potential, ψ_t is the non-symmetric potential due to tidal forces, and ψ_d is the non-symmetric part of the gravitational potential due to distortion of the figure of the star caused by the presence of the companion star. If the coordinates of the point P are the radius r, the polar angle θ and the azimuthal angle ϕ, the components of the potential at P can be written as (Kopal 1959):

$$\begin{aligned}
\psi &= \psi_s + \psi_t + \psi_d \\
\psi_s &= \frac{GM_\psi}{r} \\
\psi_t &= \frac{GM_2}{R}\left(\frac{r'_0}{R}\right)^2 P_2(\lambda) + \frac{GM_2}{R}\left(\frac{r'_0}{R}\right)^3 P_3(\lambda) + \frac{GM_2}{R}\left(\frac{r'_0}{R}\right)^4 P_4(\lambda) \\
\psi_d &= \frac{4\pi GM_2}{r^3R^3}P_2(\lambda)\int_0^{r_0}\rho\frac{r'^7_0}{M_\psi}\frac{5+\eta_2}{2+\eta_2}dr'_0 + \frac{4\pi GM_2}{r^4R^4}P_3(\lambda)\int_0^{r_0}\rho\frac{r'^9_0}{M_\psi}\frac{6+\eta_3}{3+\eta_3}dr'_0 \\
&+ \frac{4\pi GM_2}{r^5R^5}P_4(\lambda)\int_0^{r_0}\rho\frac{r'^{11}_0}{M_\psi}\frac{7+\eta_4}{4+\eta_4}dr'_0
\end{aligned} \tag{3.53}$$

In Eq. (3.53), M_2 is the mass of the disturbing companion star, R is the mutual separation between the centers of mass of the two stars, $\lambda = \cos\phi\sin\theta$, r_0 is the radius of the equipotential surface at θ_0, and ϕ_0 is defined such that $BP_2(\lambda_0)+CP_3(\lambda_0)+DP_4(\lambda_0) = 0$, where $\lambda_0 = \cos\phi_0\sin\theta_0$. P_j (j=2, 3, 4) is the jth order Legendre polynomial, and Y_j is the tesseral harmonic relating r to r_0 on a given equipotential surface:

$$r(r_0,\theta,\phi) = r_0\left[1 + \sum_2^4 Y_j\right]. \tag{3.54}$$

We do not consider terms further than the fourth-harmonic because the fifith harmonic Y_5 is found to be as small as $(Y_2)^2$, and this we agreed to ignore. So, Y_j's are given by:

$$Y_j = \frac{M_2}{M_\psi}\sum_{j=2}^{4}\frac{2j+1}{j+\eta_j(r_0)}\left(\frac{r_0}{R}\right)^{j+1}P_j(\lambda), \tag{3.55}$$

The quantity η_j is of particular interest to our study, because we can derive from it the apsidal motion constants by using our theoretical stellar models (see Sect. 3.1). The evaluation of the quantity above can be done by numerically integrating the Radau's equation:

$$r_0\frac{d\eta_j}{dr_0} + 6\frac{\rho(r_0)}{\bar{\rho}(r_0)}(\eta_j+1) + \eta_j(\eta_j-1) = j(j+1). \tag{3.56}$$

This equation is slightly different form Eq. (3.16). The spherical radius, r, which appears in Eq. (3.16) was replaced by r_0, the mean radius of the distorted configuration.

Here, η_j can also be associated to the logarithmic derivative of tesseral harmonics, Y_j, with respect to r_0,

$$\eta_j = \frac{r_0}{Y_j}\frac{\partial Y_j}{\partial r_0}. \tag{3.57}$$

Y_js are a measure of the deviation from the sphericity caused by tidal forces.

If we define the radial parts of the non-symmetric tesseral harmonics, namely the constants $B(r_0)$, $C(r_0)$ and $D(r_0)$, as

$$\begin{aligned} B(r_0) &= \frac{M_2}{M_\psi}\left(\frac{r_0}{R}\right)^3 \frac{5}{2+\eta_2}, \\ C(r_0) &= \frac{M_2}{M_\psi}\left(\frac{r_0}{R}\right)^4 \frac{7}{3+\eta_3} \quad \text{and} \\ D(r_0) &= \frac{M_2}{M_\psi}\left(\frac{r_0}{R}\right)^5 \frac{9}{4+\eta_4}, \end{aligned} \tag{3.58}$$

the equipotential surface, Eq. (3.54), can be rewritten as

$$r(r_0,\theta,\phi) = r_0\Big[1 + B(r_0)P_2(\lambda) + C(r_0)P_3(\lambda) + D(r_0)P_4(\lambda)\Big], \tag{3.59}$$

In order to relate r_0 to r_ψ, we evaluate the volume integral from $r = 0$ to r given by Eq. (3.75) and the resulting expression is

$$\begin{aligned} V_\psi &= \frac{4\pi r_0^3}{3}\Bigg[1 + \frac{3}{5}B^2 + \frac{3}{7}C^2 + \frac{2}{35}B^3 + \frac{6}{35}B^2D + \frac{4}{35}BC^2 \\ &+ \frac{20}{231}BD^2 + \frac{6}{77}C^2D + \frac{18}{1001}D^3 + \frac{1}{3}D^2\Bigg]. \end{aligned} \tag{3.60}$$

For simplicity, the arguments of constants $B(r_0)$, $C(r_0)$ and $D(r_0)$ were suppressed. From the equation above, r_ψ is given by

$$\begin{aligned} r_\psi &= r_0\Bigg[1 + \frac{3}{5}B^2 + \frac{3}{7}C^2 + \frac{2}{35}B^3 + \frac{6}{35}B^2D + \frac{6}{35}B^2D \\ &+ \frac{4}{35}BC^2 + \frac{20}{231}BD^2 + \frac{6}{77}C^2D + \frac{18}{1001}D^3 + \frac{1}{3}D^2\Bigg]^{1/3}. \end{aligned} \tag{3.61}$$

By means of an iterative procedure, r_ψ and r_0 can be calculated through Eq. (3.61).

Since the local effective gravity is given by

$$g = \frac{\partial\psi}{\partial n} = \left[\left(\frac{\partial\psi}{\partial r}\right)^2 + \left(\frac{1}{r}\frac{\partial\psi}{\partial\theta}\right)^2 + \left(\frac{1}{r\sin\theta}\frac{\partial\psi}{\partial\phi}\right)^2\right]^{1/2}, \tag{3.62}$$

g can be found by differentiation of Eq. (3.53).

The integrals in Eq. (3.53) and its derivatives must be evaluated numerically. Once the values of $\langle g\rangle$ and $\langle g^{-1}\rangle$ are known for a set of points on an equipotential surfaces,

$S_\psi\langle g\rangle$ and $S_\psi\langle g^{-1}\rangle$ can be found, respectively, from Eqs. (3.23) and (3.24) by numerically integrating over θ and ϕ, as follows:

$$
\begin{aligned}
S_\psi\langle g\rangle \;=\; & \int_0^{2\pi}\int_0^{\pi}\Bigg\{\Bigg[\Bigg(-\frac{GM_\psi}{r'^2}-\frac{12\pi GM_2}{r'^4R^3}P_2(\lambda)\int_0^{r_0}\rho\frac{r_0'^7}{M_\psi}\frac{5+\eta_2}{2+\eta_2}dr_0' \\
&+\frac{4\pi GM_2}{r'^3R^3}P_2(\lambda)\rho\frac{r_0^7}{M_\psi}\frac{5+\eta_2}{2+\eta_2}\frac{\partial r_0}{\partial r'}-\frac{16\pi GM_2}{r'^5R^4}P_3(\lambda)\int_0^{r_0}\rho\frac{r_0'^9}{M_\psi}\frac{6+\eta_3}{3+\eta_3}dr_0' \\
&+\frac{4\pi GM_2}{r'^4R^4}P_3(\lambda)\rho\frac{r_0^9}{M_\psi}\frac{6+\eta_3}{3+\eta_3}\frac{\partial r_0}{\partial r'}-\frac{20\pi GM_2}{r'^6R^5}P_4(\lambda)\int_0^{r_0}\rho\frac{r_0'^{11}}{M_\psi}\frac{7+\eta_4}{4+\eta_4}dr_0' \\
&+\frac{4\pi GM_2}{r'^5R^5}P_4(\lambda)\rho\frac{r_0^{11}}{M_\psi}\frac{7+\eta_4}{4+\eta_4}\frac{\partial r_0}{\partial r'}+\frac{2GM_2r_0}{R^3}P_2(\lambda)\frac{\partial r_0}{\partial r'} \\
&+\frac{3GM_2r_0^2}{R^4}P_3(\lambda)\frac{\partial r_0}{\partial r'}+\frac{4GM_2r_0^3}{R^5}P_4(\lambda)\frac{\partial r_0}{\partial r'}\Bigg)_{r'=r}\Bigg]^2 \\
&+\Bigg[\Bigg(\frac{4\pi GM_2}{r'^4R^3}\frac{\partial P_2(\lambda)}{\partial\theta}\int_0^{r_0}\rho\frac{r_0'^7}{M_\psi}\frac{5+\eta_2}{2+\eta_2}dr_0'+\frac{4\pi GM_2}{r'^4R^3}P_2(\lambda)\rho\frac{r_0^7}{M_\psi}\frac{5+\eta_2}{2+\eta_2}\frac{\partial r_0}{\partial\theta} \\
&+\frac{4\pi GM_2}{r'^5R^4}\frac{\partial P_3(\lambda)}{\partial\theta}\int_0^{r_0}\rho\frac{r_0'^9}{M_\psi}\frac{6+\eta_3}{3+\eta_3}dr'_0+\frac{4\pi GM_2}{r'^5R^4}P_3(\lambda)\rho\frac{r_0^9}{M_\psi}\frac{6+\eta_3}{3+\eta_3}\frac{\partial r_0}{\partial\theta} \\
&+\frac{4\pi GM_2}{r'^6R^5}\frac{\partial P_4(\lambda)}{\partial\theta}\int_0^{r_0}\rho\frac{r_0'^{11}}{M_\psi}\frac{7+\eta_4}{4+\eta_4}dr'_0+\frac{4\pi GM_2}{r'^6R^5}P_4(\lambda)\rho\frac{r_0^{11}}{M_\psi}\frac{7+\eta_4}{4+\eta_4}\frac{\partial r_0}{\partial\theta} \\
&+\frac{2GM_2r_0}{r'R^3}P_2(\lambda)\frac{\partial r_0}{\partial\theta}+\frac{GM_2}{r'R}\left(\frac{r_0}{R}\right)^2\frac{\partial P_2(\lambda)}{\partial\theta}+\frac{3GM_2r_0^2}{r'R^4}P_3(\lambda)\frac{\partial r_0}{\partial\theta} \\
&+\frac{GM_2}{r'R}\left(\frac{r_0}{R}\right)^3\frac{\partial P_3(\lambda)}{\partial\theta}+\frac{4GM_2r_0^3}{r'R^5}P_4(\lambda)\frac{\partial r_0}{\partial\theta}+\frac{GM_2}{r'R}\left(\frac{r_0}{R}\right)^4\frac{\partial P_4(\lambda)}{\partial\theta}\Bigg)_{r'=r}\Bigg]^2 \\
&+\Bigg[\Bigg(\frac{4\pi GM_2}{r'^4R^3\sin\theta}\frac{\partial P_2(\lambda)}{\partial\phi}\int_0^{r_0}\rho\frac{r_0'^7}{M_\psi}\frac{5+\eta_2}{2+\eta_2}dr'_0+\frac{4\pi GM_2}{r'^4R^3\sin\theta}P_2(\lambda)\rho\frac{r_0^7}{M_\psi}\frac{5+\eta_2}{2+\eta_2}\frac{\partial r_0}{\partial\phi} \\
&+\frac{4\pi GM_2}{r'^5R^4\sin\theta}\frac{\partial P_3(\lambda)}{\partial\phi}\int_0^{r_0}\rho\frac{r_0'^9}{M_\psi}\frac{6+\eta_3}{3+\eta_3}dr'_0+\frac{4\pi GM_2}{r'^5R^4\sin\theta}P_3(\lambda)\rho\frac{r_0^9}{M_\psi}\frac{6+\eta_3}{3+\eta_3}\frac{\partial r_0}{\partial\phi} \\
&+\frac{4\pi GM_2}{r'^6R^5\sin\theta}\frac{\partial P_4(\lambda)}{\partial\phi}\int_0^{r_0}\rho\frac{r_0'^{11}}{M_\psi}\frac{7+\eta_4}{4+\eta_4}dr'_0+\frac{4\pi GM_2}{r'^6R^5\sin\theta}P_4(\lambda)\rho\frac{r_0^{11}}{M_\psi}\frac{7+\eta_4}{4+\eta_4}\frac{\partial r_0}{\partial\phi} \\
&+\frac{2GM_2r_0}{r'R^3\sin\theta}P_2(\lambda)\frac{\partial r_0}{\partial\phi}+\frac{GM_2}{r'R\sin\theta}\left(\frac{r_0}{R}\right)^2\frac{\partial P_2(\lambda)}{\partial\phi}+\frac{3GM_2r_0^2}{r'R^4\sin\theta}P_3(\lambda)\frac{\partial r_0}{\partial\phi} \\
&+\frac{GM_2}{r'R\sin\theta}\left(\frac{r_0}{R}\right)^3\frac{\partial P_3(\lambda)}{\partial\phi}+\frac{4GM_2r_0}{r'R^5\sin\theta}P_4(\lambda)\frac{\partial r_0}{\partial\phi} \\
&+\frac{GM_2}{r'R\sin\theta}\left(\frac{r_0}{R}\right)^4\frac{\partial P_4(\lambda)}{\partial\phi}\Bigg)_{r'=r}\Bigg]^2\Bigg\}^{1/2}d\sigma, \qquad (3.63)
\end{aligned}
$$

where r_0 is given by Eq. (3.59).

$S_\psi\langle g^{-1}\rangle$ is obtained by exchanging the expression for $\frac{\partial\psi}{\partial n}$ in Eq. (3.63) by that for $\left(\frac{\partial\psi}{\partial n}\right)^{-1}$.

The surface element, $d\sigma$, of a rotationally and tidally distorted gas sphere, is given by

$$\begin{aligned} d\sigma &= \left\{ \left[r'^2 + r_0^2 \left(B\frac{\partial P_2(\lambda)}{\partial\theta} + C\frac{\partial P_3(\lambda)}{\partial\theta} + D\frac{\partial P_4(\lambda)}{\partial\theta} \right)^2 \right] \right. \\ &\times \left[r'^2 \sin^2\theta + r_0^2 \left(B\frac{\partial P_2(\lambda)}{\partial\phi} + C\frac{\partial P_3(\lambda)}{\partial\phi} + D\frac{\partial P_4(\lambda)}{\partial\phi} \right)^2 \right] \\ &- r_0^2 \left[\left(B\frac{\partial P_2(\lambda)}{\partial\theta} + C\frac{\partial P_3(\lambda)}{\partial\theta} + D\frac{\partial P_4(\lambda)}{\partial\theta} \right)^2 \right. \\ &\times \left. \left. \left(B\frac{\partial P_2(\lambda)}{\partial\phi} + C\frac{\partial P_3(\lambda)}{\partial\phi} + D\frac{\partial P_4(\lambda)}{\partial\phi} \right)^2 \right] \right\}^{1/2} d\theta d\phi. \end{aligned} \tag{3.64}$$

In the equations above, $P_j(\lambda)$ are the Legendre polynomials, given by

$$P_2(\lambda) = P_2(\cos\phi\sin\theta) = \frac{1}{2}(3\cos^2\phi\sin^2\theta - 1), \tag{3.65a}$$

$$P_3(\lambda) = P_3(\cos\phi\sin\theta) = \frac{1}{2}(5\cos^3\phi\sin^3\theta - 3\cos\phi\sin\theta) \quad \text{and} \tag{3.65b}$$

$$P_4(\lambda) = P_4(\cos\phi\sin\theta) = \frac{1}{8}(35\cos^4\phi\sin^4\theta - 30\cos^2\phi\sin^2\theta + 3) \tag{3.65c}$$

and their derivatives with respect to θ, $\partial P_j(\lambda)/\partial\theta$, are given by

$$\frac{\partial P_2(\lambda)}{\partial\theta} = 3\cos^2\phi\sin\theta\cos\theta, \tag{3.66a}$$

$$\frac{\partial P_3(\lambda)}{\partial\theta} = \frac{15}{2}\cos^3\phi\sin^2\theta\cos\theta - \frac{3}{2}\cos\phi\cos\theta \quad \text{and} \tag{3.66b}$$

$$\frac{\partial P_4(\lambda)}{\partial\theta} = \frac{35}{2}\cos^4\phi\sin^3\theta\cos\theta - \frac{15}{2}\cos^2\phi\sin\theta\cos\theta. \tag{3.66c}$$

The partial derivatives with respect to ϕ, $\partial P_j(\lambda)/\partial\phi$, are

$$\frac{\partial P_2(\lambda)}{\partial\phi} = -3\sin^2\theta\cos\phi\sin\phi, \tag{3.67a}$$

$$\frac{\partial P_3(\lambda)}{\partial\phi} = -\frac{15}{2}\sin^3\theta\cos^2\phi\sin\phi + \frac{3}{2}\sin\phi\cos\theta \quad \text{and} \tag{3.67b}$$

$$\frac{\partial P_4(\lambda)}{\partial\phi} = -\frac{35}{2}\sin^4\theta\cos^3\phi\sin\phi + \frac{15}{2}\sin^2\theta\sin\phi\cos\phi. \tag{3.67c}$$

The expressions for $\partial r_0/\partial r$, $\partial r_0/\partial\theta$ and $\partial r_0/\partial\phi$ are:

$$\frac{\partial r_0}{\partial r} = \frac{r_0}{r + r_0^2\left[P_2(\lambda)\frac{\partial B}{\partial r_0} + P_3(\lambda)\frac{\partial C}{\partial r_0} + P_4(\lambda)\frac{\partial D}{\partial r_0}\right]}, \tag{3.68}$$

$$\frac{\partial r_0}{\partial\theta} = \frac{r_0^2\left[B\frac{\partial P_2(\lambda)}{\partial\theta} + C\frac{\partial P_3(\lambda)}{\partial\theta} + D\frac{\partial P_4(\lambda)}{\partial\theta}\right]}{r + r_0^2\left[P_2(\lambda)\frac{\partial B}{\partial r_0} + P_3(\lambda)\frac{\partial C}{\partial r_0} + P_4(\lambda)\frac{\partial D}{\partial r_0}\right]} \quad \text{and} \tag{3.69}$$

$$\frac{\partial r_0}{\partial \phi} = \frac{r_0^2\left[B\frac{\partial P_2(\lambda)}{\partial \phi} + C\frac{\partial P_3(\lambda)}{\partial \phi} + D\frac{\partial P_4(\lambda)}{\partial \phi}\right]}{r + r_0^2\left[P_2(\lambda)\frac{\partial B}{\partial r_0} + P_3(\lambda)\frac{\partial C}{\partial r_0} + P_4(\lambda)\frac{\partial D}{\partial r_0}\right]}, \tag{3.70}$$

where $\frac{\partial B}{\partial r_0}$, $\frac{\partial C}{\partial r_0}$ and $\frac{\partial D}{\partial r_0}$ are:

$$\frac{\partial B}{\partial r_0} = \frac{B}{r_0}\left(\frac{3(2+\eta_2) - r_0\partial\eta_2/\partial r_0}{2+\eta_2}\right), \tag{3.71a}$$

$$\frac{\partial C}{\partial r_0} = \frac{C}{r_0}\left(\frac{4(3+\eta_3) - r_0\partial\eta_3/\partial r_0}{3+\eta_3}\right) \quad \text{and} \tag{3.71b}$$

$$\frac{\partial D}{\partial r_0} = \frac{D}{r_0}\left(\frac{5(4+\eta_4) - r_0\partial\eta_4/\partial r_0}{4+\eta_4}\right). \tag{3.71c}$$

3.5.3 Interaction between rotation and tides

Rotation alone would render the component a rotational spheroid flattened at the poles, while tidal distortion will tend to elongate it in the direction of the other component (see Fig. 3.1).

The total potential is divided in four parts according to Eq. (3.72). ψ_s is the spherically symmetric part of the gravitational potential, ψ_r is the cylindrically symmetric potential due to rotation, ψ_t is the non-symmetric potential due to tidal forces, and ψ_d is the non-symmetric part of the gravitational potential due to distortion of the figure of the star. Note that ψ_r and the 1$^{\text{st}}$ terms of ψ_d (Eq. 3.72), related to rotation, will invoke a single second harmonic distortion, given by Eq. (3.37). If the coordinates of the point P are the radius r, the polar angle θ and the azimuthal angle ϕ, the components of the potential at P can be written as (Kopal 1959):

$$\begin{aligned}
\psi &= \psi_s + \psi_r + \psi_t + \psi_d \qquad (3.72)\\
\psi_s &= \frac{GM_\psi}{r}\\
\psi_r &= \frac{1}{2}\Omega^2\sin^2\theta\\
\psi_t &= \frac{GM_2}{R}\left(\frac{r_0'}{R}\right)^2 P_2(\lambda) + \frac{GM_2}{R}\left(\frac{r_0'}{R}\right)^3 P_3(\lambda) + \frac{GM_2}{R}\left(\frac{r_0'}{R}\right)^4 P_4(\lambda)\\
\psi_d &= -\frac{4\pi}{3r^3}P_2(\cos\theta)\int_0^{r_0}\rho\frac{r_0'^7}{M_\psi}\Omega^2\frac{5+\eta_2}{2+\eta_2}dr_0' + \frac{4\pi GM_2}{r^3R^3}P_2(\lambda)\int_0^{r_0}\rho\frac{r_0'^7}{M_\psi}\frac{5+\eta_2}{2+\eta_2}dr_0'\\
&+ \frac{4\pi GM_2}{r^4R^4}P_3(\lambda)\int_0^{r_0}\rho\frac{r_0'^9}{M_\psi}\frac{6+\eta_3}{3+\eta_3}dr_0' + \frac{4\pi GM_2}{r^5R^5}P_4(\lambda)\int_0^{r_0}\rho\frac{r_0'^{11}}{M_\psi}\frac{7+\eta_4}{4+\eta_4}dr_0'
\end{aligned}$$

In Eq. (3.72), M_2 is the mass of the disturbing companion star, Ω is the rotation angular velocity of the distorted star, R is the mutual separation between the centers of mass of the two stars, $\lambda = \cos\phi\sin\theta$, r_0 is the mean radius of the equipotential surface at θ_0 and ϕ_0, which are defined such that $-AP_2(\cos\theta_0) + BP_2(\lambda_0) + CP_3(\lambda_0) + DP_4(\lambda_0) = 0$, where $\lambda_0 = \cos\phi_0\sin\theta_0$. P_j is the jth order Legendre polynomial, and Y_j is the tesseral harmonic relating r to r_0 on a given equipotential surface. To the order of accuracy we

have been working, both distortions are simply additive, so that the external surface of the primary should be given by

$$r(r_0,\theta,\phi) = r_0\Big[1 + Y_{\rm rot} + \sum_2^4 Y_j\Big]. \tag{3.73}$$

In their turn, the Y_j's are given by Eq. (3.55) and the $Y_{\rm rot}$ is given by Eq. (3.37). The quantity η_j is of particular interest to our study, because we can derive from it the apsidal motion constants from the theoretical stellar models (see Sect. 3.1). The evaluation of the quantity above can be done by numerically integrating the Radau's equation:

$$r_0\frac{d\eta_j}{dr_0} + 6\frac{\rho(r_0)}{\bar{\rho}(r_0)}(\eta_j+1) + \eta_j(\eta_j-1) = j(j+1). \tag{3.74}$$

This equation is slightly different form Eq. (3.16). The spherical radius, r, which appears in Eq. (3.16) was replaced by r_0, the mean radius of the distorted configuration and η_j can also be associated to the logarithmic derivative of tesseral harmonics, Y_j, with respect to r_0. The Y_2 term includes the second order effects of rotation and tides. The remaining Y_j are affected only by tidal distortions. This assumption is valid only in this approximation. If second order terms in Y_j were taken into account, as discussed in Kopal (1989), Eq. (3.74) will contain quantities of the order of the squares of the individual η_j's and cross-terms of both second order η_2's, $\eta_{2,\rm tid}$ and $\eta_{2,\rm rot}$.

If we define the radial parts of the tesseral harmonics, namely the constants $A(r_0)$ (according to Eq. 3.40) and $B(r_0)$, $C(r_0)$ and $D(r_0)$ (according to Eq. 3.58), the equipotential surface, Eq. (3.73), can be rewritten as

$$r(r_0,\theta,\phi) = r_0\Big[1 - A(r_0)P_2(\cos\theta) + B(r_0)P_2(\lambda) + C(r_0)P_3(\lambda) + D(r_0)P_4(\lambda)\Big], \tag{3.75}$$

In order to relate r_0 to r_ψ, we evaluate the volume integral from $r=0$ to r given by Eq. (3.75) and the resulting expression is

$$V_\psi = \tfrac{4\pi r_0^3}{3}\Bigg[1 + \tfrac{3}{5}A^2 + \tfrac{3}{5}AB + \tfrac{3}{5}B^2 + \tfrac{3}{7}C^2 - \tfrac{2}{35}A^3 - \tfrac{3}{35}A^2B + \tfrac{9}{140}A^2D + \tfrac{3}{35}AB^2 + \tfrac{2}{35}AC^2$$
$$+\tfrac{6}{35}ABD + \tfrac{10}{231}AD^2 + \tfrac{2}{35}B^3 + \tfrac{6}{35}B^2D + \tfrac{4}{35}BC^2 + \tfrac{20}{231}BD^2 + \tfrac{6}{77}C^2D + \tfrac{18}{1001}D^3 + \tfrac{1}{3}D^2\Bigg]. \tag{3.76}$$

For simplicity, the arguments of constants $A(r_0)$, $B(r_0)$, $C(r_0)$ and $D(r_0)$ were suppressed. From the equation above, r_ψ is given by

$$r_\psi = r_0\Bigg[1 + \frac{3}{5}A^2 + \frac{3}{5}AB + \frac{3}{5}B^2 + \frac{3}{7}C^2 - \frac{2}{35}A^3 - \frac{3}{35}A^2B + \frac{9}{140}A^2D + \frac{9}{140}A^2D + \frac{3}{35}AB^2 + \frac{1}{3}D^2$$
$$+\frac{2}{35}AC^2 + \frac{6}{35}ABD + \frac{10}{231}AD^2 + \frac{2}{35}B^3 + \frac{6}{35}B^2D + \frac{4}{35}BC^2 + \frac{20}{231}BD^2 + \frac{6}{77}C^2D + \frac{18}{1001}D^3\Bigg]^{1/3}. \tag{3.77}$$

Usually, one has that r_ψ and r_0 can be calculated through Eq. (3.77) by means of an iterative procedure.

Since the local effective gravity is given by Eq. (3.62), g can be found by differentiation of Eq. (3.72). The integrals in Eq. (3.72) and its derivatives must be evaluated numerically. Once the values of $\langle g\rangle$ and $\langle g^{-1}\rangle$ are known for a set of points on an equipotential surfaces,

$S_\psi\langle g\rangle$ and $S_\psi\langle g^{-1}\rangle$ can be found, respectively, from Eqs. (3.23) and (3.24) by numerically integrating over θ and ϕ, as follows:

$$
\begin{aligned}
S_\psi\langle g\rangle \;=\; & \int_0^{2\pi}\int_0^{\pi}\Bigg\{\Bigg[\Bigg(-\frac{GM_\psi}{r'^2}+\frac{4\pi}{r'^4}P_2(\cos\theta)\int_0^{r_0}\rho\frac{r_0'^7}{M_\psi}\Omega^2\frac{5+\eta_2}{2+\eta_2}dr_0' \\
& -\frac{12\pi GM_2}{r'^4R^3}P_2(\lambda)\int_0^{r_0}\rho\frac{r_0'^7}{M_\psi}\frac{5+\eta_2}{2+\eta_2}dr_0'-\frac{4\pi}{3r'^3}P_2(\cos\theta)\rho\frac{r_0^7}{M_\psi}\Omega^2\frac{5+\eta_2}{2+\eta_2}\frac{\partial r_0}{\partial r'} \\
& +\frac{4\pi GM_2}{r'^3R^3}P_2(\lambda)\rho\frac{r_0^7}{M_\psi}\frac{5+\eta_2}{2+\eta_2}\frac{\partial r_0}{\partial r'}-\frac{16\pi GM_2}{r'^5R^4}P_3(\lambda)\int_0^{r_0}\rho\frac{r_0'^9}{M_\psi}\frac{6+\eta_3}{3+\eta_3}dr_0' \\
& +\frac{4\pi GM_2}{r'^4R^4}P_3(\lambda)\rho\frac{r_0^9}{M_\psi}\frac{6+\eta_3}{3+\eta_3}\frac{\partial r_0}{\partial r'}-\frac{20\pi GM_2}{r'^6R^5}P_4(\lambda)\int_0^{r_0}\rho\frac{r_0'^{11}}{M_\psi}\frac{7+\eta_4}{4+\eta_4}dr_0' \\
& +\frac{4\pi GM_2}{r'^5R^5}P_4(\lambda)\rho\frac{r_0^{11}}{M_\psi}\frac{7+\eta_4}{4+\eta_4}\frac{\partial r_0}{\partial r'}+\Omega^2r'\sin\theta+\Omega r'^2\sin^2\theta\frac{\partial\Omega}{\partial r'} \\
& +\frac{2GM_2r_0}{R^3}P_2(\lambda)\frac{\partial r_0}{\partial r'}+\frac{3GM_2r_0^2}{R^4}P_3(\lambda)\frac{\partial r_0}{\partial r'}+\frac{4GM_2r_0^3}{R^5}P_4(\lambda)\frac{\partial r_0}{\partial r'}\Bigg)_{r'=r}\Bigg]^2 \\
& +\Bigg[\Bigg(-\frac{4\pi}{3r'^4}\frac{\partial P_2(\cos\theta)}{\partial\theta}\int_0^{r_0}\rho\frac{r_0'^7}{M_\psi}\Omega^2\frac{5+\eta_2}{2+\eta_2}dr_0'-\frac{4\pi}{3r'^4}P_2(\cos\theta)\rho\frac{r_0^7}{M_\psi}\Omega^2\frac{5+\eta_2}{2+\eta_2}\frac{\partial r_0}{\partial\theta} \\
& +\frac{4\pi GM_2}{r'^4R^3}\frac{\partial P_2(\lambda)}{\partial\theta}\int_0^{r_0}\rho\frac{r_0'^7}{M_\psi}\frac{5+\eta_2}{2+\eta_2}dr_0'+\frac{4\pi GM_2}{r'^4R^3}P_2(\lambda)\rho\frac{r_0^7}{M_\psi}\frac{5+\eta_2}{2+\eta_2}\frac{\partial r_0}{\partial\theta} \\
& +\frac{4\pi GM_2}{r'^5R^4}\frac{\partial P_3(\lambda)}{\partial\theta}\int_0^{r_0}\rho\frac{r_0'^9}{M_\psi}\frac{6+\eta_3}{3+\eta_3}dr'_0+\frac{4\pi GM_2}{r'^5R^4}P_3(\lambda)\rho\frac{r_0^9}{M_\psi}\frac{6+\eta_3}{3+\eta_3}\frac{\partial r_0}{\partial\theta} \\
& +\frac{4\pi GM_2}{r'^6R^5}\frac{\partial P_4(\lambda)}{\partial\theta}\int_0^{r_0}\rho\frac{r_0'^{11}}{M_\psi}\frac{7+\eta_4}{4+\eta_4}dr'_0+\frac{4\pi GM_2}{r'^6R^5}P_4(\lambda)\rho\frac{r_0^{11}}{M_\psi}\frac{7+\eta_4}{4+\eta_4}\frac{\partial r_0}{\partial\theta} \\
& +\Omega^2r'\sin\theta\cos\theta+\Omega r'\sin^2\theta\frac{\partial\Omega}{\partial\theta}+\frac{2GM_2r_0}{r'R^3}P_2(\lambda)\frac{\partial r_0}{\partial\theta} \\
& +\frac{GM_2}{r'R}\left(\frac{r_0}{R}\right)^2\frac{\partial P_2(\lambda)}{\partial\theta}+\frac{3GM_2r_0^2}{r'R^4}P_3(\lambda)\frac{\partial r_0}{\partial\theta}+\frac{GM_2}{r'R}\left(\frac{r_0}{R}\right)^3\frac{\partial P_3(\lambda)}{\partial\theta} \\
& +\frac{4GM_2r_0^3}{r'R^5}P_4(\lambda)\frac{\partial r_0}{\partial\theta}+\frac{GM_2}{r'R}\left(\frac{r_0}{R}\right)^4\frac{\partial P_4(\lambda)}{\partial\theta}\Bigg)_{r'=r}\Bigg]^2 \\
& +\Bigg[\Bigg(-\frac{4\pi}{r'^4\sin\theta}P_2(\cos\theta)\rho\frac{r_0^7}{M_\psi}\Omega^2\frac{5+\eta_2}{2+\eta_2}\frac{\partial r_0}{\partial\phi}+\frac{4\pi GM_2}{r'^4R^3\sin\theta}\frac{\partial P_2(\lambda)}{\partial\phi}\int_0^{r_0}\rho\frac{r_0'^7}{M_\psi}\frac{5+\eta_2}{2+\eta_2}dr'_0 \\
& +\frac{4\pi GM_2}{r'^4R^3\sin\theta}P_2(\lambda)\rho\frac{r_0^7}{M_\psi}\frac{5+\eta_2}{2+\eta_2}\frac{\partial r_0}{\partial\phi}+\frac{4\pi GM_2}{r'^5R^4\sin\theta}\frac{\partial P_3(\lambda)}{\partial\phi}\int_0^{r_0}\rho\frac{r_0'^9}{M_\psi}\frac{6+\eta_3}{3+\eta_3}dr'_0 \\
& +\frac{4\pi GM_2}{r'^5R^4\sin\theta}P_3(\lambda)\rho\frac{r_0^9}{M_\psi}\frac{6+\eta_3}{3+\eta_3}\frac{\partial r_0}{\partial\phi}+\frac{4\pi GM_2}{r'^6R^5\sin\theta}\frac{\partial P_4(\lambda)}{\partial\phi}\int_0^{r_0}\rho\frac{r_0'^{11}}{M_\psi}\frac{7+\eta_4}{4+\eta_4}dr'_0 \\
& +\frac{4\pi GM_2}{r'^6R^5\sin\theta}P_4(\lambda)\rho\frac{r_0^{11}}{M_\psi}\frac{7+\eta_4}{4+\eta_4}\frac{\partial r_0}{\partial\phi}+\Omega r'\sin\theta\frac{\partial\Omega}{\partial\phi}+\frac{2GM_2r_0}{r'R^3\sin\theta}P_2(\lambda)\frac{\partial r_0}{\partial\phi} \\
& +\frac{GM_2}{r'R\sin\theta}\left(\frac{r_0}{R}\right)^2\frac{\partial P_2(\lambda)}{\partial\phi}+\frac{3GM_2r_0^2}{r'R^4\sin\theta}P_3(\lambda)\frac{\partial r_0}{\partial\phi}+\frac{GM_2}{r'R\sin\theta}\left(\frac{r_0}{R}\right)^3\frac{\partial P_3(\lambda)}{\partial\phi} \\
& +\frac{4GM_2r_0}{r'R^5\sin\theta}P_4(\lambda)\frac{\partial r_0}{\partial\phi}+\frac{GM_2}{r'R\sin\theta}\left(\frac{r_0}{R}\right)^4\frac{\partial P_4(\lambda)}{\partial\phi}\Bigg)_{r'=r}\Bigg]^2\Bigg\}^{1/2}d\sigma
\end{aligned}
\tag{3.78}
$$

where r_0 is given by Eq. (3.75) and $d\sigma$, the surface element of a rotationally and tidally distorted gas sphere, is given by

$$\begin{aligned} d\sigma &= \left\{ \left[r'^2 + r_0^2 \left(-A\frac{\partial P_2(\cos(\theta)}{\partial\theta} + B\frac{\partial P_2(\lambda)}{\partial\theta} + C\frac{\partial P_3(\lambda)}{\partial\theta} + D\frac{\partial P_4(\lambda)}{\partial\theta} \right)^2 \right] \right. \\ &\times \left[r'^2 \sin^2\theta + r_0^2 \left(B\frac{\partial P_2(\lambda)}{\partial\phi} + C\frac{\partial P_3(\lambda)}{\partial\phi} + D\frac{\partial P_4(\lambda)}{\partial\phi} \right)^2 \right] \\ &- r_0^2 \left[\left(-A\frac{\partial P_2(\cos\theta)}{\partial\theta} + B\frac{\partial P_2(\lambda)}{\partial\theta} + C\frac{\partial P_3(\lambda)}{\partial\theta} + D\frac{\partial P_4(\lambda)}{\partial\theta} \right)^2 \right. \\ &\times \left. \left. \left(B\frac{\partial P_2(\lambda)}{\partial\phi} + C\frac{\partial P_3(\lambda)}{\partial\phi} + D\frac{\partial P_4(\lambda)}{\partial\phi} \right)^2 \right] \right\}^{1/2} d\theta d\phi. \end{aligned} \tag{3.79}$$

$S_\psi\langle g^{-1}\rangle$ is obtained by exchanging the expression for $\frac{\partial\psi}{\partial n}$ in Eq. (3.78) by that for $\left(\frac{\partial\psi}{\partial n}\right)^{-1}$. In the equations above, the 2nd order Legendre polynomial, $P_2(\cos\theta)$, is given by Eq. (3.47) and its jth order counterparts, $P_j(\lambda)$, are given by Eq. (3.65). Their derivatives with respect to θ, $\partial P_2(\cos\theta)/\partial\theta$ and $\partial P_j(\lambda)/\partial\theta$, are given by Eq. (3.48) and (3.66), respectively. The partial derivatives with respect to ϕ, $\partial P_j(\lambda)/\partial\phi$, are given in Eq. (3.67). The expressions for $\partial r_0/\partial r$, $\partial r_0/\partial\theta$ and $\partial r_0/\partial\phi$ are:

$$\frac{\partial r_0}{\partial r} = \frac{r_0}{r + r_0^2\Big[- P_2(\cos\theta)\frac{\partial A}{\partial r_0} + P_2(\lambda)\frac{\partial B}{\partial r_0} + P_3(\lambda)\frac{\partial C}{\partial r_0} + P_4(\lambda)\frac{\partial D}{\partial r_0}\Big]}, \tag{3.80}$$

$$\frac{\partial r_0}{\partial\theta} = \frac{r_0^2\Big[- A\frac{\partial P_2(\cos\theta)}{\partial\theta} + B\frac{\partial P_2(\lambda)}{\partial\theta} + C\frac{\partial P_3(\lambda)}{\partial\theta} + D\frac{\partial P_4(\lambda)}{\partial\theta}\Big]}{r + r_0^2\Big[- P_2(\cos\theta)\frac{\partial A}{\partial r_0} + P_2(\lambda)\frac{\partial B}{\partial r_0} + P_3(\lambda)\frac{\partial C}{\partial r_0} + P_4(\lambda)\frac{\partial D}{\partial r_0}\Big]} \quad \text{and} \tag{3.81}$$

$$\frac{\partial r_0}{\partial\phi} = \frac{r_0^2\Big[B\frac{\partial P_2(\lambda)}{\partial\phi} + C\frac{\partial P_3(\lambda)}{\partial\phi} + D\frac{\partial P_4(\lambda)}{\partial\phi}\Big]}{r + r_0^2\Big[- P_2(\cos\theta)\frac{\partial A}{\partial r_0} + P_2(\lambda)\frac{\partial B}{\partial r_0} + P_3(\lambda)\frac{\partial C}{\partial r_0} + P_4(\lambda)\frac{\partial D}{\partial r_0}\Big]}, \tag{3.82}$$

where $\frac{\partial A}{\partial r_0}$ is given by Eq. (3.52) and $\frac{\partial B}{\partial r_0}$, $\frac{\partial C}{\partial r_0}$ and $\frac{\partial D}{\partial r_0}$ are given by Eq. (3.71).

3.5.4 Rotational inertia

Rotational inertia (or momentum of inertia) is an important tool for studying tidal evolution theories. A good knowledge of stellar rotational inertia is required to predict the circularization and synchronization time scales (Zahn 1977).

Unfortunately, it is difficult to find tabulated values of momenta of inertia for reliable stellar configurations. Motz (1952) computed values of rotational inertia by using the existing (and unrealistic) models at that time. Ruciński (1988) obtained values of the radii of gyration for low-mass zero-age main sequence stars. The radius of gyration of a

body is the distance between a given axis of this body [1] and its center of gyration[2]. It is given by

$$\beta = \sqrt{\frac{I}{MR^2}}, \tag{3.83}$$

where I is the rotational inertia of the star, and M and R are the stellar mass and radius, respectively. Claret & Giménez (1989b) presented radii of gyration calculations for the more massive stars during the hydrogen burning phases. They used standard models, in which the stars are described by spherically symmetric configurations.

As a consequence of considering in the total potential its tidal and rotational disturbing contributions, the rotational inertia of the star is changed. Law (1980) has derived the rotational inertia of the rotationally distorted mass shell related to the given mesh point

$$\Delta I = \frac{2}{3} dm_\psi r_\psi^2 \left(\frac{r_0}{r_\psi}\right)^4 \left[1 + \frac{3}{20}\sum_{i=1}^{5} \alpha_i A^i (i\eta_2 + 5)\right], \tag{3.84}$$

where

$$\alpha_i = \frac{5}{i!(5-i)!} \int_0^\pi P_2^i(\cos\theta) \sin^3\theta d\theta. \tag{3.85}$$

Here, we describe how we derived a new expression for the rotational inertia by taking into account both rotational and tidal distortions. The rotational inertia of a spherical shell (where the angular velocity is kept constant) can be written as

$$\Delta I = R^2 dm, \tag{3.86}$$

where $R = r\sin\theta$, and $dm = \rho r^2 \sin\theta dr d\theta d\phi$. Then,

$$\Delta I = \rho \int_0^{2\pi}\int_0^\pi \int_{r_1}^{r_2} r^4 \sin^3\theta dr d\theta d\phi = \frac{\rho}{5}\int_0^{2\pi}\int_0^\pi (r_2^5 - r_1^5)\sin^3\theta d\theta d\phi, \tag{3.87}$$

where r_1 and r_2 are the suitable equipotential surfaces of the distorted configuration

$$\begin{aligned} r_1 &= r_{01}[1 - A(r_{01})P_2(\cos\theta) + B(r_{01})P_2(\lambda) + C(r_{01})P_3(\lambda) + D(r_{01})P_4(\lambda)] \\ r_2 &= r_{02}[1 - A(r_{02})P_2(\cos\theta) + B(r_{02})P_2(\lambda) + C(r_{02})P_3(\lambda) + D(r_{02})P_4(\lambda)]. \end{aligned}$$

The P_j's are the non-radial parts of the axisymmetric tesseral harmonics (Y_j's) and they are a measure of the deviation from the sphericity. The deviations associated with these harmonics, P_j, with the order j higher than 2 do not contribute significantly to the total departure from the spherical symmetry (Claret & Willems 2002). Besides, if we consider all the terms in the r_1 and r_2 expressions, the number of terms in the Eq. (3.87) will increase from 42 (forty two) to 252 (two hundred fifty two). So, we derived a new expression for the rotational inertia of a tidally and rotationally distorted mass shell

[1] In a rotating body, the rotation axis is considered. If no axis is specified, the centroidal axis, which is the line joining the centroid of each cross section along the length of an axial member such as truss diagonal, is assumed.

[2] The center of gyration of a body is defined as that point at which the whole mass might be concentrated (theoretically) without altering the body's rotational inertia. In other words, this is the center about which the body can rotate without moving linearly or vibrating.

related to a given mesh point by considering only the deviations of order less than 2. In this way, ΔI becomes

$$\begin{aligned}\Delta I &= \frac{\rho}{5}\int_0^{2\pi}\int_0^{\pi}\Big\{r_{02}^5[1-A(r_{02})P_2(\cos\theta)+B(r_{02})P_2(\lambda)]^5 \\ &\qquad - r_{01}^5[1-A(r_{01})P_2(\cos\theta)+B(r_{01})P_2(\lambda)]^5\Big\}\sin\theta^3 d\theta d\phi. \quad (3.88)\end{aligned}$$

The powers of 5 (five) of the terms inside brackets can be expanded by using the "multinomial theorem", given by

$$(x_1+x_2+...+x_p)^n = \sum_{\substack{0\le a_1,a_2,...,a_p\le n\\ a_1+a_2+...+a_p=n}}\binom{n}{a_1,a_2,...,a_p}x_1^{a_1}x_2^{a_2}...x_p^{a_p}, \quad (3.89)$$

where n and p are integers and non-negative numbers. The numbers

$$\binom{n}{a_1,a_2,...,a_p} = \frac{n!}{a_1!a_2!...a_p!} \quad (3.90)$$

are the "multinomial coefficients". The summation is taken over all combinations of the indices a_1 through a_p such that $a_1+a_2+...+a_p=n$; $a_1,a_2,...,a_p$, must be integers and non-negative numbers. Here we are interested in the special case where $n=5$ and $p=3$.

By applying this theorem to Eq. (3.88), we have

$$\begin{aligned}\Delta I &= \frac{\rho}{5}\Bigg\{r_{02}^5\int_0^{2\pi}d\phi\int_0^{\pi}\sin^3\theta d\theta\sum_{\substack{0\le a_1,a_2,a_3\le 5\\ a_1+a_2+a_3=5}}\Big(\tfrac{5!}{a_1!a_2!a_3!}\Big)\Big[-A(r_{02})P_2(\cos\theta)\Big]^{a_2}\Big[B(r_{02})P_2(\lambda)\Big]^{a_3} \\ &\quad - r_{01}^5\int_0^{2\pi}d\phi\int_0^{\pi}\sin^3\theta d\theta\sum_{\substack{0\le a_1,a_2,a_3\le 5\\ a_1+a_2+a_3=5}}\Big(\tfrac{5!}{a_1!a_2!a_3!}\Big)\Big[-A(r_{01})P_2(\cos\theta)\Big]^{a_2}\Big[B(r_{01})P_2(\lambda)\Big]^{a_3}\Bigg\} \quad (3.91)\end{aligned}$$

We can make use of the relation $\int_x\sum_i f(x_i)dx_i=\sum_i\int_x f(x_i)dx_i$, and rewrite the Eq. (3.91), as

$$\Delta I = \frac{\rho}{5}\sum_{\substack{0\le a_1,a_2,a_3\le 5\\ a_1+a_2+a_3=5}}k_a\Big[-r_{02}^5A^{a_2}(r_{02})B^{a_3}(r_{02})+r_{01}^5A^{a_2}(r_{01})B^{a_3}(r_{01})\Big], \quad (3.92)$$

where

$$k_a = \left(\frac{5!}{a_1!a_2!a_3!}\right)\int_0^{2\pi}\int_0^{\pi}P_2^{a_2}(\cos\theta)P_2^{a_3}(\lambda)\sin^3\theta d\theta d\phi. \quad (3.93)$$

By considering

$$\begin{aligned} r_{01} &= r_0, \\ r_{02} &= r_{01}+dr_{01}=r_0+dr_0, \\ A(r_{01}) &= A, \\ B(r_{01}) &= B, \\ A(r_{02}) &= A(r_{01})+dA(r_{01})=A+dA \quad \text{and} \\ B(r_{02}) &= B(r_{01})+dB(r_{01})=B+dB, \end{aligned}$$

the expression in brackets in the Eq. (3.92) can be written as

$$\Big[-r_{02}^5 A^{a_2}(r_{02})B^{a_3}(r_{02}) + r_{01}^5 A^{a_2}(r_{01})B^{a_3}(r_{01})\Big] = \Big[-(r_0+dr_0)^5(A+dA)^{a_2}(B+dB)^{a_3} + r_0^5 A^{a_2}B^{a_3}\Big]. \tag{3.94}$$

The first three powers in Eq. (3.94) can be expanded by using the "binomial theorem", which is actually a particular case of the "multinomial theorem", Eq. (3.89), for $p = 2$. In this case, as the increment terms are small if compared with the correspondent variables, the terms of order higher than 2 can be ignored. Then, Eq. (3.94) becomes

$$\Big[-r_0^5 A^{a_2} a_3 B^{a_3-1}dB - r_0^5 a_2 A^{a_2-1}B^{a_3}dA - 5r_0^4 A^{a_2}B^{a_3}dr_0\Big] = \tag{3.95a}$$

$$-r_0^4 dr_0\Big[r_0 a_3 A^{a_2}B^{a_3-1}\frac{dB}{dr_0} + r_0 a_2 B^{a_3}A^{a_2-1}\frac{dA}{dr_0} + 5A^{a_2}B^{a_3}\Big] = \tag{3.95b}$$

$$-r_0^4 dr_0 A^{a_2}B^{a_3}\Big[a_3\frac{r_0}{B}\frac{dB}{dr_0} + a_2\frac{r_0}{A}\frac{dA}{dr_0} + 5\Big] = \tag{3.95c}$$

$$-r_0^4 dr_0 A^{a_2}B^{a_3}\Big[a_3\,\eta_2 + a_2\,\eta_2 + 5\Big], \tag{3.95d}$$

where η_2 is the internal structure constant of order 2. The derivatives of the constants A and B with respect to r_0 are given by Eqs. (3.52) and (3.71). So, $\frac{r_0}{A}\frac{dA}{dr_0}$ and $\frac{r_0}{B}\frac{dB}{dr_0}$ in Eqs. (3.95), are equal to η_2.

Now we can rewrite the Eq. (3.92), as

$$\Delta I = -\frac{\rho}{5}r_0^4 dr_0 \sum_{\substack{0\le a_1,a_2,a_3\le 5\\ a_1+a_2+a_3=5}} k_a A^{a_2}B^{a_3}\Big(a_2\,\eta_2 + a_3\,\eta_2 + 5\Big). \tag{3.96}$$

Since $dm_\psi = 4\pi\rho r_\psi^2 dr_\psi$,

$$\Delta I = -\frac{1}{20\pi}dm_\psi r_\psi^2\left(\frac{r_0^4}{r_\psi}\right)^5\frac{dr_0}{dr_\psi}\sum_{\substack{0\le a_1,a_2,a_3\le 5\\ a_1+a_2+a_3=5}} k_a A^{a_2}B^{a_3}\Big[\eta_2\,(a_2+a_3)+5\Big], \tag{3.97}$$

where k_a is given by the Eq. (3.93).

In the special situation in which only tidal forces distorte the star, the rotational inertia of a given mass shell is

$$\Delta I = \frac{4}{3}dm_\psi r_\psi^2\left(\frac{r_0}{r_\psi}\right)^4\frac{dr_0}{dr_\psi}\Big[1 + \frac{3}{80\pi}\sum_{p=1}^{5}k_p B^p(p\eta_2+5)\Big], \tag{3.98}$$

where k_p is given by

$$k_p = \frac{5}{p!(5-p)!}\int_0^{2\pi}\int_0^{\pi} P_2^p(\lambda)\sin^3\theta d\theta d\phi. \tag{3.99}$$

3.6 Results

We computed theoretical values of internal structure constants by using our new version of the ATON evolutionary code, which is able to reproduce stars with spherically symmetric configurations, as well as tidally and rotationally distorted stars (as described in Sect. 3.5). The grids cover a mass range from 0.09 to 3.8 $M_\odot$ and were computed from early stages of pre-main sequence phase up to main sequence phase. The radiative opacities are taken from Iglesias & Rogers (1993), extended by Alexander & Ferguson (1994) tables in the low-temperature regime. The OPAL equation of state (Rogers et al. 1996) is used in the range $3.7<\log T<8.7$, while in the low-T high density regime we use the Mihalas et al. (1988) EOS (Equation Of State). The nuclear network includes 14 elements and 22 reactions; the relevant cross-sections are taken from Caughlan & Fowler (1988). We adopted the solar metallicity with Z=0.0175 and Y=0.27. The classical Mixing Length Theory (MLT – Böhm-Vitense 1958) was used to treat the convective transport of energy. The mixing length parameter has been fixed to $\alpha=\Lambda/H_p=1.5$. This is the α value which, according to our calibration, best reproduces the solar radius at the solar age by using gray models. For the sake of simplicity, only 20 models are presented for each evolutionary track.

We present four sets of evolutionary models, namely: single non-rotating stars (which we also called standard set of models), non-rotating stars in binary systems (models distorted only by tidal forces), single rotating stars (models distorted only by rotation) and rotating stars in binary systems (which we also called rotating binary models). In cases in which rotation is present, we assumed diferential rotation in radiative regions and rigid body rotation in convective zones. For the range $0.6-1.25\mathrm{M}_\odot$, the initial angular momentum-mass relation can be easily obtained from the respective mass-radius and mass-moment of inertia relations from Kawaler (1987):

$$J_{\rm kaw} = 1.566\times10^{50}\left(\frac{\rm M}{\rm M_\odot}\right)^{0.985} \quad \text{cgs.} \tag{3.100}$$

For stars in binary systems we suppose separations typical for close binaries (7 times the radius of the star whose evolution is followed) and the disturbing star is supposed to be a mass point of the same mass as its primary.

Here, we present the values of internal structure constants and momentum of inertia at the ZAMS. We also followed the evolution of these quantities in the pre-main sequence phase. In Sect. (3.6.1) and Appendix (A.1) we present the results for standard models. In this case, the star is supposed to be spherically symmetric. More realistic models, which consider departure from the sphericity due to rotation and/or tidal forces, are used to derive internal structure constants and momenta of inertia. In Sect. (3.6.2) and Appendix (A.2) the case of non-rotating stars in binary systems is studied. Rotating single stars are considered in Sect. (3.6.3) and Appendix (A.3). And, finally, the more interesting case, that of rotating stars in binary systems, is investigated in Sect. (3.6.4) and Appendix (A.4).

3.6.1 Internal structure constant for single non-rotating stars

In Table (3.1) we show the values of the internal structure constants (ISC) and the radius of gyration (β), Eq. (3.83), for standard stellar models at the ZAMS. In column 1

we have the stellar mass (in $M_\odot$); in column 2 the logarithm of the stellar luminosity in solar units; in column 3, the logarithm of the effective temperature (K), in column 4, the logarithm of the surface gravity (cgs); in columns 5, 6 and 7 we have the logarithm of the internal structure constants, k_2, k_3, k_4, respectively, and in column 8, we have the radius of gyration (cgs). The corresponding evolutionary tracks are given in Appendix (A.1).

Table 3.1: Internal structure constants and gyration radii for ZAMS standard models.

Mass ($M_\odot$)	log(L/L$_\odot$)	log($T_{\rm eff}$)	log (g)	log(k_2)	log(k_3)	log(k_4)	β
0.09	−3.32122	3.43644	5.41172	−0.69496	−1.11389	−1.39363	0.4600
0.10	−3.01021	3.48389	5.33626	−0.71575	−1.14173	−1.42713	0.4554
0.20	−2.25402	3.52547	5.04742	−0.76992	−1.21732	−1.52124	0.4453
0.30	−1.93350	3.54445	4.97890	−0.74917	−1.19129	−1.49182	0.4489
0.40	−1.67671	3.56238	4.91879	−0.79248	−1.24582	−1.55598	0.4402
0.50	−1.38393	3.58846	4.82724	−0.91330	−1.36425	−1.67253	0.4119
0.60	−1.06429	3.62533	4.73427	−1.11292	−1.57029	−1.87884	0.3808
0.70	−0.75942	3.66437	4.65250	−1.31993	−1.79363	−2.10753	0.3534
0.80	−0.48087	3.70271	4.58530	−1.49580	−1.98579	−2.30509	0.3314
0.90	−0.34985	3.72749	4.60457	−1.54909	−2.07193	−2.40448	0.3216
1.00	−0.12828	3.75378	4.53390	−1.74765	−2.30769	−2.65626	0.2957
1.20	0.31812	3.79345	4.32538	−2.30285	−2.99721	−3.42458	0.2361
1.40	0.67844	3.82184	4.14554	−2.72355	−3.54841	−4.09312	0.1962
1.60	0.95354	3.85948	4.07901	−2.84017	−3.70612	−4.29543	0.1861
1.80	1.18080	3.90054	4.06713	−2.82775	−3.69157	−4.28060	0.1869
2.00	1.37506	3.93673	4.06339	−2.80522	−3.66847	−4.25781	0.1887
2.30	1.63358	3.98137	4.04412	−2.77735	−3.63472	−4.22174	0.1913
2.50	1.78019	4.00838	4.04178	−2.74705	−3.60224	−4.18952	0.1930
2.80	1.97646	4.04428	4.03833	−2.70151	−3.55389	−4.13989	0.1967
3.00	2.09462	4.06563	4.03554	−2.67646	−3.52419	−4.10809	0.1984
3.30	2.25818	4.09403	4.02697	−2.64965	−3.49390	−4.07665	0.2014
3.50	2.34971	4.11292	4.03653	−2.61088	−3.45267	−4.03391	0.2037
3.80	2.48235	4.13750	4.03795	−2.57366	−3.41645	−3.99784	0.2069

3.6.2 Internal structure constants for non-rotating stars in binary systems

In table (3.2), we show the values of the internal structure constants and the radius of gyration (Eq. 3.83) for tidally distorted stellar models at the ZAMS. Same header as in Table (3.1). The corresponding evolutionary tracks are given in Appendix (A.2).

Table 3.2: Internal structure constants and gyration radii for ZAMS tidal distorted models.

Mass ($M_\odot$)	log(L/L$_\odot$)	log($T_{\rm eff}$)	log (g)	log(k_2)	log(k_3)	log(k_4)	β
0.09	−3.31963	3.43675	5.41136	−0.69967	−1.11929	−1.39941	0.4600
0.10	−3.00981	3.48392	5.33598	−0.72007	−1.14675	−1.43254	0.4554
0.20	−2.25284	3.52548	5.04626	−0.77561	−1.22466	−1.52986	0.4453
0.30	−1.93338	3.54445	4.97878	−0.75514	−1.19888	−1.50066	0.4489
0.40	−1.67236	3.56259	4.91529	−0.79768	−1.25338	−1.56514	0.4402
0.50	−1.38201	3.58849	4.82543	−0.91924	−1.37245	−1.68227	0.4119
0.60	−1.06324	3.62516	4.73253	−1.11493	−1.57412	−1.88415	0.3808
0.70	−0.75837	3.66389	4.64955	−1.31969	−1.79456	−2.10965	0.3534
0.80	−0.48079	3.70262	4.58486	−1.50335	−1.99536	−2.31605	0.3314
0.90	−0.34498	3.72806	4.60197	−1.56734	−2.09529	−2.43091	0.3215
1.00	−0.12680	3.75389	4.53287	−1.75686	−2.31906	−2.66879	0.2960
1.20	0.31835	3.79345	4.32515	−2.31252	−3.00854	−3.43639	0.2361
1.40	0.68113	3.82160	4.14192	−2.73507	−3.56066	−4.10512	0.1964
1.60	0.95602	3.85901	4.07464	−2.85298	−3.71984	−4.30878	0.1861
1.80	1.18516	3.89952	4.05872	−2.84769	−3.71186	−4.30078	0.1867
2.00	1.37887	3.93588	4.05619	−2.81576	−3.67905	−4.26808	0.1889
2.30	1.63454	3.98107	4.04196	−2.78843	−3.64696	−4.23410	0.1913
2.50	1.78425	4.00726	4.03322	−2.76594	−3.62160	−4.20898	0.1929
2.80	1.97827	4.04383	4.03469	−2.71545	−3.56899	−4.15503	0.1967
3.00	2.09799	4.06479	4.02877	−2.69436	−3.54300	−4.12708	0.1984
3.30	2.25808	4.09406	4.02716	−2.65939	−3.50647	−4.09001	0.2015
3.50	2.35323	4.11228	4.03044	−2.62556	−3.46863	−4.04986	0.2039
3.80	2.48704	4.13681	4.03047	−2.59603	−3.44068	−4.02359	0.2069

3.6.3 Internal structure constants for single rotating stars

In Table (3.3) we show the values of the internal structure constants and the radius of gyration, Eq. (3.83), for rotating stellar models at the ZAMS. Same header as in Table (3.1). The corresponding evolutionary tracks are given in Appendix (A.3).

Table 3.3: Internal structure constants and gyration radii for ZAMS rotating models.

M ($M_\odot$)	log(L/$L_\odot$)	log($T_{\rm eff}$)	log (g)	log(k_2)	log(k_3)	log(k_4)	β	P(d)
0.09	−3.5403	3.3831	5.4499	−0.7119	−1.1329	−1.4134	0.4657	0.0324
0.10	−3.2990	3.4267	5.4643	−0.7421	−1.1704	−1.4558	0.4666	0.0237
0.20	−2.3161	3.5086	5.1436	−0.8662	−1.3370	−1.6571	0.4452	0.0431
0.30	−1.9701	3.5350	5.0252	−0.7934	−1.2461	−1.5542	0.4520	0.0777
0.40	−1.7070	3.5552	4.9498	−0.8075	−1.2697	−1.5854	0.4465	0.1166
0.50	−1.4201	3.5812	4.8572	−0.9087	−1.3659	−1.6790	0.4185	0.1635
0.60	−1.1007	3.6174	4.7578	−1.0979	−1.5585	−1.8707	0.3857	0.2227
0.70	−0.7912	3.6567	4.6694	−1.3053	−1.7787	−2.0941	0.3573	0.2919
0.80	−0.5084	3.6964	4.5998	−1.4872	−1.9784	−2.3000	0.3346	0.3825
0.90	−0.2677	3.7282	4.5334	−1.6967	−2.2194	−2.5524	0.3101	0.5266
1.00	−0.1446	3.7498	4.5403	−1.7516	−2.3102	−2.6583	0.2984	0.6073
1.20	0.2747	3.7896	4.3563	−2.2449	−2.9259	−3.3422	0.2431	1.2161
1.40	0.6715	3.8174	4.1449	−2.7466	−3.5686	−4.1078	0.1961	1.0918
1.60	0.9423	3.8548	4.0797	−2.8700	−3.7417	−4.3329	0.1852	1.3889
1.80	1.1764	3.8958	4.0588	−2.8640	−3.7321	−4.3239	0.1856	1.6818
2.00	1.3736	3.9324	4.0530	−2.8320	−3.6974	−4.2884	0.1877	1.9457
2.30	1.6306	3.9784	4.0388	−2.7973	−3.6567	−4.2460	0.1903	2.3968
2.50	1.7790	4.0055	4.0347	−2.7714	−3.6281	−4.2160	0.1925	2.6902
2.80	1.9759	4.0420	4.0321	−2.7280	−3.5831	−4.1701	0.1960	3.1246
3.00	2.0949	4.0634	4.0285	−2.7018	−3.5521	−4.1369	0.1980	3.4392
3.30	2.2537	4.0933	4.0303	−2.6550	−3.5018	−4.0853	0.2015	3.8568
3.50	2.3535	4.1107	4.0255	−2.6394	−3.4831	−4.0653	0.2031	4.1852
3.80	2.4867	4.1356	4.0273	−2.6014	−3.4427	−4.0230	0.2063	4.5782

3.6.4 Internal structure constants for rotating stars in binary systems

In Table (3.4) we show the values of the internal structure constants and the radius of gyration, Eq. (3.83), for rotationally and tidally distorted stellar models at the ZAMS. Same header as in Table (3.1) The corresponding evolutionary tracks are given in Appendix (A.4).

Table 3.4: Internal structure constants and gyration radii for ZAMS rotationally and tidally distorted models.

Mass ($M_\odot$)	log(L/$L_\odot$)	log($T_{\rm eff}$)	log (g)	log(k_2)	log(k_3)	log(k_4)	β	P(d)
0.09	−3.5403	3.3831	5.4499	−0.7119	−1.1329	−1.4134	0.4657	0.0324
0.10	−3.2987	3.4267	5.4642	−0.7429	−1.1717	−1.4576	0.4666	0.0237
0.20	−2.3161	3.5086	5.1436	−0.8662	−1.3370	−1.6571	0.4452	0.0431
0.30	−1.9701	3.5350	5.0251	−0.7929	−1.2456	−1.5537	0.4520	0.0778
0.40	−1.7068	3.5552	4.9497	−0.8073	−1.2691	−1.5844	0.4465	0.1166
0.50	−1.4201	3.5812	4.8572	−0.9087	−1.3659	−1.6790	0.4185	0.1635
0.60	−1.1006	3.6174	4.7578	−1.0992	−1.5601	−1.8723	0.3857	0.2227
0.70	−0.7909	3.6566	4.6688	−1.3036	−1.7757	−2.0906	0.3574	0.2924
0.80	−0.5084	3.6964	4.5998	−1.4872	−1.9784	−2.3000	0.3346	0.3825
0.90	−0.2676	3.7282	4.5332	−1.6967	−2.2194	−2.5523	0.3101	0.5269
1.00	−0.1446	3.7498	4.5403	−1.7516	−2.3102	−2.6583	0.2984	0.6073
1.20	0.2747	3.7896	4.3563	−2.2449	−2.9259	−3.3422	0.2431	1.2160
1.40	0.6715	3.8174	4.1449	−2.7466	−3.5686	−4.1078	0.1961	1.0918
1.60	0.9434	3.8546	4.0779	−2.8740	−3.7455	−4.3370	0.1851	1.3954
1.80	1.1742	3.8963	4.0632	−2.8585	−3.7304	−4.3239	0.1860	1.6650
2.00	1.3736	3.9324	4.0527	−2.8327	−3.6990	−4.2903	0.1876	1.9462
2.30	1.6308	3.9783	4.0384	−2.7987	−3.6581	−4.2473	0.1903	2.3989
2.50	1.7790	4.0055	4.0347	−2.7714	−3.6281	−4.2160	0.1925	2.7032
2.80	1.9758	4.0420	4.0324	−2.7272	−3.5836	−4.1721	0.1960	3.1317
3.00	2.0949	4.0634	4.0285	−2.7018	−3.5521	−4.1369	0.1980	3.4378
3.30	2.2564	4.0926	4.0248	−2.6627	−3.5090	−4.0926	0.2010	3.9051
3.50	2.3531	4.1108	4.0264	−2.6401	−3.4846	−4.0669	0.2032	4.1748
3.80	2.4845	4.1360	4.0312	−2.5960	−3.4371	−4.0170	0.2067	4.5384

3.7 Discussion

In this section, we discuss the results presented in Sect. (3.6) and the differences obtained with each model. As already expected, the effects of rotational distortions are greater than those of tidal distortions. We investigate the ZAMS models in order to quantify such differences. We calculate how different the non-standard values of the second order internal structure constant are as compared with the standard ones for each stellar mass at the ZAMS. The binary models produced values of $\log k_2$ lower than the standard models, on average, by a factor of about 0.0076, with a maximum difference of 0.0132 being found for the $1.8\mathrm{M}_\odot$ model. For the rotating models and for the rotating binary models this average factor is 0.0276 and 0.0277, respectively, while the maximum difference was the same for both models, 0.1401, for the $0.9\mathrm{M}_\odot$ model.

For the gyration radii, we found, for a given mass at the ZAMS, values slightly higher for the binary rotating models than for those calculated with the standard models. This is due to the combined differences between the radius and the rotational inertia of each model at the ZAMS.

In general, the models distorted only by tidal forces are similar to the standard ones and the models distorted only by rotation are similar to the rotating binary models. This is a consequence of the fact that the rotation effects are more important than the tidal ones. Here, we will concentrate in investigating the differences between the standard models and the rotating binary models, because rotating stars in binary systems is the case of scientific interest for studying apsidal motion.

In Fig. (3.3) we show the path followed by our standard models (solid lines) and our rotationally and tidally distorted models (dashed lines) fora the following masses: 0.09, 0.2, 0.3, 0.4, 0.6, 0.8, 1.0, 1.2, 1.8, 2.0 and $3.8\,\mathrm{M}_\odot$. We can see that the rotationally and tidally distorted pre-MS evolutionary tracks have lower effective temperature than their standard counterparts. The low mass tracks are more sensitive to distortion effects.

In Fig. (3.4) we plotted the $\log(k_2)$ as a function of the logarithm of the stellar age (years). This figure illustrates the significant change in mass concentration during the pre-main sequence evolution, especially for higher masses. For clarity we report only some selected masses, which are the same as in Fig. (3.3). For ages less than 1Myr the $\log k_2$ do not vary significantly, neither with time nor with mass (see Fig. 3.4). For models with mass lower than $0.3\,\mathrm{M}_\odot$, $\log k_2$ remains roughly constant during the evolution. For masses greater than $0.4\,\mathrm{M}_\odot$ the values of $\log k_2$ are constant until a given age, after which they start to drop. As the mass increases the decreasing of $\log k_2$ starts earlier. It seems that $\log k_2$ remains constant until the star develops a radiative core.

The right panel of Fig. (3.5) shows the values of $\log k_j$ plotted as function of $\log M$ for ZAMS standard models (solid lines) and for ZAMS rotating binary models (dashed lines). The curves corresponding to the distorted models remain below to those corresponding to the standard models. For the same reason as in Fig. (3.3), we report only the standard and rotating binary models. The three consecutive harmonics remain roughly constant in the mass range 0.09-$0.4\,\mathrm{M}_\odot$. As the mass increases from $0.4\,\mathrm{M}_\odot$ to $1.5\,\mathrm{M}_\odot$, the values of k_j drop significantly (2-3 orders of magnitude) and reach their minimum value at $1.5\,\mathrm{M}_\odot$. For masses greater than $1.5\,\mathrm{M}_\odot$ we note a parallel behaviour of the k_js. The temporal evolution of $\log(\beta)$ presents the same behaviour as the temporal evolution of $\log(k_2)$, shown in the left panel of Fig. (3.5). Also $\log(\beta)$ behaves roughly in the same way as $\log(k_j)$ as function of $\log(M)$ (open circles curve in the left panel of Fig. 3.6), showing

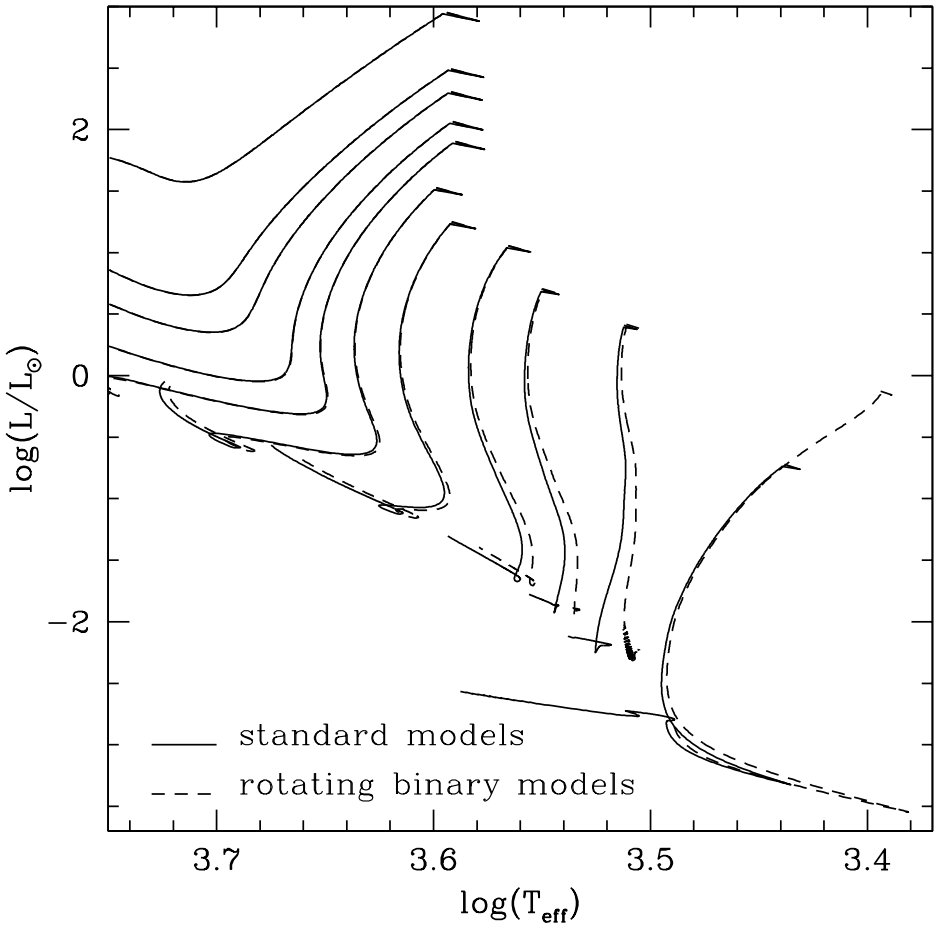

Figure 3.3: The evolutionary tracks for the standard (solid lines) and the rotating binary models (dashed lines). For clarity, we report only models with masses 0.09, 0.2 0.3, 0.4, 0.6, 0.8, 1.0, 1.2, 1.8, 2.0, and 3.8 $M_\odot$ from top to bottom).

a minimum at 1.5 $M_\odot$, corresponding to the change in the dominant energy source from the proton-proton chain to the CNO cycle as pointed out by Claret & Giménez (1989b). This similar behaviour is due to the already known linear relationship between $\log(k_j)$ and $\log(\beta)$, as can be seen in the right panel of Fig. (3.6) and also in Fig. (1) by Motz (1952). In the left panel of Fig. (3.6), we plotted the $\log(\beta)$ as a function of $\log(M)$, at the ZAMS, for our standard and non-standard models and also for those by Claret & Giménez (1989b). For masses above 1.4 $M_\odot$ our models predict a lower value of $\log(\beta)$ than the Claret & Giménez (1989b) ones. Although these models have slightly different chemical compositions, the comparison is still valid. A control made with a one solar mass model with the same initial chemical composition as those by Claret & Giménez (1989b) shows that the gyration radius at the ZAMS did not vary significantly.

Hejlesen (1987) pointed out that, for a given mass, there is a significant decrease in k_j for increasing j, and the relevance of including the higher order terms, when comparing with observations, can be judged from Eq. (3.1). $\log(k_3)$ and $\log(k_4)$ are really less important than $\log(k_2)$ in the mass range that he analysed (0.5-32 $M_\odot$), but the same statement cannot be extended to less massive stars ($M \leq 0.5\, M_\odot$). As can be seen from the right panel of Fig. (3.5), in the mass range 1.5-3.8 $M_\odot$, the decrease of $\log k_j$ for increasing

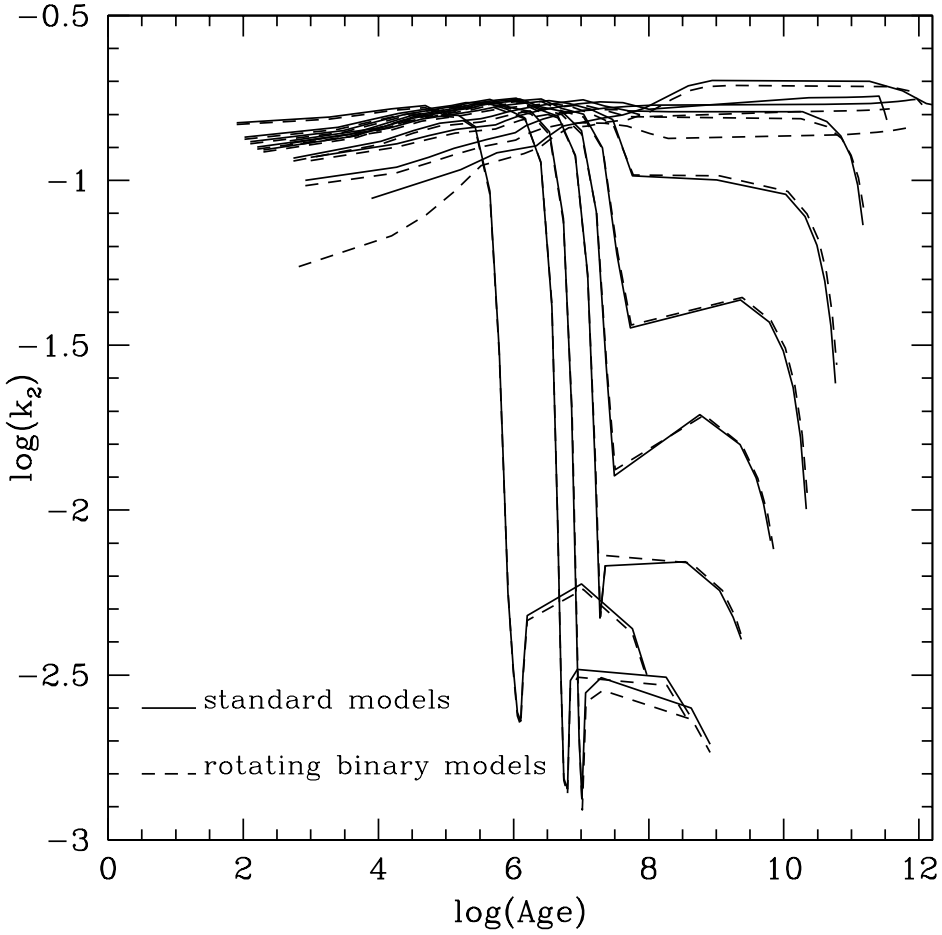

Figure 3.4: The temporal evolution of the $\log(k_2)$ for the standard (solid lines) and the rotating binary models (dashed lines). As in Fig. (3.3), we report only models with masses 0.09, 0.2 0.3, 0.4, 0.6, 0.8, 1.0, 1.2, 1.8, 2.0, and 3.8 $M_\odot$ (from bottom to top).

j is two times the same dropping observed for stars less massive than 0.5 $M_\odot$. In the low-mass range, the assumption that the harmonics of order greater than j=2 can be neglected, widely used when analysing the apsidal motion of binary systems, seems not to be justified.

From Fig. (3.7), we can compare the differences of the stellar radii as a function of stellar age and mass, produced by the standard (solid lines) and distorted (dotted lines) models. From this figure we can see that, for a 0.5 $M_\odot$ star, the stellar radius at the ZAMS obtained by the rotating binary models are slightly smaller than that produced by the standard models. For the one solar mass model, this difference, although less important, is still observed. On the other hand, for the 2 $M_\odot$ model the situation is the opposite: the distorted models predict a larger stellar radius at the ZAMS than the standard models. The threshold mass for this transition is at about 1.3-1.5 $M_\odot$. According to Sackmann (1970), this behavior in the effects of rotation shows up in all physical quantities of a star. In this work, we verify that tidal effects act in the same way as rotational ones but on a smaller scale. Such a behavior is primarily explained by the cross-over from the proton-proton chain to the CNO cycle, that occurs around 1.5 $M_\odot$, depending on the initial chemical composition.

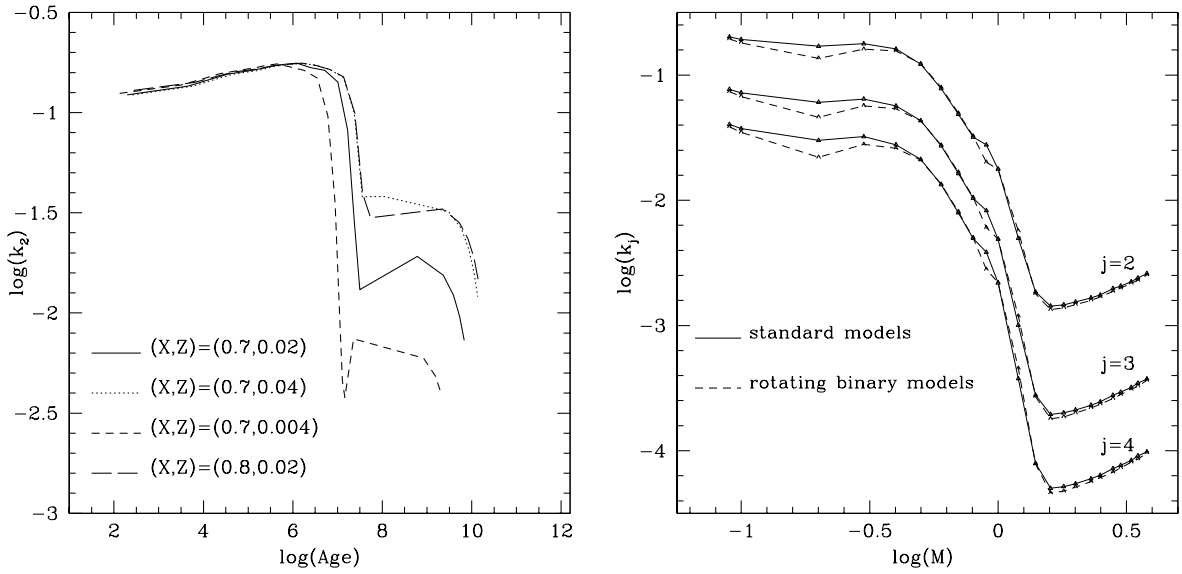

Figure 3.5: **Left**: we have $\log(k_2)$ as a function of the logarithm of stellar age for $1\,M_\odot$ standard models and for the following initial chemical compositions: (X,Z)= (0.7,0.02), (0.07,0.04), (0.7,0.004) and (0.8,0.02). **Right**: we plotted $\log(k_j)$ as function of log (M) for ZAMS models. The curves in solid lines represent the standard models and the dashed lines refers to the rotating binary models.

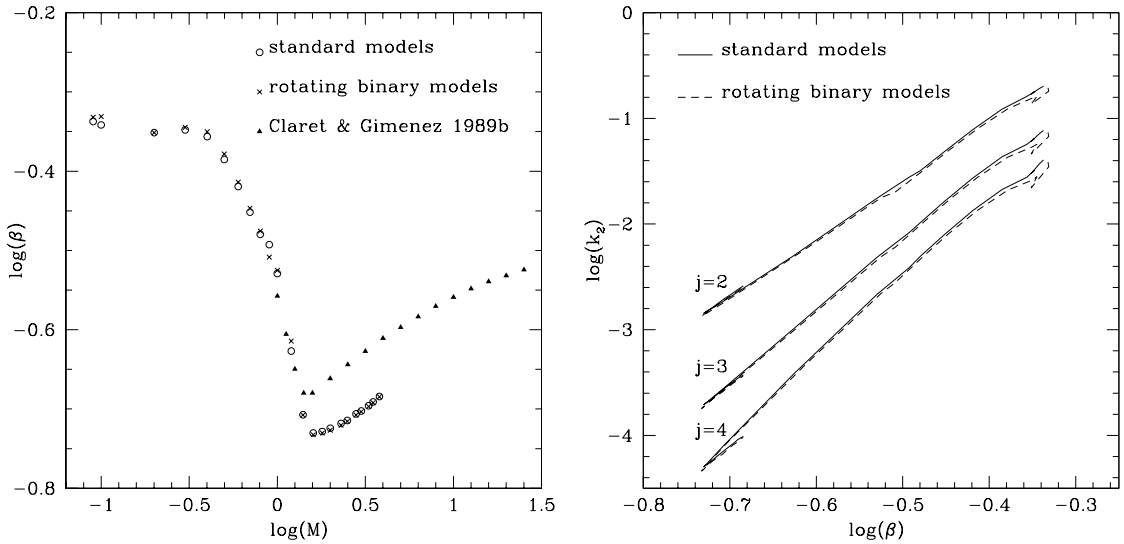

Figure 3.6: **Left:** With open circles, we plotted our standard models and with crosses we show our rotating binary models in the $\log(\beta)$ - log (M) plane. The full triangles correspond to the results by Claret & Giménez (1989b). **Right:** $\log(k_j)$ (j =2 3, 4) as a function of $\log(\beta)$ for ZAMS models. Solid lines correspond to standard models and dashed lines refer to rotating binary models.

3.7.1 Comparison with other works

In this section, we compare the results obtained by our standard models with those produced by other standard models available in the literature.

Our standard values of internal structure constants at the ZAMS are in qualitative agreement with those obtained by Hejlesen (1987), Claret & Giménez (1989a) and Claret

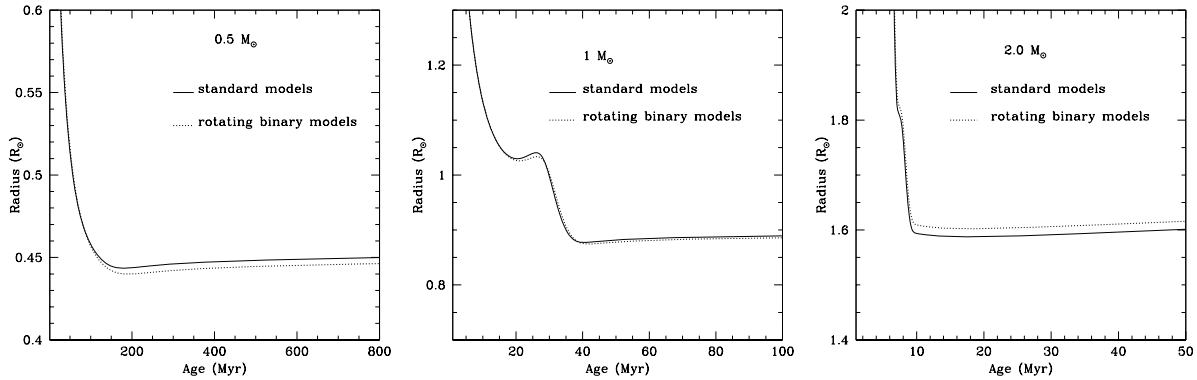

Figure 3.7: The comparison between the predicted stellar radii by our standard models and rotationally and tidally distorted ones. We report only the 0.5, 1.0 and 2.0 $M_\odot$. Solid curves denote standard models and dotted ones stand for rotating binary models.

& Giménez (1992).

Here, it is important to remember that the observed apsidal motion rates indicate that real stars are more centrally condensed than predicted by theoretical models, and this means that the lower the value of k_2 the closer to real (observed) stellar configurations we are. In this way, we say the lower k_2 the "better". In this section, we present theoretical individual stellar values of $\log(k_2)$. They cannot be directly compared with observed ones because the latter depends on the properties of the two binary system's components.

In order to do a better comparison between our results and the previous ones, we computed additional grids of $1\,M_\odot$ standard models, with different values of the mixing length parameter (α=2.0 and α=1.5), and with four different initial chemical compositions, (X,Z)=(0.7,0.02), (0.7,0.04), (0.7,0.004) and (0.8,0.02). From the left panel of Fig. (3.5), where we plotted the temporal evolution of $\log(k_2)$ for α=1.5 and the initial chemical compositions mentioned above, one can have an insight on how the metallicity affects the value of the second order internal structure constant. During the first 1 Myr the chemical composition does not alter $\log(k_2)$, but it becomes important from this age on. The metal poorer stars evolve to more centrally condensed configurations (lower values of $\log k_2$) than their metal richer counterparts. As can be seen from the left panel of Fig. (3.5), using the initial chemical composition (X,Z)=(0.7,0.04) (dotted lines) produces roughly the same effect on the evolution of $\log(k_2)$ as using the initial chemistry (X,Z)=(0.8,0.02) (long-dashed lines).

For the initial chemical composition (X,Z)=(0.7,0.02), we could compare the value of $\log(k_2)$ computed by our $1\,M_\odot$ model with three values available in the literature. From Table (3.5), we can see that, for this chemical composition and α=1.5, our $1\,M_\odot$ model produces $\log(k_2)$ lower than that obtained by Claret & Giménez (1992). For the metallicity in question and α=2.0, our $1\,M_\odot$ model produces $\log(k_2)$ value greater than that obtained by Claret & Giménez (1989a), which, by its turn, is greater than $\log(k_2)$ value of Hejlesen (1987). Now, let us consider the α which fits the sun for each model, namely, α=1.5 (for this work and Claret & Giménez 1992) and α=2.0 (for Claret & Giménez 1989a and Hejlesen 1987). Still remaining on the same metallicity, the best value of $\log(k_2)$ is obtained by Hejlesen (1987), followed by ours, Claret & Giménez (1989a) and Claret & Giménez (1992), in this order. Although Claret & Giménez (1992) set of models use updated opacities, for (X,Z)=(0.7,0.02) they obtained a value of k_2 for

Table 3.5: The comparison between our results (obtained with standard models) on internal structure constant and those previously existing in the literature. We are comparing $\log(k_2)$ values for a $1\,M_\odot$ model at the ZAMS.

Reference	α_{MLT}	(X,Z)	$\log(k_2)$
Hejlesen (1987)	2.0	(0.7,0.02)	−1.768
Claret & Giménez (1989a)	2.0	(0.7,0.02)	−1.747
Claret & Giménez (1992)	1.5	(0.7,0.02)	−1.619
this work	1.5	(0.7,0.02)	−1.763
this work	2.0	(0.7,0.02)	−1.669
Hejlesen (1987)	2.0	(0.7,0.04)	−1.614
this work	1.5	(0.7,0.04)	−1.479
this work	2.0	(0.7,0.04)	−1.400
Hejlesen (1987)	2.0	(0.7,0.004)	−2.035
this work	1.5	(0.7,0.004)	−2.128
this work	2.0	(0.7,0.004)	−2.027
Hejlesen (1987)	2.0	(0.8,0.02)	−1.578
this work	1.5	(0.8,0.02)	−1.626
this work	2.0	(0.8,0.02)	−1.538

$1\,M_\odot$ model at the ZAMS, which is 1.34 times greater than that obtained by Claret & Giménez (1989a). On the other hand, the former models produce $\log(k_2)$ lower than the latter ones for masses greater than $1.1\,M_\odot$.

For the remaining initial chemical compositions, we could compare our $1\,M_\odot$ model's results only with those by Hejlesen (1987). By comparing this two models for α=2.0, we realize that Hejlesen (1987) found a "better" value of k_2 than us. This can be due to the fact that our best fit to the sun is obtained with α=1.5. When we turn our attention to the models with α which reproduces the solar radius at the solar age (α=1.5 for this work and α=2.0 for Hejlesen 1987 models) we see: 1) for (X,Z)=(0.7,0.04), Hejlesen's (1987) models produce $\log(k_2)$ lower than our models; 2) for the two other metallicities, (X,Z)=(0.7,0.004) and (X,Z)=(0.8,0.02), our models reproduce more realistic internal structure constants. The $\log(k_2)$ values obtained by each author, at the ZAMS, are listed in Table (3.5). Although Hejlesen (1987) obtained the lowest values of k_2 for some metallicities, he used older opacities (Cox & Stewart 1969). The ATON2.3 code has many update and modern features regarding the physics of stellar interiors, such as most up to date OPAL Rogers & Iglesias (1993) opaicties and OPAL Rogers et al. (1996) equation of state.

3.8 Comparison between theory and observations

In order to test our new models, we chose the very interesting double-lined eclipsing binary system EK Cep (P=$4^d.42$). Double-lined eclipsing binary systems are often good candidates to test evolutionary models, but very few systems have as high number of constraints as in the case of EK Cep. The mass and radius of the primary component of this system are $M_1 = 2.029 \pm 0.023\,M_\odot$ and $R_1 = 1.579 \pm 0.007\,R_\odot$, while for the secondary, this values are $M_2 = 1.124 \pm 0.012\,M_\odot$ and $R_2 = 1.315 \pm 0.006\,R_\odot$ (Claret 2006). As described in this paper, EK Cep has accurate determination of absolute parameters (at

Table 3.6: Absolute dimensions of EK Cep. masses, radii and luminosities are given in solar units, effective gravities in cgs units and effective temperatures in K. Data obtained from Claret (2006).

	Primary	Secondary
Mass ($M_\odot$)	2.029 ± 0.023	1.124 ± 0.012
Radius ($R_\odot$)	1.579 ± 0.007	1.315 ± 0.006
$\log(g)$ (cgs)	4.349 ± 0.010	4.251 ± 0.006
log ($L/L_\odot$)	1.17 ± 0.04	0.19 ± 0.07
log ($T_{\rm eff}$)(K)	3.954 ± 0.010	3.756 ± 0.015

least concerning masses and radii), its secondary component is a pre-main sequence star, the apsidal motion presented by the system has a high relativistic contribution, the less massive component has its Lithium abundance measured and, also, the metallicity of the binary is evaluated. Among these characteristics, the most important one for our analysis is the fact that EK Cep B is the only known pre-main sequence system with apsidal motion measured.

EK Cep was discovered as an eclipsing binary system by Strohmeier (1959) from photographic observations. The photometric elements and the spectroscopic orbit of the system were first presented by Ebbighausen (1966a, 1966b), and further revised by other authors. The apsidal motion of EK Cep was first reported in Khaliullin (1983a). Tomkin (1983) determined the masses and the radii for the primary and secondary components of the system. He also noted that the secondary is oversized in comparison with a main sequence star with the same mass and supposed that it might still be contracting towards

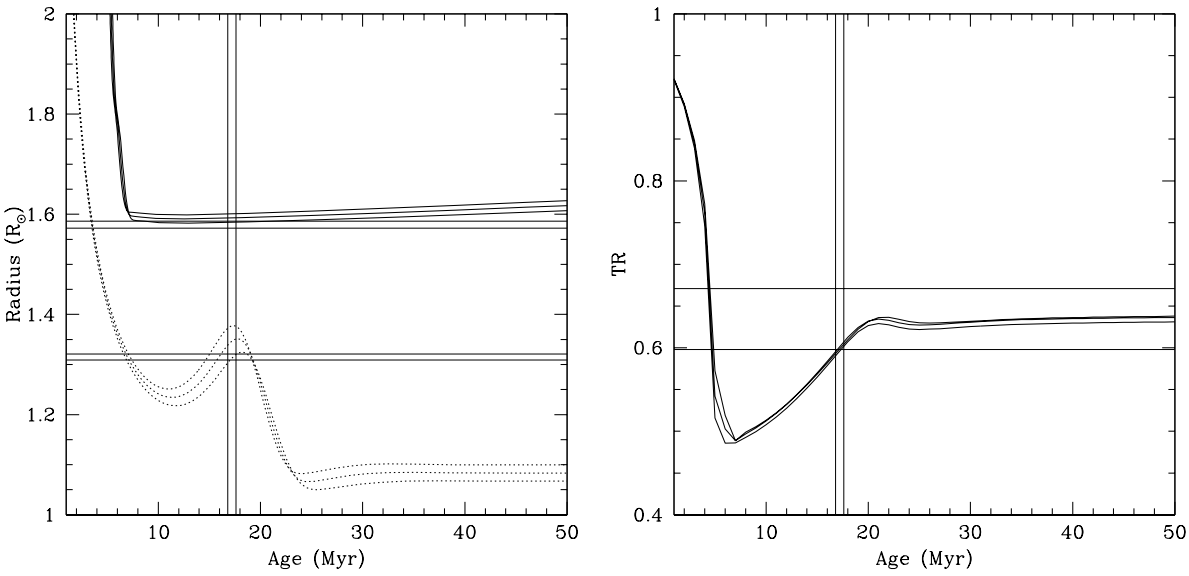

Figure 3.8: Radii (left) and effective temperature ratios (right) predicted by our binary rotating models for EK Cep components determined mass. The additional tracks refer to the maximum and minimum mass of each component star, according to the errors in their determination. Full lines denote the primary while dotted ones denote the secondary. Note that there is an acceptable agreement between radii and TR for a same isochron (vertical line). Horizontal lines represent the error bars in radii and TR determinations.

the main sequence. A study of the evolutionary status of both components made by Hill & Ebbighausen (1984) revealed that both the brighter and the fainter component are zero-age main sequence objects, despite Tomkin's (1983) suggestion about the secondary. Giménez & Margrave (1985) obtained a good agreement between theoretical apsidal motion rates (calculated with their models) and observationally determined rates. Popper (1987) reported some anomalies in the secondary of EK Cep, such as low effective gravity and temperature and the excess radiation in the blue band, that appears to be consistent with the hypothesis of the pre-main sequence nature of this star. From high-resolution spectroscopy in the LiI λ6708 Å region of the EK Cep binary system, Martín & Rebolo (1993) determined the lithium abundance of EK Cep B and provided new evidence that it has not settled onto the ZAMS. Claret et al. (1995) compared the observed parameters of EK Cep with theoretically predicted values. They derived a common age for the system around 2×10^7 years and confirmed the fainter component as a pre-main sequence star, while the more massive companion is in the beginning of the Hydrogen-burning phase. For the evolutionary age, they estimated the newtonian apsidal motion rate that is in agreement with the observations, considering the predicted relativistic contribution of about 40%. These authors also followed the lithium depletion during the computation of their models, which is consistent with the abundances determined by Martín & Rebolo (1993). The evolutionary status of EK Cep was studied by other authors in order to explain its several observed properties. Yildiz (2003) modeled the component stars by invoking a rapidly rotating core for the primary. Marques et al. (2004) investigated the role of overshooting in the modeling of pre-MS evolution of the secondary. The more recent analysis made about EK Cep was that by Claret (2006). Due to problems with the empirical determination of the effective temperatures of the component stars, he adopted the effective temperature ratio, which is better determined from the light curve analysis than their absolute values. Inconsistency found in the photometric distances for both components supports this approach. The other constraints Claret (2006) used in his analysis are radii, apsidal motion and lithium depletion, besides the effective temperature ratio. By using a rotating model (assuming local conservation of the angular momentum), with α=1.4 and (X,Z)=(0.7075,0.0175), he fitted the radii and the effective temperature ratio in the same isochrone (24.2×10^6 years).

In order to analyze the evolutionary status of EK Cep with the absolute dimensions given in Table (3.6), we followed the same approach as Claret (2006). As emphasized by this author, before computing stellar models for a given star it is fundamental to define clearly which observational parameters will be used as constraints. Here we will also adopt the masses, radii and effective temperature ratio. Apsidal motion and lithium depletion are used as additional constraints after obtaining an acceptable solution. By using our rotating binary models, we fitted the physical properties of the two component stars of EK Cep simultaneously at the same isochron. We used a mixing length parameter α=1.5 and an initial chemical composition of (X,Z)=(0.67,0.012). We tried to remain as close as possible to the solar composition based on the suggestion by Martín & Rebolo (1993) about the metallicity of the system, which corresponds to a metal content typical of a young disk solar-type star. From Fig. (3.8), we can see that, with these specific models we were able to reproduce radii and the effective temperature ratio for EK Cep system within the uncertainties. The age derived is around $(17.2 \pm 0.4)\times10^6$ years.

In Fig. (3.9), we place with crosses the stellar components of EK Cep system in the classical HR diagram. In Fig. (3.10), we place EK Cep stars in the $\log(g)$ versus $\log(T_{\rm eff})$

plane. The squares represent the errors in their positions. We also report the evolutionary tracks corresponding to the dynamically determined masses for both components of the system. We plotted, also, the tracks for the minimum and maximum masses for each component according to the errors in mass determinations. Evolutionary tracks were obtained with our new binary rotating models. The primary is represented by continuous lines while the secondary is represented by dotted lines.

We can see from these figures, that our tracks reproduce very well the position of the secondary both in the HR diagram and in the $\log(g)$ versus $\log(T_{\rm eff})$ plane. Its position in both planes is consistent with its pre-main sequence nature. On the other hand, even if we consider the errors involved, the primary position cannot be fitted by a model with the same input parameters, such as $\alpha_{\rm MLT}$, initial composition, rotation law, etc., as the secondary. This is because we decided to use radius and effective temperature ratio as constraints for our models, instead of using effective temperatures only. The opposite is also true: the model which best fits the components positions in the HR diagram does not reproduce the observed stellar radii and effective temperature ratio. For example, with the initial chemical composition (X,Z)=(0.7125,0.019) we obtain a good fit in the HR diagram and in the $\log(g)$ vs. $\log(T_{\rm eff})$ but we cannot fit the stellar radii.

The lithium depletion for both components was followed by our computations whose

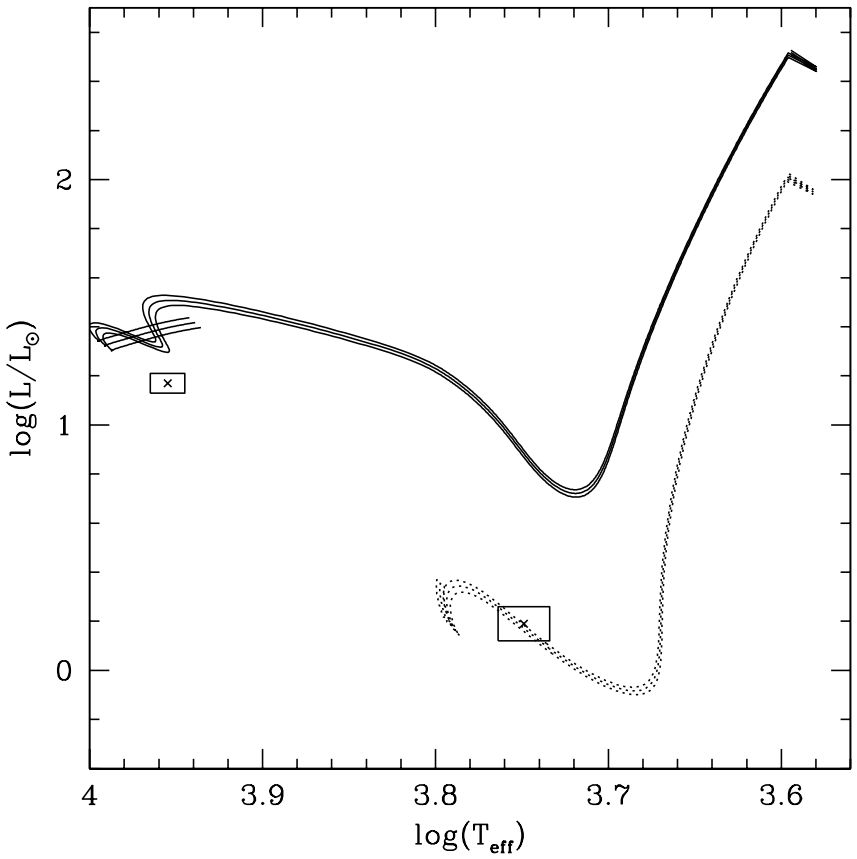

Figure 3.9: EK Cep components and corresponding mass tracks in the classical HR diagram ($\log(L/L_\odot)$ vs. $\log(T_{\rm eff})$). We show evolutionary tracks for the dynamically determined masses (with their errors). The crosses inside the squares are the components' loci in the HR diagram with respective errors. Same remarks as Fig. (3.8).

nuclear network is discussed in Ventura et al. (1998a). In the left panel of Fig. (3.11), we display the lithium content, log (Li/H), as a function of the stellar age. Continuous lines denote the primary while dotted ones denote the secondary (both with errors in the mass determinations). For the primary, the lithium evolution curve of the minimum allowed mass crosses the corresponding curve for the maximum mass. This does not happen for the less massive component. We have used an initial lithium abundance of log (Li/H)=3.1 (as D'Antona & Montalbán 2003). We do not find any depletion for the primary during its pre-main sequence evolution. For the secondary, we find a depletion of about 0.25 dex at the age of $(17.2 \pm 0.4) \times 10^6$ years, corresponding to a lithium abundance of log (Li/H)=2.85±0.04, that is consistent with the surface value log (Li/H)=3.1±0.3, derived by Martín & Rebolo (1993).

Finally, let us investigate the apsidal motion rate of EK Cep with the same evolutionary models. The orbital eccentricity was assumed to be 0.109 ± 0.003 and the orbital inclination 89.3 ± 0.1 degrees (Petrova & Orlov 1999). The anomalistic period of EK Cep, determined by Claret (2006), is $P = 4.4278062 \pm 0.0000005$ days. In the right panel of Fig. (3.11) we plotted the variation of the internal structure constants for the observed mass (with their errors) as a function of the evolutionary ages. Again, continuous lines denote the primary and dotted ones denote the secondary. We used our rotating binary models to analyze the temporal evolution of $\log(k_2)$. The vertical line indicate the

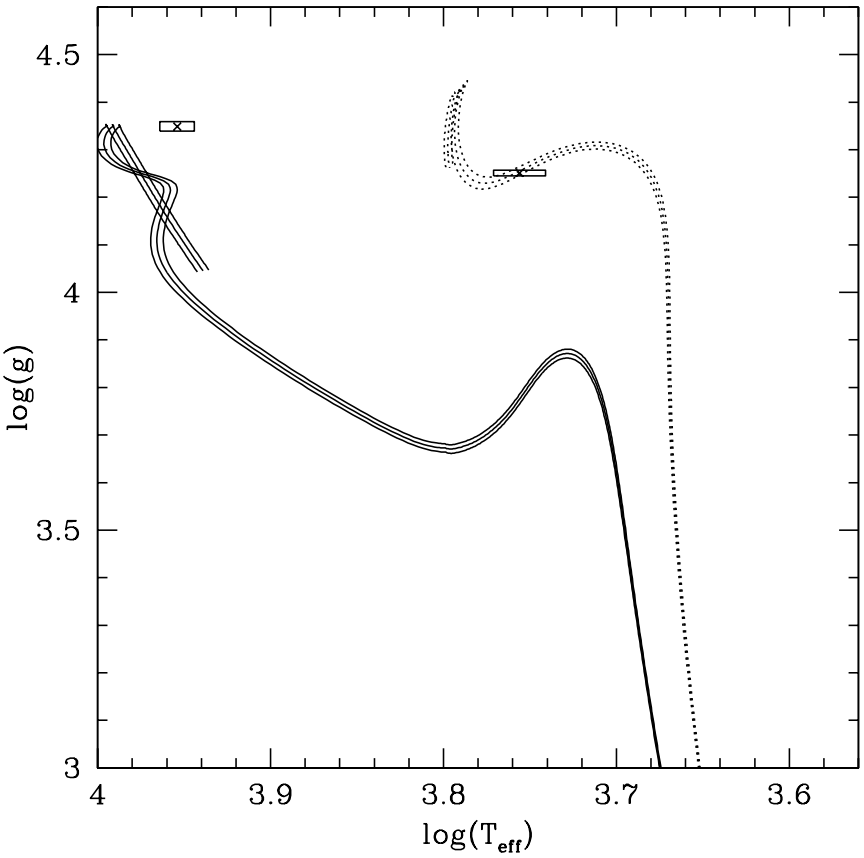

Figure 3.10: EK Cep components and corresponding mass tracks in the classical HR diagram ($\log(g)$ vs. log ($T_{\rm eff}$ plane). Same remarks as Fig. (3.8).

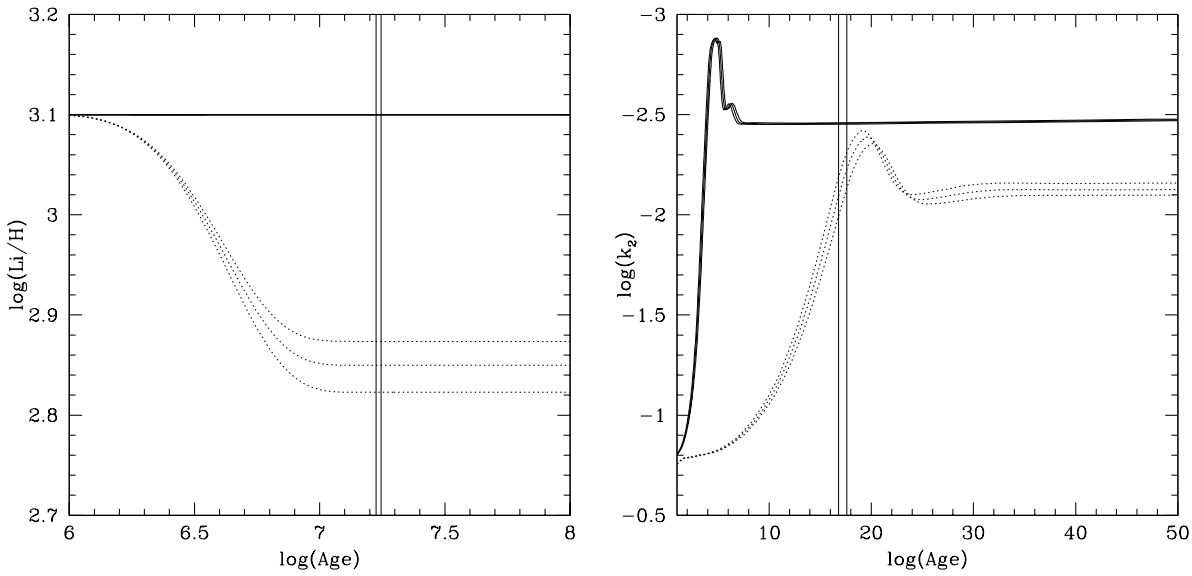

Figure 3.11: **Left:** Temporal evolution of Lithium abundances for EK Cep range of masses (2.006-2.052 $M_\odot$ for the primary and 1.112-1.136 $M_\odot$ for the secondary). **Right:** The second order apsidal motion constant as a function of the stellar age for EK Cep. In both panels we present the theoretical predictions of our binary rotating models. Same remarks as in Fig. (3.8).

age at which we took the internal structure constants to derive the apsidal motion rate. From the models for the observed masses and radii of the binary system, we derived the internal structure constants for both stars at the age of $(17.2 \pm 0.4)\times10^6$ yr. The models predict that values of k_2 are 0.0035 ± 0.0007 and 0.0086 ± 0.0009, for the primary and the secondary components, respectively. By using Eq. (3.18) we obtained the predicted apsidal motion constant for the system log $(\bar{k}_{2\,\mathrm{theo}})$=$-2.21\pm0.05$. From Eq. (3.2) and this theoretical value, we obtained the newtonian contribution of the apsidal motion rate ($\dot{\omega}_N$=0.00040 ± 0.00005 deg/cycle). We also calculated the relativistic contribution of the advance of periastron ($\dot{\omega}_R$=0.000439 ± 0.000003 deg/cycle), which corresponds to about 52% of the total rate. In this way, our models predict an apsidal motion rate of $\dot{\omega}$=0.00084 ± 0.00005 deg/cycle and, consequently, an apsidal period of U_{theo}=5200 ± 300 years. These values can be compared with the observed ones. Claret (2006) used a series of works (Khaliullin 1983b, Giménez & Margrave 1985, Hill & Ebbighausen 1984, Claret et al. 1995, and others) to derive the observed apsidal motion rate of this system. He reported the observed mean value of the internal structure constant, as log$(\bar{k}_2)$=-2.09 ± 0.09, which is equivalent to an observed apsidal motion of about $\dot{\omega}_{\mathrm{obs}}$=$0.00097\pm0.00015$ deg/cycle, after the relativistic correction. This apsidal motion rate produces an apsidal period of U_{obs}=4500 ± 700 years. From Table (3.7), where our results are summarized, it can be seen that our predicted values are in good agreement with the observed ones and the differences lie within the errors. The results obtained by Claret (2006) are also reported.

Table 3.7: Summary of the apsidal motion related quantities.

Quantity	Predicted	Observational	Claret 2006
$\log(k_2)$	-2.21 ± 0.05	-2.09 ± 0.09	-2.11 ± 0.06
U (years)	5200 ± 300	4500 ± 700	4600 ± 400
$\dot{\omega}$ (deg/cycle)	0.00084 ± 0.00005	0.00097 ± 0.00015	0.00095 ± 0.00008

3.9 Conclusions

For the first time, we computed values of internal structure constants for for low-mass pre-main sequence stars and developed an evolutionary model that takes into account the combined effect of rotation and tidal forces due to a companion stars. For all sets of models, namely, standard, rotating and rotating binary models, we tabulated the internal structure constants (k_2, k_3 and k_4) and the gyration radii (defined in Eq. 3.83) for ZAMS models and their temporal evolution. Our standard values were compared with those available in literature and are found to be in agreement with them. Our values for k_2, obtained with our standard models, are smaller than the last published values by Claret & Giménez (1992). Our rotating binary models produce internal structure constants even smaller than our standard ones. We remember the reader that the observations indicate that the values of k_2 should be smaller in real stellar configurations.

In the low-mass range, the assumption that the harmonics of order greater than j=2 can be neglected, widely used when analysing the apsidal motion of binary systems, seems not to be justified. We verify that tidal effects acts in the same way as rotational ones but in a smaller scale. Besides, the rotationally and tidally distorted models produce opposite effects in the physical quantities of a star for masses below 1.3-1.5 $M_\odot$ and for masses above this threshold (Fig. 3.7). This behavior in distortion effects is caused by the transition from the p-p chain and CNO cycle. The non-standard evolutionary tracks are cooler than standard ones, mainly for low mass stars (Fig. 3.3). As can be seen from Fig. (3.5), distorted models predict more concentrated stars at the ZAMS than standard models. Due to the combined differences between the radius and the rotational inertia obtained with standard models and distorted ones, the gyration radii produced by the latter models are slightly larger, for a given mass at the ZAMS, than those yielded by the former ones.

Using our new set of evolutionary tracks computed with rotating binary models we investigated the evolutionary status of the interesting double-lined eclipsing binary system EK Cep. Its primary, a 2.029 $M_\odot$ star, seems to be in the Hydrogen-burning phase, and its secondary, a solar-like star (1.124 $M_\odot$), is confirmed as a pre-main sequence star. We followed the same approach as Claret (2006), in our analysis. Instead of using the absolute values of the effective temperature of each component, we decide to use the stellar radii and the temperature ratio, to avoid the uncertainties involved in individual temperatures determinations. These values were reproduced by using a model with an initial chemical composition of (X,Z)=(0.67,0.012) and an α mixing length parameter of α=1.5. We also followed the lithium content during the pre-main sequence evolution of both components. As expected, we do not find any significant depletion for the primary, while the Li depletion for the secondary agrees with the observed values within the uncertainties. The quantities related to the apsidal motion of the system were also derived in this work (see Table 3.7). The predicted values for the apsidal motion rate and period

are, respectively, $\dot{\omega}_{\rm theo}$=0.00084±0.00005 deg/cycle and $U_{\rm theo}$=5200±300 years, while the observed values are $\dot{\omega}_{\rm obs}$=0.0097±0.00015 deg/cycle and $U_{\rm obs}$=4500±700. Again, differences remains within the errors. As mentioned above, we were able to model EK Cep with our rotating binary models (and with the standard ones, also). Nevertheless, some uncertainties still remain. So, our model, as well as the models proposed by other authors, cannot be considered as definitive. From both the theoretical and the observational point of view, there are improvements that could be done in order to reduce uncertainties and discrepancies. On the theoretical side, we can use a better approximation for the companion star, by considering the simultaneous evolution of the two components of a binary system. From the observational point of view, one can reduce the uncertainties on the absolute dimensions, specially on the effective temperatures.

Chapter 4

Theoretical Values of the Rossby Number

4.1 Introduction

Magnetic activity in solar-type stars encompasses a variety of phenomena, such as starspots, activity cycles, heated outer atmospheres, X-ray emission, and many others. The driving mechanism for this activity is generally attributed to a dynamo that results from the interaction between rotation and convective motions in the star's outer envelope (Sect. 4.2). Theoretical work by a number of researchers indicates that for main-sequence, solar-type stars the field is generated and amplified at the *tachocline*, the thin layer of differential rotation between the convection zone and the nearly rigidly rotating radiative interior. For stars of spectral type ranging from mid-F to early-M dwarfs, rotation and activity are thought to be controlled by this process, also called an $\alpha-\Omega$ dynamo (Mohanty & Basri 2003). Its efficiency is strongly dependent on the rotation rate and convective timescales. Young and rapidly rotating stars are, in general, very active. Specific models of dynamo theory, such as the $\alpha-\Omega$ type, have been successful in explaining the qualitative features of solar activity (Weiss & Tobias 2000).

Activity is strongly correlated with rotation velocity in the mid-F to mid-M dwarfs; it increases rapidly with the projected velocity, $v \sin i$, then saturates above some threshold velocity (~ 10 km/s). This relationship is evident only down to K types. As we go from M to M6 types the rotation activity connection becomes less clear. Mohanty & Basri (2003) analyzed rotation velocities and chromospheric Hα activity, derived from high-resolution spectra, in a sample of mid-M to L field dwarfs. They found that, in the spectral type range M4-M8.5, the saturation-type rotation-activity relation is similar to that in earlier types, but the activity saturates at a significantly higher velocity in the M5.5-M8.5 dwarfs than in the M4-M5 ones. This may result from a change in the dynamo behaviour in later spectral types.

For fully convective stars, such as pre-MS late type stars, this theory cannot be readily applied, as they miss the tachocline. However, since magnetic indicators, such as active regions and strong flaring, have also been reported for those stars, dynamo mechanisms operating on the full convection region have also been proposed (e.g. Durney et al. 1993).

On the other hand, as shown in Fig. (4.1), observations of stellar activity in solar-type stars have shown a very tight relationship between chromospheric Ca II flux and the Rossby number *Ro* (Noyes et al. 1984), defined as the ratio of the rotation period, P_{rot}, to the convective turnover time, τ_c. The Rossby number plays an important role in dynamo models, being related to the growth rate of the field. It is an indicator of rotation which, by its turn, indicates magnetic activity. For solar-type stars, since τ_c cannot be directly measured, *Ro* is generally computed through a polynomial fit of τ_c to the B-V color index. $\tau_c(B-V)$ is a theoretically-derived convective overturn time, calculated assuming a mixing length to scale height ratio $\alpha \sim 2$ (Noyes et al. 1984).

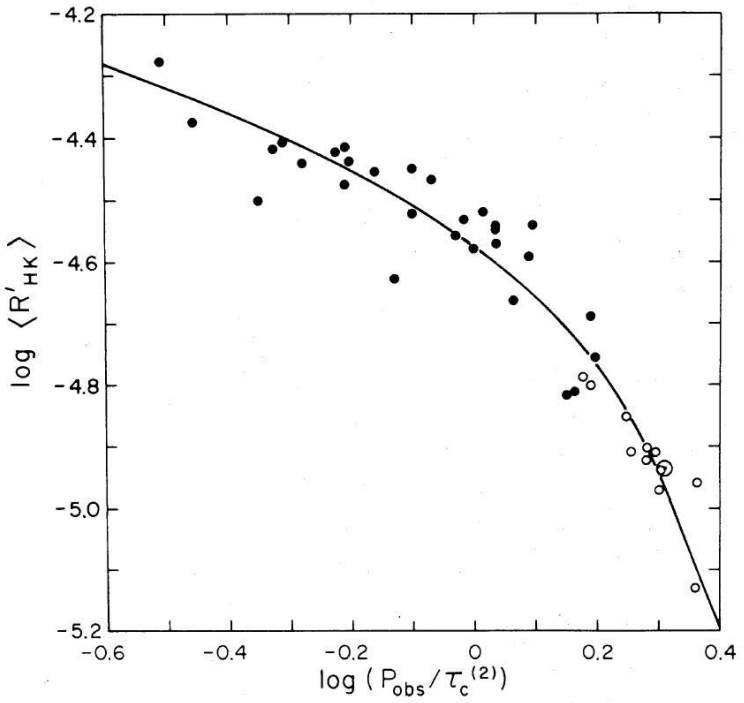

Figure 4.1: Chromospheric Ca II flux vs. Rossby number for main sequence stars. Closed and open circles represent "young" and "old" stars (Noyes et al. 1984).

For pre-main sequence stars, Rossby numbers have been used to study the relationship between X-ray emission and magnetic fields (e.g. Flaccomio et al. 2003c, Feigelson et al. 2003). In this case, however, a clear relationship between activity and rotation is not seen as in the case of main-sequence stars, and one has to resort to evolutionary models for estimating Rossby numbers.

Though current stellar evolutionary codes are not yet able to deal with magnetic fields, a first step towards that direction is the introduction of rotation on those models, as it is a key component of stellar dynamos. This is the case of the `ATON 2.3` evolutionary code, in which both rotation and internal angular momentum redistribution have been introduced. Such capabilities allow us to make some exploratory work towards a future version that can handle magnetic field generation from first principles.

We computed convective turnover times and Rossby numbers for a range of rotating low-mass stellar models, and discuss their behavior with time from the pre-MS to the zero-age main sequence. Some comparisons with previous work in the literature are also

made. A substantial part of this chapter was published in Landin et al. (2005).

4.2 The solar dynamo

In this section, we give a short description of the solar magnetic field. For a comprehensive overview of solar dynamo theory as a whole an excellent place to start is the recent article by Ossendrijver (2003)

The stellar convective zone consists of a plasma, i.e. a gas that contains electrically charged particles, which is continuously moving around. Since the plasma is moving, the charged particles are moving and we obtain electrical currents. However, electrical currents generate magnetic fields (Ampere's law). These magnetic fields in turn generate electric currents (Faraday's law) and therefore we obtain the following loop: electric current - magnetic field - electric current - magnetic field - electric current - magnetic field etc, etc. As long as this loop is not interrupted the Sun will always produce magnetic fields.

However, this is a very simplified picture of the solar dynamo and does not tell us anything about the properties of the motions of the plasma. The flow of the plasma has to fulfill certain properties for the dynamo to work. These properties are:

1. The flow has to be turbulent. A laminar flow does not work.

2. The flow has to be fully three-dimensional.

3. The flow has to be helical.

Thus we need very complicated flows in order to generate any magnetic fields whatsoever. Another important ingredient for dynamo action is differential rotation, i.e. the fact that the Sun rotates faster at the equator than at the poles. In other words the rotation rate of the Sun varies with latitudes (but also with radius).

The lines of magnetic field of the star is stretched, twisted an folded by the motions of the plasma within the solar convection zone. In order to increase the magnetic field strength, the motions of the plasma have to continuously transform a meridional magnetic field into an azimuthal magnetic field and vice versa. A meridional magnetic field is basically a field that points from the north to south or south to north, while an azimuthal magnetic field points from east to west or west to east (left panel of Fig. 4.2). So, we get another loop: meridional magnetic field - azimuthal magnetic field - meridional magnetic field - azimuthal magnetic field etc. Again the Sun will produce magnetic field as long as this cycle is not interrupted.

Let us now describe how the flow of the plasma achieves this loop. Firstly, the solar differential rotation stretches the magnetic field and winds it around the Sun. This stretching takes a meridional magnetic field and stretches it into a azimuthal magnetic field (see Figs. 4.2 and 4.3). This only happens because the Sun rotates faster at the equator than at the pole. If the Sun would rotate at the same rate everywhere (as a solid body) nothing would happen to the magnetic field and the dynamo would not work. The effect of stretching the magnetic field by differential rotation is often referred to as the omega-effect (see Fig. 4.3). Now that we stretched the meridional magnetic field into a azimuthal magnetic field we need to do the opposite. This is done by the alpha-effect

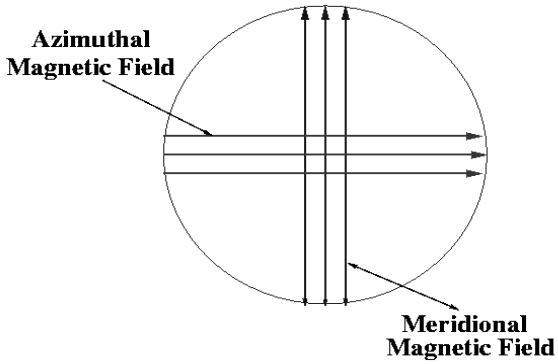

Figure 4.2: Azimuthal and meridional fields in the dynamo theory.

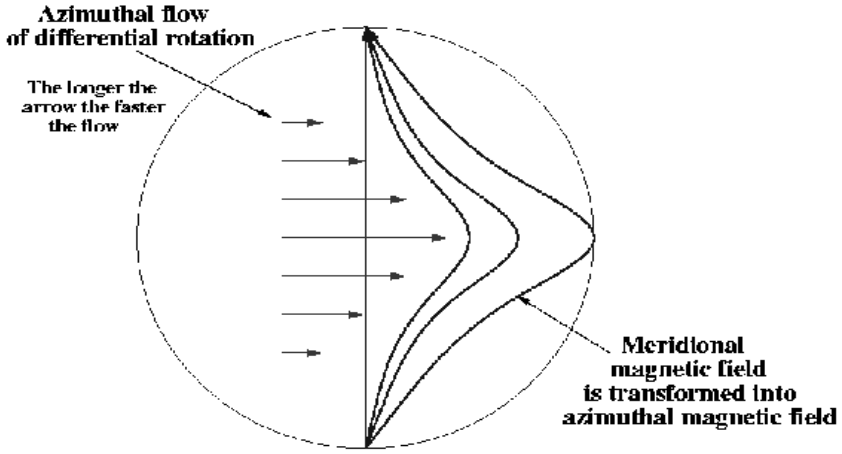

Figure 4.3: The ω-effect in the dynamo theory.

which is due to the interaction of convection and rotation. The alpha-effect basically takes the azimuthal magnetic field generated by the omega-effect and transforms it back into meridional flow. Exactly how this works is at present not well understood.

4.3 Input physics

The `ATON 2.3` code has many updated and modern features regarding the physics of stellar interiors, of which a full account can be found in Ventura et al. (1998a). Some of its most important features are: most up to date OPAL (Rogers & Iglesias 1993) opacities, supplemented by those of Alexander & Ferguson (1994) for lower (T$< 6000K$) temperatures; diffusive mixing and overshooting; convection is treated under both the mixing length theory (MLT) or the Full Spectrum of Turbulence (FST) from Canuto & Mazzitelli (1991,1992) and Canuto et al. (1996).

The approach for including structural effects of rotation and internal angular momentum redistribution in the `ATON 2.3` code is described elsewhere (Mendes et al. 1999a, 2003). Angular momentum losses in the star's external layers due to magnetized stellar winds are also taken into account, in the form of a boundary condition at the surface. We adopted the prescription used in Chaboyer et al. (1995) with a "wind index" $n = 1.5$,

which reproduces well the Skumanich (1972) law $v \propto t^{-1/2}$:

$$\frac{\partial J}{\partial t} = K \left(\frac{R}{R_\odot}\right)^{2-n} \left(\frac{M}{M_\odot}\right)^{-n/3} \omega^{1+4n/3}, \qquad \omega < \omega_{\rm crit}, \tag{4.1}$$

$$\frac{\partial J}{\partial t} = K \left(\frac{R}{R_\odot}\right)^{2-n} \left(\frac{M}{M_\odot}\right)^{-n/3} \omega \omega_{\rm crit}^{4n/3}, \qquad \omega \geq \omega_{\rm crit}, \tag{4.2}$$

where $\omega_{\rm crit}$ introduces a critical rotation level at which the angular momentum loss saturates. The constant K in our models was calibrated by adjusting a $1\,M_\odot$ model so that its surface velocity matches the current solar rotation rate at the equator.

4.4 Rossby number calculations

Convective turnover times and Rossby numbers were computed for models ranging from 0.6 to $1.2\,M_\odot$ (in $0.1\,M_\odot$ increments) with solar chemical composition. For ease of comparison with a previous work by Kim & Demarque (1996), that provided the first theoretical calculations of Rossby number, convection was treated according to the MLT, with the free parameter α set to 1.5 (which fits the solar radius at the solar age for a gray non-rotating model). Rotation was modeled according to rigid body law in convective zones and local conservation of angular momentum in radiative regions (Mendes et al. 1999a). The initial rotation for all models was taken from the Kawaler (1987) relations between mass and angular momentum for low-mass stars (see Eq. 3.100).

Fig. (4.4) depicts the rotation period as a function of age for all models, and shows the typical spin-up during contraction followed by the longer phase of continuous spin-down.

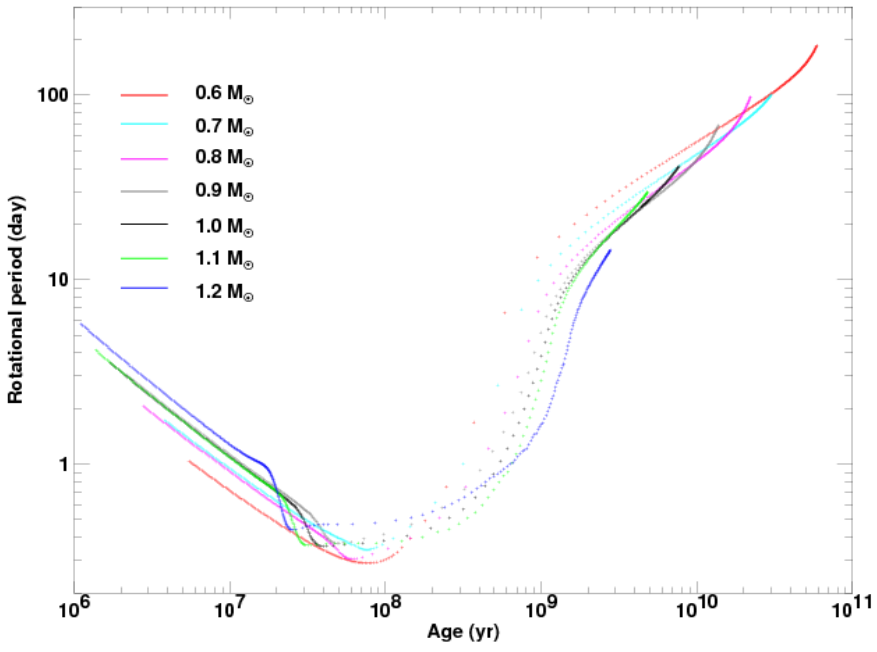

Figure 4.4: Rotation period plotted against age, for each model mass.

For the $1\,M_\odot$ model, this results in an initial velocity of nearly $3\,km\,s^{-1}$ at the beginning of the Hayashi phase. This is about one order of magnitude below the value used by Kim & Demarque (1996), but we decided to adopt a lower initial rotational velocity because, in this way, our models are able to reproduce the observed angular velocity of TTauri stars at the corresponding age. The local convective turnover time, τ_c, was calculated at a distance of one-half the mixing length, $\alpha\,H_P/2$, above the base of the convection zone. Its value is computed through the equation $\tau_c = \alpha\,H_P/v$.

Fig. (4.5) shows the temporal evolution of the local convective turnover time (in seconds). For a given mass, it decreases during the Hayashi contraction and reaches its minimum when the contraction stops. After that, τ_c remains constant until the stars reach a main sequence configuration.

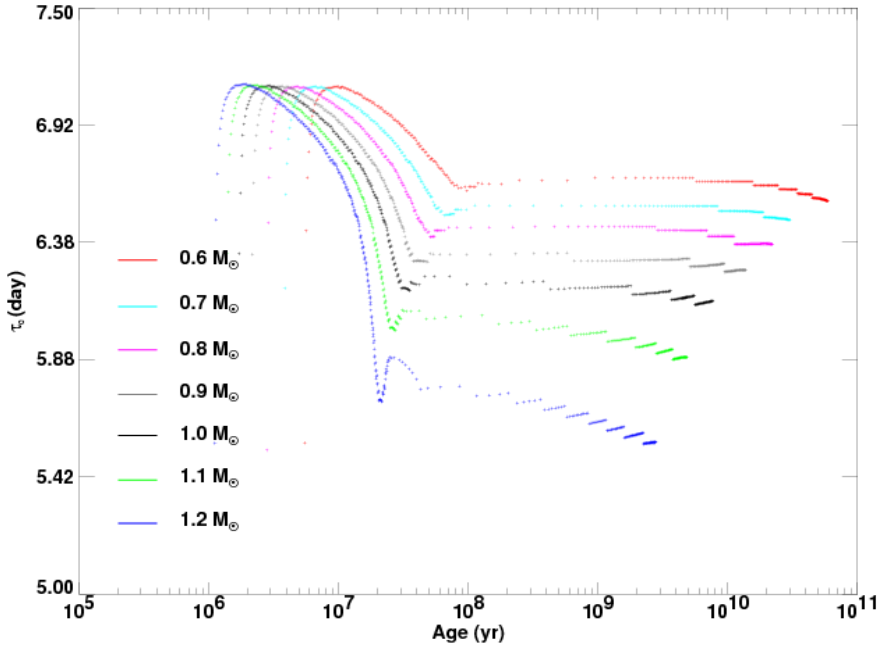

Figure 4.5: "Local" convective turnover times as a function of age for all models.

However, most relevant for our purposes are Figs. (4.6) and (4.7), which show the profiles of the "global" convective turnover time, defined as

$$\tau_c = \int_{R_b}^{R_\star} \frac{dr}{v}, \tag{4.3}$$

and the "dynamo number" Ro^{-2}, respectively, as functions of age. These figures show that τ_c also decreases substantially during contraction to the ZAMS, but after that remains nearly constant and depends only on the mass. With regard to Ro, it is seen that it follows τ_c during contraction but, after that, increases as expected since the rotation period also increases.

By using the evolutionary tracks, we constructed a set of isochrones for the ages of 0.2, 0.5, 0.7, 1.0, 2.0, 4.55 (solar age), 10 and 15 Gyr. In Table (4.1), we list their characteristics, such as stellar mass (column 1), logarithm of the effective temperature

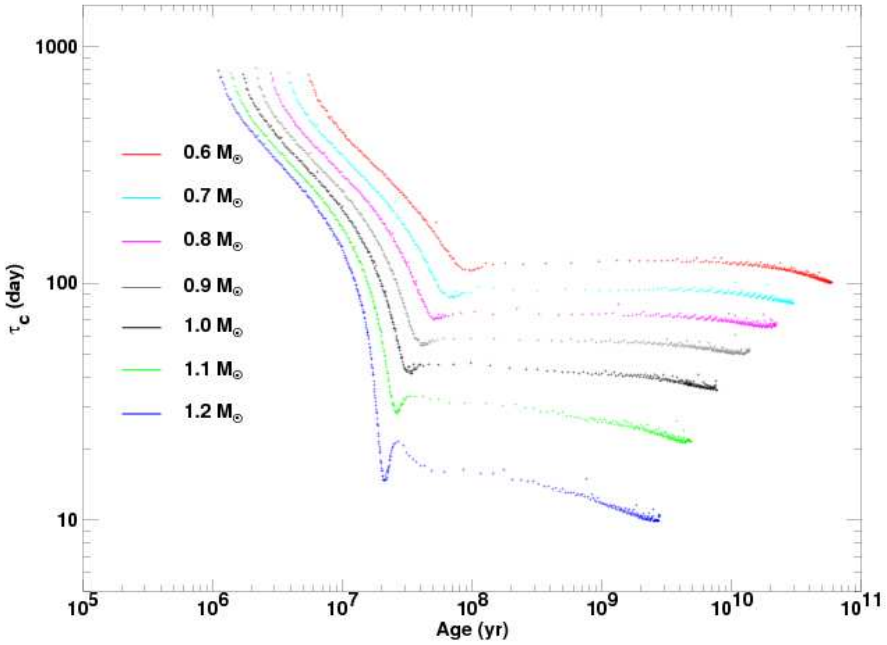

Figure 4.6: "Global" convective turnover time as a function of age for each model mass.

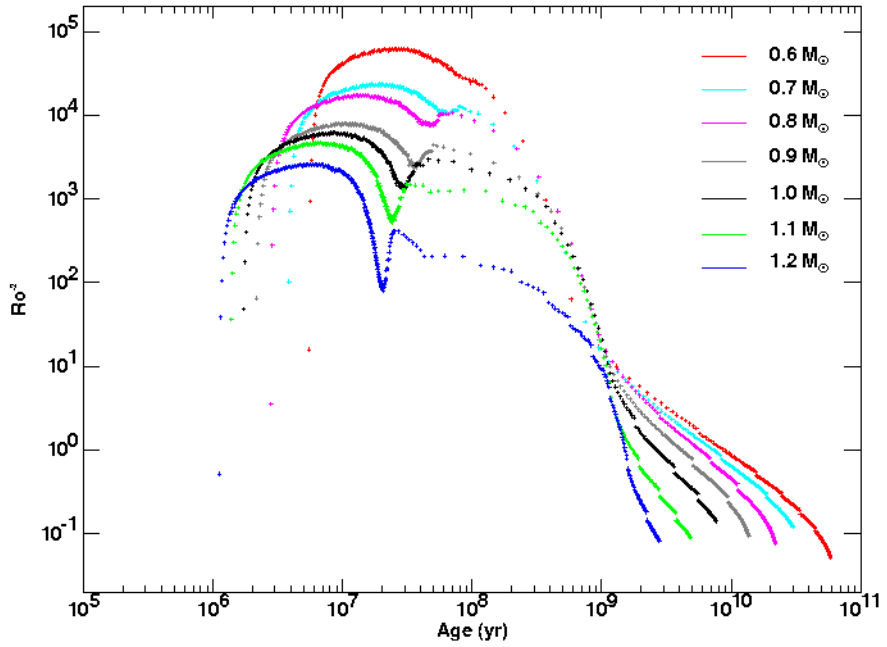

Figure 4.7: The dynamo number as a function of age for each model mass.

(column 2), logarithm of the stellar luminosity (column 3), global convective turnover time (column 4), dynamo number (column 5) and the rotation period, in days, (column 6). In the left panel of Fig. (4.8), we show a plot of the global convective turnover time versus T_{eff} for each mass model. The local convective turnover time gives the same result as the global τ_c except for a scaling factor (Kim & Demarque 1996), because the convective turnover timescale is weighted towards the deepest part of the convection zone, where the

shortcomings of the mixing length approximation are least important. Isochrones for the global convective turnover time versus period are shown in the right panel of Fig. (4.8).

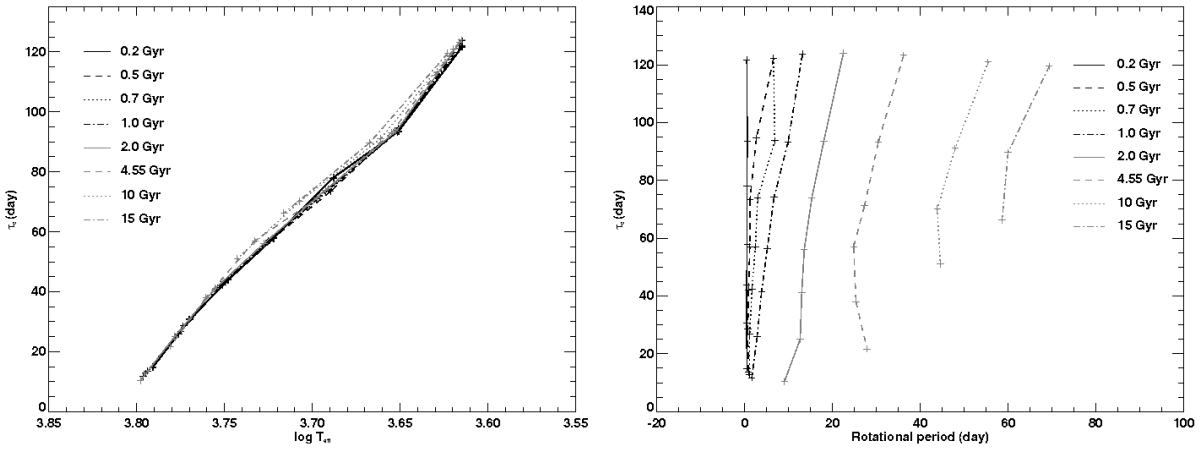

Figure 4.8: The global convective turnover time as a function of effective temperature and age (left) and the same quantity as a function of rotation period and age (right).

In the left panel of Fig. (4.9), we show the rotation period versus the logarithm of the effective temperature. The rightmost points (those with the lowest temperatures) correspond to the lowest mass considered, namely, $0.6\,M_{\odot}$. In our models, we treat rotation, in convective zones, according to the rigid body law and, in radiative regions, rotation was modeled by assuming local conservation of angular momentum. To the best of our knowledge, this is the best way to mimic stellar rotation. If we assume that it is a correct treatment for stellar rotation, Fig. (4.9) can be used to uniquely determine the mass and the age of a star by observing its effective temperature and the rotation period. In the right panel of the same figure, we plotted the inverse square of the Rossby number versus the rotation period. Once more, the rightmost point of each line represents the lowest mass. Also this figure can be used to infer an stellar mass and age from observational quantities. In this case, measurements of rotation period and an activity index (related to the Rossby number) are useful to estimate stellar mass and age. Of course, these determinations are model dependent and are subjected to the assumptions made in each model. Our predictions for the dynamo number differ quantitatively from that of Kim & Demarque (1996) by two orders of magnitude. This difference is addressed to a different input value used in both works for the angular velocity.

Fig. (4.10) shows the dynamo number Ro^{-2} as a function of effective temperature and age. After establishing an empirical relation between Ro^{-2} and magnetic activity indices, one can use Fig. (4.10) to determine the stellar mass and age from the effective temperature and an activity index.

We believe that this set of results can be useful to support observational studies of active pre-main sequence stars, as well as for testing stellar models against observations.

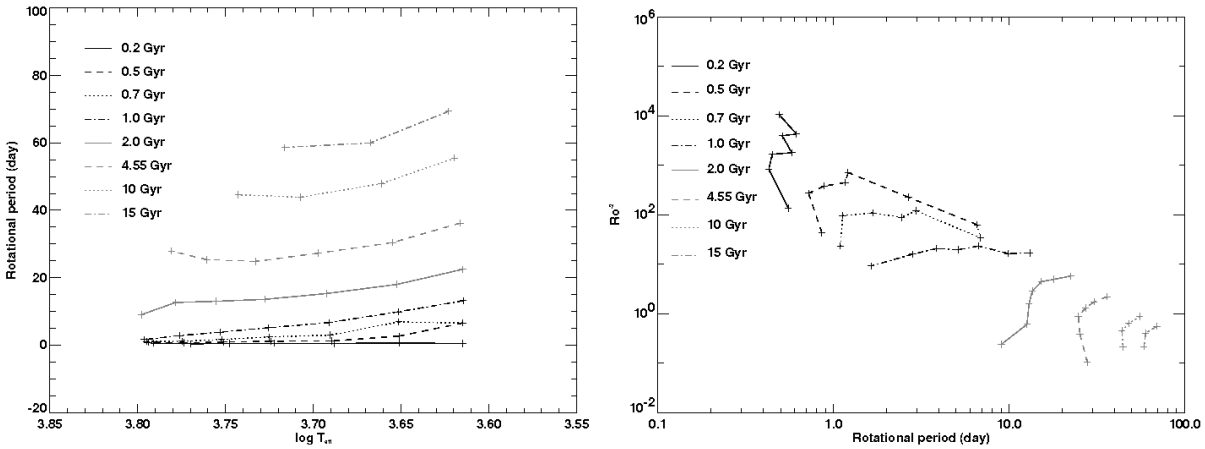

Figure 4.9: **Left:** Rotation period as a function of effective temperature and age. **Right:** The dynamo number as a function of rotation period and age. For clarity, we do not report the 15 Gyr isochron.

4.5 Conclusions

To the best of our knowledge, the only work that reports *Ro* calculations for rotating pre-main sequence stars is the one by Kim & Demarque (1996). Our results show the same trends for *Ro* and τ_c found in that work, such as, for example, the decrease of τ_c during the pre-main sequence phase and its nearly constant value from that point on. The main difference occurs in the values of *Ro*: in certain cases, our values are lower by two orders of magnitude. Though a full analysis of these discrepancies are still going on, they can be traced at least to differences in the initial rotation rates and internal angular momentum mechanism adopted in both cases.

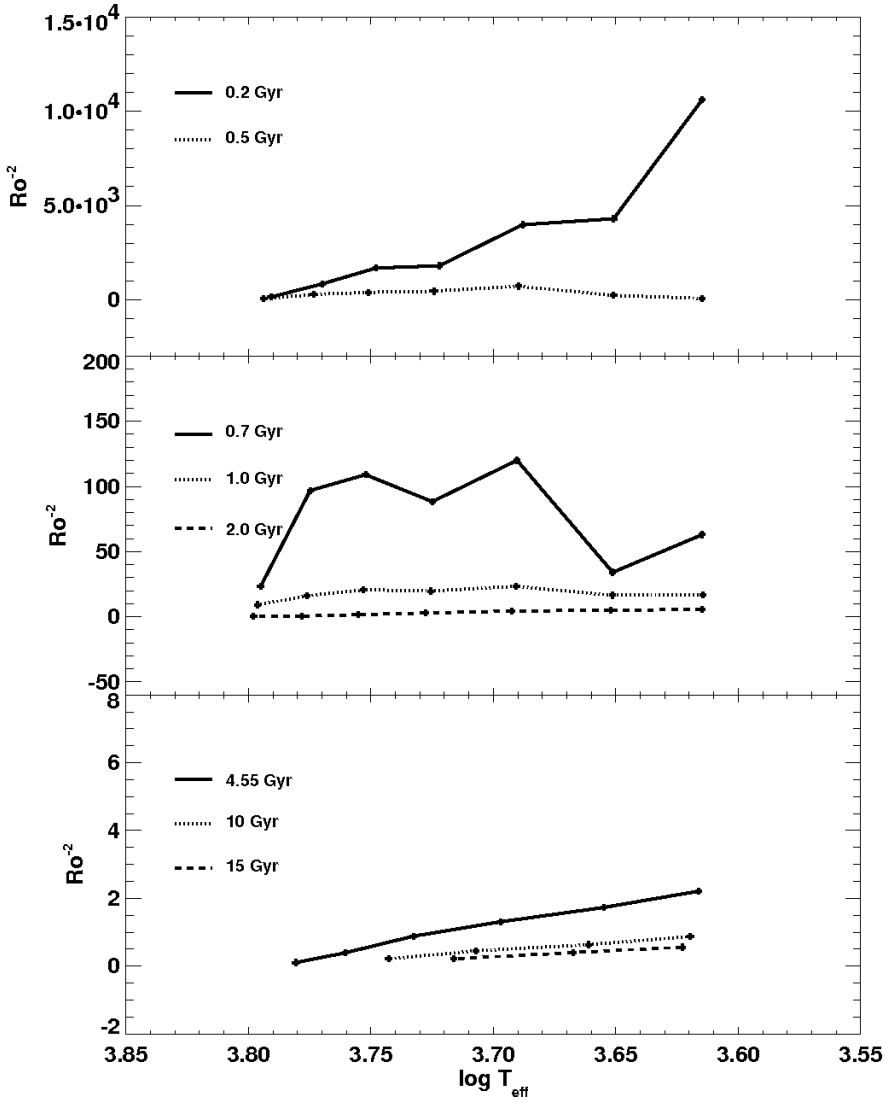

Figure 4.10: Dynamo number as a function of temperature and age (days) for isochrones of 0.2, 0.5, 0.7, 1.0, 2.0, 4.55 (solar age), 10 and 15 Gyr.

Table 4.1: Isochrones for all models.

Mass ($M_\odot$)	log (T_{eff})	log ($L/L_\odot$)	τ_c (days)	Ro^{-2}	Rotation Period (d)
			0.2Gyr		
0.60	3.6149	−1.13415	120.2859	4863.1904	0.7537
0.70	3.6508	−0.85839	93.5565	4295.6924	0.6156
0.80	3.6880	−0.60034	78.0725	3979.4875	0.5109
0.90	3.7221	−0.36201	57.8066	1798.2704	0.5793
1.00	3.7489	−0.14360	43.3016	1312.1923	0.5107
1.10	3.7698	0.05327	30.7249	840.2523	0.4290
1.20	3.7908	0.23910	14.7793	135.7796	0.5523
			0.5Gyr		
0.60	3.6147	−1.12873	122.2169	63.0188	6.5857
0.70	3.6511	−0.85175	94.6016	226.0953	2.6779
0.80	3.6900	−0.58831	73.6797	292.8649	1.8939
0.90	3.7244	−0.34844	58.0709	278.6011	1.4871
1.00	3.7514	−0.12971	42.1280	280.3475	1.0378
1.10	3.7738	0.07390	27.3749	228.5956	0.7949
1.20	3.7940	0.26196	13.0489	41.0794	0.8864
			0.7Gyr		
0.60	3.6145	−1.12643	123.7466	16.8957	13.1607
0.70	3.6512	−0.84898	93.7444	34.1065	6.8875
0.80	3.6903	−0.58609	73.9136	120.0507	2.9580
0.90	3.7249	−0.34448	57.0625	88.3630	2.4377
1.00	3.7522	−0.12387	42.2890	109.0130	1.6735
1.10	3.7750	0.08300	26.4771	78.0264	1.2622
1.20	3.7950	0.27319	12.7794	23.3266	1.0950
			1Gyr		
0.60	3.6146	−1.12405	125.1279	9.9933	17.0856
0.70	3.6516	−0.84516	93.3750	11.2314	11.9879
0.80	3.6909	−0.58074	74.3170	15.2874	8.2820
0.90	3.7257	−0.33755	56.8681	13.2240	6.3101
1.00	3.7530	−0.11541	41.5055	20.7376	3.8614
1.10	3.7761	0.09587	26.5180	12.8111	3.1773
1.20	3.7962	0.29010	11.7439	9.1811	1.6389
			2Gyr		
0.60	3.6150	−1.11848	124.0540	4.7964	24.6171
0.70	3.6524	−0.83706	93.7042	4.3440	19.2509
0.80	3.6927	−0.56723	75.4010	4.0526	16.0603
0.90	3.7277	−0.31785	56.6820	2.6826	14.0612
1.00	3.7553	−0.08623	41.0925	1.5957	13.0118
1.10	3.7784	0.13731	24.3629	0.5856	12.9089
1.20	3.7979	0.34697	10.1410	0.2333	9.1969
			4.55 Gyr		
0.60	3.6164	−1.10583	123.8610	2.0500	37.5970
0.70	3.6550	−0.81612	93.5239	1.6472	31.2073
0.80	3.6971	−0.53350	71.1808	1.3054	27.2848
0.90	3.7328	−0.26479	53.8329	0.8621	25.1410
1.00	3.7605	−0.00313	38.5843	0.3882	25.4702
1.10	3.7807	0.25745	21.7490	0.1025	28.0496
			10 Gyr		
0.60	3.6197	−1.07964	121.5720	0.8441	56.4212
0.70	3.6611	−0.77012	91.0848	0.6311	47.9352
0.80	3.7071	−0.45204	70.1379	0.4487	43.8889
0.90	3.7429	−0.12265	51.3548	0.2098	44.9542
			15 Gyr		
0.60	3.6229	−1.05529	119.5294	0.5580	69.3882
0.70	3.6677	−0.72121	90.7505	0.3918	60.4867
0.80	3.7164	−0.35712	66.5298	0.2118	59.0670

Chapter 5

Non-Gray Atmospheres

At any point inside a star, photons of different energies may be found traveling in various directions. These photons constitute the radiation field at a particular point and time. Photons passing through matter may be scattered or absorbed by atoms, ions and molecules. They may also be emitted as a result of charged particle motions, or from excited atomic and molecular states. These processes, taken collectively, result in modifications of the radiation field passing through matter. When this happens the matter and the radiation are coupled.

The energy flows through the star, from the interior to the atmosphere, and this flux can be transported by three mechanisms: radiative transfer, convective transport and conduction. The efficiency of these process is mainly determined by the quantity of energy to be transported by the particles of the medium, by the number of existing particles and by their velocities. Besides, the opacity of the material to the motion of the particles that carry the energy plays an important role in the process of energy flow. The energy transport in atmospheres of most stars is radiative. In this case, the opacity is characterized by the cross section of the particles and by their numerical density.

In order to understand the processes that take place when the light is radiated to space, we use an equation that describes the energy transport through the stars, the *Radiative Transfer Equation* (RTE). One of the great problems in stellar atmospheres is to find out a solution to this equation, because in the outermost regions of a star the mean free path of the particles is large and the diffusion approximation is not valid. The nature of the transfer equation depends on the geometry of the medium through which the energy flows. The source function, which is the local contribution given to the radiation field, is influenced by the nature of the physical medium. Sometimes the source function depends on the radiation field itself. So, for each different condition existing in atmosphere, we will have a different solution of the RTE.

As getting formal solutions of the RTE is not a simple task, theoretical astrophysicists have been seeking solutions to an idealized radiative transfer problem known as the *gray atmosphere*. In the gray atmosphere approximation the increase of the temperature T from the surface moving inwards is described via a relationship between T and the optical depth (τ), and the pressure is calculated by integrating the hydrostatic equilibrium

equation. The matching between the interior and the external layers is made at τ=2/3. Substantially, any link between pressure and temperature, fixed by the either convective or radiative gradient, is ignored. This approximation has the advantage that a complete solution can be obtained for the radiation field irrespective of the physical details of the atmosphere. In the gray atmosphere approach, the opacity is independent of frequency. Thus, all frequencies can be treated equally, as far as the radiative transfer is concerned. The independence of the radiative transfer from frequency has the interesting consequence that all aspects of the mathematical description are independent of frequency. But, on the other hand, we know that the physical processes of interaction between radiation and matter are not frequency independent. Certainly, bound-bound transitions cannot be considered as gray processes. However, there are some bound-free transitions that exhibit only weak frequency dependence over substantial regions of the spectrum. If those regions are responsible for the part of the spectrum containing most of the radiant flux, then the atmosphere will be very similar to a gray atmosphere. Absorption due to the H^- ion is relatively frequency-independent along the visible part of the spectrum, and in some stars it is the dominant source of opacity. However, the main source of a gray opacity is the electron scattering. Thompson scattering by free electrons is frequency-independent by definition, and for stars hotter than about 25,000 K, it is the dominant source of opacity along the range of wavelengths encompassing the maximum flow of energy. Thus, the O and B stars have atmospheres that, to a very high degree, may be regarded as gray ones.

Very low mass stars are characterized by effective temperatures in the range of 2000K$\leq$ $T_{\rm eff}\leq$5000K, whereas brown dwarfs and extra-solar giant planets can cover a much cooler temperature regime, down to 100K. Such low effective temperatures allow the presence of stable molecules, whose bands constitute the main source of absorption along the characteristic frequency domain. Such particular conditions are responsible for strong non-gray effects and significant departure of the spectral energy distribution from a black body emission (Baraffe & Allard 1997). Observations of cooler stellar and sub-stellar objects have revealed the presence of a wide variety of molecular absorbers and numerous condensates that complicate accurate modeling of these cool stellar atmospheres (Allard et al. 1997). In the non-gray treatment, a self-consistent integration is performed down to an optical depth at which the diffusion approximation is valid (Morel et al. 1994), and includes the treatment of atmospheric convection, which cannot be neglected at low $T_{\rm eff}$'s. The use of frequency-dependent opacities may also modify the onset of convection within the atmosphere, and both the $T_{\rm eff}$ and the colors of the tracks can be strongly affected. The necessity of adopting outer boundary conditions based on realistic non-gray atmosphere models for the pre-MS and low mass MS was pointed out by Chabrier & Baraffe (1997) and references therein, who have shown that the use of radiative T(τ) relations or gray atmosphere models is invalid when molecules form near the photosphere, at $T_{\rm eff}$ below 4000K. Outer boundary conditions based on the gray assumptions yield hotter models for a given mass. According to Baraffe et al. (1998) the use of an inappropriate outer boundary condition, such as the Eddington approximation, yields an overestimation of $T_{\rm eff}$ for a given mass up to 300 K.

5.1 Convection treatment in the atmosphere

The analysis made by Heiter et al. (2002) revealed that spectroscopic and photometric observations are best reproduced by the models when using an inefficient convection treatment in atmospheres. Convective transport of energy in stellar atmospheres is one of the most complex astrophysical problems. Many of the approximations usually admitted for the stellar interior, such as diffusive radiative transfer, are no longer valid. Moreover, through most of a convective stellar atmosphere, radiative losses are large enough to make convection less efficient in transporting energy than radiation. Only stars which have a surface convection zone extending deep into the stellar envelope can maintain efficient convective energy transfer near the bottom of their atmosphere.

One strong motivation to apply a more complete description of stellar turbulent convection stems from the result that low values of the scale length parameter α, e.g., 0.5, are required to fit Balmer line profiles for the sun and other cool dwarfs (Fuhrmann 1993), while much larger values (between 1 and 2) are necessary to reproduce their observed radii (Morel 1994). Likewise, α has to be varied over an even larger domain ($1<\alpha<3$) to reproduce the red giant branch in HR diagrams of galactic open clusters and associations for stars with masses ranging from $1M_{\odot}$ to $20M_{\odot}$ (Stothers 1997, 1995).

D'Antona & Montalbán (2003) have shown that a stellar model is fully described only when we specify not only the atmospheric model used as boundary conditions to the interior, but also the convection parameters used for the atmospheric grid, including the value of the optical depth at which the boundary conditions are taken, that is, the photospheric matching point, $\tau_{\rm ph}$. In fact, until now, the expensive model atmosphere computations have been generally performed only for one specific convection model, e.g., a given ratio of mixing length to pressure scale height, in the Mixing Length Theory (MLT), $\alpha=\alpha_{\rm atm}$. The value of α can be changed only in the computation in the interior ($\alpha=\alpha_{\rm in}$), e.g. to fit the solar radius in the solar model. However, if a large value of $\tau_{\rm ph}$ is chosen as matching point between the atmosphere and the interior, the most superadiabatic part of the convection zone is all included in the atmosphere. Consequently, the changing of $\alpha_{\rm in}$ does not affect the model in the same way as a full change the convection parameter in the whole model, including the atmosphere.

There is broad consensus in the literature that the treatment of superadiabatic convection in the pre-MS affects the tracks location to a great extent. In a series of works focusing on understanding the role played by different physical inputs on the pre-MS evolution, D'Antona & Mazzitelli (1997), D'Antona & Montalbán (2003), and Montalbán et al. (2004) outlined the major impact of convection modeling on the location of the stellar tracks in the HR diagram. Convection was found to be by far the most relevant ingredient influencing the determination of the mass and age of observed stars.

When modeling convection, it is essential to specify the mixing scale Λ, i.e. the typical distance that convective eddies travel before dissolving and delivering their excess gravothermal heat to the environment. The role played by Λ is relevant for the determination of the temperature gradient, as the conservation of flux implies that a larger Λ must be compensated by a lower degree of overadiabaticity. The convective flux behaves as $F_C \sim \Lambda^2$ in zones where most of the energy is carried by convection. Conversely, within low efficiency convective regions, $F_C \sim \Lambda^8$. The impact of the choice of Λ is therefore more evident where convection is not efficient. The pre-MS tracks result to be particularly sensitive to convective modeling, because the surface convection extends to most of the

(if not the whole) star, and the low densities involved (particularly in the early phases of gravitational contraction) make the convective process highly inefficient.

Presently, the main ways of computing convection in stellar envelopes, for wide grids of stellar models, are:

1. The traditional mixing length theory — MLT (Böhm-Vitense 1958, and subsequent variations of this same model) — assumes that both the dimension of the convective eddies and the mixing length are proportional to the local value of the pressure scale height, i.e. $\Lambda = \alpha H_p$, where α is a free parameter that is usually calibrated in order to reproduce the solar radius.

2. In the Full Spectrum of Turbulence model — FST (Canuto et al. 1996) — the whole spectrum of eddies' dimensions is considered, and the mixing length is taken as the distance of the nearest convective border.

3. MLT, in which the α value for each gravity and $T_{\rm eff}$ is calibrated upon 2D or 3D hydrodynamical simulations.

Ludwig et al. (1999), using their 2D radiation hydrodynamic models, have provided a calibration of the parameter α in a wide region of $T_{\rm eff}$'s and gravities[1] to be used in the computation of *gray* stellar models. These 2D models indicate that convection in the pre-MS is on average more 'efficient' than in the MS, corresponding to a larger α. The idea of calibrating the average α using numerical simulations has been extended by now to a few 3D computations: Ludwig et al. (AHS, 2002), for an M dwarf at $T_{\rm eff}$ = 2800 K and $\log(g)$=5, find $\alpha \simeq 2.1$; and Trampedach et al. (1999), for the range of main sequence gravities and $\log T_{\rm eff}$=3.68–3.83, find $\alpha \simeq 1.6$–1.8 in the whole range. Asplund et al. (2000) have compared 2D and 3D atmosphere models of the Sun, and found that the 2D solar model has marginally larger gradients than the 3D one. Although an extrapolation to regions not explicitly computed is not allowed, these few 3D models, also indicate efficient convection in the overadiabatic envelope. Montalbán & D'Antona (2006) have computed gray models by using this calibration: the tracks they obtain are very similar to the FST tracks[2]. Unfortunately, a very efficient convection in pre-MS is *not* consistent with the lithium depletion patterns of young open clusters (D'Antona & Montalbán 2003). Any attempt to calibrate convection efficiency in pre-MS by means of comparisons between binary masses dynamically determined and those assigned from different sets of evolutionary tracks, seems to be ambiguous (Landin et al. 2007).

[1] α is mapped in the domain $T_{\rm eff}$=4300−7100 K, $\log(g)$=2.54−4.74

[2] The FST convection model corresponds to *very efficient convection*, as shown by the quasi-coincidence of the resulting tracks with the tracks employing the MLT α calibrated on the 2D hydrodynamic models. We find confusing and misleading the statement by Baraffe et al. (2002), who point out that the FST model is very *inefficient* in the upper solar layers, where it provides results that are not consistent with the hydrodynamic simulations of convection for the solar model (nevertheless, remember that the FST model provides a better fit than MLT for the spectrum of solar oscillations, see e.g. Canuto & Christensen-Dalsgaard, 1998). What matters in the description of the pre-MS is the average efficiency of convection in the *whole* superadiabatic envelope, and this is very large for the FST, roughly corresponding to an α value in the MLT description somewhat larger than 2.

5.2 Non-gray boundary conditions in the ATON code

The outward integration of the structural equations of stellar interior must match the inward integration of the equations of its atmosphere at a given point. This point is the value of optical depth at which the boundary conditions are taken or, in other words, the photospheric "matching point" $\tau_{\rm ph}$. This matching point can vary according to the approximation used to obtain the atmospheric parameters.

In previous versions of the ATON code (including that by Mendes et al. 1999a, with rotation) a gray model provides the atmospheric parameters used as external boundary conditions to the interior. The internal structure is matched at $\tau_{\rm ph}$=2/3 with the values of P and T found via a Krishna-Swamy (1966) $T(\tau)$ relation.

Recently, the ATON2.0 code, without the modifications including rotation by Mendes et al. (1999a), was updated with non-gray boundary conditions, by using the NextGen (Allard & Hauschildt 1997, hereafter AH) and the ATLAS9 (Heiter et al. 2002) atmosphere models.

In the non-gray tracks presented by Montalbán et al. (2000), the NextGen atmosphere models were used as boundary conditions. The AH grid is available for the following ranges: $3.5 \leq \log(g) \leq 6.0$ in gravity, $-2.0 \leq [{\rm M/H}] \leq 0.0$ in metallicity and 1500 K$\leq {\rm T_{eff}} \leq$ 10,000 K in temperature. The AH models adopt classical Mixing Length Theory (MLT) with α=1.0.

After that, the ATLAS9 atmosphere models were included in the ATON2.0 code, providing another alternative to establish the atmospheric parameters (Montalbán et al. 2001). In these models convection is treated either in the Mixing Length Theory (MLT) or in the Full Spectrum of Turbulence (FST) formulation. Both ATLAS9 grids, the MLT (with α=1.25) and the FST formulations are used to treat the convection in the atmosphere. They are available for metallities ranging from [M/H]=$-$2.0 to +1.0 dex, but only the tables with solar metallicity was incorporated in the ATON2.0 code. These grids range from 2.0 to 5.0 in $\log(g)$ and from 4,000 K to 10,000 K in effective temperatures.

In order to follow the evolution of very low mass stars starting from early, low-gravity stages, we implemented in the code the PMS tables with the more recent low-gravity models by Allard et al. (2000), hereafter AHS. These PMS models can be understood as an extension, towards low gravities and low temperatures, of the the already referred NextGen models. The AHS grid is available for the solar metallicity, for gravities in the range of $2.0 \leq \log(g) \leq 3.5$ and temperatures in the interval of 2,000 K$\leq {\rm T_{eff}} \leq$6,800 K.

The NextGen and PMS original tables, besides a lot of other information, give us the temperature, pressure, physical depth, extension of the convective zone and density values for several optical depths ranging from 0.0 to 100 for a given combination of effective temperature and gravity. By using linear interpolation, we created a simplified table containing the physical quantities cited above for each of the following typical values of optical depth: τ=1, 3, 10 and 100.

Instead of using two different NextGen derived models, we merged the original NextGen tables with their PMS counterparts. Eventually, we obtained rectangular tables in the range $2 \leq \log(g) \leq 6$ and 2000 K$\leq {\rm T_{eff}} \leq$6800 K.

After the present work, the ATON2.4 code can now, besides the inclusion of the effects of rotation (Mendes et al. 1999a), determine the boundary conditions to the interior by using not only the classical gray models, but also the MLT and FST grids of the ATLAS9, the NextGen and the PMS non-gray models. For all these non-gray models, the match

with the interior can be done at four different optical depth, τ=1, 3, 10 and 100. Once the optical depth is chosen, $P(\tau)$, $T(\tau)$ and $\rho(\tau)$ are obtained by third order interpolating their values in the $T_{\rm eff}$ vs. $\log(g)$ plane.

5.3 Applications of the new rotating non-gray version of ATON2.4 code

This new version of the code was used to generate new sets of rotating non-gray pre-MS tracks, in order to analyse the rotational properties and evolution of a sample of young pre-MS stars in the Orion Nebular Cluster (ONC, Landin et al. 2006). In order to analyze the importance of convection in the pre-MS and in the ONC rotational properties, we computed three different sets of models by varying the mixing lenth parameter: α=1.0, α=2.0 and α=2.2. Our main goal is to improve our understanding of the appropriate physical constraints to be used for a general description of the evolution of stellar structure and its angular momentum with time. We are particularly interested in the choice of the stellar initial angular momentum and its variation with time and, also, in the importance of convection efficiency during the pre-MS. To do this, we check our models with respect to sets of relevant observations. A substantial part of this chapter was published in Landin et al. (2006).

5.3.1 An overview of theoretical pre-main sequence models

Since the pioneering works by Henyey et al. (1955) and Hayashi (1961), it is commonly accepted that pre-MS stars derive their luminosity by gravitational contraction, with the only exception of the short deuterium burning phase. Derivation of masses of young stellar associations has, then, generally been made by standard hydrostatic stellar models including deuterium burning, an approach that we will use in this work. This procedure rests on the assumption that neither the residual accretion after the protostellar phase nor the uncertainty in the zero point of ages affect the results in a strong way.

Nevertheless, the theoretical description of moderately low and low mass objects is affected by the first principle uncertainties in the description of some physical inputs, in particular opacities, convection, equation of state (D'Antona 1993) and treatment of boundary conditions (BCs, Chabrier & Baraffe 1997). Since the low mass stars in the pre-MS are fully convective and over-adiabatic, any change in the convective model substantially alters the location of the track in the theoretical HR plane. The use of a less efficient treatment of convection leads to larger temperature gradients, so that, for a given luminosity, the structure readjusts on a more expanded configuration, with a consequent shift of the track to lower effective temperatures ($T_{\rm eff}$) (e.g. D'Antona & Mazzitelli 1994, 1997; D'Antona & Montalbán 2003). The path followed by the theoretical pre-MS tracks on the HR diagram is also dependent on the boundary conditions used to fit the numerical integration of the structural equations of the interior with the atmosphere. The use of a non-gray atmospheric treatment shifts the tracks to cooler $T_{\rm eff}$s within an extended interval of masses and ages (Montalbán et al. 2004). The effect due to the non-grayness of the atmosphere is, in many cases, overwhelmed by the uncertainties related to the treatment of convection, that has a similar, but even stronger effect on the tracks, with

only a few exceptions that are relevant for this work, as will be discussed in Sects. (5.3.6) and (5.3.3).

5.3.2 An overview on the observational data of ONC

Young stellar clusters provide a unique opportunity to test stellar pre-MS models. Many studies in the past have been focused on the Orion Nebula Cluster (ONC), because it contains thousands of pre-MS objects. Hillenbrand (1997) measured the V and I magnitudes (and colors) of ∼900 stars and located them in the theoretical HR diagram by using bolometric corrections and taking into account the interstellar extinction for the determination of colors and bolometric magnitudes. In spite of the non-negligible uncertainties weighting on the derivation of these stellar parameters (Hillenbrand et al. 1997), such a work has been widely used, in connection with theoretical pre-MS tracks, to infer important information concerning the cluster itself. The mass and age distributions and the slope of the mass function can all be estimated by inferring the appropriate mass and age for each observed star. It is clear that the results obtained with this approach will depend to a certain extent on the set of tracks used to perform the analysis, and on the physical inputs adopted to calculate the evolution. This is confirmed by the fact that, specifically for the ONC, studies that used different sets of evolutionary tracks reached significantly different conclusions, particularly with respect to the mass and age distribution, and, more important, to the age spread and, consequently, to the evolutionary history of the star formation process within the cluster (Palla & Stahler 1999).

In the past few years, new detailed observational studies of the ONC have been undertaken, focused on the rotational properties of the stars. Stassun et al. (1999) and Herbst et al. (2002) measured the rotational periods of ∼400 stars belonging to the ONC. All of them are in the Hillenbrand (1997) sample, so they can be located on the HR diagram. More recently, Stassun et al. (2004) and Flaccomio et al. (2003a, 2003b) reanalyzed all the archival *Chandra* observations of the ONC studying in great detail the X-ray properties of the observed objects, in an attempt to elucidate the origin of X-ray emission in pre-MS stars. All this available information renders the ONC an excellent laboratory to test stellar evolution theories of the pre-MS phase.

None of the previous analyses of the ONC rotational database has been done using non-gray models, and the effect of using different convection efficiencies has not been extensively tested. We therefore decided to use this database to test and calibrate our new sets of non-gray tracks for rotating stellar models, with masses in the range $0.085 \leq M/M_{\odot} \leq 3.8$. As a byproduct, we will have insight on how much the rotational properties of this population depend on the choice of the evolutionary tracks. At present, there is no definitive observational constraint that can be used to choose among the tracks obtained by using different convection inputs. In this work we derive masses and ages with different sets, in order to appreciate how much the results we are presently interested in, namely those on the angular momentum evolution, depend on the choice. In particular, we will test the role of (a) boundary conditions (gray and non-gray), (b) different convection efficiencies in the framework of the MLT, and (c) rotating and non-rotating models.

As indicated by the non-negligible differences among the set of tracks adopted, we show that the detailed period distribution as a function of mass and age is dependent on the physical inputs. However, the qualitative information on the rotational distribution of stars of different mass in the ONC remains similar, and we confirm that the distribution

of periods is bimodal only for masses larger than a "transition" mass depending on the convection model.

5.3.3 Physical input of the models used to analyze the ONC stars

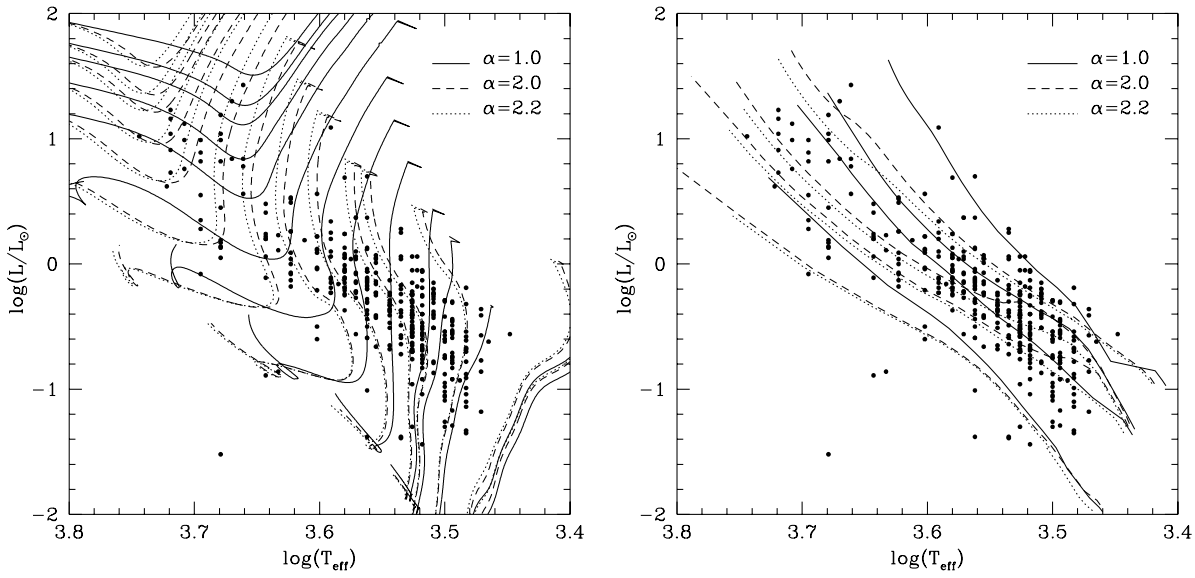

Figure 5.1: Paths followed by the theoretical tracks (left) and isochrones (right) of the rotating models calculated with three different values of the free parameter α determining the mixing length. For clarity, we report only the following masses calculated with our three sets of tracks (α1.0, α2.0, α2.2): 0.09, 0.1, 0.2, 0.3, 0.35, 0.5, 0.7, 1.0, 1.4, 2.0, 2.5, 3.0, 3.3 and 3.8 $M_\odot$ from bottom to top. The observational data from Hillenbrand (1997) are represented by • symbols.

We computed pre-MS stellar evolutionary tracks in the mass range $0.085 \leq M/M_\odot \leq 3.8$. We adopted the solar chemistry with Z=0.0175 and Y=0.27, while the starting deuterium abundance in mass fraction, following Linsky (1998), was set to $X(D)=2\times10^{-5}$. The evolution starts from a fully convective configuration with central temperatures in the range $5.3<\log(T_c)<5.8$, follows deuterium and lithium burning and end at the main sequence configuration. The micro-physics inputs (opacities, equation of state, nuclear network) were the same used in the distorted models presented in Sect. (3.6).

5.3.3.1 Boundary conditions

The boundary conditions were obtained with our new rectangular table (NextGen + PMS models) at τ=10. The ATLAS9 tables were not used because, since they are available only for temperatures above $T_{\rm eff}$=4000 K, they cannot be used to compute models below $\sim 0.7 M_\odot$. Consequently, the FST formulation was not used to treat convection in our analysis. Gray models were computed for comparison with previous results.

The gray tracks of models with α=1.0 are systematically hotter than their non-gray counterparts, although the difference in T_{eff} varies with the mass. For the lowest masses of our sample, i.e. M$\leq$0.2M$_\odot$, the high gravities allow the differences to remain within $\Delta T_{eff}\sim$100 K. This difference increases to $\sim$250 K at 0.6M$_\odot$ and reaches a maximum of $\sim$400 K in 1M$_\odot$ models, the largest differences happening at the end of the Hayashi track, as can be seen in Fig. (5.3). The stars for which the pre-MS tracks are most sensitive to the boundary conditions are those with masses in the range 0.4M$_\odot\leq$M$\leq$1 M$_\odot$: the difference in T_{eff} slightly increases along each track, and reaches a maximum of $\Delta T_{eff}\sim$ 400 K, when the radiative core is formed.

The T_{eff} of more massive stars are less influenced by the atmospheric treatment. These differences in T_{eff} lead to the assignment of a different mass to a given observed star. We verify that, consistent with the above discussion, this effect is negligible for the lowest masses, while it leads to differences of the order of $\sim$0.1M$_\odot$ for M$\sim$0.3$-$0.5M$_\odot$, where, as we shall see, the bulk of the ONC population is found. For larger masses the differences are larger because the tracks for different masses are closer to each other.

5.3.3.2 Convective treatment

Apart from the quoted cases, in which α can be calibrated on hydrodynamic models, the necessity to simplify the numerical treatment of convection leads stellar modelists to use a single α for the convection zone and for all the evolutionary phases. This choice is equivalent to adopting an average efficiency of the convective transport on the whole extension of the convective region, and on all the evolutionary phases. There is no good reason to assume that the α that, e.g., fits the solar radius should be used for other masses and for different evolutionary phases. Further, the efficiency of convection might change considerably within a convective zone, thus requiring the use of a variable α. Thus a preliminary investigation of the effects of changing this parameter is mandatory. We computed sets of models with three different values of the α parameter: the models with α_{in}=2.0 (α2.0 set) allow a fit of the solar radius for non-rotating models[3]; the models with α_{in}=2.2 (α2.2 set) are chosen to provide a "very efficient convection" set. Both these sets are termed HCE (high convection efficiency) sets. We further provide tracks with α_{in}=1.0 (α1.0 set), which define our LCE (low convection efficiency) models . This latter choice, according to D'Antona & Montalbán (2003), confirmed in Sect. (5.3.3.5), leads to a better agreement with the lithium vs. T_{eff} relation observed in young open clusters stars. Remember, however, that the adopted BCs come from model atmospheres computed, down to τ_{ph}=10, with α_{atm}=1.0 (see the discussion in Sect. 5.2 and in Montalbán et al. 2004). We show in Fig. (5.1) the comparison between tracks (left panel) and isochrones (right panel) of these three sets, showing the well known fact that both masses and ages are affected by the choice of the convection model. The observed stellar loci are also reported. In the early phases, with the exception of the D-burning phase, gravitational contraction is the only source of energy. The densities and temperatures increase until the central regions become radiatively stable; shortly after, H-burning takes over as the main energy source. We see from the left panel of Fig. (5.1) that the α2.0 and α2.2 tracks are systematically hotter, the differences being larger for higher masses and smaller for older ages. This behavior can be understood on the basis of the different degree of overadiabaticity

[3]Also Baraffe et al. (1998) and Montalbán et al. (2004) find a similar α_{in} (=1.9) to reproduce the solar radius.

present in the various masses at different ages. The exact temperature profile depends on the overadiabaticity ($\nabla - \nabla_{\rm ad}$), which is defined as the excess of the effective temperature gradient in comparison with the adiabatic temperature gradient, and it is only noticeably different from zero at the border of the convective zone, where convection becomes inefficient. We investigated the evolution of the degree of overadiabaticity at τ=10 for some mass tracks and for the three values of the mixing length parameter (α) used in this work. We found that the lower the α parameter, the higher the overadiabaticity at τ=10.

The two panels of Fig. (5.2) show, respectively, the evolution of the overadiabaticity at τ=10 and of the width (in solar masses) of the external region of the star where $(\nabla - \nabla_{\rm ad}) > 10^{-4}$. For clarity we report only the α1.0 and α2.0 models. The luminosity is on the abscissa as a time indicator. A detailed inspection of Fig. (5.2) shows:

1. the overadiabaticity at τ=10 of the α1.0 models is systematically higher than their α2.0 counterparts. This can be understood on the basis of the intrinsic lower efficiency of the convective model adopted, due to a lower mixing length;

2. due to the higher internal densities of the less massive models (hence, greater convective efficiencies), the overadiabaticity differences increase with the mass;

3. in the less massive models the differences above tend to narrow with age;

4. the extension in mass of the overadiabatic region is also systematically higher in the α1.0 models, and tends to shrink with age.

We verified that models of the same mass belonging to the two sets of tracks follow the same $L(t)$ relation. The differences in the location of the tracks are, therefore, to be totally ascribed to differences in the effective temperatures. Since the interior of these structures is practically adiabatic (in the center, $(\nabla - \nabla_{\rm ad}) < 10^{-7}$ in all cases), the radius is mainly determined by the degree of the overadiabaticity. This explains why larger differences are found for higher masses. In the lowest masses the efficiency of convection increases at older ages, so that the sensitivity to the adopted model for convection is strongly reduced. The low mass tracks approach each other at low luminosities (see Fig. 5.1).

5.3.3.3 The role of convection coupled with the non-gray atmospheres

We note a point that is generally overlooked, but that is crucial in order to understand the relevant parameters in track building: Montalbán et al. (2004) have shown that the problem of convection is intertwined in a subtle way with the problem of non-gray boundary conditions. For example, in the MLT framework, convection in the pre-MS should be described not only by the ratio $\alpha = l/H_p$ in the interior of the star ($\alpha_{\rm in}$), below the non-gray atmosphere, but also by the value that this parameter has in the atmosphere itself ($\alpha_{\rm atm}$), and by the matching point between atmosphere and interior ($\tau_{\rm ph}$). In particular, the two widely used sets of model atmosphere by Baraffe et al. (1998) are referred to as the set built with α=1.9 and the set having α=1.0. Thus, they are supposed to provide a clue to how the tracks vary by changing from a moderately high convective efficiency, represented by the set α=1.9, to a low convection efficiency represented by the set α=1. However, in Baraffe et al. (1998), the parameter α refers only to the value of $\alpha_{\rm in}$, and is misleading for two reasons: (1) the set $\alpha_{\rm in}$=1.9 stops at masses M$\geq$0.6M$_\odot$, and only the set $\alpha_{\rm in}$=1.0 is available for masses M<0.6M$_\odot$; (2) for both sets, the atmospheric model

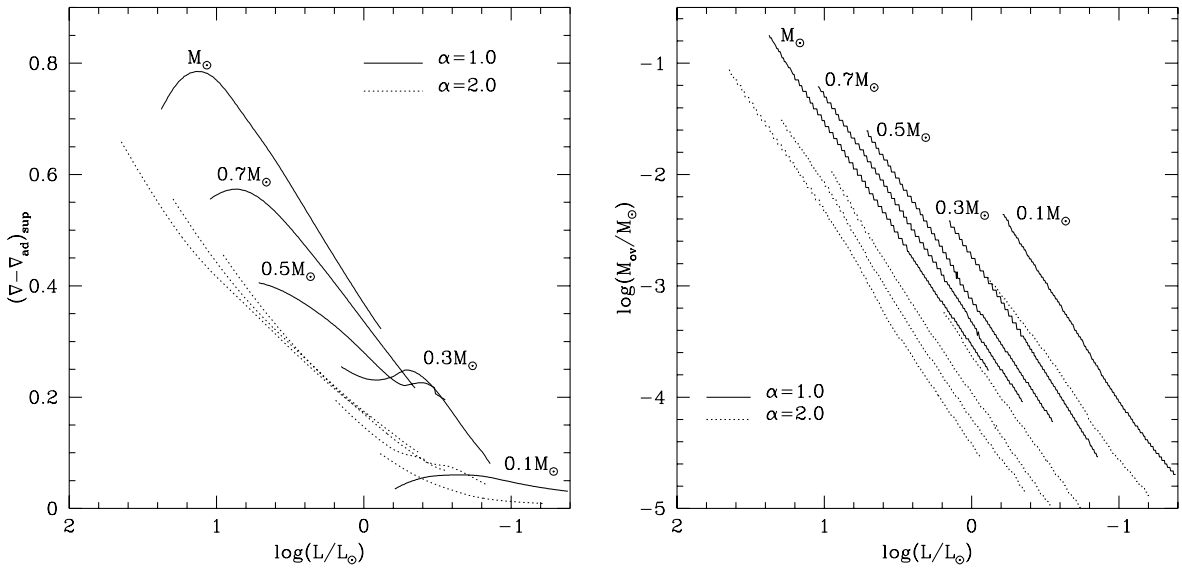

Figure 5.2: **Left**: Variation with luminosity of the overadiabaticity of the stellar layer at τ=10 of some pre-MS models calculated with different values of the parameter α entering the mixing length expression. **Right**: The variation with luminosity of the fraction of the mass of the star where $(\nabla - \nabla_{\rm ad}) > 10^{-4}$, for the same masses shown in the left panel. For clarity we show only models α1.0 and α2.0.

grid adopted is the same, and computed with $\alpha_{\rm atm}$=1.0. Montalbán et al. (2004) have shown that the fact that most of the superadiabatic part of the envelope is computed with a very inefficient convection ($\alpha_{\rm atm}$=1.0) shifts the $T_{\rm eff}$ by ∼150 K for the solar pre-MS. Thus, one may be led to attribute the smaller $T_{\rm eff}$ of the Baraffe et al. (1998) tracks to the use of the non-gray atmospheres, whereas they are due in part to the fact that these non-gray atmospheres are computed with LCE.

In Fig. (5.3) we show the evolutionary tracks for 0.3, 0.4, 0.7 and 1.0$M_\odot$, respectively in blue, red, magenta and black curves. Continuous lines stand for non-gray tracks with α=1.0, dotted lines refers to non-gray α=2.2 tracks and dashed lines correspond to gray α=1.0 tracks. In this figure we used non-rotating models. For the 0.3 and 0.4 $M_\odot$ (blue and red tracks in Fig. 5.3), the mass range of interest in our analysis, we can notice that the role of convection is more important than that of (non-)grayness, but only in earlier phases of pre-MS. As tracks evolve in their Hayashi phases, the differences between tracks with the same boundary conditions and different convection efficiency decreases. The differences between tracks with different boundary conditions and with α=1.0 remains roughly constant during the evolution (mainly for the 0.4 $M_\odot$), but in the bottom of the Hayashi track these mass tracks are more influenced by the boundary conditions.

5.3.3.4 Rotation and initial angular momentum

Rotation was modeled according to the rigid body law. This choice is motivated by the fact that most of the low mass stars are still fully convective in the evolutionary stages of interest for this study. As a first attempt, the initial angular momentum $J_{\rm in}$ for all models was estimated according to the prescriptions by Kawaler (1987). In that work, a relationship between angular momentum and stellar mass for stars earlier than F0 was

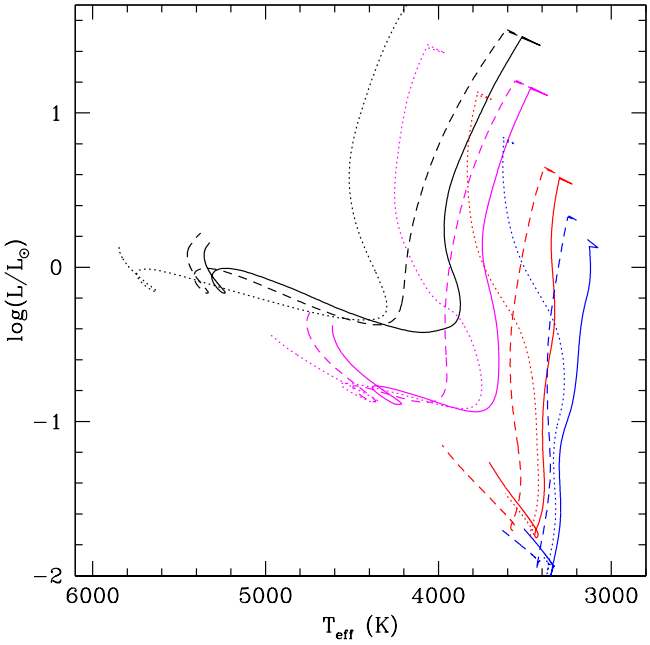

Figure 5.3: Paths followed by theoretical evolutionary tracks of the non-rotating models for 0.3, 0.4, 0.7, 1.0 $M_{\odot}$, respectively in blue, red, magenta and black. The non-gray α=1.0 models are reported with continuous lines, with dotted lines we plotted the non-gray α=2.2 models and the gray α=1.0 models are showed with dashed lines.

derived using main-sequence (MS) stellar models, and an estimate of the mean initial angular momentum-mass relation was made for stars of later spectral type. As masses larger than about $1.5M_{\odot}$ do not lose much angular momentum during their early evolutionary phases, it can be assumed that these stars reach the MS with the same angular momentum that they had at the beginning of their evolution. Kawaler (1987) was able to reproduce the observational relation at $M>1.5M_{\odot}$ using his own models for radiative stars and, then, he extended the models to lower mass stars. For these, however, the observations do not provide a direct comparison with the initial angular momentum, as their rotation has been slowed down during the main sequence lifetime (but not significantly during the pre-MS, if we adopt the hypothesis of pre-MS disk locking in the same way as Bouvier et al. 1997). For the range $0.6-1.25M_{\odot}$, the initial angular momentum-mass relation can be easily obtained from Kawaler's (1987) work (see Eq. 3.100). Once started with this initial angular momentum, we keep it constant in our models during the pre-MS according to the above mentioned hypothesis, whose validity will be checked later. This expression will then be extended to smaller masses as a result of the present study. The comparisons made in this work will help us to calibrate different models of angular momentum evolution.

Before proceeding with the analysis of the observational data of ONC, we would like to perform another comparison between the theoretical models in order to investigate the convection efficiency in the pre-MS on the light of lithium depletion.

5.3.3.5 The lithium depletion

In Fig. (5.4) we plotted, on the left panel, the temporal evolution of lithium depletion of our rotating models for 0.6, 0.7, 0.8, 0.9 and 1.0 $M_\odot$ and, on the right panel, its non-rotating counterpart. Solid curves represent the LCE models, while dotted and dashed lines refers to the HCE models. From this two panel figure, we can see that HCE models deplete more lithium than LCE models. If rotation is not considered, the two HCE models predict roughly the same Li depletion for a given value of α. When rotation is taken into account, the models, however, became much more sensitive to the convection efficiency. This result can also be seen from Table (5.1).

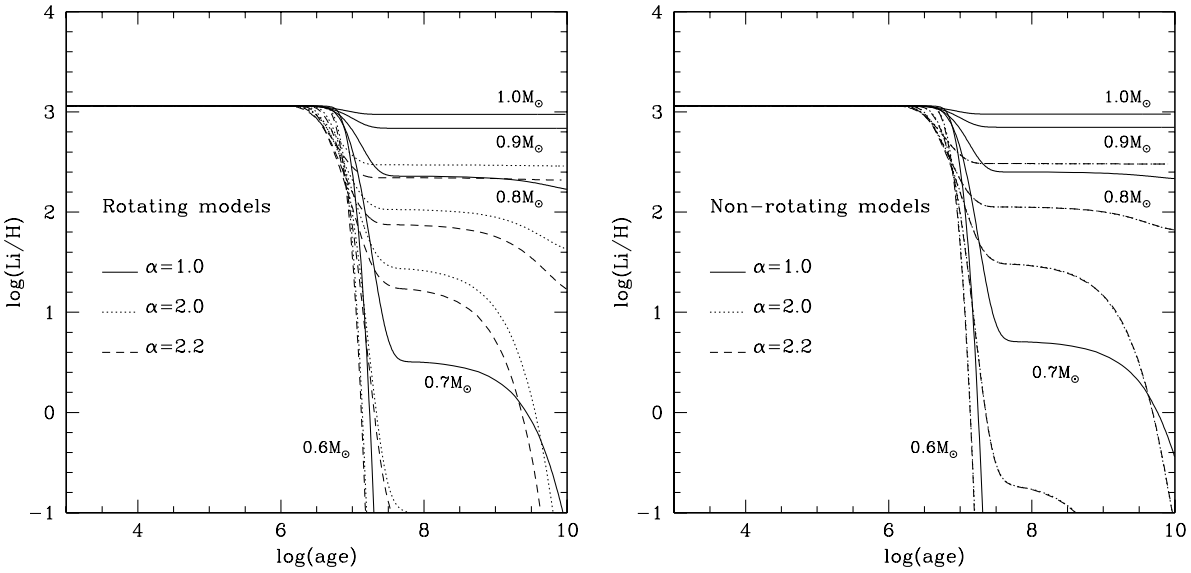

Figure 5.4: The temporal evolution of lithium depletion for our rotating (left) and non-rotating (right) models. The continuous lines, the dotted lines and the dashed lines stand for α=1.0, α=2.0 and α=2.2 models, respectively. We report the following masses: 0.6, 0.7, 0.8, 0.9 and 1.0 $M_\odot$. We have used an initial Li abundance of log (Li/H)=3.1.

Table (5.1) shows the lithium concentrations for our three sets of tracks and their non-rotating counterparts. We report the values for 0.7, 0.8, 0.9, 1.0 and 1.2 $M_\odot$ at 10^8yr. A

Table 5.1: Lithium abundances at the age of 10^8yr for 0.7, 0.8, 0.9, 1.0 and 1.2 $M_\odot$. We report the values obtained with different sets of our non-gray models, with ("rot") and without ("non-rot") rotation. The initial lithium concentration is *log* (Li/H)=3.1.

Models	$0.7M_\odot$	$0.8M_\odot$	$0.9M_\odot$	$1.0M_\odot$	$1.2M_\odot$
rot α=1.0	0.540	2.397	2.877	3.016	3.081
rot α=2.0	−0.991	1.459	2.057	2.510	2.939
rot α=2.2	−1.171	1.256	1.899	2.382	2.884
non-rot α=1.0	0.740	2.440	2.887	3.018	3.081
non-rot α=2.0	−0.734	1.505	2.085	2.523	2.933
non-rot α=2.2	−0.731	1.502	2.087	2.523	2.933

comparison between log (Li/H) found with rotating and non-rotating models, keeping α fixed, is qualitatively in agreement with the abundances found by Mendes et al. (1999a), i.e., rotating models provide greater lithium depletion especially for low-mass stars at the age in question. Another comparison between the abundances found with different values of α, keeping the rotation status fixed, confirms the results by D'Antona & Montalbán (2003): the lithium depletion of the HCE models is too large to be consistent with the lithium depletion observed by Soderblom et al. (1993) and Garcia Lopez et al. (1994) in young open clusters, which can be reproduced only by the LCE α1.0 models. In Fig. (5.5), we compare the lithium depletion predicted by our three sets of models (rotating and non-rotation) with the observational data cited above. The comparison was made at 10^8 yr, the age of Pleiades, the young open cluster analyzed in this figure. We have normalized the lithium abundances in the models to an initial abundance log(Li/H)=3.1 (as D'Antona & Montalbán 2003). As we can see, only circles (α=1.0) can fit the open cluster lithium data and the presence of rotation makes the models cooler and more lithium depleted.

On the contrary, the solar radius is reproduced only by the α2.0 model, and 2D hydrodynamic computations indicate HCE in the pre-MS. We regard this result as an indication that the efficiency of convection in the pre-MS might be affected by other parameter(s). The "second parameter" affecting lithium depletion is identified as the stellar rotation rate by Siess & Livio (1997) and in the papers by Ventura et al. (1998b) and D'Antona et al. (2000). The first authors propose that α is smaller in fast rotating pre-MS stars due to the twisting of convective cells, the others show that the action of the dynamo-induced magnetic field due to the interaction of rotation and convection modifies the structure of the convective layers and reduces lithium depletion.

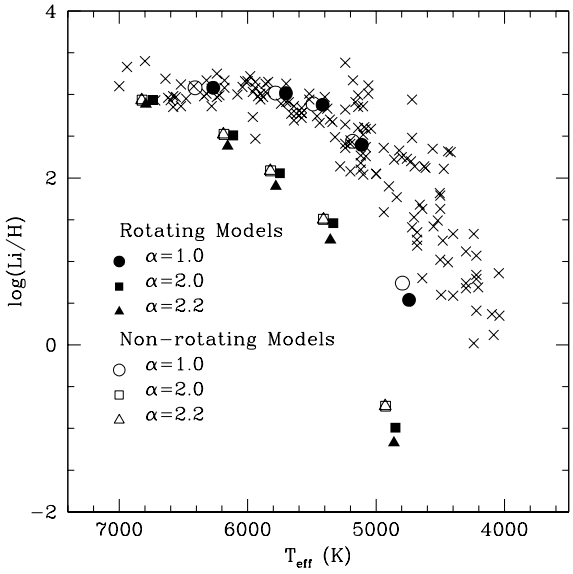

Figure 5.5: Lithium depletion vs. T_{eff} for observational data of Pleiades from Soderblom et al. (1993) and Garcia Lopez et al. (1994) in young open clusters (crosses) compared to lithium depletion predicted by our rotating (full symbols) and non-rotating models (open symbols) at 10^8 yr for the three sets of α models. We have used an initial Li abundance of log (Li/H)=3.1.

5.3.4 Data from the literature - ONC

In order to study angular momentum evolution in the pre-MS phase, we compare our sets of evolutionary tracks with observational data of the ONC stars. To accomplish this goal we need some key parameters, such as effective temperatures and luminosities (to infer masses and ages of the stars) and also the rotation period and an index that allows us to distinguish between different kinds of angular momentum evolutions.

The ONC data we used have been kindly provided by Dr. Keivan Stassun, who has widely worked on the rotational properties of ONC (Stassun et al. 1999, 2004). Our final study sample is composed of a combination of data from the following sources:

1. Rotation periods: Stassun et al. (1999), Herbst et al. (2002);
2. Effective temperatures and luminosities: Hillenbrand (1997);
3. Infrared continuum excess, Δ[I−K]: Hillenbrand et al. (1998);
4. Ca II equivalent width, EW(Ca II): Hillenbrand (1997), Hillenbrand et al. (1998);
5. X-ray luminosities: Stassun et al. (2004).

The rotation period diagnostic was obtained by photometry, interpreting the periodic photometric variability as caused by rotation, probably due to the presence of stellar spots.

The IR excess (Δ[I−K]) was obtained from combined optical and infrared photometric data. Extinction and spectral typing uncertainties are the main sources of errors in Δ[I−K] estimates. For earlier spectral type stars ($\lesssim$ K2) the errors are negligible (<0.05 mag), for spectral types in the range K2−M3, typical errors are between 0.1−0.3 mag, and it is largest for the latest spectral types, where mis-classification causes relatively larger errors.

The EW(Ca II) was obtained from the optical spectroscopic study by Hillenbrand (1997) and analyzed by Hillenbrand et al. (1998). Their measurements uncertainty is estimated at 0.5Å, based on measurements of multiple spectra of the same star.

In order to obtain more reliable values for L_X of ONC stars, Stassun (2004) reanalyzed all archival *Chandra*/ACIS observations of these objects using updated calibrations and including time-filtering of flares.

The effective temperatures and luminosities were obtained from optical spectroscopy and photometry.

5.3.5 Derivation of masses and ages

For each of the three sets of tracks previously discussed, we assigned to each observed point a mass and an age by linearly interpolating between the two nearest tracks. An inspection of Fig. (5.1) can help us understand, at least qualitatively, the differences that we should find by varying α. For each observed star in the α2.0 and α2.2 sets, we assign a systematically smaller mass than in the α1.0 models, hence a younger age (we recall that this evolutionary phase is governed by gravitational contraction, that proceeds on a Kelvin-Helmoltz time scale $\tau_{\rm KH} \propto \frac{M^2}{RL}$). If the α2.0 or α2.2 sets are used, we therefore expect a mass distribution shifted to lower masses and, on the average, a younger population. Typical internal errors are $\lesssim$ 0.2 dex in $\log(L/L_\odot)$ for all spectral types and are $\lesssim$ 0.02 dex in $\log(T_{\rm eff})$ for late-type (K−M) stars, but increase towards earlier spectral

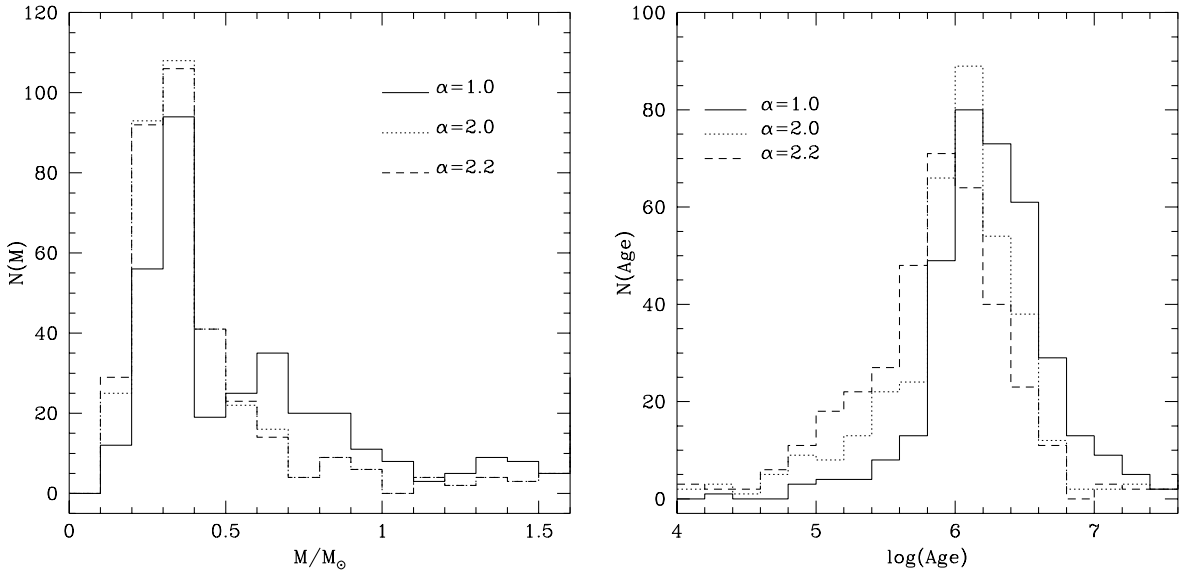

Figure 5.6: Mass (left) and age (right) histograms based, respectively, on masses and ages assigned to the observed stars in the ONC using three different sets of tracks, calculated with three prescriptions for convection, α=1.0, 2.0 and 2.2.

types. This leads to an uncertainty in the determination of mass that is $\lesssim 0.1 M_\odot$ for $M<0.5 M_\odot$, and gradually increases to $\sim 0.2 M_\odot$ for $M \sim 1\, M_\odot$. The attribution of age is mainly influenced by the uncertainty on the luminosity, that makes the age uncertain by $\sim$1 Myr at the age of 1 Myr. This poses the problem of whether the age distribution we find should be considered either as the result of a burst of star formation or as a real indication of age differences from star to star. In the course of the investigation we favour a statistical interpretation of data as an indication of some age evolution, based on the evolution of rotational periods.

The left panel of the Fig. (5.6) shows the mass distribution of the observed stars, obtained by using the three sets. Only masses $M<1.6\, M_\odot$ are plotted because they represent most of the stars in the sample. The mass function for the α1.0 set peaks in the mass interval $0.3-0.4\, M_\odot$, but we also note the presence of a significant group of stars with masses in the range $0.2-0.3\, M_\odot$ and another group in the interval of $0.6-0.9\, M_\odot$. For the HCE models, this latter group of objects becomes less relevant and the mass function peaks in the mass interval $0.2-0.4 M_\odot$. The right panel of Fig. (5.6) confirms that the age distribution depends on the choice of α. We note that a slightly younger population is obtained as the value of α increases, and, in α2.0 and α2.2 cases, a very young group of stars appears at ages $\sim 1-2\times 10^5$yr, but is not present for LCE (α1.0) models. This can be understood by considering, in the right panel of Fig. (5.1), the relative location of observed points and theoretical isochrones. Age differences are also due to the different slope of the isochrones corresponding to the two sets of tracks, which, in turn, are related to the differential variation of temperature with mass. In HCE models there is a group of objects with ages clustering around 100, 000 yr. For the α2.0 case this young group is made up of $\sim$40 stars and for the α2.2 set its presence is still more evident, exhibiting $\sim$70 objects.

After analysing the rotation period of ONC stars as a function of the inferred mass,

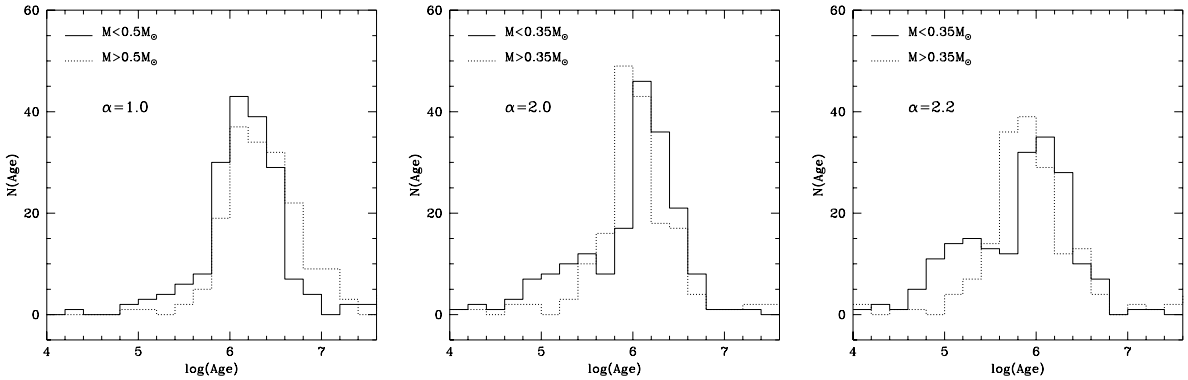

Figure 5.7: The comparison between age distributions of the observed stars with assigned mass lower and higher than M_{tr}. The M_{tr} value is $0.5M_{\odot}$ for LCE models and $0.35M_{\odot}$ for HCE models.

we define a transition mass, M_{tr}, for HCE and LCE models, on the basis of the rotation periods distribution. Here we compare, in Fig. (5.7), the age distribution for two different ranges of mass, $M>M_{tr}$ and $M<M_{tr}$ (see the definition of M_{tr} in Sect. 5.3.7.1). We see from the left panel of Fig. (5.7) that in the α1.0 set the two populations show a similar distribution. On the contrary, the age distribution of the two groups for HCE models is very different. Thus, while the existence of a group of younger stars would be possible in the formation history of the ONC, it should be present for any mass. The discrepancy in the age distribution may be again an indication that the α1.0 set provides a better description of the ONC stellar population, in agreement with the lithium depletion discussed in Sect. (5.3.3.5) and with the previous analysis made by D'Antona & Montalbán (2003). In any case, this certainly is not final and we proceed with the analysis by using the three sets of tracks.

5.3.6 Comparison with gray models

We compare now the effects introduced by the two major factors, i.e. convection and boundary conditions. Although for masses $M>1\,M_{\odot}$ the treatment of convection is more relevant than the boundary conditions adopted in determining the effective temperature of tracks (Montalbán et al. 2004), for the interesting range of mass for the ONC comparison, namely $0.2-0.4\,M_{\odot}$, and the non-gray models, convection is important mainly in the early evolutionary phases. At later phases (ages >1Myr), convection becomes more adiabatic and the non-grayness becomes the main factor affecting the track location.

For gray atmospheric treatment, keeping α fixed to 1.0 would concentrate the same mass distribution at $M\sim0.2-0.3\,M_{\odot}$. There would also be a considerable reduction of the population with masses in the range $0.6<M/M_{\odot}<1$. A larger effect would be obtained if we had used gray models with α=2.0. In this case, the mass function would be peaked in the range $0.1<M/M_{\odot}<0.3$, and the average age of the observed stars would be slightly younger than ∼1Myr. This latter result was obtained by Herbst et al. (2002) during their analysis of the ONC population using the tracks by D'Antona & Mazzitelli (1994) that use gray approximation and the very efficient FST model for convection.

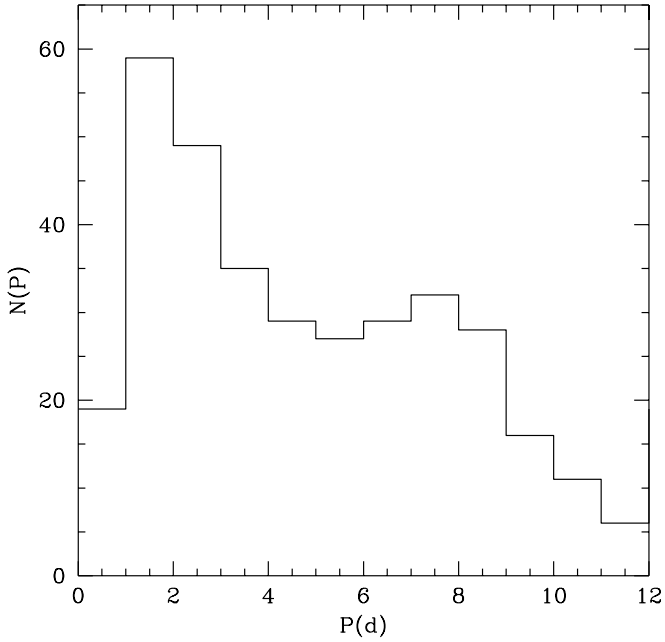

Figure 5.8: The period histogram of all observed ONC objects. The total distribution of periods has a bimodal character, showing a primary peak of fast rotators (P∼2 days) and a secondary peak of slow rotators (P∼8 days).

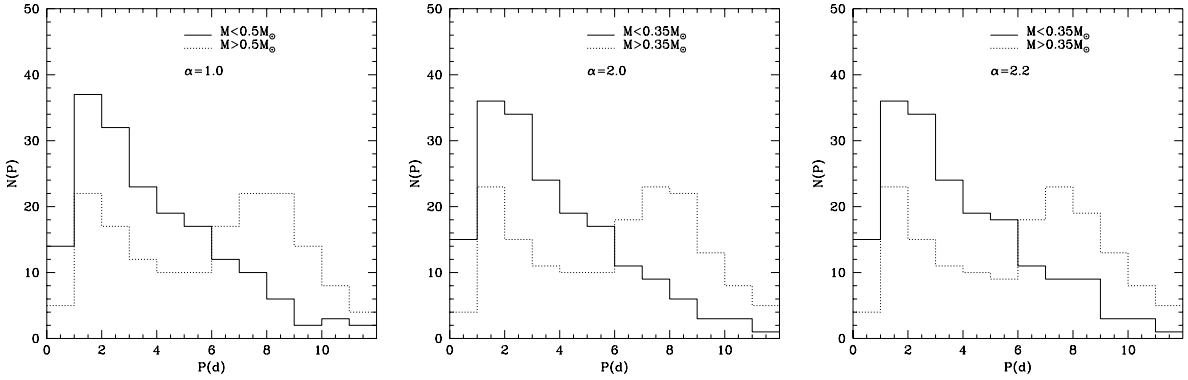

Figure 5.9: Period histograms showing the dependence on mass of the period distribution of the ONC objects. Stars more massive than M_{tr} have a bimodal period distribution and their less massive counterparts rotate faster and exhibit a unimodal distribution. This behavior can be seen independently of the choice of α. The M_{tr} values are as in Fig. (5.7).

5.3.7 Stellar rotation in the ONC

5.3.7.1 The dichotomy in period distribution for different mass ranges

We examine in Fig. (5.8) the distribution of the observed rotational periods. We note the presence of a primary peak corresponding to fast rotators with $1 \lesssim \mathrm{P(d)} \lesssim 3$, and a secondary peak at P∼8d. The former can be associated with spin up due to the conservation of the total angular momentum. The latter indicates the presence of a mechanism acting to prevent stellar spinning up, at least in the early evolutionary phases. Attridge & Herbst (1992), Choi & Herbst (1996) suggested that this can be due to a "disk

Table 5.2: Main physical parameters of the present gray (G) and non-gray (NG) models. $\mathcal{N}_<$ ($\mathcal{N}_>$) is the percentage of the N_t stars that have mass less (greater) than M_{tr} for different rotation periods (P). See text for details.

Models	Mass range ($M_\odot$)	Age range (Myr)	M_{tr} ($M_\odot$)	$\mathcal{N}_<$ P<4d	$\mathcal{N}_<$ P>6d	$\mathcal{N}_>$ P>6d
G α=1.0	0.2−0.3	0.6−2.5	0.35	65%	19%	53%
G α=1.5	0.1−0.3	0.3−1.3	0.25	65%	19%	54%
NG α=1.0	0.2−0.4	1−2	0.5	63%	18%	53%
NG α=2.0	0.2−0.4	0.6−2.5	0.35	67%	18%	55%
NG α=2.2	0.2−0.4	0.4−1.6	0.35	67%	23%	54%

locking" mechanism, caused by magnetic coupling between the star and the disk (Königl 1991). Following Herbst et al. (2002) we investigate in detail the rotational status of the various masses involved. The rotational properties of the stars vary considerably with mass: stars with masses larger than a threshold value, M_{tr}, have a clearly bimodal distribution, while the less massive sample ($M \leq M_{tr}$) contains only a tail of slow rotators. This behavior was first observed by Attridge & Herbst (1992) and discussed by Herbst et al. (2002). We define the "transition mass", M_{tr}, which depends on the track set chosen for the analysis, in order to maximize the effect of bimodality. Although the dichotomy does not depend on the chosen set, the transition mass varies according to it. For LCE models it is $0.5M_\odot$, while a reasonable value is $0.35M_\odot$ for HCE models. If we had used our gray models with α=1.5, M_{tr} would have been even smaller, namely, $0.25M_\odot$, in agreement with the findings by Herbst et al. (2002), who used the HCE FST models by D'Antona & Mazzitelli (1994). In Fig. (5.9) we show period histograms for stars less and more massive than M_{tr}, respectively. The secondary peak at P$\sim$ 8d, already seen in the Fig. (5.8), is present only in the population at $M>M_{tr}$, while the low mass objects show a clear trend towards short periods. Table (5.2) shows the percentages of slow and fast rotators (here defined by the limitations P>6d and P<4d, respectively). Fast rotators contain more than 60% of stars with $M<M_{tr}$. On average, only 20% of stars with $M<M_{tr}$ and $\sim$54% of those with $M>M_{tr}$ have P>6d.

This dichotomy indicates that either (i) disk locking is responsible for the presence of the secondary peak, and stars with $M>M_{tr}$ tend to be embedded in their disks longer than their low mass counterparts, (ii) the locking time is similar, but masses $>M_{tr}$ evolve faster and a larger fraction of their pre-MS lifetime is locked, or (iii) the "locking period" of the group with $M<M_{tr}$ is significantly lower than $\sim$8d. Our analysis confirms possible interpretations of the observed distribution of periods given by Herbst et al. (2002) (see their Fig. 15, here reproduced in our Fig. 5.10). The uncertainty on the convection model simply alters the transition mass from $\sim 0.25M_\odot$ to a maximum of $0.5M_\odot$ for LCE models.

5.3.8 Disk locking and the disk lifetime

Following the suggestion by Herbst et al. (2002), that the longer period peak in the distribution indicates that some stars are locked in their disks with a period near 8 days, we simply considered the stars with periods larger than a threshold period (P_{thresh}), which we put at 8d, as locked. For stars at $P<P_{thresh}$, unlocked stars according to our criterion,

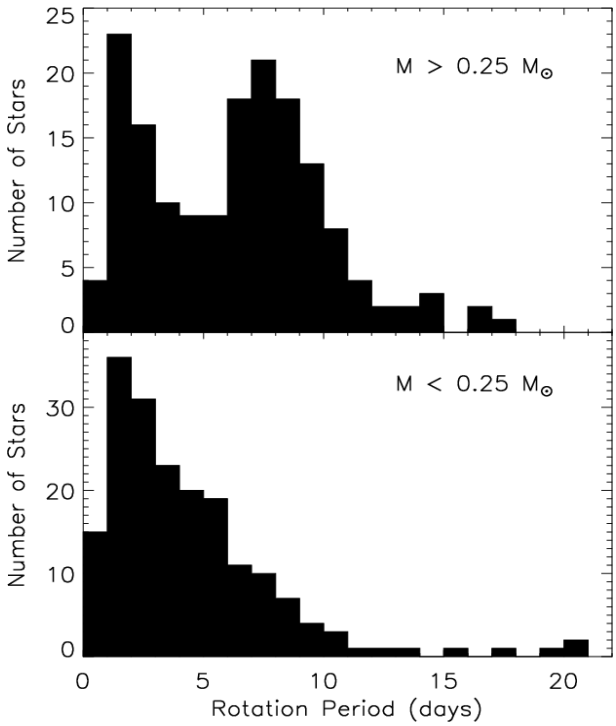

Figure 5.10: Histograms showing the period distribution for ONC stars with masses exceeding 0.25 $M_\odot$ (top panel) and with masses less than 0.25 $M_\odot$ (bottom panel). Mass estimate based on the models of D'Antona & Mazzitelli (1994). This figure corresponds to Fig. 15, from Herbst et al. (2002).

we determine the epoch at which their period was equal to 8 days. This would be the time at which the stars would have lost their disks, and began a constant angular momentum evolution. Here we consider that angular momentum losses by magnetic braking are negligible at the pre-MS, since its timescale is much longer than the evolutionary timescale during pre-MS evolution. The temporal variations of radius and angular velocity were determined on the basis of our tracks once the mass was assigned. Following this hypothesis, we found some stars which had P=P_{thresh} at an age younger than 10^5yr. In our interpretation, these stars have lost their disks very early and can be considered to have evolved without a disk. In this way, we identify three distinct populations:

1. early fast rotators – stars locked only for ages $< 10^5$yr,
2. slow rotators – stars probably still disk embedded,
3. moderate rotators.

Stars in the last group may have lost their disks at ages greater than 10^5yr. They represent, on average, ∼45% of the stars of the whole sample and this percentage do not change significantly with the choice of α. As long as the assumption that the locking period is independent of mass is valid, the disks seem to survive longer for higher masses. For all sets of tracks, the percentage of early fast rotators is ∼40% for M<0.4$M_\odot$, and gradually drops below ∼12% for M>0.6$M_\odot$.

The mass distribution of the slow and early fast rotators is shown in Fig. (5.11). We note, in particular, the maximum at 0.6−0.8 $M_\odot$ (for LCE models) and 0.3−0.5 $M_\odot$ (for HCE models) characterizing the slow rotator population (dotted line). We can compare the fraction of early fast rotators identified in the ONC with the non-accreting fraction of TT and Brown Dwarfs in star forming regions of similar ages (ρ Oph and Taurus,

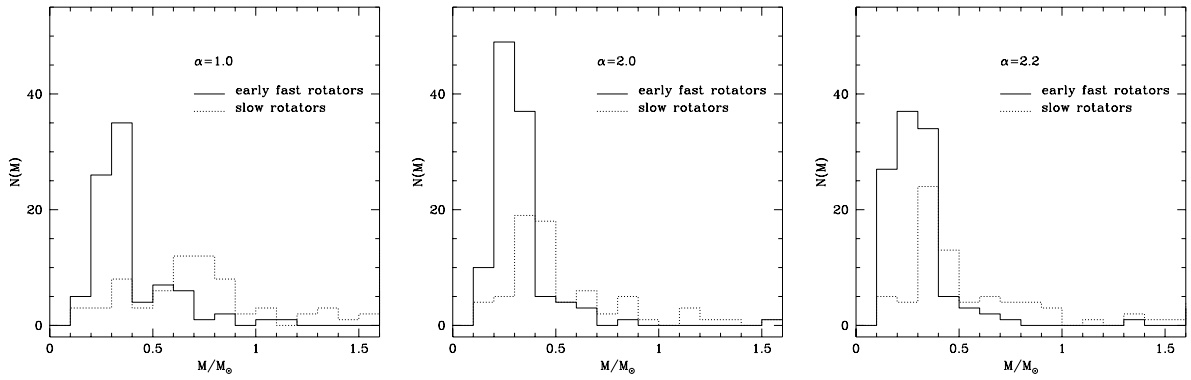

Figure 5.11: The mass distribution of the sources which according to our analysis rotate fast since early evolutionary phases (solid lines) compared to those that are slow rotators in the current epoch (dotted lines). This comparison is shown for the three sets of models (α1.0, α2.0 and α2.2).

Mohanty et al. 2005). The lower limit to this non-accreting fraction is ∼35%, not very different from our result.

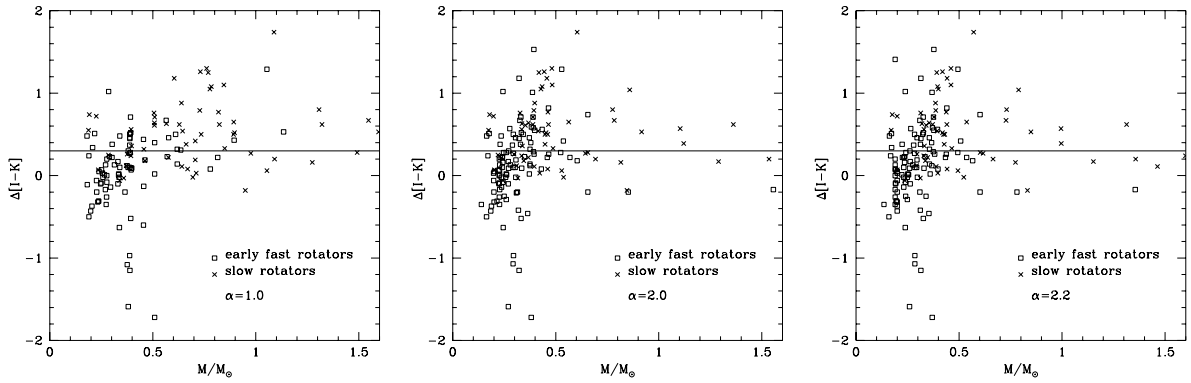

Figure 5.12: The observed infrared excess of our sample stars plotted against their inferred mass according to the three sets of models used in this work.

In our analysis we use the rotation period as an indicator of the presence of a disk surrounding these stars. In order to test the reliability of this hypothesis, we should use several observational indicators of the presence of disk and accretion, like the infrared excess Δ[I−K], the equivalent width of Ca II line, the excess in the L-band and Hα, Ca, O emission lines. Near IR excess as disk indicators and EW Ca II as accretion diagnostic must be used with caution (Hillenbrand 1997). But, as this is mainly a theoretical work, we will check what is already in the literature for ONC stars, namely IR excess Δ[I−K] and EW Ca II, mainly as additional arguments.

It is expected that still locked stars have Δ[I−K]>0.3, and those that evolved without disk, should have infrared excess significantly lower than this threshold value (Herbst et al. 2002). We report in Fig. (5.12) the observed stars on the plane Δ[I−K] vs. mass. We can see that sources that we identified as still locked (slow rotators - crosses) are mainly concentrated above the Δ[I−K]=0.3 line, while those that evolved without a disk (early

fast rotators - open squares) lie mainly below it, for the three sets of models. This straight correlation between the infrared excess and our derivation of the presence of a disk agrees with our theoretical considerations.

The equivalent width of Ca II lines is commonly used as an indicator of an active accretion process. For accreting stars we expect emission lines and EW(Ca II)<-1, while for non-accreting objects we have EW(Ca II)>1 (Flaccomio et al. 2003b). We cannot expect a direct correlation between Δ[I$-$K] and EW(Ca II), because some stars might still have a disk, although no longer accreting. Yet, we expect that the observed stars with EW(Ca II)<-1 and Δ[I$-$K]>0.3 should have a disk surrounding them, and the disk locking mechanism should be active. We could identify $\sim$40 stars with known rotation periods that satisfy both requirements, about 30% of which are actually identified as still disk embedded according to our criterion ($P>P_{thresh}$=8d). Part of the remaining have long rotation periods, very close to P_{thresh}, which suggest the presence of a disk.

5.3.9 An alternative view: the role of the magnetic field

The idea that disk-locking is responsible for the dichotomy observed, which eventually leads to the presence of two peaks in the distribution of periods of the ONC stars, was recently criticized by Barnes (2003), who argued that the possible role of disks can be only to set an initial distribution of periods, since disk-locking should affect all the stars equally.

Based on the observed color-period diagrams of several open clusters (e.g. IC 2391, α Per, Pleiades, M34, etc.), Barnes (2003) found that a double population with distinct rotational properties characterizes any stellar association. Further, he found that a systematic trend with age is apparent, namely, that older clusters have a smaller number of rapid rotators, that eventually disappear at ages $\sim$800 Myr.

Barnes (2003) interpreted these observations as a result of a different morphology of the magnetic field configuration. According to his suggestion, rapid rotators have small scale magnetic fields associated with their convective region, which cannot be anchored either to the inner radiative core or to the star's external layers. All the fully convective stars should belong to this group. Conversely, the slowly rotating stars are characterized by large scale magnetic fields, probably associated with the presence of an interface dynamo between the external convective region and the internal radiative zone. In this case, the process of spinning down the star is much more efficient. The dynamo, that is probably created by the decoupling between the convective and radiative zones, anchors the spun-down convective envelope to the rapidly rotating core, thus favouring a constant migration of the stars belonging to the rapidly rotating group to the slowly rotating sample. This should explain the complete absence of the fast rotator sequence at old ages (see Barnes 2003, Fig. 1, reproduced here in our Fig. 5.13). Due to the young age of the ONC, both populations should be present there, as we found above.

This interpretation is not correct if we take our results at face value: if we rely on our attribution of masses and ages, the great majority of the stars observed are indeed fully convective, i.e. should all belong to the rapidly rotating sequence. We suggest that the magnetic field itself plays a role in inhibiting convection (Gough & Tayler 1966; Moss 1968; Ventura et al. 1998b) and favours an earlier appearance of a radiative core in the stars having $M>M_{tr}$. Consequently, we do not reject the idea that the presence of a double population is indeed due to the magnetic field configuration, rather than to the

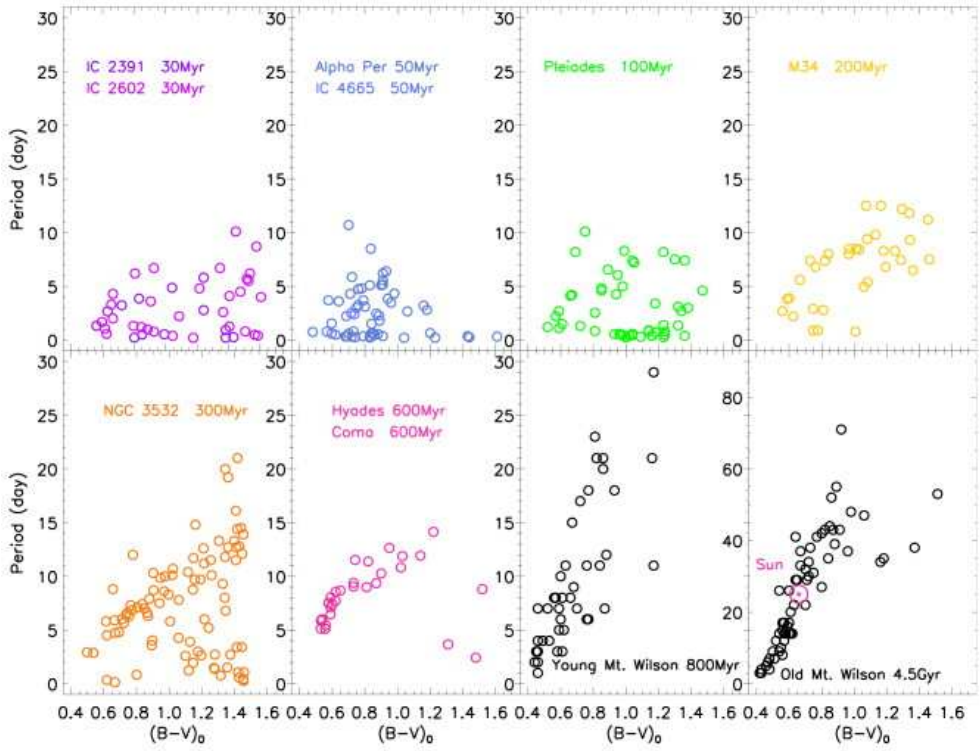

Figure 5.13: Color-period diagrams (on a linear scale) for a series of open clusters and for the young and old Mount Wilson stars. Note the change in scale for the old Mount Wilson stars. Two sequences of slow and fast rotators, called I and C, respectively, are visible, as is a cuneiform gap between them (Fig. 1 from Barnes 2003).

effects of a disk-locking mechanism.

5.3.10 A constant angular momentum evolution?

For those stars that we identified to have lost their disks in early evolutionary phases, i.e., the early fast rotators, we may test the hypothesis that they evolved at constant angular momentum from the beginning. The distribution of these objects in the P vs. inferred age plane is shown in Fig. (5.14) for α=1.0, α=2.0 and α=2.2 models. We used different symbols as mass identifiers. We can see a clear trend towards shorter periods for older ages, especially for the α1.0 models, possibly indicating angular momentum conservation. We checked the possibility of reproducing the observed rotational pattern with age by means of our rotating models. This approach allows us to find out the range of initial angular momenta that, for each mass, must be used to calculate the models. We limit this analysis to the subsample of mass range given in Table (5.2). We divided the observed sources into three classes of mass, indicated in Fig. (5.14) with open circles ($\circ$) masses in the interval $0.2<M/M_{\odot}<0.3$, with full squares ($\blacksquare$) $0.3<M/M_{\odot}<0.4$ and with crosses ($\times$) $M>0.4\,M_{\odot}$. Solid lines indicate the temporal variation of rotation periods, according to the evolution of our three sets of models with masses M=0.2, 0.3 and $0.4\,M_{\odot}$, calculated by assuming an initial angular momentum following the prescriptions given in Eq. (3.100). We note that the temporal evolution of the periods vary with the parameter α, as it affects the radius of the stars. These curves can only reproduce the upper envelope of the observed loci, but, particularly at the ages shared by the bulk of the ONC stellar

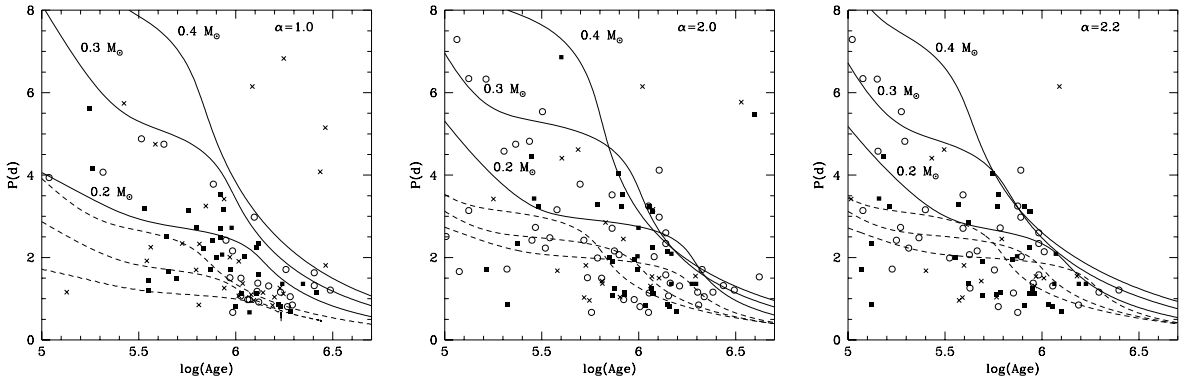

Figure 5.14: The temporal evolution of the periods of our three sets of models with masses in the range $0.2\,M_\odot \leq M \leq 0.4\,M_\odot$ evolved starting with an initial angular momentum calculated on the basis of the Kawaler (1987) prescription (solid lines), and with the same values multiplied by a factor of 3 (dashed lines). The stars that we suppose evolve with a constant angular momentum, i.e., without a disk, are also shown. The ∘ symbols identify the mass range $0.2<M/M_\odot<0.3$, ■ is used for $0.3<M/M_\odot<0.4$, and × for stars with $M>0.4\,M_\odot$.

population, they lead to rotation velocities too slow with respect to most of the observed values.

To reproduce the rotation period of the fastest stars, we need to use an initial angular momentum at least three times larger than that prescribed by Kawaler (1987), if we use LCE models, and even larger for HCE models. To fully bracket the observed periods it is necessary to assume a distribution of initial angular momenta $J_{\rm in}$, at least, in the range $J_{\rm kaw}<J_{\rm in}<3J_{\rm kaw}$. This result can be used to extend the Kawaler (1987) prescription to the very low mass stars.

5.3.11 The X-ray emission of the ONC stars

Flaccomio et al. (2003a, 2003b) and Stassun et al. (2004) performed deep analyses of the archival *Chandra* data and derived the L_X luminosity of all the sources included in the Hillenbrand (1997) sample. Their goal was to correlate L_X of pre-MS stars with the factors most likely driving the X-ray emission itself, i.e., accretion and rotation. Their main finding was the lack of a clear correlation between L_X and rotation period. They interpreted this result as evidence that the ONC pre-MS stars are indeed in the "super-saturated" regime of the rotation-activity relationship. This seems to be confirmed by the average value of the fractional X-ray luminosity $\log(L_X/L_{\rm bol})\sim-3.6$, that is slightly smaller than the main sequence saturation value of $\log(L_X/L_{\rm bol})\sim-3$.

Concerning the relationship between accretion and X-ray emission, Stassun et al. (2004) found that accreting stars have X-ray luminosities on average lower than their non-accreting counterparts, as a possible result of X-ray extinction by circumstellar gas in magnetospheric accretion columns. We could not find any clear correlation between EW(Ca II) and L_X, although this might be a consequence of the smaller sample of stars with evidence of accretion (i.e. EW(Ca II)<-1) used in the present work, compared to the complete sample by Hillenbrand (1997) and Hillenbrand et al. (1998) analyzed by Stassun et al. (2004).

We used our mass determinations to look for any relationship between stellar mass and X-ray luminosity. In agreement with Flaccomio et al. (2003a), we find that L_X is

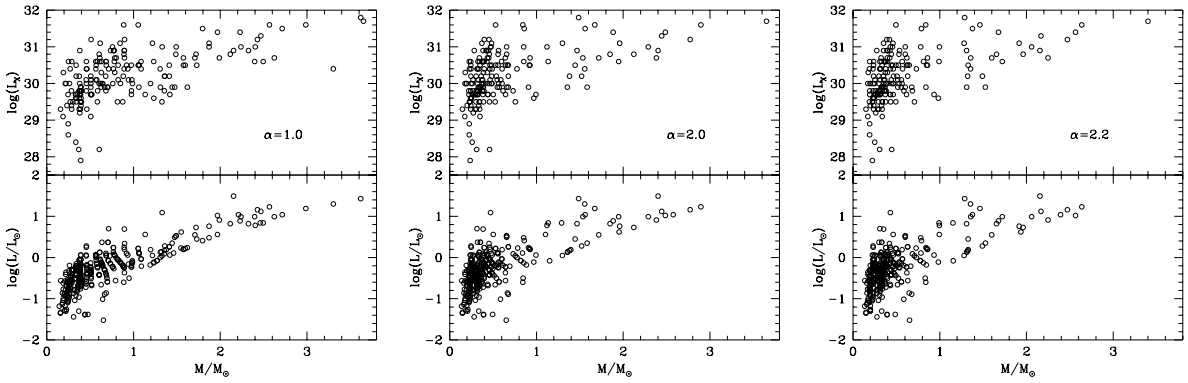

Figure 5.15: **Top**: L_X luminosity (ergs/s) plotted against mass (obtained with our three sets of models) for the ONC observed sources with known rotation periods. **Bottom**: The same as top, with bolometric luminosity on the vertical axis.

correlated with mass (upper panels of Fig. 5.15). This trend is not due to a qualitative difference in the X-ray emissions, but rather to a general correlation between mass and bolometric luminosity (lower panels of Fig. 5.15). This is confirmed in Fig. (5.16), where we see that the L_X/L_{bol} ratio is practically independent of mass for the three α models we have used. We note the high dispersion around the average value of $\log(L_X/L_{bol})\sim-3.6$, present at lowest masses, that is probably connected to the lower luminosities of these objects.

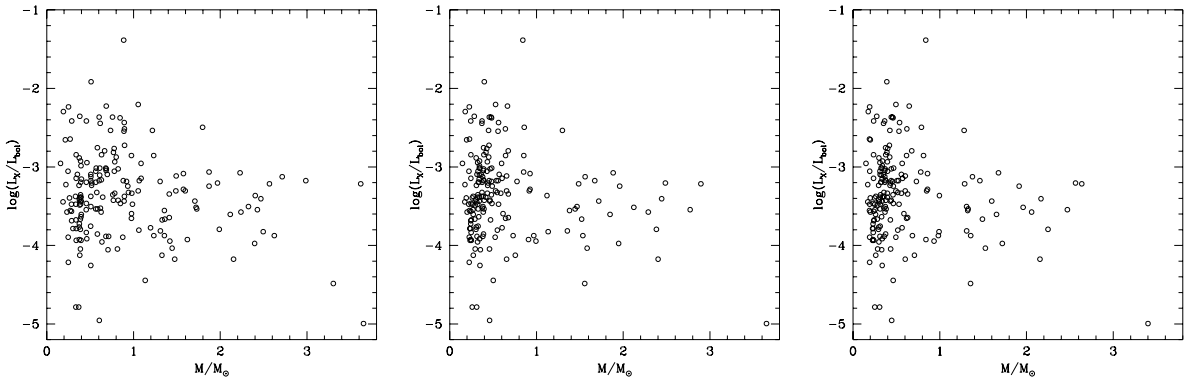

Figure 5.16: The fractional X-ray luminosity as a function of mass for the same stars and models shown in Fig. (5.15).

5.3.12 Conclusions

We use the observed stellar population of the ONC to test our pre-MS evolutionary tracks, to better understand the main physical properties characterizing the evolution of young stars. By comparing the location of the tracks in the HR diagram with the position of the observed objects, we assign to any single star a mass and an age, for three different convection efficiency models.

We confirm the well known result, that the treatment of convection is generally the most relevant physical input in determining $T_{\rm eff}$s of pre-MS tracks in the HR diagram. The boundary conditions adopted also play a non-negligible role in determining the path followed by the evolutionary sequences on the HR plane. Gray models are systematically hotter than their non-gray counterparts. This effect, for the range of masses and ages at which most of the ONC population is found, has a similar quantitative effect as a change of the convective model. The use of non-gray models is recommended to describe these early evolutionary phases.

On the observational side, we find that the bulk of the observed stars in the ONC have masses in the range $0.2M_{\odot} \leq M \leq 0.4M_{\odot}$, for all non-gray models. The age distributions are more affected by the choice of the MLT parameter α. Ages are 1−2 Myr from the α1.0 set, 0.6−2.5Myr for α2.0 set and 0.4−1.6Myr for α2.2 models. This study confirms the presence of a dichotomy in the rotational properties between the objects with $M<M_{\rm tr}$, whose period distribution peaks at short values, and stars with $M>M_{\rm tr}$, that present a secondary peak at P∼8d. The transition value of mass between the two populations is at $M\sim0.5M_{\odot}$ for LCE and at $M\sim0.35M_{\odot}$ for HCE models. If disk-locking is responsible for the secondary peak observed in the overall period distribution, these results can be interpreted by assuming either that stars with $M<M_{\rm tr}$ lose their disk earlier, or that their locking period is shorter. The X-ray emission shows no correlation with period, supporting the suggestion that these stars are indeed in the super-saturated regime of the rotation-X ray luminosity relationship. The correlation of the X-ray flux with mass appears to be the consequence of the increased average luminosity of more massive objects.

For the low-mass stars that presumably evolved without a disk, we find that our results are consistent with an evolution-conserving angular momentum. The comparison between the model period evolution and the observed values suggests that initial angular momenta at least 3 times larger than those found by means of the Kawaler (1987) law are needed for stars with mass in the range $0.2\,M_{\odot} \leq M \leq 0.4\,M_{\odot}$. This analysis was not possible for the higher masses sample, due to the lack of a statistically meaningful sample of rapidly rotating stars.

The idea that the double population of the ONC can be explained on the basis of a different morphology of the stellar magnetic fields seems to be ruled out by the fact that almost all the observed sources are fully convective, according to our interpretation, but not all fast rotators. However, a mechanism (e.g. the magnetic field itself) inhibiting convection might favour an earlier appearance of the radiative core, at least in some of the stars. In our analysis we found other indications that convection in the pre-MS may be affected by other parameter(s): although 2D hydrodynamic simulations predict HCE in the pre-MS, we find two results in favour of LCE: (1) the lithium depletion in HCE models is too large to be consistent with the pre-MS depletion shown in young open clusters; (2) the age distribution derived from HCE models for two groups of smaller and higher masses is very different. It may be that the lower convection efficiency needed in the pre-MS is due to the structural effect of the dynamo-induced magnetic field, as suggested by Ventura et al. (1998b) and D'Antona et al. (2000). This possibility leads us not to dismiss the idea of an earlier appearance of a radiative core in the $M>M_{\rm tr}$ group.

The evolutionary tracks (for masses ranging from 0.085 to $1.6M_{\odot}$) and isochrones (from 2×10^5 to 1×10^7Myr) are available from the web site: `www.mporzio.astro.it/~tsa`

Chapter 6

Final Remarks

In this chapter, we present a general conclusion of our work. A more specific conclusion of each topic has already been given in the respective chapters, along the work. Our work contributed to improve the capability of the ATON code in reproducing observations, but some discrepances between theory and observations still remain. Questions such as turbulence, magnetic fields and others, must be adressed in order to improve agreement between theory an observation and to solve some shortcomings of stellar modeling. Some directions for future work will be also presented.

6.1 General conclusions

In this work, we introduced some physical and structural improvements in the stellar evolutionary code ATON2.3 (Mendes 1999b, 1999a) in order to save computing time and to investigate the evolution of low mass stars. In Chap. (2), we describe how we changed the computational structure of the code, by means of a mechanism that allows starting the run at an intermediate step of evolution, since the initial steps have already been registered in a previous execution. This is the mechanism of *checkpointing*. The version of the ATON code with checkpointing was used throughout this work in order to introduce further improvements. The internal structure of a star and its equilibrium configuration were discussed in Chap. (3). Internal structure constants are important parameters in stellar astrophysics, used to predict the apsidal motion rate in eccentric binary systems. They give us information about the degree of mass concentration of a star. By numerically integrating the Radau's equation (Eq. 3.16) we obtained the quantities η_j (j=2, 3, 4) needed to calculate the apsidal motion constants (or also, the internal structure constants) by means of Eq. (3.17). Considering stars as gas spheres is an unreliable approximation, since there exists some effects such as rotation and tidal forces, that deviate the stellar configuration from the sphericity. We took these effects into account in the ATON code by replacing the spherically symmetric surfaces by suitable non-symmetrical equipotential surfaces characterized by the total potential ψ given in Eq. (3.72). We used the KT70 method for introducing tidal disturbing potentials and coupling them to the rotational

potential, but instead of using a Roche potential, we use a more refined potential function in order to take into account the terms related to the tidal forces and to the distortion that affect the figure of the star. Following this approach, we obtained the correction factors $f_{\rm p}$ (Eq. 3.30) and $f_{\rm t}$ (Eq. 3.32) to be applied in the four stellar structure equations (Eqs. 3.31) in order to obtain stellar models of a rotationally and tidally distorted star. We also derived a new expression for the rotational inertia of a star distorted by the disturbing effects cited above, and used it to obtain the gyration radius, β, (Eq. 3.83), an important parameter used to predict circularization and synchronization timescales. By using standard and distorted models, we computed evolutionary models for masses varying from $0.09{\rm M}_{\odot}$ to $3.8{\rm M}_{\odot}$. The values of apsidal motion constants for low-mass stars as well as those of the gyration radii at the ZAMS are tabulated in Tables (3.1), (3.2), (3.3) and (3.4), for standard, non-rotating binary, single rotating and rotating binary models, respectively. The corresponding pre-main sequence values are presented in Appendix (A). Rotational effects affects the stars in the same way, being the influence of rotation the most important, comparatively. Distorted models produce internal structure constants that are smaller and, consequently, closer to those of real stars (according to the present observations of apsidal motion periods) than standard models, keeping constant other inputs parameters. Our k_j and β values are also smaller than those tabulated by Claret & Giménez (1989a, 1992) for the same initial chemical composition and mixing length which each model must use to fits the sun. Besides, we verify that the effects of tidal and rotational distortions affect the stellar physical quantities in opposite ways for masses below and above $\sim 1.3-1.5\,{\rm M}_{\odot}$. In order to test our new set of rotating binary models, we used it to investigate the evolutionary status of the peculiar double-lined eclipsing binary system EK Cep. It has accurate determination of absolute dimensions and well known properties, as apsidal motion, lithium contents for the secondary and a published evaluation of its metallicity. Moreover, the secondary is a pre-main sequence star. This system was analyzed following the same approach as Claret (2006). Stellar radii and the effective temperature ratio were reproduced on the same isochrone for the observed masses by models with α=1.5 and (X,Z)=(0.67,0.012). By using our models, we were not able to reproduce, simultaneously, the individual values of the effective temperatures of the component stars of EK Cep. The derived age is $17.2 \pm 0.4 \times 10^6$ years. The lithium depletion for the secondary and the apsidal motion rate predicted by our models are in qualitative agreement with the observed values. The differences remain within the theoretical and observational errors.

In order to study the magnetic activity of solar-like pre-main sequence stars, we introduced in the `ATON2.3` code calculations of both the theoretical convective turnover time, τ_c, and of the Rossby Number, *Ro* (see Chap. 4). These quantities were computed for a range of rotating low-mass stellar models. We discussed their behavior as a function of time and mass and compared our results with those obtained by previous works. For a given age, τ_c decreases substantially during the contraction to the ZAMS, but, after that, it remains nearly constant. During the contraction on the Hayashi track, the *Ro* follows the same behavior as τ_c, but, after reaching a main sequence configuration, it increases as expected, since the rotation period also increases in this phase. We calculate theoretical isochrones that can be used to infer stellar mass and age from observational quantities, such as effective temperature, rotation period and an activity index. Our theoretical results are in agreement with those by Kim & Demarque (1996), which, to the best of our knowledge, is the only work that reports such calculations for rotating stars.

Aiming at investigating stellar evolution of low-mass stars starting from early, low-gravity stages, we updated the `ATON2.3` code with non-gray boundary conditions, by using the NextGen (Allard & Hauschildt 1997), ATLAS9 (Heiter et al. 2002) and NextGen PMS (Allard et al. 2000) atmosphere models (details in Chap. 5). This new version of the code was used to generate new sets of rotating non-gray tracks that were used to analyze the rotational properties of a sample of young pre-main sequence stars in the Orion Nebula Cluster (ONC) (Landin et al. 2006) and to understand the main physical properties characterizing the evolution of young stars. By comparing the location of the tracks in the HR diagram with the position of the observed objects, we assign to any single star a mass and an age, for three different convection efficiency degrees, α=1.0, α=2.0 and α=2.2. We confirm that the convection treatment is generally the most important physical input in determining effective temperatures of pre-main sequence evolutionary tracks. The path followed by the evolutionary sequences on the HR diagram is also affected by the boundary conditions, being the gray models hotter than their non-gray counterparts. For the particular range of masses and ages at which most of the ONC population is found, non-gray effects are more important than the convection efficiency. The bulk of the observed stars in the ONC have masses in the range $0.2M_{\odot} \leq M \leq 0.4M_{\odot}$, independent of the α value. On the other hand, age distributions are strongly affected by the choice of the MLT parameter. Our work confirms the dichotomy present in the rotational properties of the ONC objects (Herbst et al. 2002). For masses below a given threshold value, defined as transition mass (M_{tr}), the period distribution has a single peak at short period values, while for masses above M_{tr} the distribution has a secondary peak at about 8 days. By assuming that disk-locking is the mechanism responsible for the secondary peak in the overall distribution, two interpretations are possible: either 1) stars with $M<M_{tr}$ lose their disks earlier or, 2) their locking period is shorter. The X-ray emissions of ONC stars were also analyzed but no correlation with period was found, supporting the suggestion that these stars are indeed in the super-saturation regime of the rotation-X-ray luminosity relationship. For the stars that presumably evolved without a disk, we found that our results are consistent with an evolution-conserving angular momentum. The comparison between the model predicted rotation periods and the observed values suggests that initial angular momenta at least 3 times larger than those prescribed by Kawaler's (1987) prescription are needed for stars with mass in the range $0.2\,M_{\odot} \leq M \leq 0.4\,M_{\odot}$. The idea that the double population of the ONC can be explained by means of a different morphology of the stellar magnetic fields seems to be ruled out by the fact that almost all the observed sources are fully convective, according to our interpretation and have a range of periods. We found indications that convection in pre-main sequence can be affected by other parameters. Although 2D hydrodynamic simulations predict high convection efficiency (HCE) in the pre-main sequence, we found two results in favour of low convection efficiency (LCE): 1) the lithium depletion predicted by HCE models is too large to be consistent with the values observed in young open clusters; 2) the age distribution derived from HCE models for two groups of smaller and higher masses is very different.

All these changes introduced in the `ATON` code helped us to better understand stellar structure and evolution and study the input parameters that influence the path followed by tracks. It is important to concentrate efforts in including new physical effects in stellar evolutionary codes, always aiming to better reproduce observations.

6.2 Future works

In this section, we briefly present some improvements that should be done in the ATON code. The first one concerns the equations currently used in the code to obtain the meridional circulation velocity, $U(r)$. The second one refers to the the inclusion of the rotation-induced diffusion of chemicals in the microscopic diffusion process. The inclusion of the effects of a gradient in the chemical composition in the code is also aimed. Finally, we discuss the importance of treating the interaction between magnetic fields and rotation in a consistent way.

6.2.1 Approximations to the meridional circulation velocity

It is well know that stellar rotation causes a thermal imbalance that, by its turn, produces meridional circulation currents. Even if the star initially rotates as a rigid body, the circulation currents change the internal angular velocity profile, leading to differential rotation, which in turn can trigger a number of hydrodynamical instabilities in the non-viscous stellar plasma, resulting in turbulent motions. In order to readjust the stellar angular velocity profile, the angular momentum must be internally redistributed.

These two physical effects, rotation and internal angular momentum redistribution, were introduced in the ATON code by Mendes (1999b). The first effect is implemented according to the Kippenhahn & Thomas (1970) work while the second one follows the framework established by Chaboyer & Zahn (1992). The original expressions for the $U(r)$ (Zahn 1992) were derived for massive main sequence stars with radiative envelopes, being not suitable to describe the circulation process in the low mass, pre-main sequence stars. Some approximations in this theory must be revised in order to treat the instabilities driven by rotation in such young stars. Particularly, the gravitational contribution to the total energy, which is not negligible in early evolutionary phases, must be considered according to Maeder & Zahn (1998) approximation. Mendes (1999b) used their approach for the $U(r)$, but tests with a $1\,\mathrm{M}\odot$ pre-main sequence models yield negative values for this quantity in a considerable fraction of the radiative region. This means that the circulation currents sink in the poles and rises in the equator, which increases the thermal imbalance instead of acting against it. In order to get a more suitable expression for the $U(r)$ arising in solar-like pre-MS stars, we intend to use the revised $U(r)$ expression given by Zahn (private communication). This is a fundamental change that must be done in the code, since the next aimed improvements depends strongly on the $U(r)$.

6.2.2 Rotation-induced diffusion of chemicals

Chaboyer & Zahn (1992) and Zahn (1992) presented a treatment to the meridional circulation and turbulence in rotating stars by assuming that turbulence is anisotropic in radiative regions and that horizontal motions are stronger than the vertical ones. They considered the effects of the meridional circulation in the internal transport of both chemicals and angular momentum, which are still described by a diffusion equation, but the internal angular momentum obeys an advection-diffusion equation. Although Chaboyer & Zahn (1992) and Zahn (1992) give a suitable treatment to the effects of the meridional circulation, they consider only one of the many instabilities resulting the anisotropic turbulence. This approach was adopted by Mendes (1999b), but, in addition, he considered

most of hydrodynamic instabilities related to rotation. However, this approach is used only when the chemical elements are instantaneously mixed. A more realistic approximation to the mixing of chemicals would be the rotation-induced diffusion, which we aim to introduce in the code in the near future.

The rotation-induced diffusion of chemicals is very important for stellar evolution, since it could explain the anomalous abundances in high-mass stars and the lithium depletion in less massive ones. In order to take this effect into account, we need, first, to compute the effective diffusion coefficient, which depends on the stellar radius, meridional circulation velocity and both the vertical an the horizontal diffusivities (see Eq. 5.2 by Mendes 1999b). This improvement is relatively easy to implement, since the code already calculates all necessary variables to compute such coefficient. The next step, in order to introduce the rotation-induced diffusion of chemicals, is to use the microscopic diffusion process, already implemented a previous version of `ATON` code. This consists basically in adding the value of the effective diffusion coefficient computed at each diffusion time step to the microscopic diffusion coefficient.

6.2.3 Effects of a μ-gradient

The nuclear reactions build up a gradient of molecular weight, ∇_μ, throughout the star. These chemical inhomogeneities, by its turn, are advected by the meridian flow, until the "μ-currents" are strong enough to cancel the meridian velocity $U(r)$ at some depth. Thereafter, the star is divided in two homogeneous regions, separated by a "μ-barrier" of increasing strength, which can only be prevented if the rotation approaches the break-up speed, i.e. if the centrifugal force is close to the local gravity (Zahn 1993). In this approach, the situation is quite different because the chemical inhomogeneities are eroded by the anisotropic turbulence.

According to Mestel (1953), who investigated the effects of a gradient in the chemical composition in the mixing caused by meridional circulation in rotating stars, whenever such gradient exists, the meridional circulation creates a non-spherical distribution of chemical composition which tends to prevent the circulation itself. In this way, the presence of a μ-gradient has an inhibiting effect on the rotation-induced mixing. However, the extention of such inhibition is not yet well understood and the available results are still controversial.

In order to take the μ-gradient effect into account in the `ATON` code, we intend to follow the suggestion by Maeder & Zahn (1998), in which the dependence of the resulting meridional circulation velocity on the ∇_μ is not only considered through the contribution due to the horizontal variations but also by including it in the expression for the superadiabatic gradient. In semiconvection regions, they found that the usual expression for $U(r)$, without ∇_μ, would predict an inverted circulation (which is equivalent to obtain a negative value for $U(r)$). With the inclusion of a ∇_μ in the $U(r)$ expression, as described by their Eq. (4.38), this and other unphysical situations do not occur. Maybe, the missing effect of a ∇_μ in our calculations of the meridional circulation velocity is the cause of our resulting negative velocity.

6.2.4 Interaction between rotation and magnetic fields

It is well know that magnetic fields play an important role in a number of astrophysical processes. In the final stages of star formation, when the protostar is still growing in mass due to residual accretion, the magnetic interactions may mediate gas accretion and launch the bipolar jets that typically announce the birth of a new star (Larson 2003). Approaching the main-sequence, magnetic braking slows down rotation, and the thermal effect of the magnetic field is expected to vanish for solar-type stars (D'Antona et al. 2000). Besides, magnetic fields play an essential role in stellar angular momentum evolution because the only way to extract angular momentum from a single star seems to be the magnetic coupling to the surrounding gas. In order to model this process in Classical TTauri stars, a dipolar magnetic field has been assumed with the axis of the dipole aligned with the axis of rotation (Bouvier et al. 1993). However, observational tests do not support the assumption of an aligned dipole (Küker & Rüdiger 1999). So, in such a modeling, it is very important to know the true field geometry, which may vary from star to star.

The geometry of stellar magnetic fields is, in general, a complicating factor considering its modeling in the existing evolutionary models, which are essentially one-dimensional, but some efforts have been done to accomplish this goal. Lydon & Sofia (1995) developed a strategy to modify the equations of stellar structure and evolution (including mixing length theory) for the effects of a large scale magnetic field confined within a star. D'Antona et al. (2000) presented evolutionary models for the pre-main sequence, including zero-order thermal modifications that are due to a parametric inclusion of magnetic field effects. Their main result is that, whichever is the convection treatment, the inclusion of magnetic fields leads to cooler models and to lower lithium depletions in the pre-main sequence. By using a more realistic approximation, Li et al. (2006) developed a two-dimensional stellar evolutionary code for studying solar variability due to structural changes produced by varying internal magnetic fields of arbitrary configurations.

As discussed by Spruit (1999, 2002), the magnetic field can be created in radiative layers of stars with differential rotation. Even a small toroidal field is subject to an instability (called "Tayler instability" by Spruit), which creates a vertical field component. Differential rotation winds up this vertical component, so that many new horizontal field lines are produced. These horizontal field lines become progressively closer and denser in a star presenting differential rotation, and, therefore, a much stronger horizontal field is built. This is the dynamo process described by Spruit. The Tayler instability is characterized by a short timescale. The magnetic shear instability may be present, but it is of much less importance. In a series of works, Maeder & Meynet (2003, 2004, 2005) and Eggenberger (2005) studied the relative importance of rotational and magnetic effects in high mass stars, by calculating the magnetic instabilities that may rise in differentially rotating stars and create magnetic fields. They conclude that the Tayler instability and the Tayler-Spruit dynamo are of major importance for stellar evolution, both for the transport of angular momentum and for the transport of chemical elements.

The development of a stellar evolutionary code that treats simultaneously rotation and magnetic fields is of high importance for studying the results on tracks, surface composition, rotation, and for analyzing the coupling between magnetic fields and differential rotation. In the near future, with a forthcoming version of the `ATON` code which will treat properly the instabilities driven by rotation, we will focus our efforts on the rotational

evolution in order to understand how magnetic fields interact with differential rotation.

At another parallel task, the ATON 2.0 code is undergoing significant enhancements concerning the nuclear evolution, with a wider nuclear network that includes 30 nuclear species, and some small physical changes in the equation of state, also. With the aim of transforming the ATON code in a more powerful tool for understand observed stellar properties, we intend to include all these features in the rotating version and create a unified version of the ATON code.

Chapter 7

Síntese do trabalho em língua portuguesa

Uma versão resumida do trabalho realizado durante o curso de doutorado é apresentada neste capítulo. Maiores detalhes podem ser obtidos nos demais capítulos.

7.1 Introdução

7.1.1 Tema de pesquisa

O tema deste trabalho está relacionado com estudos teóricos computacionais de determinados efeitos físicos na evolução estelar, como atmosferas não-cinza, distorções de maré na estrutura de equilíbrio devido à presença de uma outra componente em sistemas binários, cálculos de constantes de estrutura interna, importantes nos estudos de movimentos apsidais, e do Número de Rossby, relacionado com atividade magnética (através de estimativas de índices de atividade e de escalas de tempos convectivos).

Para realizarmos este trabalho, utilizamos o código de estrutura e evolução estelar `ATON2.3` (Mendes et al. 1999b), ao qual tivemos acesso por meio de uma colaboração científica internacional entre meu orientador, Dr. Luiz Paulo Ribeiro Vaz, e os pesquisadores italianos, Dra. Francesca D'Antona e Dr. Italo Mazzitelli, autores do código no qual introduzimos os efeitos físicos citados acima. O primeiro resultado desta colaboração foi a tese de doutorado do Dr. Luiz Themýstokliz Sanctos Mendes, que introduziu os efeitos de rotação e redistribuição de momentum angular no referido código e que é meu co-orientador no presente trabalho. Parte do meu curso de doutorado, assim como o de Luiz T.S. Mendes, foi realizado no *Osservatorio Astronomico di Roma, Itália*, sob a co-orientação da Dra. D'Antona. Desta vez, contamos também com a valiosa colaboração do Dr. Paolo Ventura.

Este trabalho foi realizado basicamente em três etapas:

1. Introdução de melhorias na estrutura do código, como a possibilidade de se fazer uma parada de controle (*"check point"*), visando facilitar a verificação e correção das implementações e modificações físicas no modelo, realizadas na etapa 2;

2. Aperfeiçoamento do modelo computacional, através da inclusão dos efeitos físicos citados acima (atmosferas não-cinza, distorções de maré, etc.);
3. Utilização do modelo, com suas novas características, como ferramenta na análise de dados observacionais de estrelas.

Como as implementações da etapa 2 são independentes, a medida que foram inseridas no modelo, o mesmo já pode ser usado na análise de dados observacionais, como, por exemplo, na localização de estrelas pré-sequência principal no diagrama de Hertzprung-Russel (diagrama HR).

7.1.2 Relevância e justificativa do tema de pesquisa

Os modelos de estrutura e evolução estelar tradicionais, isto é, sem rotação, campos magnéticos, etc., são capazes de explicar as características globais das estrelas. Porém, nas últimas décadas, a quantidade e a precisão dos dados observacionais apresentaram um crescimento significativo, evidenciando, assim, as limitações desses modelos mais simples.

A inclusão de novos efeitos físicos nos modelos de evolução estelar melhoram significativamente as comparações entre os mesmos e os dados observacionais. Há aproximadamente vinte anos, descobriu-se que a perda de massa por ventos estelares causava grande impacto na evolução estelar. Entretanto, algumas discrepâncias significativas permaneceram e a inclusão de rotação possibilitou um progresso substancial na comparação com as abundâncias químicas observadas. Segundo Maeder & Meynet (2003), a introdução de aproximações que considerem o campo magnético é a próxima, mas não a última, nessa série de modificações, cujos efeitos devem influenciar todos os resultados dos modelos de evolução estelar.

O grande interesse dos estudiosos da evolução estelar é reproduzir, satisfatoriamente, as propriedades e condições estruturais dos interiores das estrelas, conciliando assim, os resultados teóricos alcançados com os modelos e dados obtidos com as observações. Por essa razão, muito se esforça para considerar, da forma mais realista possível, os processos físicos que afetam as propriedades fundamentais das estrelas.

O código `ATON2.3` (Mendes et al. 1999b), que está sendo adotado como ponto de partida neste trabalho, já leva em conta a rotação estelar, redistribuição de momentum angular e possui uma característica peculiar, que é o tratamento da turbulência no transporte de energia por convecção, fenômenos que, comprovadamente por dados observacionais, fazem parte do cenário de evolução estelar. No entanto, sabe-se que, em regiões do interior estelar, os campos magnéticos podem ser gerados por efeitos de dínamo, ou seja, interação entre rotação e convecção (Spruit 2002). Além de incorporar no modelo o tratamento de campos magnéticos e seu efeito combinado com rotação, outras aproximações físicas, mais facilmente implementáveis nos códigos existentes, têm se mostrado necessárias para explicar as observações. Algumas dessas modificações já estão sendo incorporadas por outros autores em seus modelos, a saber:

- distorções de maré na estrutura de equilíbrio, devidas à presença de uma ou mais componentes em sistema múltiplos;
- cálculo das constantes de movimentos apsidais;
- uso de atmosferas estelares não cinza;
- estudos sobre correlação entre rotação e atividade estelar através de estimativas de escalas de tempos convectivos.

De modo geral, pode-se dizer que a estrutura de equilíbrio de uma estrela é, basicamente, esfericamente simétrica. No entanto, essa estrutura pode sofrer algumas deformações causadas por forças rotacionais e/ou por forças de maré, devido a ação da gravidade exercida por estrelas companheiras, em sistemas binários ou múltiplos. As distorções no potencial devido à rotação já são consideradas na versão 2.3 do código `ATON`, porém as distorções devido às forças de maré ainda não foram incorporadas e estas são menos significativas que aquelas. No entando, quando há a presença simultânea de rotação e maré, os efeitos das distorções nos parâmetros físicos são apreciáveis. Estes efeitos se tornam ainda mais realçados no caso de sistemas binários sincronizados. Maiores detalhes sobre estes efeitos de distorções podem ser encontrados em Mohan et al. (1990).

Uma outra modificação que precisa ser incorporada no código `ATON2.3`, é melhorar o tratamento usado na modelagem da atmosfera estelar. A aproximação cinza (isto é, supor que o coeficiente de absorção seja independente da frequência) fornece, em geral, um valor maior para a massa mínima para a queima do hidrogênio e modelos mais quentes e mais densos para uma mesma massa, se comparados a modelos não-cinza, superestimando $T_{\rm eff}$ (Montalbán et al. 2000). Atmosferas não-cinza, assim como presença de campos magnéticos, exercem influência direta na localização, no diagrama HR, de estrelas pré-sequência principal. A utilização deste tipo de atmosfera, faz com que os interiores se tornem sistematicamente mais frios (e com massa mínima para a queima do hidrogênio menor), se comparados àqueles gerados com modelos de atmosfera cinza (ou sem campos magnéticos), para um determinado valor de massa (Burrows et al. 1993). Como, pelos modelos atuais, aceita-se que a energia é transportada por convecção dentro de estrelas na fase de pré-sequência principal, parece plausível que, rotação ou campos magnéticos (ou o efeito de ambos), possam inibir a eficiência do transporte convectivo de energia, seja por diminuir a quantidade de energia levada por convecção ou por fazer com que o gradiente de temperatura crítico para a instabilidade convectiva seja maior.

Como tem-se descoberto objetos estelares e subestelares cada vez mais frios, a presença de moléculas e partículas condensadas têm complicado enormemente o entendimento de suas propriedades físicas. Modelos precisos de atmosferas estelares que incluam estes processos, são a chave para estabelecer os parâmetros atmosféricos destes objetos. Esses modelos possuem um papel crucial em determinar características estruturais ajustando as condições superficiais de interiores dos modelos e fornecendo transformações aos vários planos observacionais. Eles também podem revelar características espectroscópicas de anãs marrons (estrelas cuja massa total não é suficiente para disparar a queima do hidrogênio) e ajudar a estabelecer sua detectabilidade (Allard et al. 1997).

Como a principal aplicação dos modelos evolutivos estelares tem sido a investigação das etapas que acontecem ao longo da evolução estelar, os modelos computacionais têm sido constantemente melhorados com o intuito de minimizarem as discrepâncias existentes entre suas previsões e os dados observacionais disponíveis na literatura. Sendo assim, é necessário inserir no código o cálculo de constantes de movimentos apsidais, a partir das constantes de estrutura interna, para permitir a interpretação das taxas de movimentos apsidais obtidas observacionalmente. Um dos objetivos de incluir no modelo as distorções de maré na estrutura de equilíbrio da estrela é obter valores mais realistas das constantes de estrutura interna, uma vez que elas sofrem influência direta de tais distorções.

7.2 Mudanças estruturais no código ATON2.3

Todos os modelos de estrutura e evolução estelar apresentam limitações diversas, uma vez que muitos processos físicos relevantes são complexos e ou são considerados de forma aproximada ou são integralmente ignorados, seja pelas dificuldades matemáticas associadas, seja pela falta de compreensão dos mesmos. Mesmo os processos físicos mais simples, sobre os quais hoje se tem domínio, são incorporados nos modelos, em sua maioria, de forma simplificada, devido, em parte, aos excessivos tempos de cálculo que estes requerem. Este fato torna a introdução de melhorias, físicas ou numéricas, nos códigos, tarefas árduas e demoradas, principalmente nas fases iniciais e de testes.

7.2.1 Implementação das mudanças estruturais

Para melhorar a performance do programa e facilitar o teste e controle das modificações são necessárias algumas mudanças em sua estrutura. Após análise do código disponível, decidimos que algumas melhorias de ordem estrutural deveriam ser introduzidas no código ATON2.3. Com o uso da ferramenta NagWare Fortran Tools, Release 4.0, 1990 (The Numerical Algoritms Group Limited), para a análise, depuração e transformação de códigos escritos em FORTRAN 77, fizemos o controle da existência de variáveis não inicializadas e convertemos todo o código para precisão dupla. Além disso, padronizamos a disposição do código, mudando o espaçamento entre as linhas, alinhando todas as estruturas de COMMON, etc. Esses procedimentos devem preceder uma modificação há muito desejada, que é o controle do uso de memória para implementar um mecanismo de *"checkpoint"*, ou seja, de poder interromper o programa em determinado estágio do cálculo e ser capaz de reassumir, posteriormente, o cálculo sem qualquer perda de precisão numérica. O *"checkpoint"* consiste em executar o código evolutivo até um dado estágio arbitrário, gravar, em um arquivo binário, todas as variáveis necessárias para continuar os cálculos a partir daquele ponto, sem a necessidade dos cálculos anteriores.

Para implementar este procedimento, duas rotinas foram agregadas ao código e outras foram modificadas para se adequarem à sua nova estrutura. Uma das novas rotinas, em um determinado ponto de execução do código, grava em arquivo binário (de aproximadamente 9MB), todas as variáveis globais indispensáveis à retomada dos cálculos a partir de um ponto intermediário. Quando se faz necessário restaurar a memória de um determinado modelo em um dado ponto de execução, o programa utiliza uma outra rotina especialmente criada para ler todo esse conjunto de dados do arquivo binário correspondente. Com essas variáveis armazenadas em sua memória, o código pode retomar os cálculos e gerar os mesmos resultados que uma execução semelhante que tivesse partido do ponto inicial, com um evidente ganho de tempo de cálculo.

7.2.2 Importância do *"checkpoint"*, ou ponto de controle

O mecanismo de *"checkpoint"* é fundamental quando se trabalha na modificação de modelos computacionais, principalmente nos casos em que o programa utilizado é complexo e gasta muito tempo para ser executado. Para termos uma idéia de como o tempo computacional varia com a complexidade do programa, vamos considerar o tempo de execução gasto por algumas versões do código ATON para reproduzir as características de uma estrela de mesma massa e metalicidade que o Sol, rodando em um processador XEON

de 1,8 GHz. A versão 2.0 é relativamente simples e gasta 3 minutos para reproduzir as características dessa estrela sem considerar rotação, partindo da pré-sequência principal (PSP) e chegando até o final da sequência principal (SP), o que equivale para o código uma idade de 7,6 bilhões de anos. Mas este tempo torna-se quatro vezes maior se deixamos essa mesma estrela evoluir até 10 bilhões de anos, já em sua fase pós-sequência principal. O código `ATON2.3`, é uma versão mais realista do modelo evolutivo em questão. Ele pode tratar a estrela girando de uma das seguintes formas: como um corpo rígido ou com rotação diferencial ao longo de toda a estrela, ou, ainda, apresentando rotação mista, de corpo rígido em regiões convectivas e com rotação diferencial em zonas radiativas. No primeiro e no segundo casos, o código gasta aproximadamente treze minutos e no terceiro, vinte e cinco minutos para gerar o modelo estelar desde a PSP até o final da SP. Os dados sobre a pós-sequência principal não foram apresentados porque a versão 2.3 do código ainda não foi devidamente testada nesta fase.

Tendo em vista que, à medida que mais fenômenos físicos são inseridos no código evolutivo, maior se torna o tempo de execução necessário, percebemos que uma parada de controle foi uma ferramenta extremamente útil durante a implementação de atmosferas não cinza e, provavelmente o será em implementações futuras de fenômenos mais complexos como campos magnéticos. Este mecanismo torna-se mais importante ainda quando se está na fase de testes, pois o mesmo permite que todas as variáveis essenciais do modelo, até um determinado passo, sejam armazenadas em um arquivo e lidas posteriormente para dar continuação à execução. Uma vez que os passos iniciais do programa sejam os mesmos, não é necessário refazer os cálculos desde o início. Sendo assim, a implementação do *"checkpoint"* tem como objetivo principal, reduzir o tempo que deverá ser gasto para inserir no código as melhorias físicas desejadas. Entretanto, podemos utilizar a opção para estudos de efeitos de diferentes aproximações que são ativadas após determinadas fases, como, por exemplo, transferência de massa em sistemas binários e/ou perda de massa em determinadas fases evolutivas da estrela.

7.3 Distorções na estrutura de equilíbrio devido às forças rotacionais e de maré

Um sistema binário de estrelas consiste de um par de estrelas que giram em torno de seus próprios eixos, ao mesmo tempo que orbitam em torno do centro de massa do sistema. Nem sempre os eixos de rotação intrínseca e o orbital estão alinhados desde o início do processo de formação, assim como a órbita começa, em geral, com uma excentricidade significativa e com as estrelas componentes não sincronizadas com a velocidade orbital. Entretanto, devido às forças de deformação que aparecem, o sistema tende a alinhar os eixos, sincronizar as componentes na velocidade de rotação orbital por ocasião da passagem pelo periastro e, finalmente, a circularizar a órbita. Quando os períodos de rotação e de revolução são iguais, dizemos que se trata de um sistema binário sincronizado. Dessas duas estrelas, geralmente, uma delas, chamada de primária, é maior e mais quente que a outra (chamada de secundária), tanto em tamanho quanto em massa. Dependendo do estágio evolutivo das componentes, muitas vezes a de maior massa não é a estrela maior ou a de temperatura efetiva mais alta. Nesses casos, é sempre necessário especificar o que se entende por componente "primária", se a de maior massa (o que é o mais comum quando se trata de sistemas binários espectroscópicos) ou se a de $T_{\rm eff}$ mais alta (o que

é o mais comum quando se trata de sistemas eclipsantes). Devido aos efeitos de rotação e de maré causados pela presença da companheira, as componentes do sistema binário tornam-se distorcidas rotacionalmente e por forças de maré.

A estrutura de equilíbrio de estrelas com rotação e estrelas em sistemas binários não apresenta simetria esférica. Enquanto as forças rotacionais distorcem a configuração da estrela que roda, em relação à forma originalmente esfericamente simétrica de uma estrela parada (Fig. 3.1), as forças de maré, causadas pela atração gravitacional de uma companheira, distorcem a configuração de uma estrela em um sistema binário (Fig. 3.1). No caso de estrelas com rotação em um sistema binário tanto as forças rotacionais quanto as de maré distorcem sua forma.

O estudo analítico do problema de determinar os efeitos combinados das forças de rotação e maré nas estruturas de equilíbrio de estrelas é bastante complexo. Métodos alternativos têm sido geralmente usados na literatura para estudar estes efeitos.

Kopal (1972, 1974) desenvolveu em detalhes o conceito de equipotenciais de Roche e coordenadas de Roche para estudar os problemas de estrelas distorcidas rotacionalmente e por efeitos de maré em sistemas binários. Kippenhahn & Thomas (1970), daqui pra frente KT70, propuseram um método para determinar a estrutura de equilíbrio de modelos estelares em que rotação e distorções por efeitos de maré estão presentes. Este método tem a vantagem de possibilitar, a partir de um código de estrutura estelar esférica, obter-se facilmente um modelo de estrutura não esférica. Uma descrição detalhada do método pode ser vista na Seção (3.4).

Para se obter a estrutura interna de uma esfera gasosa distorcida por forças rotacionais e de maré, o sistema de Eqs. (3.31) tem que ser numericamente integrado, sujeito à condições de contorno adequadas. Neste caso, o cálculo da superfície equipotencial real é um problema complicado. KT70 propuseram que as superfícies equipotenciais reais da estrela distorcida poderiam ser substituídas pelas superfícies equipotenciais de Roche apropriadas (ver Eq. 3.19).

Ao invés de usar o potencial de Roche, preferimos seguir o tratamento mais refinado dado por Endal & Sofia (1976) para a função potencial, acrescido de um potencial perturbativo devido às forças de maré. Usando a expansão de Clairaut-Legendre para o potencial gravitacional de um corpo auto-gravitante (Kopal 1959), introduzimos termos adicionais ao potencial total referentes às partes cilindricamente simétrica e assimétrica do potencial gravitacional devido às distorções rotacionais e de maré, respectivamente. A Eq. (3.72) representa o potencial total usado neste trabalho. Uma descrição detalhada (a) da implementação dos efeitos de distorção por rotação e forças de maré e (b) do cálculo teórico das constantes de movimento apsidais pode ser vista na Seção (3.5). Como consequência da presença destes potenciais perturbativos, a inércia rotacional da estrela muda. Sendo assim, uma nova expressão para esta grandeza foi derivada na Seção (3.5.4).

Estas implementações foram introduzidas no código `ATON2.3`, com a finalidade de obter estimativas mais realistas para as constantes de movimentos apsidais (k_j, j=2, 3 e 4) e compará-las com os valores obtidos a partir de dados observacionais. Na Seção (3.1) nós apresentamos as expressões usadas nos cálculos observacionais destas constantes. Na Seção (3.6) apresentamos novos modelos evolutivos incluindo valores teóricos das constantes de estrutura interna e raio de giração (Eq. 3.83) para quatro conjuntos de modelos: padrão, distorcido por rotação, distorcido por forças de maré e distorcido por ambos efeitos. Os modelos cobrem o intervalo de massas que vai de 0,09 a 3,8 $M_\odot$. O raio de giração de um corpo é a distância entre um dado eixo deste corpo (por exemplo,

o eixo de rotação) e seu centro de giração[1].

Os modelos distorcidos apresentam valores de k_2 menores que os modelos padrão, ou seja, valores mais próximos aos obtidos observacionalmente. Como os valores de k_2 disponíveis na literatura foram obtidos com modelos padrão fizemos uma comparação entre estes e as nossas estimativas para esta grandeza para o caso padrão. Comparamos modelos de mesma composição química inicial e $\alpha_{\rm MLT}$ que cada modelo precisa usar para reproduzir o raio solar na idade atual e percebemos que nossos valores concordam com os anteriomente publicados (Hejlesen 1987, Claret & Giménez 1989a, Claret & Giménez 1992), sendo que os nossos valores estão mais de acordo com os observados que os modelos acima.

Usamos os modelos distorcidos por forças de maré e rotação para analisar um interessante sistema binário eclipsante de linha dupla, EK Cep, com o objetivo de testar nossas modificações. Para a investigação do estado evolutivo da estrela, usamos a mesma aproximação que Claret (2006). Adotamos como vinculo para nossos modelos a razão das temperaturas efetivas, ao inveś de usar seus valores individuais. Usando trilhas correspondentes às massas determinadas dinamicamente, conseguimos reproduzir os raios das estrelas e a razão das temperaturas efetivas (não seus valores individuais) na mesma isócrona ($17,2 \pm 0.4$ M anos), com (X,Z)=(0,67, 0,012) e α=1,5. A fração de lítio, $\log(Li/H)$, prevista pelos modelos de 1,124 $M_\odot$, referentes à secundária, na idade de $17,2 \pm 0.4 \times 10^6$ anos, concorda com o valor medido por Martín & Rebolo (1993). A partir dos valores individuais de k_2 estimados pelos modelos referentes a cada uma das massas determinadas, obtivemos o valor médio teórico desta grandeza e calculamos o valor previsto para a taxa de movimento apsidal do sistema ($\dot{\omega}$). Uma comparação entre $\dot{\omega}_{\rm teórico}$ e $\dot{\omega}_{\rm observado}$ (Claret 2006), mostra que nossas previsões concordam com as observações e as diferenças estão dentro dos erros.

7.4 Cálculo teórico do Número de Rossby

Atividade magnética em estrelas como o Sol abrange um grande número de fenômenos, tais como manchas estelares, ciclos de atividade, aquecimento de camadas atmosféricas externas, emissão em raios-X e muitos outros. Geralmente, estes fenômenos são atribuídos ao dínamo estelar, que é um mecanismo que resulta da interação entre rotação diferencial e os movimentos convectivos no envelope externo das estrelas. Do ponto de vista teórico, existem indicações de que o campo magnético de estrelas parecidas com o Sol, na sequência principal, é gerado e amplificado na *tachocline*, uma fina camada que roda diferencialmente entre a zona convectiva e o interior radiativo. Para estrelas de tipo espectral entre F e M, acredita-se que a rotação e a atividade são controladas por um mecanismo do tipo α-Ω (Mohanty & Basri 2003). Já para o caso de estrelas completamente convectivas, como estrelas de baixa massa na pré-sequência principal, esta teoria não pode ser aplicada, uma vez que elas não possuem a tachocline. No entanto, elas apresentam fenômenos típicos de atividade magnética e espera-se que outro tipo de dínamo, como o dínamo tipo α^2 que depende de movimentos turbulentos, opere neste tipo de estrela e gere o campo magnético responsável pela atividade estelar observada (Küker & Rüdiger 1999). Uma quantidade muito importante no estudo de atividade magnética estelar é o Número de Rossby, *Ro*.

[1]O centro de giração de um corpo é definido como o ponto no qual toda a massa do corpo poderia estar concentrada (teoricamente) sem alterar seu momentum de inércia.

Ro é definido como sendo a razão entre o período de rotação e a escala de tempo de movimentos convectivos, τ_c. Na teoria de dínamo, o Número de Rossby está relacionado com a taxa de crescimento do campo magnético. Para estrelas na sequência principal, *Ro* tem sido usado para estudar a relação entre emissão em raio-X e campos magnéticos (Flaccomio et al. 2003c, Feigelson et al. 2003).

Neste trabalho apresentamos cálculos auto-consistentes de Números de Rossby e tempos de escala convectico (do inglês, *convective turnover time*) para uma série de modelos de estrelas de baixa massa e que levam em conta a rotação estelar. O comportamento destas grandezas durante a pré-sequência principal foi analizado, discutido e comparado com os resultados de trabalhos anteriores.

O "convective turnover time" local foi calculado a uma distância de metade do comprimento de mistura, $\alpha H_p/2$, acima da base convectiva. O Número de Rossby é calculado através da relação $Ro = P_{\rm rot}/\tau_c$. O "convective turnover time" global é definido como a integral do inverso da velocidade convectiva local ao longo de toda a região convectiva.

Geramos trilhas evolutivas que vão de 0,6 $M_\odot$ à 1,2 $M_\odot$, com composição química inicial solar e $\alpha_{\rm MLT}$=1,5. Em zonas convectivas usamos rotação de corpo rígido e em regiões radiativas a rotação é diferencial.

Como pode ser visto na Fig. (4.6), para um dado valor de massa o "convective turnover time" global diminui durante a contração de Hayashi e atinge seu valor mínimo quando a contração termina. Permanece, então, constante até que a estrela atinge uma configuração de estrela na sequência principal. *Ro* segue o mesmo comportamento de τ_c durante a contração de Hayashi, mas, depois disso, aumenta, como já era de se esperar, uma vez que o período de rotação também aumenta. Usando as trilhas evolutivas, construimos também, isócronas para as idades de 0,2, 0,5, 0,7, 1,0, 2,0, 4,55 (idade do Sol), 10 e 15 bilhões de anos. No lado esquerdo da Fig. (4.8), mostramos a variação do "convective turnover time" global com a temperatura efetiva e a idade. Como as curvas são isócronas, um aumento de temperatura pode ser entendido como um aumento na massa. No lado direito desta mesma figura, temos o τ_c global em função do período de rotação. A variação do período de rotação com a temperatura efetiva é mostrada na Fig. (4.9). Se supusermos que os efeitos da rotação são tratados corretamente, podemos usar esta figura para determinar unicamente a massa e a idade de uma estrela através de dados observados de sua temperatura efetiva e período de rotação. Na Fig. (4.10) mostramos o Número de Dínamo, Ro^{-2}, em função da temperatura efetiva e a idade. Depois de estabelecer uma relação empírica entre Ro^{-2} e os índices de atividade magnética, pode-se usar a Fig. (4.10) para determinar a massa e a idade da estrela a partir da temperatura efetiva e um índice de atividade.

Pelo que sabemos, o presente trabalho é o segundo na literatura a apresentar cálculos teóricos de tempos de escala convectivos e Números de Rossby para estrelas com rotação na sequência principal. Os primeiros a realizarem tais cálculos foram Kim & Demarque (1996). Nossos resultados estão de acordo com os obtidos por estes autores principalmente no que se refere ao comportamento geral de τ_c e *Ro* (Figs. 4.4, 4.5, 4.6, 4.7, 4.8, 4.9, 4.10). A principal diferença se refere aos valores de *Ro*: em alguns casos, nossos valores são até duas ordens de magnitude menores que os de Kim & Demarque (1996). A principal causa desta diferença está possivelmente relacionada com a taxa de rotação inicial usada nos modelos. Acreditamos que esse conjunto de resultados possam dar uma contrapartida teórica útil à estudos observacionais de atividade estelar na pré-sequência principal, podendo também ser usados para testar os modelos com as observações.

7.5 Inclusão de atmosferas não-cinza

No interior estelar, encontram-se fótons de várias frequências, viajando em todas as direções através do material da estrela. Estes fótons constituem o campo de radiação em um dado ponto e instante. A medida que a radiação flui ao longo da estrela, os fótons do campo de radiação irão, fatalmente, interagir com o material estelar, ora sendo absorvidos por algum átomo, ora sendo espalhados para uma outra direção. Pode ocorrer também que fótons sejam adicionados ao campo de radiação através de emissão.

A energia flui através da estrela, do interior para a atmosfera, e esse fluxo pode ocorrer por meio de três mecanismos: *t*ransferência radiativa, *t*ransporte convectivo e *c*ondução. A eficiência desses processos é determinada, principalmente, pela quantidade de energia a ser carregada pelas partículas do meio, pelo número de partículas existentes e por suas velocidades. Além disso, a opacidade do material ao movimento das partículas que carregam a energia, também afeta a eficiência. No caso de radiação, a opacidade é caracterizada pela seção de choque e pela densidade.

Na atmosfera estelar, contudo, a energia é transportada, principalmente, através de radiação. Para entender os processos que afetam a luz radiada para o espaço, usamos uma *equação de transferência radiativa*, que descreve o transporte de energia ao longo das estrelas. Encontrar uma solução para esta equação constitui um dos grandes problemas em atmosferas estelares, pois nestas regiões o livre caminho médio das partículas é grande e a aproximação de difusão não é válida. A natureza da equação de transferência depende da geometria e do meio através do qual a energia flui. A natureza do meio físico exerce influência sobre detalhes da função fonte, que é a contribuição local dada ao campo de radiação. Em determinados casos, a função fonte pode depender do próprio campo de radiação. Então, a forma da solução deve ser diferente para diferentes condições que possam existir.

Uma aproximação que foi bastante usada no século passado para resolver uma equação de transferência, foi a "atmosfera cinza". Embora esta seja uma situação idealizada, esse tratamento tem a vantagem de se poder obter uma solução completa para o campo de radiação sem recorrer aos detalhes físicos da atmosfera. Nesse modelo, a opacidade é independente da frequência, de modo que a equação de transferência pode ser tratada da mesma forma, qualquer que seja o valor da frequência.

Como esse modelo é uma aproximação de atmosfera cinza é uma representação inexata do que ocorre numa atmosfera estelar, principalmente em estrelas de baixa temperatura efetiva, sua aplicabilidade é limitada. Dentre as transições atômicas que ocorrem nas atmosferas, algumas dependem fortemente da frequência, outras apresentam uma fraca dependência na frequência em uma grande região do espectro. Se estas regiões espectrais correspondem àquelas que contém a maior parte do fluxo radiativo, a atmosfera será muito parecida com uma atmosfera cinza. Um exemplo clássico de fonte de opacidade cinza é o espalhamento de elétrons. O espalhamento Thomson por elétrons livres é, por definição, independente da frequência e, para estrelas cuja temperatura superficial é maior que 25 000 K, esta é a fonte dominante de opacidade ao longo do intervalo de comprimentos de onda que abrange o fluxo máximo de energia.

Porém, na maioria dos casos, o modelo de atmosferas não-cinza não se aplica e devemos considerar a dependência com a frequência de todos os processos físicos importantes neste cenário. Para reproduzir corretamente dados observacionais de estrelas mais frias, tais como anãs marrons e estrelas de baixa massa, e compreender melhor a estrutura e evolução

das mesmas, além do uso de modelos de atmosferas não-cinza, são necessárias outras considerações, tais como ETNL (*Equilíbrio Termodinâmico Não Local*), e utilização de tabelas de opacidade mais completas (Kurucz 1992, 1993).

Em um código de evolução estelar, parâmetros físicos atmosféricos servem de condições de contorno externa para os cálculos do interior. No código `ATON2.3` estes parâmetros são calculados com um modelo de atmosfera cinza. Uma das melhorias apresentadas neste trabalho, é a implementação do cálculo destes parâmetros usando um modelo mais realista de atmosfera não-cinza. Utilizamos os modelos de atmosfera não-cinza desenvolvidos por dois grupos distintos:

1. Grupo Nextgen (NextGen - Allard & Hauschildt 1997 e PMS - Allard et al. 2000). O primeiro abrange os intervalos 3,5<$\log g$<6,0 e 4000 K <$T_{\rm eff}$<10 000 K, enquanto o segundo abrange os intervalos 2,0<$\log g$<3,5 e 2000 K<$T_{\rm eff}$<6800 K. Através de uma junção das duas tabelas no intervalo comum de temperaturas, obtivemos uma tabela retangular nos intervalos 2,0<$\log g$<6,0 e 2000 K<$T_{\rm eff}$<6800 K para metalicidade 0,0 e profundidades óticas τ= 1, 3, 10 e 100.
2. Grupo de Kupka (ATLAS9 - Heiter et al. 2002). Neste caso a convecção é tratada ou com a formulação MLT (Mixing Length Theory) ou com a formulação FST (Full Spectrum of Turbulence) para os mesmo valores de metalicidade e profundidade ótica que o Nextgen porém no intervalo de temperatura de 4000 K<$T_{\rm eff}$<10 000 K e no intervalo de gravidade de 2,0<$\log g$<5,0.

Com esta nova versão do código, foi possível calcular várias trilhas evolutivas de estrelas de baixa massa partindo da pré-sequência principal. Esse conjunto de trilhas foi utilizado para estudar algumas propriedades físicas e rotacionais das estrelas jovens da Nebulosa de Orion (ou Orion Nebula Cluster - ONC) que têm período de rotação, temperatura efetiva e luminosidade determinados. A comparação entre os resultados teóricos e os dados experimentais nos permitiram extrair algumas informações relativas a essa classe de objetos, principalmente no que diz respeito à distribuição de momentum angular inicial. A interpretação dos dados depende das considerações iniciais feitas nos modelos, sendo a eficiência da convecção um dos principais fatores, seguida das condições de contorno utilizadas. Geramos três conjuntos de modelos com diferentes valores de α, parâmetro que determina a eficiência do transporte convectivo na aproximação da teoria do comprimento de mistura. Analisamos as propriedades rotacionais das estrelas da Nebulosa de Orion com esses três conjuntos de modelos e investigamos as diferenças obtidas. As estimativas de massa não variam muito com a escolha de α, sendo que intervalo de massas típico é 0,2-0,4 $M_{\odot}$. A determinação de idades, por sua vez, é mais influenciada pela eficiência da convecção. A análise das propriedades rotacionais das estrelas de ONC começam pela observação de uma bimodalidade da distribuição geral dos períodos com um pico em períodos curtos e um segundo pico em períodos mais longos (Fig. 5.8). Nossa análise confirma que as propriedades rotacionais dessas estrelas estão estreitamente relacionadas com a massa. Verificamos a presença de uma dicotomia nas propriedades rotacionais dos objetos em ONC. Para estrelas com massa abaixo de um certo valor, definido como massa de transição ($M_{\rm tr}$), a distribuição de períodos possui um único pico em torno de 2 dias, enquanto para estrelas cujas massas são maiores que $M_{\rm tr}$ a distribuição apresenta também um pico secundário em torno de 8 dias (ver Fig. 5.9 que mostra a dicotomia na distribuição de períodos para os três conjuntos de modelos). Supondo que um mecanismo de "disk-locking" é o responsável pelo segundo pico na distribuição geral,

podemos dar três interpretações ao fenômeno: 1) estrelas com $M<M_{tr}$ perderam o disco mais jovens, 2) seu "locking-period" é menor, ou 3) o período no qual elas permanecem ligadas ao disco é o mesmo, independentemente da massa, mas estrelas com massa $>M_{tr}$ evoluem mais rápido e passam a maior parte de suas fases pré-sequência principal ligadas aos seus discos. A massa de transição depende fortemente das considerações físicas feitas nos modelos. Para os modelos com atmosferas cinza $M_{tr}\sim0{,}25M_{\odot}$. Para modelos com alta eficiência convectiva $M_{tr}\sim0{,}35M_{\odot}$ e para aqueles com baixa eficiência convectiva $M_{tr}\sim0{,}5M_{\odot}$ (estes valores estão listados na Tabela 5.2). Partindo da hipótese de que as estrelas perdem o disco quando os seus períodos de rotação são 8 dias, definimos três classes de estrelas em ONC: 1) estrelas que evoluiram praticamente sem disco; 2) estrelas que ainda estão circundadas pelos seus discos e 3) estrelas que rodam moderadamente. A evolução das estrelas que, segundo nosso critério, evoluiram sem disco, é consistente com a aproximação de evolução com momentum angular constante. Uma comparação entre o período de rotação previsto pelos modelos e os valores observados sugere que o momentum angular inicial seja pelo menos três vezes o valor estimado por Kawaler (1987) para estrelas no intervalo $0{,}2M_{\odot}\leq M\leq0{,}4M_{\odot}$. Encontramos indicações de que a convecção na pré-sequência principal pode ser afetada por outros parâmetros. Embora simulações 2D prevêm convecção eficiente (HCE) nesta fase evolutiva, encontramos dois resultados em favor da convecção pouco eficiente (LCE): a exaustão de lítio prevista por modelos HCE é muito alta e não está de acordo com os valores observados em aglomerados abertos jovens; 2) a distribuição de idades produzida por modelos HCE para dois grupos de objetos (de massas maiores e menores que M_{tr}) é muito diferente.

Não encontramos nenhuma correlação entre as emissões de raios-X e os períodos das estrelas em ONC, sugerindo que estas estrelas ainda estão no regime de super-saturação da relação entre rotação e luminosidade em raios-X. A idéia de que a dicotomia na distribuição de períodos possa ser explicada por diferentes morfologias dos campos magnéticos estelares, sugerida por Barnes (2003), aparentemente não deve ser aplicada às estrelas ONC, uma vez que quase todos os objetos são completamente convectivos, de acordo com nossa análise evolutiva e, no entanto, possuem períodos diversos. Contudo, tal hipótese não deve ser totalmente descartada, pois há mecanismos como, por exemplo, a presença de campos magnéticos, que podem modificar os critérios de estabilidade, inibindo a convecção, e assim favorecer o aparecimento de um caroço radiativo precocemente.

7.6 Conclusões

Os resultados do presente trabalho contribuiram para aumentar a capacidade do código de estrutura e evolução estelar `ATON` em reproduzir dados observacionais. Mas apesar dos esforços que vêm sendo feitos neste sentido, algumas discrepâncias ainda permanecem em aberto e serão tratadas em um futuro próximo.

A primeira modificação que fizemos no código `ATON` foi a implementação de um mecanismo que nos permite começar a execução de um determinado modelo em um ponto intermediário da evolução, desde que os passos iniciais tenham sido devidamente registrados em execuções anteriores (Capítulo 2). Este mecanismo é chamado de *checkpoint* e sua principal utilidade é economizar tempo computacional durante a fase de implementação e teste de futuras modificações no programa. As vantagens da nova versão do código com o checkpoint foram utilizadas nas demais implementações descritas neste trabalho.

A estrutura interna de uma estrela e sua configuração de equilíbrio foram discutidas no Capítulo (3). As constantes de estrutura interna são parâmetros importantes em astrofísica estelar e são usados para prever a taxa de movimento apsidal em sistemas binários. Elas nos dão informações sobre o grau de concentração de materia de uma estrela. Seus cálculos foram introduzidos no código `ATON` através da Eq. (3.17), sendo que os valores de η_j (j=2, 3, 4) foram previamente obtidos integrando-se numericamente a equação de Radau (Eq. 3.16). Apesar dos primeiros modelos (modelos padrão) considerarem que as estrelas fossem esferas gasosas, sabe-se que efeitos como rotação e forças de maré distorcem estas estruturas, afastando-as das formas esfericamente simétricas. Neste trabalho, introduzimos estes efeitos no código `ATON` e investigamos suas influências na estrutura interna da estrela. Para tal, utilizamos o método de KT70 no qual as superfícies esfericamente simétricas são substituídas por superfícies equipotenciais não-simétricas adequadas, caracterizadas pelo potencial total ψ (Eq. 3.72). Ao invés de usar um potencial de Roche, como no método de KT70, preferimos utilizar uma expressão mais refinada para a função potencial no qual incluimos os termos relativos aos potenciais perturbativos e às componentes não-simétricas do potencial gravitacional devido às distorções da figura da estrela. Seguindo esta aproximação obtivemos os fatores de correção para as equações constitutivas (Eqs. 3.31) para obter a configuração estrutural de uma estrela distorcida por rotação e por forças de maré. Uma vez que a forma da estrela é alterada por estes potenciais perturbativos, o momentum de inércia de uma estrela distorcida também muda, deduzimos, então, uma nova expressão para esta grandeza levando em conta estes efeitos.

Usando modelos padrão e distorcidos, obtivemos quatro conjuntos de trilhas evolutivas que vão de 0,09$M_\odot$ a 3,8$M_\odot$. Os efeitos devido à rotação são quantitativamente mais importantes que os devido às forças de maré. Para cada trilha calculamos os valores das constantes de estrutura interna (k_2, k_3 e k_4) e dos raios de giração ao longo da evolução na pré-sequência principal. Nossos valores de k_j foram comparados com os calculados por outros autores. Nossos valores obtidos com modelos padrão são menores que aqueles obtidos por Claret & Giménez (1992), sendo que os valores obtidos com nossos modelos distorcidos são ainda menores. Gostaríamos de ressaltar que os valores teóricos de k_j publicados até então apresentam-se acima dos valores observados.

Para testar nossos modelos distorcidos, utilizamos o sistema binário eclipsante EK Cep cuja secundária é um estrela na pré-sequência principal. Usando trilhas evolutivas para as massas determinadas dinamicamente, com (X, Z)=(0,67, 0,012) e α=1,5, conseguimos reproduzir as dimensões absolutas do sistema (exceto os valores individuais das T_{eff}) em uma mesma isócrona ($17,2 \pm 0.4$ milhões de anos), assim como a taxa de movimento apsidal e a abundância de lítio.

Como era de nosso interesse investigar a evolução de estrelas de baixa massa na pré-sequência principal, foi fundamental modificar as condições de contorno do código `ATON` de atmosferas cinza para não-cinza. Para tal, utilizamos dois modelos de atmosferas não-cinza: o do grupo NextGen (Allard & Hauschildt 1997, Allard et al. 2000) e o do grupo ATLAS9 (Heiter et al. 2002). O primeiro trata a convecção com a teoria do comprimento de mistura (do inglês, Mixing Length Theory - MLT) e usam α=1,0. Utilizamos os modelos chamados NextGen; que cobre o intervalo de 4000 K a 10 000 K, gravidade; e o PMS que vai de 2000 k a 6800 k e em temperatura, e 3,5$\leq\log g\leq$6,0 em logarítmo da gravidade; e o PMS que vai de 2000 K a 6800 K e 2,0$\leq\log g\leq$3,5. Ambos para a metalicidade solar e profundidades óticas τ=1, 3, 10, 100. O segundo grupo trata a convecção tanto com o

MLT quanto com a teoria do espectro completo de turbulência (do inglês, Full Spectrum of Turbulence - FST) para os mesmos valores de metalicidades e profundidades óticas que o NextGen, porém no intervalo de temperatura de $4000\,\mathrm{K} \leq T_{\mathrm{eff}} \leq 10\,000\,\mathrm{K}$ e no intervalo de gravidade de $2{,}0 \leq \log g \leq 5{,}0$.

Com a nova versão do código, foi possível calcular várias trilhas evolutivas de estrelas de baixa massa partindo da pré-sequência principal. Este conjunto de trilhas foi utilizado para estudar algumas propriedades físicas e rotacionais das estrelas jovens da nebulosa de Orion que têm período de rotação, temperatura efetiva e luminosidade determinados. A comparação entre os resultados teóricos e os dados experimentais nos permitiram extrair algumas informações relativas a esta classe de objetos, principalmente no que diz respeito à distribuição de momentum angular inicial.

A interpretação dos dados depende das considerações iniciais feitas nos modelos, sendo a eficiência da convecção um dos principais fatores.

7.7 Trabalhos futuros

As melhorias físicas que ainda não estão devidamente implementadas no código de estrutura e evolução estelar `ATON` e que são de nosso imediato interesse, estão estreitamente relacionadas com a rotação e redistribuição de momentum angular.

O tratamento padrão de redistribuição de momentum angular (Zahn 1992) não é adequado para descrever fases evolutivas nas quais a principal contribuição energética não seja a energia nuclear, como é o caso da fase pré-sequência principal. Tratamentos alternativos foram analisados e, em breve, serão implementados no código com o objetivo de se obter uma expressão mais adequada para a corrente de circulação meridiana. Uma outra melhoria importante é a inclusão do coeficiente de difusão dos componentes químicos, devido à rotação, no processo de difusão microscópica. Pretendemos também incluir um tratamento dos efeitos de um gradiente de peso molecular nas correntes circulatórias internas. Ao contrário da inclusão de campos magnéticos, os aperfeiçoamentos citados acima não apresentam grandes dificuldades. Acredita-se que considerar de maneira adequada a interação entre rotação e campos magnéticos nos modelos de estrutura e evolução estelar representará um grande progresso para melhorar comparações entre teoria e observações.

References

Alexander, D.R., Ferguson, J.W., 1994, ApJ 437, 879.
Allard, F., & Hauschildt, P.H., 1997, Nextgen, see `http://dilbert.physat.uga.edu/~yeti/mdwarfs.html` (AH).
Allard, F., Hauschildt, P.H., Alexander, D.R., Starrfield, S., 1997, ARA&A 35, 137.
Allard, F., Hauschildt, P.H., Schweitzer, A., 2000, ApJ 539, 366 (AHS).
Asplund, M., Ludwig, H.-G., Nordlund, Å., Stein, R.F., 2000, A&A 359, 669.
Attridge, J.M., Herbst, W., 1992, ApJ 398, 61.
Baraffe, I., Chabrier, G., Allard, F., Hauschildt, P.H., 1998, A&A 337, 403.
Baraffe, I., Allard, F., 1997, arXiv:astro-ph/9705077 v1.
Baraffe, I., Chabrier, G., Allard, F., Hauschildt, P.H., 2002, A&A 382, 563.
Barnes, S.A., 2003, ApJ 586, 464.
Basri, G., Bertout, C., 1989, ApJ 341, 340.
Batten, A.H., 1973, in *Binary and Multiple Systems of Stars*, Pergamon Press, Oxford.
Bodenheimer, P., 1965, ApJ 144, 709.
Böhm-Vitense, E., 1958, Z. Astroph. 46, 108.
Bouvier, J., Cabrit, S., Fernandez, M., Martín, E.L., Matthews, J.M., 1993, A&A 272, 176.
Bouvier, J., Forestini, M., Allain, S., 1997, A&A 326, 1023.
Brooker, R.A., Olle, T.W., 1955, MNRAS,115, 101.
Burrows A., Hubbard W.B., Saumon W., Lunine J.I., 1993, ApJ 406, 158.
Canuto, V.M., Mazzitelli, I., 1991, ApJ 370, 295.
Canuto, V.M., Mazzitelli, I., 1992, ApJ 389, 724.
Canuto, V.M., Goldman, I., Mazzitelli, I., 1996, ApJ 473, 550.
Canuto, V.M., Christensen-Dalsgaard, J., 1998, Ann. Rev. Fluid Mech. 30, 167.
Carson, T.R., 1976, ARA&A 14, 95.
Caughlan, G.R. Fowler, W.A., 1988, Atomic Data Nucl. Tab. 40, 283.
Chabrier, G., Baraffe, I., 1997, A&A 327, 1039.
Chandrasekhar, S., 1933, MNRAS 93, 390.
Chandrasekhar, S., 1939, in *An introduction to the study of stellar structure*, University of Chicao Press.
Chaboyer, B., Zahn, J.-P., 1992, A&A 253, 173.
Chaboyer, B., Demarque, P., Pinsonneault, M.H., 1995, ApJ 441, 865.
Choi, P.I., Herbst, W., 1996, AJ 111, 283.
Claret, A., Giménez, A., 1989a, A&AS 81, 1.
Claret, A., Giménez, A., 1989b, A&AS 81, 37.
Claret, A., Giménez, A., 1991, A&AS 87, 507.
Claret, A., Giménez, A., 1992, A&AS 96, 255.
Claret, A., Giménez, A., 1993, A&A 277, 487.
Claret, A., Gimenez, A., Martín, E. L., 1995, A&A 302, 741.

Claret, A., Giménez, A., 2001, LNP 563, 1.
Claret, A., Willems, B., 2002, A&A 388, 518.
Claret, A., 2006, A&A 445, 1061.
Clayton, D.B., 1968, in *Principles of stellar evolution and nucleosynthesis*, McGraw-Hill, New York.
Cox, A.N., Stewart, J.N., 1969, Nautshnij Informatsij 15, 1.
Cox, A.N., Stewart, J.N., 1970, ApJS 19, 243.
Cowling, T.G., 1938, MNRAS 98, 734.
D'Antona, F., Mazzitelli, I., 1984, A&A 138, 431.
D'Antona, F., 1993, Inside the stars, Proceedings of the 137th IAU Colloquium, eds. A. Baglin & W. Weiss, ASP Conf. Ser. 40, 395, San Francisco.
D'Antona, F., 2000, Star formation from the small to the large scale, ESLAB Symp. (33: 1999: Noordwijk, The Netherlands), eds. F. Favata, A. Kaas & A. Wilson, ESA SP 445, 161.
D'Antona, F.,Ventura, P., Mazzitelli, I., 2000, ApJ 543, 77.
D'Antona, F., Mazzitelli, I., 1994, ApJS 90, 467.
D'Antona, F., Mazzitelli, I., 1997, MmSAI 68, 807.
D'Antona, F., Montalbán, J., 2003, A&A 412, 213.
Durney, B.R., De Young, D.S., Roxburgh, I.W., 1993, Sol. Phys. 145, 207.
Ebbighausen, E.G., 1966a, AJ 71, 642.
Ebbighausen, E.G., 1966b, AJ 71, 730.
Eggenberger, P., Maeder, A., Meynet, G., 2005, A&A 440, 9.
Endal, A. S., Sofia, S., 1976, ApJ 210, 184.
Faulkner, J., Roxburgh, I.W., Strittmatter, P.A., 1968, ApJ 151, 203.
Feigelson, E.D., Gaffney, J.A., Garmire, G., Hillenbrand, L.A., Townsley, L., 2003, ApJ 584, 911.
Flaccomio, E., Damiani, F., Micela, G., Sciortino, S., Harnden, JR., F.R., Murray, S.S., Wolk, S.J., 2003a, ApJ 582, 382.
Flaccomio, E., Damiani, F., Micela, G., Sciortino, S., Harnden, JR., F.R., Murray, S.S., Wolk, S.J., 2003b, ApJ 582, 398.
Flaccomio, E., Micela, G., Sciortino, S., 2003c, A&A 402, 277.
Fuhrmann, K., Axer, M., Gehren, T., 1993, A&A 271, 451.
Garcia Lopez, R.J., Rebolo, R., Martín, E.,L., 1994, A&A 282, 518.
Giménez, A., 1985, ApJ 297, 405.
Giménez, A., Margrave, T.E., 1985, AJ 90, 358.
Goulpil, M.J., Schatzman, E.L., Zahn, J.-P. (eds.), 1989, Proceedings of Rotation and Mixing in Stellar Interior Conference, Spring-Verlag.
Gough, D.O., Tayler, R.J., 1966, MNRAS 133, 85.
Hadjidemetriou, J., 1967, Adv. Astr. Astrophys. 5, 131.
Hartmann, L., MacGregor, K.B., 1982, AJ 259, 180.
Hartmann, L., Cassen, P., & Kenyon, S.J., 1997, ApJ 475, 770.
Hauschildt, P.H., Allard, F., Baron, E., 1999, ApJ 512, 377.
Hayashi, C., 1961, PASJ 13, 450.
Heiter, U., Kupka, F., van't Veer-Menneret, C., Barban, C., Weiss, W.W., Goupil, M.-J., Schmidt, W., Katz, D., Garrido, R., 2002, A&A 392, 619.
Hejlesen, P.M., 1987, A&AS 69, 251.
Henyey, L.G., Lelevier, R., Levee, R.D., 1955, PASP 67, 154.
Henyey, L.C., Forbes, J.E., Gould, N.L., 1964, ApJ 139, 306.

Herbst, W., Bailer-Jones, C.A.L., Mundt, R., Meisenheimer, K., Wackermann, R., 2002, A&A 396, 513.
Hill, G., Ebbighausen, E.G., 1984, AJ 89, 1256.
Hillenbrand, L.A., 1997, AJ 113, 1733.
Hillenbrand, L.A., Strom, S.E., Calvet, N., Merril, K.M., Gatley, I., Makidon, R.B., Meyer, M.R., Skrutskie, M.F., 1998, AJ 116, 1816.
Iben, I., 1965, ApJ 141, 993.
Iglesias, C.A., Rogers, F.J., 1993, ApJ 412, 752.
Jeffery, C.M., 1984, MNRAS 207, 323.
Kawaler, S.D., 1987, PASP 99, 1322.
Keller, G., Meyerott, R.E., 1955, ApJ 122, 32.
Khaliullin, Kh.F., 1983a, AZh. 60, 72.
Khaliullin, Kh.F., 1983b, Sov. Astron. 27, 43.
Kim, Y.C., Demarque, P.S., 1996, ApJ 457, 340.
Kippenhahn, R., Thomas, H.C., 1970, in *Stellar Rotation*, Sletteback, A. & Reidel, D., eds.
Königl, A., 1991, ApJ 370, L39.
Kopal, Z., 1959, in *Close Binary Systems*, (New York: Wiley).
Kopal, Z., 1972, Adv. Astron. Astrophys. 9, 1.
Kopal, Z., 1974, Astrophys. Space Sci. 27, 389.
Kopal, Z., 1978, in *Dynamics of Close Binary Systems*, Reidel, Dordreccht.
Kopal, Z., 1989, in *The Roche Problem*, Kluwer Academic Publishers, Dordrecht.
Krishna Swamy, K.S., 1966, ApJ 145, 174.
Küker, M., Rüdiger, G., 1999, A&A 346, 922.
Kurucz, R.L., 1992, RMxAA 23, 181.
Kurucz, R.L., 1993, ASP Conf. Ser. 44, 87.
Kushawa, R.S., 1957, ApJ 125, 242.
Landin, N.R., Mendes, L.T.S., Vaz, L.P.R., 2005, AIPC 784, 607.
Landin, N.R., Ventura, P., D'Antona, F., Mendes, L.T.S., Vaz, L.P.R., 2006, A&A 456, 269.
Landin, N.R., Ventura, P., D'Antona, F., Mendes, L.T.S., Vaz, L.P.R., 2007, in preparation.
Langer, G.E., Hoffman, R., Sneden, C., 1993, PASP 105, 301.
Larson, R.B., 2003, Rep. Prog. Phys. 66, 1651.
Law W.-Y., 1980, Ph.D. Thesis, Yale Universty.
Levi-Civita, T., 1937, Amer. J Math. 59, 225.
Li, L.H., Ventura, P., Basu, S., Sofia, S., Demarque, P., 2006, ApJS 164, 215.
Linsky, J.L., 1998, Space Sci. Rev. 84, 285.
Ludwig, H., Freytag, B., Steffen, M., 1999, A&A 346, 111.
Ludwig, H.-G., Allard, F., Hauschildt, P.-H., 2002, A&A 395, 99.
Lydon, T.J. Sofia, S., 1995, ApJSS 101, 357.
Maeder, A., Meynet, G., 2003, A&A 411, 543.
Maeder, A., Meynet, G., 2004, A&A 422, 225.
Maeder, A., Meynet, G., 2005, A&A 440, 1041.
Maeder, A., Zahn, J.-P., 1998, A&A 334, 1000.
Marques, J.P., Fernandes, J., Monteiro, M.J.P.F.G., 2004, A&A 422, 239.
Martín, E.L., Claret, A., 1996, A&A 306, 408.
Martín, E.L., Rebolo, R., 1993, A&A 274, 274.
Martynov, D.YA., 1948, Izv. Engelhardt Obs. No. 25

Martynov, D.Ya., 1973, in Eclipsing Variable Stars, V.P. Tsesevich (ed.), IPST Astrophys. Library, Jerusalem, p. 291
Mazzitelli, I., 1989, ApJ 340, 249.
Mazzitelli, I., D'Antona, F., Caloi, V., 1995, A&A 302, 382.
Mendes, L.T.S., D'Antona, F., Mazzitelli, I., 1999a, A&A 341, 174.
Mendes, L.T.S., 1999b, Ph.D. Thesis, Federal University of Minas Gerais.
Mendes, L.T.S., Vaz, L.P.R., D'Antona, F., Mazzitelli, I., 2003, Open Issues in Local Star Formation and Early Stellar Evolution, edited by J. Lépine, and J. Gregorio-Hetem, Astrophysics and Space Science Library 299, Kluwer Academic Publishers, Dordrecht, The Netherlands.
Mestel, L., 1953, MNRAS 113, 716.
Mestel, L., 1999, *Stellar Magnetism*, Oxford, Claredndon.
Mihalas, D., Dappen, W., Hummer, D.G., 1988, ApJ 331, 815.
Mihalas, D., 2001, Publ. Astron. Soc. Aust. 18, 311.
Mohan, C., Saxena, R. M., Agarwal, S. R., 1990, Ap&SS 163, 23.
Mohanty, S., Basri, G., 2003, AJ 583, 451.
Mohanty, S., Jayawardhana, R., Basri, G., 2005, ApJ 626, 498.
Montalbán, J., D'Antona, F., Mazzitelli, I., 2000, A&A 360, 935.
Montalbán, J., Kupka, F., D'Antona, F., Schmidt, W., 2001, A&A 370, 982.
Montalbán, J., D'Antona, F., 2006, MNRAS in press.
Montalbán, J., D'Antona, F., Kupka, F., Heiter, U., 2004, A&A 416, 1081.
Montesinos, B., Thomas, J.H., Ventura, P., Mazzitelli, I., 2001, MNRAS 326, 877.
Morel, P., van't Veer-Menneret, C., Provost, J., Berthomieu, G., Castelli, F., Cayrel, R., Goupil, M.J., Lebreton, Y., 1994, A&A 286, 91.
Moss, D.L., 1968, MNRAS 141, 165.
Motz, L., 1952, AJ 115, 562.
Noyes, R.W., Hartmann, S.,W., Baliunas, S., Duncan, D.K., Vaughan A., 1984, ApJ 279, 763.
Ossendrijver, M., 2003, A&A 11, 287.
Palla, F., Stahler, W.S., 1990, ApJ 360, L47.
Palla, F., Stahler, W.S., 1993, ApJ 418, 414.
Palla, F., Stahler, W.S., 1999, ApJ 525, 772.
Papaloizou, J.C.B., Wheelan, J.A.J., 1972, MNRAS 164, 1.
Petrova, A.V., Orlov, V.V., 1999, AJ 117, 587.
Pinsonneault, M.H., 1988, Ph.D. Thesis, Yale University.
Popper, D.M., 1987, ApJ 313, 81.
Press, W.H., Teukolsky, S.A., Vetterling, W.T., Flannery, B.P., 1992, Numerical Recipes in Fortran 77: The art of Scientific Computing, Cambridge University Press.
Rogers, F.J., Iglesias, C.A., 1993, ApJ 412, 572.
Rogers, F.J., Swenson, F.J., Iglesias, C.A. , 1996, ApJ 456, 902.
Ruciński, S.M., 1969, Acta Astron. 19, 125.
Ruciński, S.M., 1988, AJ 95, 1895.
Russell, H.N., 1928, MNRAS 88, 642.
Sahade, J., Wood, F.B., 1978, in *Interacting Binary Stars*, Pergamom Press, Oxford.
Sackmann, I.J., Anand, S.P.S., 1969, ApJ 155, 257.
Sackmann, I.J., 1970, A&A 8, 76.
Schwarzschild, M., 1958, in *Structure and Evolution of the Stars*, Princeton Univ. Press.
Siess, L., Livio, M., 1997, ApJ 490, 785.
Skumanich, A., 1972, ApJ 171, 565.

Soderblom, D.R., Jones, B.F., Balachandran, S., Stauffer, J.R., Duncan, D.K., Fedele, S.B., Hudon, J.D., 1993, AJ 106, 1059.
Spruit, H.C., 1999, A&A 349, 189.
Spruit, H.C., 2002, A&A 381, 923.
Stahler, S.W. 1988, ApJ 332, 804.
Stassun, K.G., Mathieu, R.D., Mazeh, T., Vrba, F.J., 1999, AJ 117, 2941.
Stassun, K.G., Ardila, D.R., Basri, G., Mathieu, R.D., 2004, AJ 127, 3537.
Sterne, T.E., 1939, MNRAS 99, 662.
Stothers, R.B., Chin, C., 1995, ApJ 440, 297.
Stothers, R.B., Chin, C., 1997, ApJ 478, L103.
Strohmeier, W., 1959, *kleine Veröff. Bamberg*, No. 27.
Strom, K.M., Strom, S.E., Edwards, S., Cabrit, S., Skrutskie, M.F., 1989, AJ 97, 1451.
Swenson, F.J., Faulkner, J., Rogers, F.J., Iglesias, C.A., 1994, ApJ 425, 286.
Tomkin, J., 1983, ApJ 271, 717.
Tout, C.A., Livio, M., Bonnell, I.A., 1999, MNRAS 310, 360.
Trampedach, R., Stein, R.F., Christensen-Dalsgaard, J., Nordlund, Å. 1999, Theory and tests of convection in stellar structure, ASP Conf. Ser. 173, 233.
Ureche, V., 1976, IAU Symp. No. 73, P. Eggleton ed., Reidel, Dordrecht.
Ventura, P., Zeppieri, A., Mazzitelli, I., D'Antona, F., 1998, A&A 334, 953.
Ventura, P., Zeppieri, A., Mazzitelli, I., D'Antona, F., 1998, A&A 331, 1011.
Yildiz, M., 2003, A&A 409, 689.
Walter, F.M., 1987, PASP 99, 31.
Weiss, N.O., Tobias, S.M., 2000, Sp. Sci. Rev. 94, 99.
Willems, B., Claret, A., 2003, A&A 410, 289.
Zahn, J.-P., 1966, AnAp. 29, 489.
Zahn, J.-P., 1975, A&A 41, 329.
Zahn, J.-P., 1977, A&A 57, 383.
Zahn, J.-P., 1989, A&A 220, 112.
Zahn, J.-P., 1992, A&A 265, 115.
Zahn, J.-P., 1993, SSRv. 66, 285.

Appendix A

Pre-main sequence stellar evolutionary models including internal structure constants

A.1 Standard models: single non-rotating stars

Pre-main sequence evolutionary tracks for standard stellar models are given in Tables (A.1) to (A.23). In the first column we have the logarithm of the stellar age (years); in the second column, the logarithm of the stellar luminosity in solar units; in column 3, the logarithm of the effective temperature (K), in column 4, the logarithm of the surface gravity (cgs); in columns 5, 6 and 7 we have the logarithm of the internal structure constants, k_2, k_3, k_4, respectively, and in column 8, we have the radius of gyration (in cgs units).

Table A.1: Evolutionary tracks including internal structure constants and gyration radii for 0.09 $M_\odot$ pre-MS standard models.

$\log(age)$	$\log(L/L_\odot)$	$\log(T_{\rm eff})$	$\log(g)$	$\log(k_2)$	$\log(k_3)$	$\log(k_4)$	β
3.8975	−0.72054	3.43826	2.81834	−1.05419	−1.57227	−1.93262	0.3918
5.2168	−0.94463	3.45269	3.10013	−0.96727	−1.47484	−1.82306	0.4051
5.7548	−1.15876	3.46350	3.35752	−0.91599	−1.40712	−1.74467	0.4146
6.3383	−1.31886	3.47042	3.54529	−0.89493	−1.37683	−1.70722	0.4191
6.4894	−1.49207	3.47693	3.74455	−0.87044	−1.34557	−1.67017	0.4238
6.7322	−1.71254	3.48382	3.99255	−0.83501	−1.30164	−1.61990	0.4305
7.0035	−1.93346	3.48925	4.23521	−0.82363	−1.28082	−1.59190	0.4332
7.3027	−2.15378	3.49265	4.46910	−0.81148	−1.26373	−1.56957	0.4359
7.6111	−2.37449	3.49454	4.69739	−0.80184	−1.24923	−1.55098	0.4379
7.9326	−2.59468	3.49471	4.91826	−0.78227	−1.22461	−1.52208	0.4419
8.2629	−2.81499	3.49055	5.12193	−0.74665	−1.18100	−1.47263	0.4490
8.5898	−3.03567	3.47696	5.28825	−0.71316	−1.13843	−1.42332	0.4560
8.9385	−3.25318	3.44844	5.39168	−0.69740	−1.11728	−1.39782	0.4594
11.2704	−3.21730	3.45865	5.39666	−0.69960	−1.12021	−1.40137	0.4589
11.7531	−2.98374	3.48821	5.28134	−0.72865	−1.15847	−1.44660	0.4527
12.1085	−2.81560	3.49265	5.13093	−0.76687	−1.20652	−1.50128	0.4450
12.3390	−2.79858	3.48892	5.09899	−0.77489	−1.21847	−1.51656	0.4432
12.4711	−2.76350	3.49578	5.09136	−0.77239	−1.21820	−1.51927	0.4433
12.5568	−2.75716	3.50634	5.12725	−0.75746	−1.20018	−1.50002	0.4463
12.5829	−2.69789	3.53991	5.20229	−0.87381	−1.32860	−1.64038	0.4209

Table A.2: Evolutionary tracks including internal structure constants and gyration radii for 0.10 $M_\odot$ pre-MS standard models.

$\log(age)$	$\log(L/L_\odot)$	$\log(T_{\rm eff})$	$\log(g)$	$\log(k_2)$	$\log(k_3)$	$\log(k_4)$	β
3.8575	−0.62893	3.44022	2.78030	−1.05154	−1.57208	−1.93555	0.3920
5.1759	−0.85335	3.45476	3.06288	−0.97001	−1.47972	−1.83044	0.4045
5.7077	−1.06871	3.46592	3.32289	−0.91370	−1.40668	−1.74608	0.4148
6.3023	−1.23048	3.47267	3.51166	−0.89094	−1.37356	−1.70506	0.4196
6.4509	−1.40085	3.47888	3.70686	−0.86860	−1.34397	−1.66916	0.4241
6.6946	−1.62125	3.48578	3.95485	−0.83541	−1.30278	−1.62165	0.4304
6.9700	−1.84191	3.49162	4.19889	−0.82129	−1.27936	−1.59133	0.4335
7.2707	−2.06234	3.49563	4.43535	−0.81130	−1.26410	−1.57061	0.4359
7.5804	−2.28302	3.49795	4.66532	−0.80333	−1.25179	−1.55439	0.4376
7.9011	−2.50325	3.49884	4.88909	−0.79011	−1.23458	−1.53357	0.4404
8.2439	−2.72267	3.49704	5.10133	−0.76132	−1.19940	−1.49362	0.4461
8.6710	−2.93809	3.48887	5.28407	−0.72497	−1.15385	−1.44144	0.4535
11.2833	−2.91551	3.49267	5.27671	−0.73326	−1.16452	−1.45378	0.4518
11.8838	−2.73697	3.49633	5.11278	−0.77078	−1.21171	−1.50754	0.4442
12.1732	−2.71669	3.49373	5.08210	−0.77451	−1.21751	−1.51509	0.4433
12.3297	−2.69845	3.49466	5.06759	−0.77258	−1.21746	−1.51748	0.4434
12.4313	−2.65587	3.50867	5.08105	−0.76527	−1.21008	−1.51123	0.4447
12.4937	−2.59476	3.54102	5.14934	−0.80038	−1.25804	−1.56999	0.4394
12.5060	−2.49315	3.57848	5.19758	−0.94586	−1.39598	−1.70564	0.4065
12.5159	−2.33028	3.62634	5.22612	−1.33562	−1.78816	−2.09397	0.3522

Table A.3: Evolutionary tracks including internal structure constants and gyration radii for 0.20 $M_\odot$ pre-MS standard models.

$\log(age)$	$\log(L/L_\odot)$	$\log(T_{\rm eff})$	$\log(g)$	$\log(k_2)$	$\log(k_3)$	$\log(k_4)$	β
2.9189	0.40800	3.51232	2.33279	−0.99952	−1.52206	−1.89451	0.4001
4.2656	0.18688	3.51468	2.56336	−0.95963	−1.47976	−1.84761	0.4071
4.7416	−0.03374	3.51546	2.78709	−0.92959	−1.43963	−1.79843	0.4127
5.1196	−0.25419	3.51484	3.00507	−0.90267	−1.40416	−1.75567	0.4178
5.5936	−0.46423	3.51332	3.20903	−0.87653	−1.36953	−1.71426	0.4228
6.0245	−0.64031	3.51191	3.37946	−0.85513	−1.34036	−1.67885	0.4271
6.1864	−0.82576	3.51153	3.56340	−0.83436	−1.31128	−1.64277	0.4314
6.4321	−1.04619	3.51230	3.78693	−0.81464	−1.28297	−1.60669	0.4356
6.7176	−1.26653	3.51301	4.01010	−0.79848	−1.26022	−1.57801	0.4389
7.0334	−1.48652	3.51533	4.23939	−0.78727	−1.24362	−1.55663	0.4415
7.3642	−1.70697	3.51891	4.47416	−0.78015	−1.23251	−1.54160	0.4431
7.6995	−1.92728	3.52257	4.70909	−0.77516	−1.22491	−1.53123	0.4442
8.0548	−2.14553	3.52497	4.93695	−0.77213	−1.22019	−1.52478	0.4449
10.6049	−2.20964	3.52381	4.99639	−0.76952	−1.21682	−1.52076	0.4454
11.2889	−2.19614	3.52114	4.97225	−0.76638	−1.21293	−1.51643	0.4460
11.5373	−2.19642	3.51948	4.96586	−0.76329	−1.20909	−1.51212	0.4467
11.6901	−2.19517	3.51849	4.96068	−0.76032	−1.20539	−1.50798	0.4473
11.7997	−2.19209	3.51826	4.95667	−0.75750	−1.20185	−1.50401	0.4478
11.8843	−2.18481	3.51951	4.95438	−0.75513	−1.19889	−1.50073	0.4483
11.9526	−2.16195	3.52577	4.95657	−0.75394	−1.19753	−1.49945	0.4485

Table A.4: Evolutionary tracks including internal structure constants and gyration radii for 0.30 $M_\odot$ pre-MS standard models.

$\log(age)$	$\log(L/L_\odot)$	$\log(T_{\rm eff})$	$\log(g)$	$\log(k_2)$	$\log(k_3)$	$\log(k_4)$	β
2.9991	0.69806	3.55037	2.37105	−0.92937	−1.43049	−1.78528	0.4132
4.2756	0.47190	3.55457	2.61402	−0.88880	−1.38685	−1.73730	0.4204
4.7492	0.25146	3.55701	2.84419	−0.86353	−1.35199	−1.69397	0.4255
5.1481	0.03284	3.55806	3.06701	−0.84502	−1.32647	−1.66235	0.4292
5.7330	−0.14681	3.55802	3.24650	−0.83137	−1.30774	−1.63930	0.4320
5.8791	−0.31062	3.55696	3.40608	−0.81858	−1.29039	−1.61809	0.4346
6.0987	−0.53153	3.55397	3.61503	−0.80269	−1.26801	−1.59021	0.4380
6.3586	−0.75208	3.55010	3.82012	−0.78882	−1.24805	−1.56472	0.4409
6.6461	−0.97263	3.54588	4.02377	−0.77757	−1.23171	−1.54361	0.4434
6.9519	−1.19317	3.54162	4.22725	−0.76801	−1.21817	−1.52639	0.4454
7.2770	−1.41329	3.53958	4.43922	−0.76122	−1.20808	−1.51324	0.4470
7.6188	−1.63322	3.54062	4.66331	−0.76389	−1.20787	−1.51045	0.4480
8.0003	−1.85032	3.54347	4.89182	−0.78378	−1.22948	−1.53191	0.4485
10.3679	−1.88151	3.54326	4.92219	−0.74905	−1.19119	−1.49183	0.4489
10.9213	−1.87781	3.54255	4.91562	−0.74788	−1.18965	−1.49000	0.4492
11.1540	−1.87596	3.54233	4.91291	−0.74677	−1.18815	−1.48823	0.4494
11.3025	−1.87290	3.54253	4.91066	−0.74571	−1.18673	−1.48654	0.4496
11.4112	−1.86848	3.54320	4.90892	−0.74471	−1.18536	−1.48491	0.4498
11.4867	−1.85531	3.54623	4.90785	−0.79020	−1.24571	−1.55522	0.4450
11.5271	−1.82566	3.55019	4.89405	−0.81608	−1.27188	−1.58272	0.4374

Table A.5: Evolutionary tracks including internal structure constants and gyration radii for 0.40 $M_\odot$ pre-MS standard models.

$\log(age)$	$\log(L/L_\odot)$	$\log(T_{\rm eff})$	$\log(g)$	$\log(k_2)$	$\log(k_3)$	$\log(k_4)$	β
2.7435	1.04905	3.56580	2.20670	−0.93246	−1.43378	−1.78820	0.4126
4.0392	0.82515	3.57384	2.46278	−0.88178	−1.37749	−1.72626	0.4218
4.5169	0.60466	3.57905	2.70410	−0.84858	−1.33171	−1.66959	0.4284
4.9045	0.38472	3.58224	2.93679	−0.82677	−1.30120	−1.63137	0.4329
5.5165	0.18301	3.58367	3.14425	−0.81329	−1.28210	−1.60729	0.4358
5.6822	0.04483	3.58398	3.28367	−0.80539	−1.27111	−1.59355	0.4374
5.8955	−0.17588	3.58326	3.50149	−0.79329	−1.25436	−1.57278	0.4399
6.1490	−0.39671	3.58054	3.71145	−0.78192	−1.23827	−1.55256	0.4424
6.4273	−0.61763	3.57603	3.91433	−0.77209	−1.22392	−1.53407	0.4445
6.7230	−0.83817	3.57077	4.11382	−0.76323	−1.21124	−1.51778	0.4464
7.0299	−1.05884	3.56516	4.31205	−0.75575	−1.20059	−1.50418	0.4481
7.3483	−1.27899	3.56039	4.51313	−0.77469	−1.21767	−1.51920	0.4492
7.7022	−1.49614	3.55958	4.72703	−0.78890	−1.24128	−1.54789	0.4468
8.3032	−1.68069	3.56200	4.92123	−0.79142	−1.24487	−1.55527	0.4421
10.2805	−1.63368	3.56161	4.87269	−0.79156	−1.24853	−1.56015	0.4420
10.6349	−1.60685	3.56409	4.85578	−0.82120	−1.27579	−1.58632	0.4346
10.8450	−1.57273	3.56743	4.83502	−0.86520	−1.31734	−1.62725	0.4249
10.9901	−1.52879	3.57177	4.80841	−0.92641	−1.37515	−1.68464	0.4131
11.0931	−1.47422	3.57723	4.77572	−1.01356	−1.45662	−1.76459	0.3994
11.1710	−1.40436	3.58435	4.73431	−1.13510	−1.57024	−1.87619	0.3837

Table A.6: Evolutionary tracks including internal structure constants and gyration radii for 0.50 $M_\odot$ pre-MS standard models.

$\log(age)$	$\log(L/L_\odot)$	$\log(T_{\rm eff})$	$\log(g)$	$\log(k_2)$	$\log(k_3)$	$\log(k_4)$	β
2.8043	1.14203	3.58159	2.27379	−0.90012	−1.38962	−1.73383	0.4189
4.1221	0.91933	3.59014	2.53072	−0.85519	−1.34052	−1.68026	0.4271
4.6027	0.69894	3.59611	2.77497	−0.82555	−1.29929	−1.62897	0.4332
5.0383	0.48366	3.59981	3.00505	−0.80646	−1.27229	−1.59491	0.4372
5.5295	0.31235	3.60147	3.18302	−0.79624	−1.25768	−1.57634	0.4394
5.6887	0.14147	3.60204	3.35614	−0.78819	−1.24629	−1.56193	0.4411
5.9326	−0.07908	3.60137	3.57403	−0.77896	−1.23335	−1.54572	0.4431
6.2069	−0.29992	3.59876	3.78442	−0.77035	−1.22110	−1.53022	0.4449
6.4956	−0.52076	3.59398	3.98613	−0.76260	−1.20987	−1.51577	0.4466
6.7949	−0.74147	3.58805	4.18316	−0.75558	−1.19979	−1.50281	0.4482
7.1033	−0.96201	3.58183	4.37882	−0.77446	−1.21699	−1.51800	0.4494
7.4378	−1.18013	3.57746	4.57943	−0.78912	−1.24142	−1.54792	0.4466
7.7805	−1.33434	3.58144	4.74959	−0.83493	−1.28918	−1.60011	0.4289
9.1395	−1.40731	3.58238	4.82631	−0.85507	−1.30391	−1.61207	0.4249
10.2295	−1.36382	3.58614	4.79785	−0.87938	−1.32992	−1.63890	0.4169
10.5219	−1.32096	3.59104	4.77461	−0.93718	−1.38672	−1.69518	0.4071
10.6988	−1.26934	3.59707	4.74708	−1.01078	−1.45845	−1.76624	0.3955
10.8182	−1.20854	3.60429	4.71516	−1.10026	−1.54470	−1.85160	0.3828
10.9060	−1.13573	3.61290	4.67678	−1.21199	−1.65177	−1.95778	0.3687
10.9735	−1.04710	3.62295	4.62836	−1.36590	−1.79996	−2.10496	0.3531

Table A.7: Evolutionary tracks including internal structure constants and gyration radii for 0.60 $M_\odot$ pre-MS standard models.

$\log(age)$	$\log(L/L_\odot)$	$\log(T_{\rm eff})$	$\log(g)$	$\log(k_2)$	$\log(k_3)$	$\log(k_4)$	β
2.8468	1.24114	3.59193	2.29521	−0.88286	−1.36576	−1.70416	0.4224
4.1585	1.01803	3.60131	2.55586	−0.84167	−1.32123	−1.65585	0.4300
4.6410	0.79776	3.60815	2.80349	−0.81364	−1.28209	−1.60704	0.4358
5.2474	0.58927	3.61256	3.02962	−0.79588	−1.25681	−1.57504	0.4396
5.4796	0.44964	3.61451	3.17707	−0.78759	−1.24492	−1.55986	0.4413
5.6831	0.24568	3.61590	3.38656	−0.77871	−1.23220	−1.54361	0.4433
5.9430	0.02498	3.61555	3.60587	−0.77103	−1.22134	−1.52989	0.4449
6.2272	−0.19560	3.61329	3.81741	−0.76410	−1.21146	−1.51737	0.4464
6.5220	−0.41654	3.60883	4.02053	−0.75777	−1.20231	−1.50562	0.4478
6.8218	−0.63732	3.60260	4.21636	−0.76658	−1.20816	−1.50894	0.4491
7.1379	−0.85715	3.59651	4.41184	−0.78460	−1.23298	−1.53656	0.4483
7.4677	−1.03600	3.59657	4.59093	−0.81570	−1.27045	−1.58080	0.4352
7.7611	−1.07545	3.61355	4.69829	−0.98629	−1.43771	−1.74587	0.3982
9.0095	−1.12782	3.61414	4.75303	−0.99859	−1.45142	−1.75827	0.3969
10.0268	−1.07990	3.61952	4.72662	−1.04279	−1.49612	−1.80338	0.3887
10.3127	−1.02908	3.62611	4.70217	−1.10898	−1.56155	−1.86879	0.3788
10.4881	−0.96764	3.63396	4.67213	−1.19706	−1.64870	−1.95602	0.3672
10.6082	−0.89556	3.64280	4.63543	−1.30535	−1.75449	−2.06162	0.3541
10.6955	−0.81113	3.65252	4.58985	−1.44264	−1.88807	−2.19502	0.3398
10.7617	−0.70893	3.66335	4.53097	−1.61573	−2.05368	−2.35985	0.3246

Table A.8: Evolutionary tracks including internal structure constants and gyration radii for 0.70 $M_\odot$ pre-MS standard models.

$\log(age)$	$\log(L/L_\odot)$	$\log(T_{\rm eff})$	$\log(g)$	$\log(k_2)$	$\log(k_3)$	$\log(k_4)$	β
2.7548	1.39043	3.59616	2.22982	−0.88228	−1.36437	−1.70179	0.4225
4.0828	1.16859	3.60694	2.49478	−0.84125	−1.32044	−1.65450	0.4300
4.5680	0.94813	3.61527	2.74855	−0.81207	−1.27980	−1.60402	0.4361
5.1410	0.73800	3.62106	2.98185	−0.79246	−1.25193	−1.56879	0.4402
5.4143	0.59499	3.62394	3.13636	−0.78306	−1.23843	−1.55155	0.4422
5.6105	0.40073	3.62642	3.34055	−0.77403	−1.22539	−1.53481	0.4442
5.8720	0.18007	3.62727	3.56459	−0.76672	−1.21495	−1.52148	0.4458
6.1580	−0.04059	3.62600	3.78017	−0.76070	−1.20637	−1.51060	0.4471
6.4553	−0.26149	3.62261	3.98753	−0.75522	−1.19849	−1.50052	0.4483
6.7563	−0.48229	3.61709	4.18624	−0.77795	−1.22017	−1.52063	0.4493
7.0792	−0.70035	3.61185	4.38335	−0.79051	−1.24276	−1.54905	0.4460
7.3858	−0.83837	3.61633	4.53929	−0.84990	−1.30376	−1.61408	0.4262
7.6341	−0.81286	3.64195	4.61625	−1.09247	−1.54595	−1.85403	0.3809
7.9002	−0.84594	3.65532	4.70283	−1.24444	−1.72117	−2.03579	0.3650
9.6762	−0.81823	3.65451	4.67186	−1.21069	−1.67983	−1.99166	0.3647
10.0327	−0.76687	3.66130	4.64766	−1.28122	−1.75075	−2.06301	0.3556
10.2288	−0.70618	3.66942	4.61948	−1.36169	−1.82931	−2.14135	0.3453
10.3673	−0.62993	3.67943	4.58324	−1.46966	−1.93488	−2.24695	0.3332
10.4678	−0.53869	3.68991	4.53395	−1.61656	−2.07815	−2.38997	0.3192
10.5419	−0.42984	3.69937	4.46291	−1.81131	−2.26395	−2.57446	0.3034

Table A.9: Evolutionary tracks including internal structure constants and gyration radii for 0.80 $M_\odot$ pre-MS standard models.

$\log(age)$	$\log(L/L_\odot)$	$\log(T_{\rm eff})$	$\log(g)$	$\log(k_2)$	$\log(k_3)$	$\log(k_4)$	β
2.6879	1.51621	3.59896	2.17321	−0.88074	−1.36190	−1.69833	0.4229
4.0217	1.29516	3.61087	2.44190	−0.84047	−1.31925	−1.65277	0.4301
4.5086	1.07479	3.62039	2.70037	−0.81128	−1.27868	−1.60249	0.4361
5.0432	0.86448	3.62736	2.93853	−0.79073	−1.24951	−1.56567	0.4405
5.3615	0.71696	3.63110	3.10104	−0.78021	−1.23442	−1.54643	0.4428
5.5555	0.52736	3.63457	3.30451	−0.77065	−1.22059	−1.52865	0.4449
5.8199	0.30682	3.63667	3.53345	−0.76321	−1.20986	−1.51486	0.4465
6.1084	0.08587	3.63639	3.75329	−0.75764	−1.20190	−1.50471	0.4477
6.4072	−0.13491	3.63382	3.96376	−0.75281	−1.19498	−1.49588	0.4488
6.7121	−0.35542	3.62931	4.16625	−0.78203	−1.22604	−1.52694	0.4492
7.0371	−0.56130	3.62648	4.36080	−0.79957	−1.25406	−1.56247	0.4422
7.3180	−0.65229	3.63660	4.49228	−0.90127	−1.35365	−1.66326	0.4151
7.5295	−0.56658	3.67097	4.54405	−1.22292	−1.68265	−1.99188	0.3636
7.7280	−0.54435	3.69965	4.63652	−1.44707	−1.94720	−2.27030	0.3385
9.3577	−0.56736	3.69244	4.63073	−1.36271	−1.85253	−2.17153	0.3442
9.7841	−0.51590	3.69920	4.60630	−1.43026	−1.91893	−2.23760	0.3354
9.9949	−0.45795	3.70618	4.57628	−1.51679	−2.00534	−2.32430	0.3253
10.1368	−0.38982	3.71328	4.53654	−1.62820	−2.11576	−2.43476	0.3133
10.2463	−0.30479	3.72020	4.47917	−1.78053	−2.26489	−2.58352	0.2988
10.3324	−0.19595	3.72563	4.39207	−1.99738	−2.47265	−2.78956	0.2819

Table A.10: Evolutionary tracks including internal structure constants and gyration radii for 0.90 $M_\odot$ pre-MS standard models.

$\log(age)$	$\log(L/L_\odot)$	$\log(T_{\rm eff})$	$\log(g)$	$\log(k_2)$	$\log(k_3)$	$\log(k_4)$	β
2.6419	1.62387	3.60094	2.12465	−0.87836	−1.35845	−1.69384	0.4234
3.9728	1.40321	3.61379	2.39670	−0.84024	−1.31841	−1.65128	0.4303
4.4605	1.18293	3.62425	2.65881	−0.81166	−1.27872	−1.60214	0.4362
4.9689	0.97185	3.63223	2.90183	−0.79076	−1.24908	−1.56478	0.4407
5.3170	0.82236	3.63672	3.06926	−0.77960	−1.23309	−1.54440	0.4431
5.5087	0.63697	3.64096	3.27162	−0.76958	−1.21860	−1.52578	0.4453
5.7754	0.41650	3.64415	3.50485	−0.76169	−1.20717	−1.51104	0.4470
6.0670	0.19580	3.64511	3.72938	−0.75626	−1.19937	−1.50105	0.4482
6.3678	−0.02496	3.64347	3.94358	−0.75751	−1.19834	−1.49817	0.4491
6.6775	−0.24522	3.63990	4.14957	−0.78196	−1.22785	−1.52955	0.4486
6.9943	−0.42894	3.64014	4.33423	−0.81292	−1.26758	−1.57689	0.4373
7.2523	−0.47334	3.65635	4.44349	−0.96439	−1.41549	−1.72400	0.4033
7.4339	−0.34438	3.69759	4.47946	−1.33906	−1.80629	−2.11774	0.3484
7.5892	−0.26417	3.73362	4.54338	−1.68128	−2.20916	−2.54307	0.3090
9.0155	−0.34087	3.72511	4.58603	−1.52479	−2.04248	−2.37278	0.3228
9.5483	−0.29107	3.73014	4.55637	−1.60541	−2.12380	−2.45405	0.3131
9.7769	−0.23684	3.73503	4.52171	−1.70179	−2.22224	−2.55332	0.3025
9.9226	−0.17630	3.73954	4.47921	−1.81532	−2.33683	−2.66851	0.2908
10.0306	−0.10630	3.74332	4.42434	−1.95273	−2.47226	−2.80335	0.2780
10.1246	−0.01294	3.74559	4.34005	−2.14654	−2.65678	−2.98480	0.2629

Table A.11: Evolutionary tracks including internal structure constants and gyration radii for 1.00 $M_\odot$ pre-MS standard models.

$\log(age)$	$\log(L/L_\odot)$	$\log(T_{\rm eff})$	$\log(g)$	$\log(k_2)$	$\log(k_3)$	$\log(k_4)$	β
2.2954	1.89085	3.59019	1.86040	−0.90746	−1.39647	−1.73867	0.4177
3.6550	1.67269	3.60567	2.14051	−0.86541	−1.35255	−1.69267	0.4253
4.1464	1.45262	3.61851	2.41190	−0.83246	−1.30761	−1.63785	0.4319
4.5435	1.23223	3.62932	2.67554	−0.80600	−1.27069	−1.59197	0.4374
5.1029	1.02512	3.63764	2.91592	−0.78678	−1.24336	−1.55743	0.4415
5.3018	0.89817	3.64183	3.05965	−0.77754	−1.23010	−1.54052	0.4435
5.5216	0.69054	3.64722	3.28885	−0.76636	−1.21393	−1.51973	0.4459
5.7953	0.46991	3.65099	3.52453	−0.75866	−1.20277	−1.50532	0.4476
6.0918	0.24932	3.65262	3.75165	−0.75352	−1.19536	−1.49580	0.4488
6.3961	0.02857	3.65157	3.96819	−0.77685	−1.21804	−1.51739	0.4495
6.7156	−0.18661	3.64965	4.17573	−0.79040	−1.24198	−1.54752	0.4458
7.0039	−0.31571	3.65598	4.33014	−0.84918	−1.30257	−1.61255	0.4260
7.2246	−0.27725	3.68400	4.40376	−1.09444	−1.54584	−1.85315	0.3811
7.3696	−0.11545	3.72546	4.40779	−1.55903	−2.04707	−2.36546	0.3202
7.4906	−0.03885	3.75730	4.45853	−1.89608	−2.45991	−2.80859	0.2812
8.7585	−0.13013	3.75158	4.52696	−1.71051	−2.26307	−2.60773	0.2974
9.3538	−0.08153	3.75533	4.49334	−1.80109	−2.35701	−2.70269	0.2872
9.5876	−0.03068	3.75866	4.45582	−1.90172	−2.46198	−2.80963	0.2767
9.6979	0.00841	3.76078	4.42520	−1.98100	−2.54323	−2.89155	0.2689
9.8058	0.06194	3.76269	4.37932	−2.09337	−2.65791	−3.00779	0.2588

Table A.12: Evolutionary tracks including internal structure constants and gyration radii for 1.20 $M_\odot$ pre-MS standard models.

$\log(age)$	$\log(L/L_\odot)$	$\log(T_{\rm eff})$	$\log(g)$	$\log(k_2)$	$\log(k_3)$	$\log(k_4)$	β
2.2057	2.04983	3.59157	1.78614	−0.89867	−1.38437	−1.72352	0.4194
3.5814	1.83255	3.60787	2.06862	−0.85997	−1.34491	−1.68302	0.4264
4.0773	1.61213	3.62191	2.34518	−0.82927	−1.30298	−1.63187	0.4326
4.4758	1.39195	3.63386	2.61320	−0.80462	−1.26852	−1.58900	0.4377
5.0180	1.18283	3.64370	2.86163	−0.78594	−1.24196	−1.55544	0.4417
5.2406	1.05353	3.64883	3.01145	−0.77656	−1.22849	−1.53827	0.4437
5.4589	0.85106	3.65554	3.24076	−0.76506	−1.21188	−1.51693	0.4462
5.7366	0.63068	3.66100	3.48300	−0.75654	−1.19952	−1.50098	0.4481
6.0380	0.41004	3.66444	3.71742	−0.75105	−1.19159	−1.49075	0.4493
6.3520	0.18984	3.66588	3.94337	−0.78310	−1.22731	−1.52760	0.4492
6.6604	0.00563	3.66886	4.13949	−0.80490	−1.25912	−1.56751	0.4401
6.9142	−0.05901	3.68338	4.26222	−0.92344	−1.37378	−1.68200	0.4106
7.0947	0.03668	3.71492	4.29268	−1.28431	−1.74347	−2.05206	0.3551
7.2054	0.23034	3.75110	4.24376	−1.85830	−2.38368	−2.71621	0.2855
7.2767	0.37729	3.78156	4.21865	−2.32734	−2.96962	−3.35982	0.2333
7.3557	0.25077	3.79134	4.38429	−2.16954	−2.84929	−3.26808	0.2487
8.5441	0.25361	3.79453	4.39419	−2.15625	−2.84148	−3.26661	0.2451
9.0480	0.29444	3.79635	4.36064	−2.24430	−2.93926	−3.37166	0.2368
9.2511	0.33117	3.79736	4.32797	−2.32411	−3.02555	−3.46296	0.2297
9.3704	0.36278	3.79747	4.29680	−2.39260	−3.09605	−3.53466	0.2240

Table A.13: Evolutionary tracks including internal structure constants and gyration radii for 1.40 $M_\odot$ pre-MS standard models.

$\log(age)$	$\log(L/L_\odot)$	$\log(T_{\rm eff})$	$\log(g)$	$\log(k_2)$	$\log(k_3)$	$\log(k_4)$	β
2.1323	2.18049	3.59216	1.72479	−0.89016	−1.37268	−1.70898	0.4211
3.5221	1.96407	3.60908	2.00889	−0.85430	−1.33700	−1.67310	0.4275
4.0207	1.74393	3.62398	2.28861	−0.82569	−1.29789	−1.62542	0.4333
4.4213	1.52400	3.63698	2.56055	−0.80266	−1.26563	−1.58521	0.4381
4.9454	1.31312	3.64788	2.81504	−0.78496	−1.24041	−1.55333	0.4419
5.1915	1.18200	3.65386	2.97006	−0.77573	−1.22717	−1.53644	0.4439
5.4078	0.98460	3.66166	3.19866	−0.76449	−1.21093	−1.51559	0.4464
5.6887	0.76414	3.66848	3.44641	−0.75542	−1.19778	−1.49864	0.4484
5.9937	0.54377	3.67341	3.68651	−0.76586	−1.20528	−1.50355	0.4496
6.3119	0.33006	3.67720	3.91536	−0.78542	−1.23353	−1.53613	0.4478
6.5960	0.18427	3.68437	4.08983	−0.82541	−1.27891	−1.58768	0.4332
6.8236	0.16766	3.70343	4.18269	−1.01424	−1.46394	−1.77091	0.3945
6.9735	0.30602	3.73433	4.16792	−1.49229	−1.96938	−2.28357	0.3295
7.0597	0.51773	3.76609	4.08325	−2.12054	−2.69314	−3.04648	0.2566
7.1104	0.65840	3.79256	4.04846	−2.56650	−3.27652	−3.71954	0.2106
7.1476	0.70581	3.81502	4.09091	−2.75949	−3.56567	−4.09442	0.1936
7.2039	0.52735	3.81818	4.28200	−2.40991	−3.20164	−3.71989	0.2220
7.7861	0.55540	3.83256	4.31146	−2.46469	−3.28530	−3.83730	0.2136
8.8074	0.60023	3.83315	4.26898	−2.56487	−3.39099	−3.94801	0.2062
9.0764	0.63924	3.82963	4.21592	−2.65906	−3.48146	−4.03511	0.2001

Table A.14: Evolutionary tracks including internal structure constants and gyration radii for 1.60 $M_\odot$ pre-MS standard models.

$\log(age)$	$\log(L/L_\odot)$	$\log(T_{\rm eff})$	$\log(g)$	$\log(k_2)$	$\log(k_3)$	$\log(k_4)$	β
2.1002	2.29213	3.59233	1.67179	−0.88236	−1.36194	−1.69563	0.4227
3.4764	2.07560	3.60991	1.95865	−0.84837	−1.32887	−1.66302	0.4286
3.9754	1.85540	3.62542	2.24090	−0.82165	−1.29234	−1.61850	0.4341
4.3782	1.63511	3.63926	2.51655	−0.80004	−1.26200	−1.58065	0.4386
4.8837	1.42401	3.65103	2.77473	−0.78337	−1.23820	−1.55051	0.4422
5.1507	1.29138	3.65768	2.93397	−0.77454	−1.22551	−1.53431	0.4441
5.3643	1.09885	3.66624	3.16071	−0.76381	−1.21003	−1.51444	0.4464
5.6480	0.87851	3.67431	3.41334	−0.75451	−1.19656	−1.49708	0.4485
5.9567	0.65822	3.68055	3.65859	−0.77877	−1.21980	−1.51848	0.4496
6.2652	0.46112	3.68626	3.87853	−0.79168	−1.24293	−1.54797	0.4453
6.5301	0.34706	3.69645	4.03337	−0.85318	−1.30502	−1.61368	0.4252
6.7351	0.37081	3.71778	4.09492	−1.11558	−1.56543	−1.87139	0.3778
6.8608	0.54683	3.74745	4.03757	−1.69129	−2.19385	−2.51829	0.3047
6.9287	0.74905	3.77527	3.94666	−2.30101	−2.93007	−3.31989	0.2368
6.9693	0.87245	3.79937	3.91964	−2.68760	−3.45021	−3.94550	0.1990
7.0136	0.96901	3.84551	4.00765	−2.87604	−3.73386	−4.31765	0.1818
7.0651	0.78883	3.85111	4.21022	−2.55346	−3.41109	−3.99648	0.2075
7.2950	0.81074	3.88100	4.30786	−2.50825	−3.36271	−3.95193	0.2090
8.6320	0.84922	3.87872	4.26028	−2.59998	−3.45528	−4.04441	0.2029
8.9121	0.88201	3.86740	4.18221	−2.70926	−3.56190	−4.14912	0.1958

Table A.15: Evolutionary tracks including internal structure constants and gyration radii for 1.80 $M_\odot$ pre-MS standard models.

$\log(age)$	$\log(L/L_\odot)$	$\log(T_{\rm eff})$	$\log(g)$	$\log(k_2)$	$\log(k_3)$	$\log(k_4)$	β
2.0317	2.38992	3.59232	1.62513	−0.87512	−1.35198	−1.68326	0.4241
3.4301	2.17466	3.61021	1.91198	−0.84437	−1.32288	−1.65526	0.4296
3.9317	1.95455	3.62623	2.19614	−0.81930	−1.28860	−1.61350	0.4347
4.3363	1.73424	3.64070	2.47434	−0.79891	−1.25995	−1.57776	0.4390
4.8193	1.52275	3.65330	2.73623	−0.78313	−1.23737	−1.54911	0.4424
5.1153	1.38708	3.66065	2.90130	−0.77457	−1.22506	−1.53338	0.4442
5.3261	1.19907	3.66981	3.12596	−0.76448	−1.21050	−1.51470	0.4465
5.6123	0.97865	3.67896	3.38296	−0.75516	−1.19704	−1.49736	0.4485
5.9228	0.76033	3.68634	3.63082	−0.78048	−1.22374	−1.52343	0.4492
6.2166	0.58320	3.69365	3.83718	−0.79890	−1.25243	−1.55975	0.4420
6.4657	0.49659	3.70598	3.97310	−0.89324	−1.34381	−1.65192	0.4163
6.6500	0.55826	3.72858	4.00184	−1.24220	−1.69918	−2.00692	0.3604
6.7542	0.76246	3.75649	3.90926	−1.88258	−2.42035	−2.76021	0.2820
6.8101	0.93735	3.78136	3.83385	−2.42165	−3.10031	−3.52996	0.2240
6.8446	1.04735	3.80539	3.81997	−2.74179	−3.53455	−4.06431	0.1939
6.9003	1.19452	3.88788	4.00276	−2.86498	−3.72261	−4.30858	0.1829
6.9454	1.00864	3.89058	4.19944	−2.53979	−3.39977	−3.98869	0.2084
7.0765	1.04550	3.92805	4.31248	−2.49235	−3.34508	−3.93371	0.2105
8.4305	1.05566	3.92144	4.27587	−2.54586	−3.39824	−3.98634	0.2071
8.7419	1.08668	3.90690	4.18668	−2.66309	−3.51272	−4.09906	0.1995

Table A.16: Evolutionary tracks including internal structure constants and gyration radii for 2.00 $M_\odot$ pre-MS standard models.

$\log(age)$	$\log(L/L_\odot)$	$\log(T_{\rm eff})$	$\log(g)$	$\log(k_2)$	$\log(k_3)$	$\log(k_4)$	β
2.0185	2.47689	3.59235	1.58403	−0.86848	−1.34279	−1.67183	0.4255
3.3982	2.25961	3.61047	1.87381	−0.83935	−1.31588	−1.64651	0.4306
3.8988	2.03970	3.62691	2.15946	−0.81581	−1.28366	−1.60727	0.4354
4.3040	1.81951	3.64191	2.43964	−0.79662	−1.25667	−1.57357	0.4395
4.7741	1.60770	3.65518	2.70457	−0.78166	−1.23524	−1.54634	0.4427
5.0848	1.47116	3.66299	2.87233	−0.77353	−1.22352	−1.53135	0.4444
5.2916	1.28862	3.67264	3.09347	−0.76414	−1.20996	−1.51394	0.4465
5.5798	1.06807	3.68266	3.35408	−0.76412	−1.20537	−1.50539	0.4485
5.8862	0.85685	3.69108	3.59900	−0.78293	−1.22889	−1.53018	0.4483
6.1670	0.69770	3.69968	3.79254	−0.80985	−1.26404	−1.57251	0.4381
6.4024	0.63666	3.71369	3.90961	−0.94593	−1.39674	−1.70480	0.4065
6.5668	0.73453	3.73674	3.90397	−1.38307	−1.85415	−2.16672	0.3426
6.6529	0.94691	3.76272	3.79549	−2.03583	−2.61827	−2.98385	0.2645
6.7015	1.09612	3.78584	3.73875	−2.50402	−3.22594	−3.69486	0.2159
6.7415	1.22930	3.82349	3.75620	−2.81294	−3.64321	−4.21196	0.1878
6.7974	1.39042	3.92443	3.99881	−2.84589	−3.70292	−4.28940	0.1849
6.8387	1.20157	3.92582	4.19325	−2.51610	−3.37531	−3.96459	0.2106
6.9458	1.24969	3.96758	4.31218	−2.48354	−3.33710	−3.92675	0.2120
8.2613	1.23763	3.95736	4.28335	−2.50654	−3.35836	−3.94699	0.2109
8.5965	1.26899	3.94108	4.18688	−2.61933	−3.46771	−4.05409	0.2028

Table A.17: Evolutionary tracks including internal structure constants and gyration radii for 2.30 $M_\odot$ pre-MS standard models.

$\log(age)$	$\log(L/L_\odot)$	$\log(T_{\rm eff})$	$\log(g)$	$\log(k_2)$	$\log(k_3)$	$\log(k_4)$	β
1.9530	2.58945	3.59198	1.53068	−0.85929	−1.33007	−1.65601	0.4273
3.3488	2.37345	3.61053	1.82092	−0.83313	−1.30702	−1.63529	0.4319
3.8515	2.15340	3.62742	2.10851	−0.81159	−1.27752	−1.59938	0.4363
4.2584	1.93333	3.64309	2.39125	−0.79391	−1.25260	−1.56826	0.4400
4.7100	1.72057	3.65721	2.66050	−0.78003	−1.23268	−1.54291	0.4430
5.0455	1.58156	3.66579	2.83381	−0.77234	−1.22157	−1.52867	0.4447
5.2501	1.40298	3.67599	3.05319	−0.76378	−1.20922	−1.51279	0.4466
5.5399	1.18391	3.68715	3.31690	−0.78252	−1.22538	−1.52594	0.4484
5.8327	0.98960	3.69667	3.54930	−0.79381	−1.24597	−1.55156	0.4460
6.0966	0.85574	3.70689	3.72406	−0.83354	−1.28713	−1.59636	0.4308
6.3122	0.83489	3.72288	3.80888	−1.04295	−1.49264	−1.79921	0.3892
6.4453	0.98710	3.74592	3.74880	−1.60626	−2.11022	−2.43596	0.3140
6.5125	1.17456	3.76912	3.65416	−2.18994	−2.83316	−3.24391	0.2466
6.5539	1.29797	3.79234	3.62362	−2.55834	−3.32062	−3.83392	0.2097
6.6080	1.48923	3.86823	3.73591	−2.79588	−3.62959	−4.20513	0.1886
6.6581	1.64346	3.97002	3.98885	−2.80416	−3.65662	−4.24140	0.1877
6.6963	1.45492	3.97153	4.18341	−2.47882	−3.33360	−3.92062	0.2136
6.7867	1.50803	4.01626	4.30923	−2.45291	−3.30326	−3.89091	0.2150
8.0528	1.47660	4.00263	4.28615	−2.45152	−3.29878	−3.88503	0.2157
8.4193	1.51092	3.98511	4.18175	−2.57321	−3.41683	−4.00078	0.2068

Table A.18: Evolutionary tracks including internal structure constants and gyration radii for 2.50 $M_\odot$ pre-MS standard models.

$\log(age)$	$\log(L/L_\odot)$	$\log(T_{\rm eff})$	$\log(g)$	$\log(k_2)$	$\log(k_3)$	$\log(k_4)$	β
1.9521	2.65651	3.59171	1.49878	−0.85392	−1.32258	−1.64665	0.4284
3.3255	2.43953	3.61061	1.79134	−0.82960	−1.30180	−1.62859	0.4327
3.8272	2.21927	3.62773	2.08011	−0.80933	−1.27402	−1.59476	0.4369
4.2342	1.99923	3.64372	2.36409	−0.79253	−1.25033	−1.56516	0.4404
4.6793	1.78580	3.65830	2.63583	−0.77930	−1.23131	−1.54094	0.4433
5.0223	1.64688	3.66720	2.81034	−0.77197	−1.22072	−1.52736	0.4449
5.2222	1.47342	3.67757	3.02529	−0.76401	−1.20921	−1.51256	0.4466
5.5086	1.25863	3.68930	3.28702	−0.78861	−1.23384	−1.53553	0.4480
5.7924	1.07496	3.69939	3.51102	−0.79560	−1.24980	−1.55736	0.4440
6.0470	0.95597	3.71050	3.67449	−0.84948	−1.30252	−1.61226	0.4254
6.2496	0.96148	3.72736	3.73640	−1.11620	−1.56875	−1.87560	0.3772
6.3643	1.13820	3.75002	3.65031	−1.72764	−2.26350	−2.60621	0.2979
6.4248	1.30085	3.77196	3.57544	−2.24429	−2.91983	−3.35932	0.2393
6.4636	1.41458	3.79648	3.55977	−2.56117	−3.34001	−3.87376	0.2082
6.5253	1.63807	3.89327	3.72346	−2.76742	−3.59988	−4.17660	0.1903
6.5729	1.79043	3.99483	3.97734	−2.77010	−3.62034	−4.20523	0.1895
6.6099	1.60829	3.99886	4.17560	−2.46384	−3.31746	−3.90488	0.2151
6.6939	1.65845	4.04386	4.30543	−2.43285	−3.28105	−3.86851	0.2169
7.9352	1.61809	4.02882	4.28562	−2.42164	−3.26661	−3.85270	0.2185
8.3175	1.65448	4.01092	4.17764	−2.54644	−3.38728	−3.97102	0.2093

Table A.19: Evolutionary tracks including internal structure constants and gyration radii for 2.80 $M_\odot$ pre-MS standard models.

$\log(age)$	$\log(L/L_\odot)$	$\log(T_{\rm eff})$	$\log(g)$	$\log(k_2)$	$\log(k_3)$	$\log(k_4)$	β
1.9056	2.74616	3.59122	1.45636	−0.84659	−1.31231	−1.63380	0.4300
3.2871	2.53012	3.61041	1.74918	−0.82442	−1.29434	−1.61910	0.4338
3.7905	2.30988	3.62791	2.03942	−0.80587	−1.26890	−1.58813	0.4376
4.1986	2.08988	3.64433	2.32510	−0.79028	−1.24689	−1.56062	0.4409
4.6329	1.87546	3.65948	2.60013	−0.77789	−1.22905	−1.53787	0.4436
4.9913	1.73479	3.66894	2.77862	−0.77096	−1.21904	−1.52502	0.4451
5.1865	1.56695	3.67954	2.98885	−0.78011	−1.22459	−1.52746	0.4467
5.4626	1.36302	3.69169	3.24138	−0.78963	−1.23865	−1.54256	0.4470
5.7344	1.19487	3.70258	3.45311	−0.80059	−1.25580	−1.56522	0.4401
5.9761	1.09915	3.71493	3.59823	−0.88912	−1.34064	−1.65001	0.4154
6.1558	1.14957	3.73276	3.61913	−1.26144	−1.72895	−2.04070	0.3564
6.2477	1.33464	3.75443	3.52072	−1.87369	−2.46135	−2.83723	0.2791
6.3017	1.46748	3.77604	3.47434	−2.29962	−3.01623	−3.49520	0.2322
6.3507	1.61376	3.81992	3.50359	−2.59952	−3.40639	−3.96982	0.2039
6.4106	1.84013	3.92778	3.70864	−2.73209	−3.56368	−4.14057	0.1927
6.4554	1.98696	4.02850	3.96471	−2.72728	−3.57514	−4.15888	0.1923
6.4913	1.81140	4.03502	4.16633	−2.43464	−3.28616	−3.87268	0.2177
6.5712	1.85280	4.07972	4.30374	−2.39276	−3.23850	−3.82479	0.2205
7.7968	1.80956	4.06320	4.28092	−2.37872	−3.22064	−3.80530	0.2223
8.1872	1.84889	4.04518	4.16948	−2.50495	−3.34305	−3.92540	0.2125

Table A.20: Evolutionary tracks including internal structure constants and gyration radii for 3.00 $M_\odot$ pre-MS standard models.

$\log(age)$	$\log(L/L_\odot)$	$\log(T_{\rm eff})$	$\log(g)$	$\log(k_2)$	$\log(k_3)$	$\log(k_4)$	β
1.9034	2.78869	3.59222	1.44782	−0.84187	−1.30558	−1.62534	0.4310
3.2856	2.57172	3.61129	1.74106	−0.81970	−1.28785	−1.61106	0.4346
3.7896	2.35174	3.62898	2.03179	−0.80238	−1.26403	−1.58202	0.4382
4.1984	2.13165	3.64557	2.31826	−0.78771	−1.24327	−1.55602	0.4414
4.6471	1.91827	3.66094	2.59309	−0.77606	−1.22646	−1.53457	0.4439
4.9803	1.78093	3.67033	2.76800	−0.76958	−1.21709	−1.52253	0.4453
5.1829	1.60958	3.68152	2.98414	−0.79293	−1.23926	−1.54267	0.4467
5.4529	1.41533	3.69376	3.22734	−0.79370	−1.24729	−1.55438	0.4455
5.7158	1.26184	3.70520	3.42657	−0.81139	−1.26647	−1.57691	0.4352
5.9460	1.19214	3.71863	3.55001	−0.94475	−1.39402	−1.70178	0.4033
6.1001	1.28886	3.73736	3.52819	−1.42400	−1.91885	−2.24270	0.3348
6.1780	1.45825	3.75820	3.44218	−1.98018	−2.60690	−3.01162	0.2657
6.2274	1.57536	3.78086	3.41568	−2.34132	−3.08305	−3.58852	0.2272
6.2862	1.75763	3.84808	3.50233	−2.59882	−3.40681	−3.97277	0.2035
6.3430	1.97834	3.95765	3.71988	−2.71249	−3.54228	−4.11863	0.1938
6.3857	2.10762	4.05503	3.98013	−2.70313	−3.54623	−4.12824	0.1950
6.4209	1.91551	4.05463	4.17062	−2.39392	−3.23929	−3.82315	0.2212
6.5034	1.94915	4.09915	4.31507	−2.33837	−3.17845	−3.76220	0.2252
7.7748	1.92888	4.08203	4.26684	−2.36237	−3.19909	−3.78102	0.2236
8.1295	1.96992	4.06428	4.15484	−2.49618	−3.32903	−3.90894	0.2137

Table A.21: Evolutionary tracks including internal structure constants and gyration radii for 3.30 $M_\odot$ pre-MS standard models.

$\log(age)$	$\log(L/L_\odot)$	$\log(T_{\rm eff})$	$\log(g)$	$\log(k_2)$	$\log(k_3)$	$\log(k_4)$	β
1.8938	2.85544	3.59217	1.42225	−0.83489	−1.29592	−1.61339	0.4324
3.2678	2.63964	3.61168	1.71611	−0.81578	−1.28183	−1.60319	0.4356
3.7716	2.41969	3.62955	2.00752	−0.79987	−1.25990	−1.57643	0.4389
4.1815	2.19947	3.64648	2.29546	−0.78630	−1.24067	−1.55231	0.4418
4.6325	1.98626	3.66217	2.57143	−0.77548	−1.22504	−1.53233	0.4442
4.9584	1.85099	3.67177	2.74510	−0.76950	−1.21640	−1.52123	0.4455
5.1842	1.66504	3.68443	2.98170	−0.79723	−1.24852	−1.55443	0.4460
5.4450	1.48797	3.69691	3.20869	−0.79758	−1.25423	−1.56476	0.4414
5.6938	1.36114	3.70919	3.38462	−0.84703	−1.29977	−1.61025	0.4240
5.8985	1.34749	3.72451	3.45955	−1.10960	−1.56677	−1.87502	0.3775
6.0126	1.49488	3.74382	3.38942	−1.67139	−2.22568	−2.58174	0.3021
6.0783	1.62470	3.76433	3.34163	−2.11621	−2.80271	−3.25958	0.2499
6.1264	1.73794	3.79378	3.34618	−2.40923	−3.18719	−3.73106	0.2200
6.1967	1.96943	3.89454	3.51775	−2.60685	−3.41841	−3.98770	0.2032
6.2487	2.17443	4.00403	3.75071	−2.69187	−3.52325	−4.10070	0.1954
6.2893	2.26222	4.09273	4.01771	−2.65523	−3.49857	−4.08093	0.2006
6.3258	2.04798	4.08058	4.18335	−2.32771	−3.16428	−3.74478	0.2272
6.4165	2.06959	4.12233	4.32874	−2.26192	−3.09534	−3.67667	0.2324
7.7733	2.09625	4.10631	4.23801	−2.35641	−3.18962	−3.76986	0.2247
8.0640	2.13926	4.08916	4.12638	−2.49293	−3.32212	−3.90054	0.2147

Table A.22: Evolutionary tracks including internal structure constants and gyration radii for 3.50 $M_\odot$ pre-MS standard models.

$\log(age)$	$\log(L/L_\odot)$	$\log(T_{\rm eff})$	$\log(g)$	$\log(k_2)$	$\log(k_3)$	$\log(k_4)$	β
1.8942	2.88844	3.59309	1.41848	−0.83058	−1.28987	−1.60588	0.4333
3.2702	2.67278	3.61261	1.71223	−0.81239	−1.27694	−1.59700	0.4363
3.7746	2.45275	3.63055	2.00404	−0.79743	−1.25626	−1.57170	0.4394
4.1847	2.23279	3.64762	2.29224	−0.78466	−1.23813	−1.54892	0.4422
4.6551	2.02023	3.66347	2.56821	−0.77438	−1.22326	−1.52990	0.4444
4.9484	1.89076	3.67277	2.73491	−0.78509	−1.23114	−1.53541	0.4456
5.1846	1.70156	3.68623	2.97792	−0.79881	−1.25377	−1.56218	0.4447
5.4389	1.53716	3.69886	3.19287	−0.80616	−1.26298	−1.57482	0.4370
5.6777	1.43274	3.71191	3.34949	−0.89757	−1.34786	−1.65644	0.4131
5.8579	1.46450	3.72821	3.38291	−1.26162	−1.73720	−2.05210	0.3562
5.9532	1.61286	3.74743	3.31142	−1.80505	−2.40256	−2.78854	0.2854
6.0133	1.72422	3.76898	3.28626	−2.17916	−2.89431	−3.37981	0.2428
6.0738	1.87337	3.81987	3.34069	−2.45239	−3.24354	−3.80151	0.2160
6.1401	2.10425	3.92608	3.53465	−2.61118	−3.42300	−3.99277	0.2028
6.1890	2.29437	4.03382	3.77548	−2.67379	−3.50375	−4.08026	0.1967
6.2291	2.34325	4.11363	4.04582	−2.59935	−3.44225	−4.02388	0.2056
6.2775	2.15924	4.10594	4.19908	−2.31752	−3.14710	−3.72443	0.2285
6.4047	2.15960	4.13822	4.32784	−2.24210	−3.07096	−3.65003	0.2350
7.7662	2.19984	4.12104	4.21890	−2.36175	−3.19097	−3.76917	0.2252
8.0239	2.24381	4.10420	4.10754	−2.49570	−3.32024	−3.89648	0.2152

Table A.23: Evolutionary tracks including internal structure constants and gyration radii for 3.80 $M_\odot$ pre-MS standard models.

$\log(age)$	$\log(L/L_\odot)$	$\log(T_{\rm eff})$	$\log(g)$	$\log(k_2)$	$\log(k_3)$	$\log(k_4)$	β
1.9054	2.93274	3.59450	1.41554	−0.82480	−1.28167	−1.59564	0.4345
3.2773	2.71698	3.61403	1.70942	−0.80799	−1.27047	−1.58872	0.4373
3.7821	2.49683	3.63206	2.00170	−0.79431	−1.25149	−1.56542	0.4401
4.1930	2.27702	3.64934	2.29063	−0.78258	−1.23478	−1.54438	0.4427
4.6971	2.06491	3.66542	2.56705	−0.77308	−1.22103	−1.52676	0.4447
4.9570	1.92718	3.67558	2.74544	−0.80027	−1.25112	−1.55728	0.4454
5.1896	1.75314	3.68897	2.97304	−0.80338	−1.26232	−1.57455	0.4411
5.4329	1.61273	3.70204	3.16572	−0.83692	−1.29212	−1.60437	0.4267
5.6503	1.55659	3.71650	3.27970	−1.03252	−1.48831	−1.79712	0.3891
5.7869	1.65134	3.73368	3.25368	−1.51972	−2.05477	−2.40005	0.3213
5.8660	1.76940	3.75303	3.21301	−1.96460	−2.62782	−3.06483	0.2659
5.9196	1.86434	3.77739	3.21550	−2.25071	−3.00608	−3.52994	0.2348
5.9979	2.07034	3.86434	3.35728	−2.47909	−3.27868	−3.84251	0.2142
6.0587	2.29483	3.97314	3.56801	−2.61278	−3.43178	−4.00457	0.2025
6.1041	2.45966	4.07728	3.81973	−2.63994	−3.47430	−4.05173	0.1991
6.1438	2.43554	4.13783	4.08607	−2.49036	−3.33765	−3.92093	0.2146
6.1998	2.34761	4.14846	4.21653	−2.31952	−3.14718	−3.72408	0.2276
7.0050	2.29859	4.15990	4.31130	−2.22433	−3.05453	−3.63415	0.2367
7.7570	2.34591	4.14098	4.18830	−2.35985	−3.18816	−3.76573	0.2255
7.9710	2.39056	4.12441	4.07738	−2.49935	−3.32339	−3.89939	0.2155

A.2 Binary models: non-rotating stars in binary systems

Pre-main sequence evolutionary tracks for tidally distorted stellar models are given in Tables (A.24) to (A.46). Same header as in tables of Appendix (A.1).

Table A.24: Evolutionary tracks including internal structure constants and gyration radii for 0.09 $M_\odot$ pre-MS tidal distorted models.

$\log(age)$	$\log(L/L_\odot)$	$\log(T_{\rm eff})$	$\log(g)$	$\log(k_2)$	$\log(k_3)$	$\log(k_4)$	β
2.8237	−0.12680	3.39446	2.05084	−1.25868	−1.83666	−2.25359	0.3596
4.1959	−0.35189	3.40695	2.32498	−1.16469	−1.72113	−2.11106	0.3723
4.7072	−0.57144	3.42613	2.62092	−1.10049	−1.63466	−2.00488	0.3833
5.1343	−0.79102	3.44314	2.90841	−1.02791	−1.54602	−1.90190	0.3956
5.5237	−1.01140	3.45624	3.18113	−0.95034	−1.45303	−1.79777	0.4089
6.1624	−1.21357	3.46594	3.42209	−0.91351	−1.40106	−1.73584	0.4161
6.3816	−1.35003	3.47162	3.58125	−0.89503	−1.37576	−1.70491	0.4200
6.5681	−1.55808	3.47920	3.81961	−0.86416	−1.33703	−1.65966	0.4259
6.8177	−1.77891	3.48566	4.06629	−0.83291	−1.29667	−1.61272	0.4317
7.0941	−1.99941	3.49054	4.30629	−0.82562	−1.28107	−1.59021	0.4339
7.3965	−2.22013	3.49333	4.53818	−0.81200	−1.26302	−1.56755	0.4366
7.7065	−2.44047	3.49487	4.76468	−0.80275	−1.24876	−1.54914	0.4387
8.0314	−2.66068	3.49413	4.98193	−0.77701	−1.21750	−1.51335	0.4438
8.3621	−2.88121	3.48775	5.17697	−0.74007	−1.17222	−1.46213	0.4514
8.6871	−3.10177	3.47010	5.32692	−0.71135	−1.13521	−1.41883	0.4574
9.1294	−3.31143	3.43825	5.40916	−0.69993	−1.11966	−1.39986	0.4599
11.4796	−3.14966	3.47063	5.37697	−0.70935	−1.13236	−1.41530	0.4578
11.8349	−2.91777	3.49120	5.22739	−0.74762	−1.18190	−1.47301	0.4499
12.1941	−2.80660	3.49198	5.11927	−0.77514	−1.21654	−1.51242	0.4443
12.3851	−2.79130	3.48924	5.09299	−0.78038	−1.22564	−1.52515	0.4430

Table A.25: Evolutionary tracks including internal structure constants and gyration radii for 0.10 $M_\odot$ pre-MS tidal distorted models.

$\log(age)$	$\log(L/L_\odot)$	$\log(T_{\rm eff})$	$\log(g)$	$\log(k_2)$	$\log(k_3)$	$\log(k_4)$	β
3.8575	−0.62897	3.44022	2.78201	−1.05854	−1.58093	−1.94604	0.3921
5.1760	−0.85338	3.45476	3.06355	−0.97544	−1.48601	−1.83718	0.4045
5.7078	−1.06874	3.46592	3.32318	−0.91887	−1.41273	−1.75263	0.4148
6.3023	−1.23049	3.47267	3.51181	−0.89597	−1.37944	−1.71144	0.4196
6.4509	−1.40085	3.47888	3.70693	−0.87355	−1.34972	−1.67538	0.4241
6.6946	−1.62126	3.48578	3.95489	−0.84025	−1.30841	−1.62773	0.4304
6.9700	−1.84192	3.49162	4.19891	−0.82600	−1.28483	−1.59723	0.4335
7.2707	−2.06234	3.49563	4.43536	−0.81600	−1.26951	−1.57641	0.4359
7.5804	−2.28303	3.49795	4.66533	−0.80801	−1.25716	−1.56013	0.4376
7.9011	−2.50325	3.49884	4.88910	−0.79475	−1.23991	−1.53926	0.4404
8.2439	−2.72267	3.49704	5.10134	−0.76582	−1.20459	−1.49918	0.4461
8.6710	−2.93810	3.48887	5.28407	−0.72929	−1.15887	−1.44683	0.4535
11.2846	−2.91518	3.49269	5.27645	−0.73770	−1.16968	−1.45932	0.4517
11.8845	−2.73689	3.49632	5.11269	−0.77538	−1.21701	−1.51320	0.4442
12.1736	−2.71668	3.49372	5.08207	−0.77911	−1.22283	−1.52078	0.4433
12.3299	−2.69840	3.49467	5.06759	−0.77715	−1.22277	−1.52318	0.4434
12.4314	−2.65579	3.50870	5.08110	−0.76976	−1.21532	−1.51687	0.4447
12.4938	−2.59448	3.54115	5.14958	−0.80564	−1.26380	−1.57603	0.4393
12.5061	−2.49186	3.57887	5.19784	−0.95206	−1.40236	−1.71214	0.4061
12.5160	−2.32875	3.62679	5.22640	−1.34572	−1.79860	−2.10445	0.3518

Table A.26: Evolutionary tracks including internal structure constants and gyration radii for 0.20 $M_\odot$ pre-MS tidal distorted models.

$\log(age)$	$\log(L/L_\odot)$	$\log(T_{\rm eff})$	$\log(g)$	$\log(k_2)$	$\log(k_3)$	$\log(k_4)$	β
2.9189	0.40798	3.51232	2.33437	−1.00607	−1.53048	−1.90463	0.4001
4.2657	0.18685	3.51468	2.56409	−0.96612	−1.48824	−1.85774	0.4071
4.7416	−0.03377	3.51546	2.78745	−0.93590	−1.44788	−1.80826	0.4127
5.1196	−0.25422	3.51484	3.00525	−0.90895	−1.41238	−1.76547	0.4178
5.5937	−0.46425	3.51332	3.20913	−0.88270	−1.37764	−1.72395	0.4228
6.0245	−0.64032	3.51191	3.37951	−0.86119	−1.34832	−1.68838	0.4271
6.1864	−0.82576	3.51153	3.56342	−0.84028	−1.31903	−1.65202	0.4314
6.4321	−1.04619	3.51230	3.78694	−0.82054	−1.29068	−1.61586	0.4356
6.7176	−1.26654	3.51301	4.01011	−0.80424	−1.26770	−1.58688	0.4389
7.0334	−1.48652	3.51533	4.23939	−0.79296	−1.25100	−1.56537	0.4415
7.3642	−1.70697	3.51891	4.47416	−0.78583	−1.23985	−1.55026	0.4431
7.6995	−1.92729	3.52257	4.70909	−0.78085	−1.23225	−1.53986	0.4442
8.0548	−2.14553	3.52497	4.93695	−0.77777	−1.22748	−1.53335	0.4449
10.6112	−2.20936	3.52379	4.99604	−0.77516	−1.22409	−1.52931	0.4454
11.2902	−2.19614	3.52114	4.97222	−0.77199	−1.22018	−1.52496	0.4460
11.5380	−2.19642	3.51947	4.96584	−0.76888	−1.21631	−1.52062	0.4467
11.6906	−2.19515	3.51849	4.96065	−0.76589	−1.21259	−1.51646	0.4473
11.8000	−2.19208	3.51826	4.95666	−0.76305	−1.20902	−1.51246	0.4478
11.8846	−2.18474	3.51953	4.95438	−0.76066	−1.20603	−1.50915	0.4483
11.9528	−2.16183	3.52581	4.95657	−0.75945	−1.20464	−1.50783	0.4485

Table A.27: Evolutionary tracks including internal structure constants and gyration radii for 0.30 $M_\odot$ pre-MS tidal distorted models.

$\log(age)$	$\log(L/L_\odot)$	$\log(T_{\rm eff})$	$\log(g)$	$\log(k_2)$	$\log(k_3)$	$\log(k_4)$	β
2.9991	0.69804	3.55038	2.37284	−0.93554	−1.43838	−1.79473	0.4132
4.2757	0.47189	3.55458	2.61479	−0.89482	−1.39469	−1.74663	0.4205
4.7492	0.25144	3.55701	2.84455	−0.86949	−1.35976	−1.70321	0.4255
5.1481	0.03282	3.55806	3.06719	−0.85092	−1.33415	−1.67147	0.4292
5.7330	−0.14682	3.55802	3.24660	−0.83726	−1.31543	−1.64845	0.4320
5.8791	−0.31062	3.55696	3.40613	−0.82437	−1.29794	−1.62708	0.4346
6.0987	−0.53153	3.55397	3.61506	−0.80840	−1.27545	−1.59905	0.4380
6.3586	−0.75208	3.55010	3.82013	−0.79449	−1.25542	−1.57346	0.4409
6.6461	−0.97263	3.54588	4.02378	−0.78315	−1.23893	−1.55216	0.4434
6.9519	−1.19317	3.54162	4.22726	−0.77355	−1.22533	−1.53484	0.4454
7.2770	−1.41330	3.53958	4.43922	−0.76676	−1.21522	−1.52166	0.4470
7.6188	−1.63322	3.54062	4.66332	−0.76943	−1.21501	−1.51885	0.4480
8.0003	−1.85032	3.54347	4.89183	−0.78937	−1.23664	−1.54032	0.4485
10.3665	−1.88156	3.54327	4.92224	−0.75501	−1.19877	−1.50065	0.4489
10.9210	−1.87780	3.54255	4.91562	−0.75384	−1.19721	−1.49882	0.4491
11.1538	−1.87597	3.54233	4.91291	−0.75271	−1.19570	−1.49703	0.4494
11.3024	−1.87291	3.54253	4.91066	−0.75165	−1.19427	−1.49532	0.4496
11.4111	−1.86849	3.54320	4.90892	−0.75064	−1.19289	−1.49368	0.4498
11.4865	−1.85539	3.54622	4.90789	−0.79548	−1.25288	−1.56383	0.4450
11.5269	−1.82574	3.55018	4.89407	−0.82121	−1.27869	−1.59078	0.4375

Table A.28: Evolutionary tracks including internal structure constants and gyration radii for 0.40 $M_\odot$ pre-MS tidal distorted models.

$\log(age)$	$\log(L/L_\odot)$	$\log(T_{\rm eff})$	$\log(g)$	$\log(k_2)$	$\log(k_3)$	$\log(k_4)$	β
2.7435	1.04902	3.56581	2.20852	−0.93863	−1.44166	−1.79763	0.4126
4.0392	0.82513	3.57384	2.46354	−0.88779	−1.38533	−1.73561	0.4218
4.5170	0.60464	3.57905	2.70445	−0.85444	−1.33933	−1.67865	0.4284
4.9046	0.38470	3.58224	2.93697	−0.83255	−1.30869	−1.64026	0.4329
5.5165	0.18299	3.58367	3.14434	−0.81904	−1.28957	−1.61615	0.4358
5.6822	0.04482	3.58398	3.28371	−0.81111	−1.27855	−1.60238	0.4374
5.8955	−0.17588	3.58326	3.50152	−0.79892	−1.26167	−1.58145	0.4399
6.1490	−0.39672	3.58054	3.71146	−0.78753	−1.24555	−1.56118	0.4424
6.4273	−0.61764	3.57603	3.91434	−0.77763	−1.23108	−1.54253	0.4445
6.7230	−0.83818	3.57077	4.11383	−0.76873	−1.21834	−1.52615	0.4464
7.0299	−1.05885	3.56516	4.31205	−0.76122	−1.20763	−1.51248	0.4481
7.3483	−1.27900	3.56039	4.51314	−0.78022	−1.22478	−1.52756	0.4492
7.7022	−1.49615	3.55958	4.72704	−0.79462	−1.24856	−1.55640	0.4468
8.3031	−1.68069	3.56200	4.92124	−0.79742	−1.25249	−1.56413	0.4421
10.2803	−1.63369	3.56161	4.87270	−0.79740	−1.25580	−1.56849	0.4420
10.6348	−1.60686	3.56409	4.85578	−0.82739	−1.28383	−1.59577	0.4345
10.8450	−1.57274	3.56743	4.83503	−0.87240	−1.32624	−1.63738	0.4249
10.9901	−1.52881	3.57176	4.80843	−0.93358	−1.38434	−1.69530	0.4131
11.0930	−1.47425	3.57723	4.77574	−1.01952	−1.46456	−1.77407	0.3994
11.1710	−1.40440	3.58434	4.73433	−1.14109	−1.57833	−1.88587	0.3837

Table A.29: Evolutionary tracks including internal structure constants and gyration radii for 0.50 $M_\odot$ pre-MS tidal distorted models.

$\log(age)$	$\log(L/L_\odot)$	$\log(T_{\rm eff})$	$\log(g)$	$\log(k_2)$	$\log(k_3)$	$\log(k_4)$	β
2.8043	1.14200	3.58159	2.27563	−0.90613	−1.39727	−1.74296	0.4189
4.1221	0.91931	3.59015	2.53148	−0.86107	−1.34817	−1.68936	0.4271
4.6028	0.69892	3.59611	2.77532	−0.83133	−1.30679	−1.63787	0.4332
5.0383	0.48364	3.59981	3.00521	−0.81212	−1.27961	−1.60358	0.4372
5.5295	0.31234	3.60148	3.18311	−0.80190	−1.26501	−1.58501	0.4394
5.6887	0.14147	3.60204	3.35619	−0.79380	−1.25356	−1.57052	0.4411
5.9326	−0.07908	3.60137	3.57405	−0.78453	−1.24056	−1.55423	0.4431
6.2069	−0.29992	3.59876	3.78443	−0.77588	−1.22824	−1.53866	0.4449
6.4956	−0.52076	3.59398	3.98614	−0.76809	−1.21694	−1.52412	0.4466
6.7949	−0.74147	3.58805	4.18316	−0.76103	−1.20681	−1.51107	0.4482
7.1033	−0.96201	3.58183	4.37882	−0.77997	−1.22404	−1.52628	0.4494
7.4378	−1.18013	3.57746	4.57943	−0.79486	−1.24872	−1.55642	0.4466
7.7805	−1.33434	3.58144	4.74959	−0.84118	−1.29708	−1.60926	0.4289
9.1401	−1.40730	3.58238	4.82630	−0.86106	−1.31168	−1.62122	0.4249
10.2295	−1.36381	3.58614	4.79785	−0.88560	−1.33792	−1.64828	0.4169
10.5219	−1.32095	3.59105	4.77460	−0.94372	−1.39503	−1.70484	0.4071
10.6988	−1.26933	3.59707	4.74708	−1.01767	−1.46709	−1.77622	0.3955
10.8182	−1.20853	3.60429	4.71516	−1.10889	−1.55521	−1.86343	0.3828
10.9060	−1.13572	3.61290	4.67678	−1.21943	−1.66097	−1.96835	0.3687
10.9735	−1.04709	3.62295	4.62836	−1.37366	−1.80950	−2.11588	0.3531

Table A.30: Evolutionary tracks including internal structure constants and gyration radii for 0.60 $M_\odot$ pre-MS tidal distorted models.

$\log(age)$	$\log(L/L_\odot)$	$\log(T_{\rm eff})$	$\log(g)$	$\log(k_2)$	$\log(k_3)$	$\log(k_4)$	β
2.8468	1.24110	3.59193	2.29706	−0.88882	−1.37332	−1.71316	0.4224
4.1586	1.01801	3.60131	2.55663	−0.84750	−1.32881	−1.66485	0.4300
4.6410	0.79774	3.60815	2.80383	−0.81936	−1.28950	−1.61583	0.4358
5.2475	0.58925	3.61256	3.02979	−0.80150	−1.26407	−1.58362	0.4396
5.4796	0.44963	3.61451	3.17716	−0.79320	−1.25216	−1.56841	0.4413
5.6831	0.24568	3.61590	3.38660	−0.78427	−1.23936	−1.55207	0.4433
5.9430	0.02498	3.61555	3.60590	−0.77657	−1.22848	−1.53831	0.4449
6.2272	−0.19561	3.61329	3.81742	−0.76959	−1.21852	−1.52569	0.4464
6.5220	−0.41655	3.60883	4.02053	−0.76325	−1.20936	−1.51391	0.4478
6.8218	−0.63733	3.60260	4.21636	−0.77204	−1.21516	−1.51716	0.4491
7.1379	−0.85716	3.59651	4.41185	−0.79026	−1.24015	−1.54494	0.4483
7.4677	−1.03601	3.59657	4.59094	−0.82184	−1.27816	−1.58972	0.4352
7.7611	−1.07545	3.61355	4.69828	−0.99285	−1.44611	−1.75569	0.3982
9.0094	−1.12782	3.61414	4.75304	−1.00478	−1.45956	−1.76794	0.3969
10.0268	−1.07991	3.61952	4.72662	−1.04927	−1.50455	−1.81333	0.3887
10.3127	−1.02908	3.62611	4.70217	−1.11573	−1.57027	−1.87903	0.3788
10.4881	−0.96764	3.63396	4.67213	−1.20412	−1.65773	−1.96657	0.3672
10.6082	−0.89556	3.64280	4.63543	−1.31280	−1.76391	−2.07255	0.3541
10.6955	−0.81113	3.65252	4.58985	−1.45054	−1.89793	−2.20637	0.3398
10.7617	−0.70894	3.66335	4.53097	−1.62407	−2.06398	−2.37162	0.3246

Table A.31: Evolutionary tracks including internal structure constants and gyration radii for 0.70 $M_\odot$ pre-MS tidal distorted models.

$\log(age)$	$\log(L/L_\odot)$	$\log(T_{\rm eff})$	$\log(g)$	$\log(k_2)$	$\log(k_3)$	$\log(k_4)$	β
2.7548	1.39039	3.59617	2.23166	−0.88824	−1.37195	−1.71081	0.4225
4.0829	1.16857	3.60695	2.49553	−0.84710	−1.32804	−1.66353	0.4300
4.5680	0.94810	3.61527	2.74888	−0.81780	−1.28723	−1.61281	0.4361
5.1412	0.73798	3.62107	2.98202	−0.79806	−1.25917	−1.57732	0.4402
5.4144	0.59498	3.62394	3.13644	−0.78864	−1.24563	−1.56004	0.4422
5.6105	0.40073	3.62642	3.34059	−0.77956	−1.23252	−1.54320	0.4442
5.8720	0.18007	3.62727	3.56461	−0.77224	−1.22205	−1.52983	0.4458
6.1580	−0.04059	3.62600	3.78018	−0.76618	−1.21342	−1.51888	0.4471
6.4553	−0.26150	3.62261	3.98753	−0.76069	−1.20552	−1.50878	0.4483
6.7563	−0.48230	3.61709	4.18624	−0.78345	−1.22719	−1.52886	0.4493
7.0792	−0.70035	3.61185	4.38335	−0.79627	−1.25006	−1.55754	0.4460
7.3858	−0.83837	3.61633	4.53929	−0.85624	−1.31204	−1.62381	0.4262
7.6341	−0.81285	3.64195	4.61625	−1.10372	−1.56045	−1.87042	0.3810
7.9000	−0.84584	3.65534	4.70279	−1.25380	−1.73328	−2.04977	0.3650
9.6759	−0.81825	3.65450	4.67187	−1.21455	−1.68679	−2.00074	0.3647
10.0325	−0.76691	3.66129	4.64767	−1.28342	−1.75562	−2.06974	0.3556
10.2286	−0.70622	3.66942	4.61949	−1.36645	−1.83787	−2.15215	0.3453
10.3672	−0.62998	3.67942	4.58327	−1.47400	−1.94308	−2.25722	0.3332
10.4678	−0.53876	3.68990	4.53397	−1.61248	−2.07591	−2.38911	0.3192
10.5419	−0.42991	3.69936	4.46295	−1.81135	−2.26806	−2.58066	0.3034

Table A.32: Evolutionary tracks including internal structure constants and gyration radii for 0.80 $M_\odot$ pre-MS tidal distorted models.

$\log(age)$	$\log(L/L_\odot)$	$\log(T_{\rm eff})$	$\log(g)$	$\log(k_2)$	$\log(k_3)$	$\log(k_4)$	β
2.6879	1.51617	3.59896	2.17506	−0.88672	−1.36950	−1.70737	0.4229
4.0218	1.29513	3.61087	2.44265	−0.84634	−1.32688	−1.66184	0.4301
4.5086	1.07476	3.62039	2.70069	−0.81702	−1.28611	−1.61130	0.4361
5.0433	0.86445	3.62736	2.93869	−0.79633	−1.25674	−1.57421	0.4405
5.3615	0.71695	3.63110	3.10112	−0.78578	−1.24160	−1.55490	0.4428
5.5555	0.52736	3.63457	3.30455	−0.77617	−1.22770	−1.53702	0.4449
5.8199	0.30682	3.63667	3.53347	−0.76872	−1.21694	−1.52319	0.4465
6.1084	0.08587	3.63639	3.75330	−0.76312	−1.20894	−1.51298	0.4477
6.4072	−0.13491	3.63381	3.96377	−0.75828	−1.20200	−1.50413	0.4488
6.7121	−0.35542	3.62931	4.16625	−0.78759	−1.23311	−1.53520	0.4492
7.0371	−0.56130	3.62648	4.36081	−0.80549	−1.26153	−1.57113	0.4422
7.3180	−0.65229	3.63660	4.49228	−0.90779	−1.36185	−1.67273	0.4151
7.5295	−0.56658	3.67097	4.54405	−1.23006	−1.69182	−2.00261	0.3636
7.7281	−0.54436	3.69964	4.63653	−1.45534	−1.95776	−2.28236	0.3385
9.3577	−0.56736	3.69244	4.63073	−1.37074	−1.86276	−2.18328	0.3442
9.7841	−0.51590	3.69920	4.60630	−1.43858	−1.92946	−2.24962	0.3354
9.9949	−0.45795	3.70618	4.57628	−1.52547	−2.01623	−2.33665	0.3253
10.1368	−0.38982	3.71328	4.53654	−1.63734	−2.12709	−2.44750	0.3133
10.2463	−0.30479	3.72020	4.47917	−1.79022	−2.27671	−2.59668	0.2988
10.3324	−0.19595	3.72563	4.39207	−2.00774	−2.48504	−2.80322	0.2819

Table A.33: Evolutionary tracks including internal structure constants and gyration radii for 0.90 $M_\odot$ pre-MS tidal distorted models.

$\log(age)$	$\log(L/L_\odot)$	$\log(T_{\rm eff})$	$\log(g)$	$\log(k_2)$	$\log(k_3)$	$\log(k_4)$	β
2.6419	1.62383	3.60095	2.12649	−0.88434	−1.36606	−1.70288	0.4234
3.9729	1.40318	3.61379	2.39744	−0.84612	−1.32605	−1.66036	0.4303
4.4607	1.18291	3.62427	2.65919	−0.81739	−1.28616	−1.61096	0.4362
4.9690	0.97182	3.63223	2.90198	−0.79637	−1.25632	−1.57333	0.4407
5.3170	0.82235	3.63672	3.06933	−0.78517	−1.24027	−1.55285	0.4431
5.5087	0.63697	3.64096	3.27166	−0.77510	−1.22570	−1.53413	0.4453
5.7754	0.41649	3.64415	3.50486	−0.76719	−1.21423	−1.51934	0.4470
6.0670	0.19580	3.64511	3.72939	−0.76173	−1.20640	−1.50930	0.4482
6.3678	−0.02497	3.64347	3.94359	−0.76298	−1.20536	−1.50641	0.4491
6.6775	−0.24522	3.63990	4.14958	−0.78686	−1.23421	−1.53708	0.4486
6.9943	−0.42894	3.64014	4.33423	−0.81795	−1.27429	−1.58486	0.4373
7.2523	−0.47333	3.65635	4.44349	−0.96719	−1.42022	−1.73034	0.4033
7.4339	−0.34441	3.69758	4.47946	−1.33970	−1.80787	−2.12053	0.3484
7.5893	−0.26420	3.73362	4.54342	−1.68928	−2.21993	−2.55562	0.3090
9.0160	−0.34084	3.72511	4.58601	−1.52914	−2.04744	−2.37818	0.3228
9.5485	−0.29105	3.73014	4.55635	−1.61387	−2.13597	−2.46840	0.3131
9.7769	−0.23682	3.73503	4.52170	−1.70891	−2.23221	−2.56503	0.3024
9.9226	−0.17628	3.73954	4.47919	−1.82172	−2.34532	−2.67816	0.2908
10.0307	−0.10628	3.74332	4.42432	−1.95899	−2.48053	−2.81273	0.2780
10.1246	−0.01291	3.74559	4.34002	−2.15204	−2.66405	−2.99316	0.2629

Table A.34: Evolutionary tracks including internal structure constants and gyration radii for 1.00 $M_\odot$ pre-MS tidal distorted models.

$\log(age)$	$\log(L/L_\odot)$	$\log(T_{\rm eff})$	$\log(g)$	$\log(k_2)$	$\log(k_3)$	$\log(k_4)$	β
2.2954	1.89081	3.59019	1.86221	−0.91363	−1.40433	−1.74804	0.4177
3.6551	1.67266	3.60568	2.14122	−0.87144	−1.36043	−1.70207	0.4253
4.1465	1.45259	3.61851	2.41220	−0.83832	−1.31523	−1.64691	0.4319
4.5436	1.23220	3.62932	2.67568	−0.81173	−1.27812	−1.60077	0.4374
5.1030	1.02510	3.63764	2.91599	−0.79238	−1.25059	−1.56597	0.4415
5.3018	0.89817	3.64183	3.05969	−0.78311	−1.23728	−1.54898	0.4435
5.5216	0.69054	3.64722	3.28887	−0.77188	−1.22101	−1.52806	0.4459
5.7953	0.46991	3.65099	3.52454	−0.76416	−1.20982	−1.51362	0.4476
6.0918	0.24932	3.65262	3.75165	−0.75899	−1.20238	−1.50405	0.4488
6.3961	0.02856	3.65157	3.96820	−0.78237	−1.22509	−1.52565	0.4495
6.7156	−0.18661	3.64965	4.17573	−0.79617	−1.24928	−1.55602	0.4458
7.0039	−0.31572	3.65598	4.33014	−0.85553	−1.31054	−1.62175	0.4260
7.2246	−0.27724	3.68400	4.40376	−1.10123	−1.55456	−1.86337	0.3811
7.3696	−0.11545	3.72546	4.40779	−1.56793	−2.05820	−2.37807	0.3202
7.4907	−0.03901	3.75728	4.45864	−1.90728	−2.47332	−2.82331	0.2812
8.7579	−0.13023	3.75157	4.52702	−1.71889	−2.27289	−2.61835	0.2974
9.3537	−0.08155	3.75533	4.49336	−1.81065	−2.36871	−2.71568	0.2872
9.5876	−0.03069	3.75866	4.45583	−1.91175	−2.47417	−2.82308	0.2767
9.6979	0.00841	3.76078	4.42520	−1.99125	−2.55553	−2.90505	0.2689
9.8059	0.06194	3.76269	4.37931	−2.10411	−2.67069	−3.02173	0.2588

Table A.35: Evolutionary tracks including internal structure constants and gyration radii for 1.20 $M_\odot$ pre-MS tidal distorted models.

$\log(age)$	$\log(L/L_\odot)$	$\log(T_{\rm eff})$	$\log(g)$	$\log(k_2)$	$\log(k_3)$	$\log(k_4)$	β
2.2057	2.04980	3.59158	1.78796	−0.90482	−1.39220	−1.73287	0.4194
3.5814	1.83252	3.60787	2.06933	−0.86599	−1.35278	−1.69242	0.4264
4.0773	1.61210	3.62191	2.34548	−0.83513	−1.31061	−1.64095	0.4326
4.4759	1.39190	3.63386	2.61333	−0.81035	−1.27595	−1.59780	0.4377
5.0181	1.18281	3.64370	2.86171	−0.79156	−1.24920	−1.56400	0.4417
5.2406	1.05353	3.64883	3.01149	−0.78213	−1.23568	−1.54674	0.4437
5.4589	0.85106	3.65554	3.24078	−0.77057	−1.21896	−1.52526	0.4462
5.7366	0.63067	3.66100	3.48301	−0.76203	−1.20657	−1.50925	0.4481
6.0380	0.41004	3.66444	3.71742	−0.75652	−1.19861	−1.49898	0.4493
6.3521	0.18984	3.66588	3.94338	−0.78870	−1.23442	−1.53592	0.4492
6.6604	0.00563	3.66886	4.13950	−0.81093	−1.26670	−1.57628	0.4401
6.9142	−0.05901	3.68338	4.26222	−0.93004	−1.38209	−1.69161	0.4106
7.0947	0.03669	3.71492	4.29268	−1.29185	−1.75308	−2.06321	0.3551
7.2054	0.23034	3.75111	4.24376	−1.86825	−2.39590	−2.72973	0.2855
7.2767	0.37730	3.78157	4.21864	−2.33727	−2.98117	−3.37206	0.2333
7.3557	0.25077	3.79134	4.38430	−2.17845	−2.85979	−3.27903	0.2487
8.5440	0.25361	3.79453	4.39419	−2.16526	−2.85218	−3.27787	0.2451
9.0480	0.29443	3.79635	4.36065	−2.25356	−2.95021	−3.38317	0.2368
9.2511	0.33117	3.79736	4.32797	−2.33358	−3.03666	−3.47458	0.2297
9.3704	0.36278	3.79747	4.29680	−2.40224	−3.10723	−3.54627	0.2240

Table A.36: Evolutionary tracks including internal structure constants and gyration radii for 1.40 $M_\odot$ pre-MS tidal distorted models.

$\log(age)$	$\log(L/L_\odot)$	$\log(T_{\rm eff})$	$\log(g)$	$\log(k_2)$	$\log(k_3)$	$\log(k_4)$	β
2.1323	2.18047	3.59217	1.72662	−0.89628	−1.38048	−1.71829	0.4211
3.5222	1.96403	3.60908	2.00960	−0.86031	−1.34485	−1.68247	0.4275
4.0208	1.74390	3.62398	2.28890	−0.83154	−1.30551	−1.63448	0.4333
4.4214	1.52396	3.63698	2.56069	−0.80838	−1.27305	−1.59401	0.4381
4.9455	1.31309	3.64788	2.81511	−0.79058	−1.24766	−1.56189	0.4419
5.1915	1.18199	3.65386	2.97010	−0.78131	−1.23435	−1.54491	0.4439
5.4078	0.98460	3.66166	3.19868	−0.77000	−1.21802	−1.52394	0.4464
5.6887	0.76414	3.66848	3.44642	−0.76091	−1.20483	−1.50691	0.4484
5.9937	0.54377	3.67341	3.68651	−0.77136	−1.21231	−1.51179	0.4496
6.3119	0.33006	3.67720	3.91537	−0.79112	−1.24076	−1.54456	0.4478
6.5960	0.18427	3.68437	4.08983	−0.83161	−1.28669	−1.59668	0.4332
6.8236	0.16766	3.70343	4.18269	−1.02104	−1.47256	−1.78093	0.3945
6.9735	0.30603	3.73433	4.16792	−1.50086	−1.98010	−2.29579	0.3295
7.0597	0.51773	3.76609	4.08324	−2.13025	−2.70462	−3.05904	0.2566
7.1104	0.65840	3.79256	4.04845	−2.57625	−3.28745	−3.73083	0.2106
7.1476	0.70582	3.81502	4.09090	−2.76910	−3.57650	−4.10534	0.1936
7.2039	0.52742	3.81818	4.28195	−2.42272	−3.21634	−3.73514	0.2220
7.7908	0.55546	3.83256	4.31141	−2.47020	−3.29249	−3.84498	0.2136
8.8074	0.60023	3.83313	4.26893	−2.57143	−3.39909	−3.95655	0.2062
9.0640	0.63737	3.82985	4.21864	−2.65846	−3.48263	−4.03688	0.2004

Table A.37: Evolutionary tracks including internal structure constants and gyration radii for 1.60 $M_\odot$ pre-MS tidal distorted models.

$\log(age)$	$\log(L/L_\odot)$	$\log(T_{\rm eff})$	$\log(g)$	$\log(k_2)$	$\log(k_3)$	$\log(k_4)$	β
2.1002	2.29210	3.59233	1.67362	−0.88845	−1.36971	−1.70490	0.4227
3.4765	2.07557	3.60991	1.95934	−0.85436	−1.33671	−1.67237	0.4286
3.9755	1.85538	3.62542	2.24119	−0.82750	−1.29995	−1.62755	0.4341
4.3782	1.63508	3.63926	2.51668	−0.80575	−1.26941	−1.58944	0.4386
4.8838	1.42398	3.65103	2.77481	−0.78899	−1.24546	−1.55907	0.4422
5.1507	1.29137	3.65768	2.93400	−0.78012	−1.23270	−1.54278	0.4441
5.3643	1.09885	3.66624	3.16072	−0.76933	−1.21713	−1.52279	0.4464
5.6480	0.87851	3.67431	3.41335	−0.75999	−1.20361	−1.50536	0.4485
5.9567	0.65822	3.68055	3.65859	−0.78431	−1.22687	−1.52675	0.4496
6.2652	0.46111	3.68626	3.87854	−0.79750	−1.25029	−1.55653	0.4453
6.5301	0.34706	3.69645	4.03337	−0.85963	−1.31306	−1.62295	0.4252
6.7351	0.37082	3.71778	4.09492	−1.11824	−1.56952	−1.87701	0.3778
6.8608	0.54679	3.74744	4.03759	−1.70198	−2.20814	−2.53469	0.3047
6.9287	0.74905	3.77527	3.94665	−2.30942	−2.93899	−3.32848	0.2368
6.9693	0.87243	3.79936	3.91964	−2.69685	−3.46072	−3.95596	0.1990
7.0137	0.96910	3.84571	4.00838	−2.88549	−3.74474	−4.32847	0.1818
7.0652	0.78810	3.85102	4.21061	−2.55982	−3.41911	−4.00466	0.2075
7.3069	0.81071	3.88109	4.30827	−2.51172	−3.36759	−3.95688	0.2090
8.6333	0.84966	3.87864	4.25953	−2.60637	−3.46308	−4.05223	0.2028
8.9121	0.88261	3.86725	4.18101	−2.71278	−3.56645	−4.15342	0.1957

Table A.38: Evolutionary tracks including internal structure constants and gyration radii for 1.80 $M_\odot$ pre-MS tidal distorted models.

$\log(age)$	$\log(L/L_\odot)$	$\log(T_{\rm eff})$	$\log(g)$	$\log(k_2)$	$\log(k_3)$	$\log(k_4)$	β
2.0317	2.38990	3.59233	1.62696	−0.88120	−1.35972	−1.69249	0.4241
3.4302	2.17462	3.61022	1.91269	−0.85034	−1.33070	−1.66458	0.4296
3.9318	1.95452	3.62623	2.19643	−0.82513	−1.29620	−1.62254	0.4347
4.3363	1.73421	3.64070	2.47447	−0.80462	−1.26736	−1.58654	0.4390
4.8195	1.52272	3.65330	2.73630	−0.78874	−1.24462	−1.55768	0.4424
5.1153	1.38707	3.66065	2.90133	−0.78015	−1.23225	−1.54185	0.4442
5.3261	1.19907	3.66981	3.12597	−0.77001	−1.21761	−1.52306	0.4465
5.6123	0.97864	3.67896	3.38297	−0.76066	−1.20409	−1.50564	0.4485
5.9228	0.76032	3.68634	3.63083	−0.78607	−1.23085	−1.53174	0.4492
6.2166	0.58319	3.69365	3.83719	−0.80487	−1.25995	−1.56847	0.4420
6.4657	0.49659	3.70598	3.97310	−0.89978	−1.35203	−1.66142	0.4163
6.6500	0.55826	3.72858	4.00184	−1.24944	−1.70847	−2.01781	0.3604
6.7542	0.76247	3.75649	3.90925	−1.89185	−2.43161	−2.77273	0.2820
6.8101	0.93735	3.78136	3.83384	−2.43114	−3.11110	−3.54125	0.2240
6.8446	1.04735	3.80539	3.81997	−2.75148	−3.54546	−4.07544	0.1939
6.9003	1.19452	3.88787	4.00275	−2.87467	−3.73366	−4.31990	0.1829
6.9454	1.00859	3.89057	4.19946	−2.54961	−3.41146	−4.00111	0.2085
7.0768	1.04525	3.92804	4.31270	−2.50326	−3.35823	−3.94776	0.2105
8.4297	1.05565	3.92142	4.27582	−2.55638	−3.41083	−3.99974	0.2071
8.7435	1.08808	3.90705	4.18588	−2.66911	−3.52033	−4.10711	0.1993

Table A.39: Evolutionary tracks including internal structure constants and gyration radii for 2.00 $M_\odot$ pre-MS tidal distorted models.

$\log(age)$	$\log(L/L_\odot)$	$\log(T_{\rm eff})$	$\log(g)$	$\log(k_2)$	$\log(k_3)$	$\log(k_4)$	β
2.0185	2.47686	3.59235	1.58587	−0.87453	−1.35051	−1.68104	0.4255
3.3983	2.25960	3.61048	1.87451	−0.84531	−1.32368	−1.65581	0.4306
3.8989	2.03968	3.62691	2.15974	−0.82163	−1.29125	−1.61628	0.4354
4.3041	1.81967	3.64196	2.43978	−0.80233	−1.26407	−1.58234	0.4395
4.7742	1.60767	3.65519	2.70464	−0.78728	−1.24248	−1.55490	0.4427
5.0848	1.47116	3.66299	2.87236	−0.77911	−1.23071	−1.53982	0.4444
5.2916	1.28861	3.67264	3.09349	−0.76967	−1.21707	−1.52231	0.4465
5.5798	1.06807	3.68266	3.35409	−0.76962	−1.21243	−1.51368	0.4485
5.8862	0.85684	3.69108	3.59901	−0.78860	−1.23607	−1.53856	0.4483
6.1670	0.69769	3.69968	3.79254	−0.81532	−1.27081	−1.58033	0.4381
6.4024	0.63666	3.71369	3.90961	−0.95143	−1.40367	−1.71292	0.4065
6.5668	0.73453	3.73674	3.90397	−1.38942	−1.86216	−2.17607	0.3426
6.6529	0.94692	3.76272	3.79547	−2.04255	−2.62522	−2.99068	0.2645
6.7015	1.09615	3.78584	3.73875	−2.51189	−3.23497	−3.70464	0.2159
6.7414	1.22905	3.82339	3.75603	−2.82061	−3.65169	−4.22061	0.1878
6.7974	1.39040	3.92434	3.99851	−2.85303	−3.71104	−4.29769	0.1849
6.8387	1.20178	3.92584	4.19313	−2.52604	−3.38681	−3.97642	0.2106
6.9453	1.25063	3.96762	4.31140	−2.49140	−3.34624	−3.93609	0.2119
8.2619	1.23784	3.95739	4.28326	−2.51461	−3.36744	−3.95622	0.2109
8.5966	1.26924	3.94111	4.18672	−2.62792	−3.47730	−4.06378	0.2027

Table A.40: Evolutionary tracks including internal structure constants and gyration radii for 2.30 $M_\odot$ pre-MS tidal distorted models.

$\log(age)$	$\log(L/L_\odot)$	$\log(T_{\rm eff})$	$\log(g)$	$\log(k_2)$	$\log(k_3)$	$\log(k_4)$	β
1.9530	2.58943	3.59198	1.53252	−0.86531	−1.33775	−1.66517	0.4274
3.3489	2.37341	3.61053	1.82161	−0.83907	−1.31479	−1.64456	0.4319
3.8516	2.15337	3.62742	2.10880	−0.81740	−1.28508	−1.60837	0.4363
4.2585	1.93330	3.64309	2.39138	−0.79960	−1.25999	−1.57700	0.4400
4.7101	1.72054	3.65721	2.66058	−0.78564	−1.23992	−1.55146	0.4430
5.0455	1.58156	3.66579	2.83384	−0.77791	−1.22875	−1.53714	0.4447
5.2501	1.40298	3.67599	3.05321	−0.76932	−1.21633	−1.52116	0.4466
5.5399	1.18391	3.68715	3.31691	−0.78808	−1.23249	−1.53427	0.4484
5.8327	0.98959	3.69667	3.54931	−0.79960	−1.25330	−1.56009	0.4460
6.0966	0.85574	3.70689	3.72407	−0.83982	−1.29501	−1.60546	0.4308
6.3122	0.83489	3.72288	3.80888	−1.04954	−1.50114	−1.80923	0.3892
6.4453	0.98711	3.74592	3.74879	−1.61486	−2.12096	−2.44815	0.3140
6.5125	1.17456	3.76912	3.65416	−2.19885	−2.84355	−3.25504	0.2465
6.5539	1.29798	3.79234	3.62362	−2.56753	−3.33110	−3.84471	0.2097
6.6080	1.48925	3.86824	3.73593	−2.80539	−3.64033	−4.21609	0.1886
6.6581	1.64346	3.97002	3.98886	−2.81363	−3.66744	−4.25241	0.1877
6.6963	1.45491	3.97152	4.18342	−2.48731	−3.34379	−3.93129	0.2136
6.7867	1.50802	4.01626	4.30924	−2.46131	−3.31338	−3.90154	0.2150
8.0527	1.47658	4.00263	4.28617	−2.45992	−3.30897	−3.89575	0.2157
8.4192	1.51090	3.98511	4.18177	−2.58190	−3.42713	−4.01148	0.2068

Table A.41: Evolutionary tracks including internal structure constants and gyration radii for 2.50 $M_\odot$ pre-MS tidal distorted models.

$\log(age)$	$\log(L/L_\odot)$	$\log(T_{\rm eff})$	$\log(g)$	$\log(k_2)$	$\log(k_3)$	$\log(k_4)$	β
1.9521	2.65647	3.59172	1.50062	−0.85993	−1.33024	−1.65577	0.4285
3.3255	2.43950	3.61061	1.79203	−0.83554	−1.30956	−1.63784	0.4327
3.8273	2.21924	3.62774	2.08039	−0.81513	−1.28157	−1.60374	0.4369
4.2343	1.99921	3.64372	2.36421	−0.79822	−1.25770	−1.57389	0.4404
4.6794	1.78577	3.65830	2.63590	−0.78491	−1.23854	−1.54948	0.4433
5.0223	1.64687	3.66720	2.81037	−0.77755	−1.22790	−1.53582	0.4449
5.2222	1.47341	3.67757	3.02530	−0.76955	−1.21633	−1.52093	0.4466
5.5086	1.25863	3.68930	3.28702	−0.79422	−1.24099	−1.54389	0.4480
5.7924	1.07496	3.69939	3.51103	−0.80148	−1.25723	−1.56600	0.4440
6.0470	0.95597	3.71050	3.67449	−0.85584	−1.31053	−1.62153	0.4254
6.2496	0.96148	3.72736	3.73640	−1.12302	−1.57757	−1.88599	0.3772
6.3643	1.13820	3.75002	3.65030	−1.73618	−2.27408	−2.61814	0.2979
6.4248	1.30085	3.77196	3.57544	−2.25307	−2.93013	−3.37037	0.2393
6.4636	1.41455	3.79647	3.55977	−2.57013	−3.35040	−3.88474	0.2082
6.5254	1.63845	3.89347	3.72389	−2.77696	−3.61085	−4.18805	0.1903
6.5729	1.79051	3.99497	3.97783	−2.78048	−3.63212	−4.21745	0.1895
6.6099	1.60783	3.99877	4.17567	−2.47000	−3.32504	−3.91293	0.2151
6.6939	1.65864	4.04388	4.30531	−2.43967	−3.28964	−3.87774	0.2169
7.9351	1.61801	4.02884	4.28580	−2.42926	−3.27589	−3.86263	0.2186
8.3174	1.65438	4.01094	4.17783	−2.55215	−3.39478	−3.97909	0.2093

Table A.42: Evolutionary tracks including internal structure constants and gyration radii for 2.80 $M_\odot$ pre-MS tidal distorted models.

$\log(age)$	$\log(L/L_\odot)$	$\log(T_{\rm eff})$	$\log(g)$	$\log(k_2)$	$\log(k_3)$	$\log(k_4)$	β
1.9056	2.74612	3.59122	1.45821	−0.85257	−1.31994	−1.64288	0.4300
3.2872	2.53009	3.61041	1.74988	−0.83033	−1.30207	−1.62832	0.4338
3.7905	2.30985	3.62791	2.03971	−0.81166	−1.27642	−1.59708	0.4376
4.1986	2.08984	3.64433	2.32524	−0.79597	−1.25425	−1.56933	0.4409
4.6331	1.87543	3.65948	2.60020	−0.78349	−1.23627	−1.54640	0.4436
4.9913	1.73478	3.66894	2.77864	−0.77654	−1.22621	−1.53347	0.4451
5.1865	1.56695	3.67954	2.98887	−0.78567	−1.23172	−1.53584	0.4467
5.4626	1.36302	3.69169	3.24139	−0.79533	−1.24587	−1.55100	0.4470
5.7344	1.19487	3.70258	3.45311	−0.80661	−1.26339	−1.57402	0.4401
5.9761	1.09915	3.71493	3.59823	−0.89561	−1.34886	−1.65955	0.4154
6.1558	1.14957	3.73276	3.61913	−1.26888	−1.73857	−2.05192	0.3564
6.2477	1.33465	3.75443	3.52072	−1.88217	−2.47164	−2.84863	0.2791
6.3017	1.46756	3.77606	3.47434	−2.30866	−3.02705	−3.50702	0.2322
6.3507	1.61386	3.81996	3.50365	−2.60865	−3.41685	−3.98056	0.2039
6.4106	1.84022	3.92782	3.70873	−2.74153	−3.57437	−4.15136	0.1927
6.4554	1.98701	4.02859	3.96501	−2.73669	−3.58588	−4.16969	0.1923
6.4913	1.81118	4.03499	4.16643	−2.44404	−3.29766	−3.88475	0.2177
6.5713	1.85257	4.07972	4.30395	−2.40162	−3.24926	−3.83607	0.2206
7.7977	1.80960	4.06319	4.28081	−2.38954	−3.23362	−3.81896	0.2222
8.1877	1.84893	4.04516	4.16938	−2.51645	−3.35652	−3.93939	0.2125

Table A.43: Evolutionary tracks including internal structure constants and gyration radii for 3.00 $M_\odot$ pre-MS tidal distorted models.

$\log(age)$	$\log(L/L_\odot)$	$\log(T_{\rm eff})$	$\log(g)$	$\log(k_2)$	$\log(k_3)$	$\log(k_4)$	β
1.9034	2.78865	3.59222	1.44950	−0.84784	−1.31320	−1.63441	0.4310
3.2857	2.57170	3.61129	1.74168	−0.82560	−1.29555	−1.62025	0.4347
3.7896	2.35171	3.62898	2.03204	−0.80816	−1.27154	−1.59094	0.4382
4.1985	2.13162	3.64557	2.31837	−0.79338	−1.25061	−1.56471	0.4414
4.6472	1.91825	3.66094	2.59315	−0.78165	−1.23368	−1.54308	0.4439
4.9803	1.78092	3.67033	2.76802	−0.77514	−1.22426	−1.53097	0.4453
5.1829	1.60957	3.68152	2.98415	−0.79854	−1.24643	−1.55107	0.4467
5.4529	1.41532	3.69376	3.22734	−0.79948	−1.25462	−1.56293	0.4455
5.7158	1.26184	3.70520	3.42657	−0.81756	−1.27423	−1.58589	0.4352
5.9460	1.19214	3.71863	3.55001	−0.95117	−1.40230	−1.71152	0.4033
6.1001	1.28886	3.73736	3.52818	−1.43235	−1.92955	−2.25499	0.3348
6.1780	1.45825	3.75820	3.44218	−1.98857	−2.61689	−3.02246	0.2657
6.2274	1.57537	3.78086	3.41569	−2.35000	−3.09319	−3.59917	0.2272
6.2862	1.75764	3.84809	3.50233	−2.60788	−3.41724	−3.98364	0.2035
6.3430	1.97834	3.95765	3.71990	−2.72191	−3.55303	−4.12970	0.1938
6.3857	2.10762	4.05503	3.98014	−2.71254	−3.55712	−4.13946	0.1950
6.4209	1.91550	4.05463	4.17062	−2.40084	−3.24774	−3.83202	0.2212
6.5034	1.94913	4.09915	4.31510	−2.34746	−3.18943	−3.77388	0.2252
7.7747	1.92889	4.08203	4.26684	−2.37142	−3.21004	−3.79264	0.2236
8.1295	1.96995	4.06428	4.15481	−2.50231	−3.33672	−3.91705	0.2137

Table A.44: Evolutionary tracks including internal structure constants and gyration radii for 3.30 $M_\odot$ pre-MS tidal distorted models.

$\log(age)$	$\log(L/L_\odot)$	$\log(T_{\rm eff})$	$\log(g)$	$\log(k_2)$	$\log(k_3)$	$\log(k_4)$	β
1.8938	2.85541	3.59218	1.42411	−0.84082	−1.30349	−1.62240	0.4324
3.2679	2.63961	3.61169	1.71680	−0.82166	−1.28951	−1.61235	0.4356
3.7717	2.41966	3.62955	2.00781	−0.80563	−1.26739	−1.58531	0.4389
4.1816	2.19944	3.64648	2.29559	−0.79197	−1.24800	−1.56098	0.4418
4.6326	1.98623	3.66217	2.57150	−0.78108	−1.23225	−1.54084	0.4442
4.9584	1.85098	3.67177	2.74513	−0.77507	−1.22356	−1.52966	0.4455
5.1842	1.66503	3.68443	2.98171	−0.80295	−1.25578	−1.56292	0.4460
5.4450	1.48797	3.69691	3.20870	−0.80354	−1.26177	−1.57352	0.4414
5.6939	1.36113	3.70918	3.38463	−0.85180	−1.30654	−1.61870	0.4240
5.8985	1.34749	3.72451	3.45955	−1.11830	−1.57876	−1.88919	0.3774
6.0126	1.49490	3.74382	3.38941	−1.68026	−2.23779	−2.59581	0.3021
6.0783	1.62470	3.76433	3.34164	−2.12519	−2.81467	−3.27319	0.2499
6.1264	1.73796	3.79378	3.34619	−2.41836	−3.19891	−3.74371	0.2200
6.1967	1.96945	3.89455	3.51777	−2.61651	−3.43060	−4.00072	0.2032
6.2487	2.17445	4.00404	3.75074	−2.70191	−3.53581	−4.11393	0.1954
6.2893	2.26221	4.09273	4.01773	−2.66708	−3.51314	−4.09629	0.2006
6.3259	2.04804	4.08063	4.18351	−2.33724	−3.17696	−3.75868	0.2272
6.4166	2.06938	4.12230	4.32885	−2.27236	−3.10876	−3.69138	0.2324
7.7737	2.09631	4.10630	4.23791	−2.36954	−3.20586	−3.78738	0.2247
8.0641	2.13932	4.08914	4.12624	−2.50280	−3.33485	−3.91427	0.2147

Table A.45: Evolutionary tracks including internal structure constants and gyration radii for 3.50 $M_\odot$ pre-MS tidal distorted models.

$\log(age)$	$\log(L/L_\odot)$	$\log(T_{\rm eff})$	$\log(g)$	$\log(k_2)$	$\log(k_3)$	$\log(k_4)$	β
1.8942	2.88840	3.59309	1.42034	−0.83650	−1.29742	−1.61485	0.4333
3.2703	2.67275	3.61261	1.71292	−0.81826	−1.28460	−1.60612	0.4363
3.7747	2.45271	3.63056	2.00432	−0.80318	−1.26373	−1.58056	0.4394
4.1848	2.23276	3.64762	2.29237	−0.79032	−1.24544	−1.55757	0.4422
4.6552	2.02020	3.66347	2.56829	−0.77997	−1.23046	−1.53839	0.4444
4.9484	1.89076	3.67278	2.73493	−0.79068	−1.23831	−1.54385	0.4456
5.1846	1.70155	3.68623	2.97793	−0.80459	−1.26111	−1.57075	0.4447
5.4389	1.53715	3.69886	3.19288	−0.81240	−1.27057	−1.58344	0.4370
5.6777	1.43273	3.71191	3.34950	−0.89999	−1.35185	−1.66203	0.4131
5.8579	1.46451	3.72821	3.38291	−1.26842	−1.74650	−2.06319	0.3562
5.9532	1.61287	3.74743	3.31142	−1.81210	−2.41201	−2.79958	0.2854
6.0133	1.72421	3.76898	3.28627	−2.18583	−2.90218	−3.38752	0.2428
6.0739	1.87360	3.81997	3.34085	−2.45958	−3.25199	−3.80989	0.2160
6.1401	2.10447	3.92619	3.53486	−2.61938	−3.43310	−4.00320	0.2028
6.1891	2.29451	4.03392	3.77574	−2.68216	−3.51402	−4.09070	0.1967
6.2291	2.34308	4.11364	4.04604	−2.60668	−3.45164	−4.03354	0.2057
6.2775	2.15856	4.10571	4.19886	−2.32158	−3.15277	−3.73043	0.2285
6.4017	2.15950	4.13819	4.32781	−2.24333	−3.07361	−3.65293	0.2350
7.7650	2.19970	4.12107	4.21916	−2.36054	−3.19109	−3.76935	0.2252
8.0232	2.24364	4.10423	4.10785	−2.49637	−3.32266	−3.89908	0.2152

Table A.46: Evolutionary tracks including internal structure constants and gyration radii for 3.80 $M_\odot$ pre-MS tidal distorted models.

$\log(age)$	$\log(L/L_\odot)$	$\log(T_{\rm eff})$	$\log(g)$	$\log(k_2)$	$\log(k_3)$	$\log(k_4)$	β
1.9054	2.93271	3.59451	1.41741	−0.83070	−1.28918	−1.60456	0.4345
3.2775	2.71692	3.61403	1.71016	−0.81383	−1.27809	−1.59779	0.4373
3.7822	2.49677	3.63207	2.00202	−0.80005	−1.25893	−1.57424	0.4401
4.1931	2.27697	3.64935	2.29078	−0.78823	−1.24207	−1.55300	0.4427
4.6972	2.06485	3.66542	2.56713	−0.77867	−1.22822	−1.53523	0.4447
4.9571	1.92717	3.67558	2.74547	−0.80596	−1.25838	−1.56578	0.4454
5.1897	1.75313	3.68897	2.97306	−0.80935	−1.26988	−1.58334	0.4411
5.4329	1.61272	3.70204	3.16573	−0.84316	−1.30007	−1.61363	0.4267
5.6503	1.55659	3.71650	3.27970	−1.04040	−1.49819	−1.80838	0.3891
5.7869	1.65140	3.73369	3.25365	−1.52606	−2.06172	−2.40743	0.3213
5.8660	1.76942	3.75304	3.21302	−1.97299	−2.63861	−3.07762	0.2659
5.9196	1.86431	3.77738	3.21550	−2.25905	−3.01643	−3.54167	0.2348
5.9980	2.07069	3.86449	3.35758	−2.48351	−3.28554	−3.85111	0.2141
6.0588	2.29513	3.97330	3.56836	−2.62229	−3.44351	−4.01799	0.2025
6.1041	2.45984	4.07742	3.82013	−2.64941	−3.48609	−4.06515	0.1991
6.1438	2.43517	4.13781	4.08636	−2.49603	−3.34566	−3.93049	0.2146
6.1998	2.34738	4.14837	4.21639	−2.33161	−3.16243	−3.74145	0.2277
7.0015	2.29851	4.15993	4.31149	−2.23612	−3.06931	−3.65104	0.2367
7.7563	2.34577	4.14101	4.18855	−2.37227	−3.20349	−3.78309	0.2256
7.9708	2.39048	4.12444	4.07755	−2.50738	−3.33379	−3.91146	0.2155

A.3 Rotating models: single rotating stars

Pre-main sequence evolutionary tracks for rotating stellar models are given in Tables (A.47) to (A.69). Same header as in tables of Appendix (A.1).

Table A.47: Evolutionary tracks including internal structure constants and gyration radii for 0.09 $M_\odot$ pre-MS rotating models.

$\log(age)$	$\log(L/L_\odot)$	$\log(T_{\rm eff})$	$\log(g)$	$\log(k_2)$	$\log(k_3)$	$\log(k_4)$	β	P(d)
2.8237	−0.1259	3.3938	2.0479	−1.2622	−1.8412	−2.2590	0.3592	45.1571
4.1938	−0.3507	3.4064	2.3233	−1.1683	−1.7257	−2.1163	0.3720	25.7355
4.7042	−0.5700	3.4255	2.6196	−1.1046	−1.6397	−2.0106	0.3830	13.8079
5.1313	−0.7898	3.4424	2.9076	−1.0325	−1.5516	−1.9082	0.3953	7.5910
5.5207	−1.0100	3.4554	3.1808	−0.9552	−1.4590	−1.8045	0.4087	4.3320
6.1512	−1.2132	3.4651	3.4235	−0.9185	−1.4073	−1.7429	0.4161	2.5736
6.3844	−1.3524	3.4708	3.5864	−0.9004	−1.3823	−1.7124	0.4201	1.8065
6.5657	−1.5553	3.4781	3.8198	−0.8711	−1.3456	−1.6694	0.4260	1.0883
6.8140	−1.7761	3.4844	4.0676	−0.8403	−1.3061	−1.6235	0.4322	0.6358
7.0892	−1.9967	3.4890	4.3092	−0.8347	−1.2923	−1.6031	0.4346	0.3709
7.3908	−2.2172	3.4914	4.5427	−0.8228	−1.2764	−1.5828	0.4377	0.2213
7.7000	−2.4377	3.4925	4.7715	−0.8156	−1.2645	−1.5670	0.4402	0.1334
8.0223	−2.6581	3.4911	4.9904	−0.7912	−1.2347	−1.5328	0.4461	0.0835
8.3414	−2.8792	3.4836	5.1848	−0.7540	−1.1888	−1.4805	0.4546	0.0559
8.6259	−3.1017	3.4636	5.3305	−0.7267	−1.1536	−1.4390	0.4614	0.0415
8.8533	−3.3250	3.4269	5.4088	−0.7162	−1.1391	−1.4212	0.4643	0.0352
9.2264	−3.5330	3.3846	5.4487	−0.7120	−1.1331	−1.4136	0.4656	0.0324
11.5704	−3.3642	3.4259	5.4455	−0.7160	−1.1386	−1.4204	0.4647	0.0325
11.8679	−3.1334	3.4709	5.3941	−0.7295	−1.1568	−1.4425	0.4615	0.0361
12.0443	−2.9072	3.4879	5.2337	−0.7694	−1.2080	−1.5019	0.4522	0.0498

Table A.48: Evolutionary tracks including internal structure constants and gyration radii for 0.10 $M_\odot$ pre-MS rotating models.

$\log(age)$	$\log(L/L_\odot)$	$\log(T_{\rm eff})$	$\log(g)$	$\log(k_2)$	$\log(k_3)$	$\log(k_4)$	β	P(d)
2.7698	0.0317	3.4117	2.0098	−1.2534	−1.8377	−2.2609	0.3601	34.6960
4.0376	−0.2006	3.4130	2.2480	−1.1753	−1.7393	−2.1376	0.3707	21.3106
4.5462	−0.4199	3.4233	2.5094	−1.1163	−1.6602	−2.0399	0.3808	12.3415
4.9825	−0.6395	3.4393	2.7942	−1.0537	−1.5805	−1.9446	0.3918	6.8026
5.3798	−0.8594	3.4535	3.0725	−0.9818	−1.4934	−1.8452	0.4045	3.8327
5.7826	−1.0748	3.4643	3.3329	−0.9271	−1.4224	−1.7633	0.4148	2.2221
6.3274	−1.2370	3.4709	3.5234	−0.9059	−1.3913	−1.7246	0.4198	1.4744
6.4715	−1.4075	3.4769	3.7203	−0.8849	−1.3634	−1.6906	0.4244	0.9628
6.7099	−1.6279	3.4836	3.9706	−0.8536	−1.3247	−1.6460	0.4311	0.5626
6.9813	−1.8487	3.4888	4.2174	−0.8429	−1.3053	−1.6203	0.4346	0.3277
7.2788	−2.0691	3.4919	4.4566	−0.8374	−1.2954	−1.6054	0.4374	0.1941
7.5865	−2.2898	3.4932	4.6903	−0.8343	−1.2890	−1.5957	0.4397	0.1166
7.9042	−2.5101	3.4928	4.9180	−0.8259	−1.2772	−1.5808	0.4434	0.0717
8.2330	−2.7304	3.4889	5.1309	−0.7980	−1.2433	−1.5422	0.4508	0.0463
8.5628	−2.9510	3.4767	5.3091	−0.7635	−1.1997	−1.4917	0.4599	0.0324
8.8868	−3.1710	3.4497	5.4262	−0.7459	−1.1760	−1.4630	0.4652	0.0256
10.8963	−3.2659	3.4345	5.4630	−0.7438	−1.1726	−1.4585	0.4663	0.0238
11.6527	−3.0342	3.4751	5.3929	−0.7630	−1.1984	−1.4897	0.4614	0.0273
11.9322	−2.8119	3.4879	5.2174	−0.8062	−1.2535	−1.5531	0.4506	0.0387
12.2107	−2.7561	3.4876	5.1567	−0.8187	−1.2696	−1.5716	0.4473	0.0435

Table A.49: Evolutionary tracks including internal structure constants and gyration radii for 0.20 $M_\odot$ pre-MS rotating models.

$\log(age)$	$\log(L/L_\odot)$	$\log(T_{\rm eff})$	$\log(g)$	$\log(k_2)$	$\log(k_3)$	$\log(k_4)$	β	P(d)
2.9189	0.4129	3.5112	2.3309	−1.0163	−1.5438	−1.9206	0.3994	18.1265
4.2593	0.1903	3.5131	2.5622	−0.9768	−1.5020	−1.8741	0.4065	11.0540
4.7340	−0.0305	3.5134	2.7859	−0.9479	−1.4634	−1.8266	0.4122	6.8183
5.1111	−0.2514	3.5122	3.0042	−0.9229	−1.4303	−1.7866	0.4174	4.2508
5.5372	−0.4638	3.5098	3.2097	−0.8982	−1.3977	−1.7475	0.4226	2.7307
6.0300	−0.6445	3.5076	3.3842	−0.8781	−1.3702	−1.7141	0.4271	1.8779
6.1812	−0.8206	3.5067	3.5592	−0.8598	−1.3443	−1.6818	0.4315	1.2889
6.4222	−1.0410	3.5068	3.7846	−0.8433	−1.3199	−1.6500	0.4361	0.7921
6.7061	−1.2614	3.5070	4.0118	−0.8306	−1.3015	−1.6263	0.4400	0.4845
7.0202	−1.4814	3.5085	4.2460	−0.8254	−1.2921	−1.6129	0.4429	0.2918
7.3488	−1.7017	3.5106	4.4858	−0.8270	−1.2915	−1.6096	0.4449	0.1738
7.6802	−1.9222	3.5120	4.7261	−0.8352	−1.2998	−1.6169	0.4460	0.1037
8.0171	−2.1424	3.5101	4.9636	−0.8571	−1.3259	−1.6451	0.4453	0.0634
8.2896	−2.2767	3.5077	5.1045	−0.8725	−1.3449	−1.6663	0.4443	0.0474
10.8892	−2.2628	3.5074	5.0814	−0.8610	−1.3305	−1.6498	0.4458	0.0494
11.3759	−2.2495	3.5061	5.0590	−0.8537	−1.3215	−1.6398	0.4468	0.0518
11.5951	−2.2484	3.5049	5.0519	−0.8489	−1.3157	−1.6333	0.4476	0.0526
11.7365	−2.2471	3.5041	5.0461	−0.8443	−1.3101	−1.6271	0.4484	0.0534
11.8400	−2.2450	3.5037	5.0412	−0.8399	−1.3047	−1.6212	0.4492	0.0540
11.9212	−2.2419	3.5038	5.0373	−0.8357	−1.2997	−1.6156	0.4499	0.0546

Table A.50: Evolutionary tracks including internal structure constants and gyration radii for 0.30 $M_\odot$ pre-MS rotating models.

$\log(age)$	$\log(L/L_\odot)$	$\log(T_{\rm eff})$	$\log(g)$	$\log(k_2)$	$\log(k_3)$	$\log(k_4)$	β	P(d)
2.9991	0.7007	3.5499	2.3701	−0.9399	−1.4441	−1.8016	0.4130	26.4772
4.2730	0.4734	3.5538	2.6136	−0.8993	−1.4005	−1.7536	0.4203	15.6931
4.7454	0.2530	3.5560	2.8437	−0.8747	−1.3666	−1.7113	0.4255	9.4878
5.1409	0.0340	3.5566	3.0666	−0.8570	−1.3421	−1.6809	0.4293	5.7976
5.7344	−0.1495	3.5562	3.2497	−0.8441	−1.3244	−1.6591	0.4322	3.8678
5.8795	−0.3113	3.5547	3.4066	−0.8322	−1.3081	−1.6391	0.4349	2.7357
6.0964	−0.5321	3.5511	3.6148	−0.8176	−1.2874	−1.6132	0.4384	1.7292
6.3540	−0.7527	3.5465	3.8197	−0.8052	−1.2693	−1.5899	0.4417	1.1011
6.6404	−0.9735	3.5416	4.0240	−0.7958	−1.2552	−1.5713	0.4444	0.7014
6.9447	−1.1938	3.5366	4.2282	−0.7886	−1.2446	−1.5574	0.4469	0.4470
7.2691	−1.4140	3.5339	4.4422	−0.7852	−1.2386	−1.5488	0.4489	0.2787
7.6091	−1.6340	3.5339	4.6688	−0.7852	−1.2373	−1.5458	0.4504	0.1691
7.9742	−1.8525	3.5350	4.9005	−0.8065	−1.2583	−1.5661	0.4515	0.1017
10.1769	−1.9260	3.5342	4.9768	−0.7922	−1.2447	−1.5527	0.4520	0.0867
10.8840	−1.9132	3.5335	4.9595	−0.7899	−1.2416	−1.5492	0.4523	0.0899
11.1376	−1.9125	3.5330	4.9563	−0.7884	−1.2397	−1.5469	0.4525	0.0906
11.2946	−1.9109	3.5327	4.9536	−0.7870	−1.2379	−1.5448	0.4528	0.0913
11.4080	−1.9085	3.5328	4.9513	−0.7857	−1.2362	−1.5428	0.4530	0.0918
11.4964	−1.9050	3.5333	4.9494	−0.7844	−1.2345	−1.5409	0.4533	0.0923
11.5687	−1.9002	3.5341	4.9480	−0.7833	−1.2330	−1.5390	0.4535	0.0926

Table A.51: Evolutionary tracks including internal structure constants and gyration radii for 0.40 $M_\odot$ pre-MS rotating models.

$\log(age)$	$\log(L/L_\odot)$	$\log(T_{\rm eff})$	$\log(g)$	$\log(k_2)$	$\log(k_3)$	$\log(k_4)$	β	P(d)
2.7435	1.0500	3.5654	2.2062	−0.9410	−1.4448	−1.8014	0.4125	51.3901
4.0372	0.8262	3.5735	2.4624	−0.8901	−1.3884	−1.7393	0.4217	29.8296
4.5151	0.6054	3.5785	2.7041	−0.8570	−1.3427	−1.6827	0.4285	17.6708
4.9019	0.3855	3.5816	2.9367	−0.8356	−1.3127	−1.6450	0.4330	10.5808
5.5124	0.1826	3.5828	3.1453	−0.8226	−1.2943	−1.6217	0.4360	6.6458
5.6805	0.0473	3.5829	3.2817	−0.8153	−1.2841	−1.6089	0.4376	4.8997
5.8918	−0.1736	3.5818	3.4994	−0.8039	−1.2682	−1.5892	0.4403	3.0122
6.1435	−0.3944	3.5787	3.7093	−0.7934	−1.2532	−1.5702	0.4429	1.8860
6.4205	−0.6153	3.5738	3.9123	−0.7846	−1.2401	−1.5532	0.4452	1.1992
6.7153	−0.8359	3.5681	4.1123	−0.7769	−1.2289	−1.5385	0.4474	0.7678
7.0205	−1.0565	3.5619	4.3107	−0.7710	−1.2202	−1.5271	0.4494	0.4935
7.3374	−1.2769	3.5564	4.5123	−0.7872	−1.2342	−1.5391	0.4509	0.3146
7.6850	−1.4961	3.5543	4.7274	−0.8064	−1.2623	−1.5715	0.4501	0.1934
8.1891	−1.6996	3.5555	4.9433	−0.8078	−1.2703	−1.5860	0.4457	0.1180
10.2528	−1.6659	3.5546	4.9048	−0.8141	−1.2761	−1.5901	0.4478	0.1297
10.6338	−1.6425	3.5566	4.8903	−0.8372	−1.2988	−1.6135	0.4410	0.1314
10.8530	−1.6130	3.5593	4.8728	−0.8732	−1.3331	−1.6480	0.4322	0.1335
10.9986	−1.5763	3.5627	4.8512	−0.9251	−1.3824	−1.6972	0.4215	0.1363
11.1025	−1.5315	3.5669	4.8248	−0.9944	−1.4477	−1.7622	0.4094	0.1402
11.1818	−1.4758	3.5722	4.7918	−1.0903	−1.5375	−1.8509	0.3954	0.1457

Table A.52: Evolutionary tracks including internal structure constants and gyration radii for 0.50 $M_\odot$ pre-MS rotating models.

$\log(age)$	$\log(L/L_\odot)$	$\log(T_{\rm eff})$	$\log(g)$	$\log(k_2)$	$\log(k_3)$	$\log(k_4)$	β	P(d)
2.8043	1.1429	3.5814	2.2734	−0.9077	−1.3994	−1.7455	0.4189	56.8673
4.1207	0.9200	3.5899	2.5305	−0.8627	−1.3503	−1.6919	0.4271	32.7635
4.6012	0.6996	3.5958	2.7749	−0.8331	−1.3091	−1.6407	0.4333	19.2197
5.0336	0.4840	3.5993	3.0054	−0.8142	−1.2823	−1.6068	0.4373	11.5317
5.5287	0.3132	3.6008	3.1827	−0.8043	−1.2682	−1.5888	0.4396	7.7536
5.6844	0.1457	3.6013	3.3527	−0.7968	−1.2574	−1.5751	0.4413	5.2909
5.9266	−0.0751	3.6004	3.5706	−0.7881	−1.2452	−1.5597	0.4434	3.2407
6.1995	−0.2958	3.5975	3.7810	−0.7801	−1.2338	−1.5452	0.4454	2.0196
6.4874	−0.5167	3.5925	3.9831	−0.7731	−1.2234	−1.5318	0.4472	1.2828
6.7859	−0.7374	3.5862	4.1805	−0.7670	−1.2145	−1.5201	0.4490	0.8237
7.0934	−0.9581	3.5797	4.3767	−0.7849	−1.2303	−1.5338	0.4505	0.5301
7.4232	−1.1774	3.5744	4.5775	−0.8024	−1.2575	−1.5660	0.4489	0.3344
7.7716	−1.3490	3.5760	4.7607	−0.8403	−1.2993	−1.6132	0.4344	0.2122
8.8745	−1.4442	3.5760	4.8599	−0.8596	−1.3147	−1.6276	0.4306	0.1680
10.2363	−1.3985	3.5792	4.8269	−0.8771	−1.3338	−1.6476	0.4233	0.1779
10.5400	−1.3582	3.5836	4.8046	−0.9309	−1.3864	−1.6997	0.4136	0.1829
10.7142	−1.3122	3.5888	4.7798	−0.9982	−1.4520	−1.7647	0.4028	0.1885
10.8325	−1.2591	3.5948	4.7515	−1.0788	−1.5298	−1.8416	0.3910	0.1955
10.9204	−1.1964	3.6019	4.7180	−1.1747	−1.6215	−1.9326	0.3779	0.2045
10.9886	−1.1209	3.6104	4.6772	−1.3009	−1.7423	−2.0525	0.3635	0.2168

Table A.53: Evolutionary tracks including internal structure constants and gyration radii for 0.60 $M_\odot$ pre-MS rotating models.

$\log(age)$	$\log(L/L_\odot)$	$\log(T_{\rm eff})$	$\log(g)$	$\log(k_2)$	$\log(k_3)$	$\log(k_4)$	β	P(d)
2.8468	1.2415	3.5917	2.2949	−0.8900	−1.3749	−1.7150	0.4224	66.1536
4.1572	1.0187	3.6011	2.5555	−0.8486	−1.3303	−1.6666	0.4300	37.6811
4.6398	0.7983	3.6079	2.8035	−0.8207	−1.2912	−1.6178	0.4359	21.8899
5.2427	0.5895	3.6122	3.0300	−0.8030	−1.2660	−1.5859	0.4397	13.2331
5.4810	0.4483	3.6141	3.1791	−0.7949	−1.2543	−1.5709	0.4415	9.4747
5.6841	0.2446	3.6154	3.3885	−0.7863	−1.2419	−1.5551	0.4435	5.9098
5.9435	0.0239	3.6149	3.6077	−0.7790	−1.2317	−1.5421	0.4452	3.6018
6.2272	−0.1969	3.6123	3.8192	−0.7726	−1.2224	−1.5302	0.4468	2.2339
6.5211	−0.4178	3.6075	4.0221	−0.7669	−1.2140	−1.5193	0.4484	1.4132
6.8205	−0.6386	3.6010	4.2181	−0.7740	−1.2182	−1.5211	0.4498	0.9083
7.1350	−0.8586	3.5946	4.4138	−0.7968	−1.2476	−1.5531	0.4495	0.5807
7.4682	−1.0453	3.5934	4.5987	−0.8274	−1.2857	−1.5984	0.4379	0.3681
7.7702	−1.1039	3.6072	4.7177	−0.9832	−1.4392	−1.7513	0.4031	0.2560
9.0489	−1.1611	3.6069	4.7759	−0.9843	−1.4411	−1.7520	0.4020	0.2228
10.0570	−1.1134	3.6122	4.7492	−1.0310	−1.4881	−1.7994	0.3937	0.2325
10.3437	−1.0636	3.6185	4.7250	−1.0989	−1.5555	−1.8668	0.3837	0.2404
10.5146	−1.0055	3.6259	4.6966	−1.1837	−1.6398	−1.9512	0.3724	0.2501
10.6305	−0.9393	3.6341	4.6634	−1.2841	−1.7385	−2.0499	0.3601	0.2626
10.7159	−0.8626	3.6430	4.6228	−1.4025	−1.8527	−2.1637	0.3467	0.2797
10.7815	−0.7718	3.6529	4.5716	−1.5588	−2.0040	−2.3147	0.3323	0.3045

Table A.54: Evolutionary tracks including internal structure constants and gyration radii for 0.70 $M_\odot$ pre-MS rotating models.

$\log(age)$	$\log(L/L_\odot)$	$\log(T_{\rm eff})$	$\log(g)$	$\log(k_2)$	$\log(k_3)$	$\log(k_4)$	β	P(d)
2.7548	1.3909	3.5960	2.2296	−0.8891	−1.3731	−1.7122	0.4225	89.9262
4.0822	1.1689	3.6068	2.4947	−0.8479	−1.3291	−1.6648	0.4300	50.6556
4.5670	0.9486	3.6151	2.7485	−0.8188	−1.2885	−1.6143	0.4361	29.0577
5.1357	0.7384	3.6208	2.9820	−0.7992	−1.2606	−1.5790	0.4403	17.3152
5.4153	0.5942	3.6237	3.1379	−0.7898	−1.2472	−1.5618	0.4424	12.2145
5.6114	0.3997	3.6261	3.3422	−0.7810	−1.2343	−1.5453	0.4444	7.7054
5.8726	0.1791	3.6268	3.5663	−0.7740	−1.2243	−1.5325	0.4460	4.6402
6.1582	−0.0416	3.6253	3.7818	−0.7684	−1.2163	−1.5222	0.4474	2.8474
6.4548	−0.2625	3.6217	3.9890	−0.7634	−1.2090	−1.5128	0.4488	1.7809
6.7552	−0.4832	3.6159	4.1877	−0.7850	−1.2294	−1.5316	0.4499	1.1353
7.0766	−0.7023	3.6101	4.3850	−0.7995	−1.2536	−1.5613	0.4471	0.7165
7.3873	−0.8488	3.6133	4.5467	−0.8567	−1.3138	−1.6265	0.4287	0.4692
7.6430	−0.8380	3.6365	4.6324	−1.0936	−1.5509	−1.8622	0.3848	0.3432
7.9230	−0.8783	3.6480	4.7225	−1.2347	−1.7111	−2.0272	0.3691	0.2643
9.7062	−0.8482	3.6477	4.6902	−1.2052	−1.6763	−1.9908	0.3688	0.2888
10.0617	−0.7975	3.6543	4.6659	−1.2702	−1.7397	−2.0537	0.3595	0.2996
10.2581	−0.7375	3.6622	4.6376	−1.3588	−1.8289	−2.1436	0.3490	0.3129
10.3943	−0.6635	3.6719	4.6025	−1.4628	−1.9302	−2.2449	0.3370	0.3309
10.4910	−0.5777	3.6822	4.5588	−1.5942	−2.0575	−2.3718	0.3239	0.3511
10.5632	−0.4767	3.6919	4.4958	−1.7731	−2.2303	−2.5441	0.3092	0.4010

Table A.55: Evolutionary tracks including internal structure constants and gyration radii for 0.80 $M_\odot$ pre-MS rotating models.

$\log(age)$	$\log(L/L_\odot)$	$\log(T_{\rm eff})$	$\log(g)$	$\log(k_2)$	$\log(k_3)$	$\log(k_4)$	β	P(d)
2.6879	1.5166	3.5989	2.1731	−0.8874	−1.3704	−1.7084	0.4229	117.4368
4.0213	1.2954	3.6108	2.4419	−0.8470	−1.3277	−1.6628	0.4301	65.5031
4.5081	1.0750	3.6202	2.7005	−0.8177	−1.2870	−1.6124	0.4362	37.1574
5.0395	0.8647	3.6272	2.9388	−0.7972	−1.2578	−1.5755	0.4406	21.9112
5.3622	0.7163	3.6309	3.1023	−0.7867	−1.2428	−1.5562	0.4429	15.2039
5.5562	0.5266	3.6343	3.3059	−0.7773	−1.2291	−1.5386	0.4450	9.6108
5.8204	0.3061	3.6363	3.5348	−0.7701	−1.2187	−1.5252	0.4467	5.7220
6.1086	0.0852	3.6359	3.7547	−0.7648	−1.2111	−1.5155	0.4480	3.4733
6.4069	−0.1356	3.6332	3.9651	−0.7604	−1.2047	−1.5073	0.4491	2.1540
6.7110	−0.3562	3.6284	4.1674	−0.7896	−1.2355	−1.5380	0.4497	1.3581
7.0362	−0.5643	3.6250	4.3633	−0.8081	−1.2648	−1.5748	0.4433	0.8493
7.3205	−0.6633	3.6338	4.4996	−0.9064	−1.3623	−1.6744	0.4173	0.5770
7.5379	−0.5894	3.6660	4.5578	−1.2196	−1.6823	−1.9945	0.3665	0.4408
7.7441	−0.5743	3.6927	4.6517	−1.4390	−1.9393	−2.2640	0.3417	0.3423
9.3869	−0.5946	3.6858	4.6456	−1.3555	−1.8453	−2.1660	0.3473	0.3366
9.8110	−0.5433	3.6926	4.6213	−1.4249	−1.9147	−2.2356	0.3386	0.3544
10.0218	−0.4852	3.6998	4.5917	−1.5086	−1.9974	−2.3181	0.3286	0.3774
10.1643	−0.4165	3.7073	4.5524	−1.6202	−2.1084	−2.4295	0.3167	0.4104
10.2736	−0.3309	3.7147	4.4958	−1.7694	−2.2536	−2.5740	0.3022	0.4631
10.3560	−0.2264	3.7207	4.4142	−1.9770	−2.4536	−2.7728	0.2859	0.5520

Table A.56: Evolutionary tracks including internal structure constants and gyration radii for 0.90 $M_\odot$ pre-MS rotating models.

$\log(age)$	$\log(L/L_\odot)$	$\log(T_{\rm eff})$	$\log(g)$	$\log(k_2)$	$\log(k_3)$	$\log(k_4)$	β	P(d)
2.6419	1.6242	3.6009	2.1245	−0.8849	−1.3668	−1.7037	0.4233	148.3015
3.9726	1.4034	3.6137	2.3967	−0.8466	−1.3267	−1.6611	0.4303	81.9702
4.4602	1.1832	3.6242	2.6589	−0.8180	−1.2869	−1.6118	0.4363	46.0770
4.9661	0.9720	3.6321	2.9020	−0.7970	−1.2572	−1.5743	0.4407	26.8789
5.3175	0.8219	3.6366	3.0702	−0.7859	−1.2412	−1.5539	0.4432	18.4580
5.5093	0.6363	3.6408	3.2728	−0.7760	−1.2268	−1.5354	0.4454	11.6986
5.7760	0.4159	3.6439	3.5061	−0.7683	−1.2156	−1.5209	0.4472	6.8970
6.0673	0.1952	3.6448	3.7306	−0.7631	−1.2081	−1.5113	0.4484	4.1404
6.3678	−0.0256	3.6429	3.9449	−0.7638	−1.2066	−1.5080	0.4494	2.5432
6.6767	−0.2460	3.6392	4.1507	−0.7913	−1.2393	−1.5426	0.4491	1.5843
6.9948	−0.4327	3.6389	4.3374	−0.8206	−1.2783	−1.5898	0.4384	0.9980
7.2556	−0.4841	3.6539	4.4508	−0.9632	−1.4173	−1.7285	0.4051	0.7009
7.4417	−0.3624	3.6939	4.4909	−1.3316	−1.7998	−2.1132	0.3508	0.5787
7.6043	−0.2931	3.7284	4.5597	−1.6701	−2.1998	−2.5358	0.3129	0.4970
9.0539	−0.3642	3.7196	4.5964	−1.5183	−2.0357	−2.3668	0.3258	0.4594
9.5757	−0.3144	3.7248	4.5672	−1.5980	−2.1165	−2.4478	0.3162	0.4896
9.8030	−0.2600	3.7300	4.5330	−1.6913	−2.2106	−2.5421	0.3057	0.5276
9.9488	−0.1987	3.7348	4.4906	−1.8055	−2.3263	−2.6586	0.2940	0.5789
10.0574	−0.1270	3.7389	4.4352	−1.9437	−2.4622	−2.7938	0.2810	0.6537
10.1523	−0.0295	3.7418	4.3487	−2.1427	−2.6516	−2.9802	0.2655	0.7909

Table A.57: Evolutionary tracks including internal structure constants and gyration radii for 1.00 $M_\odot$ pre-MS rotating models.

$\log(age)$	$\log(L/L_\odot)$	$\log(T_{\rm eff})$	$\log(g)$	$\log(k_2)$	$\log(k_3)$	$\log(k_4)$	β	P(d)
2.2954	1.8910	3.5901	1.8603	−0.9140	−1.4049	−1.7487	0.4177	295.0926
3.6547	1.6729	3.6056	2.1405	−0.8718	−1.3609	−1.7027	0.4253	160.6400
4.1462	1.4528	3.6185	2.4120	−0.8387	−1.3158	−1.6475	0.4319	88.7107
4.5432	1.2324	3.6292	2.6757	−0.8122	−1.2787	−1.6015	0.4374	49.5919
5.1020	1.0252	3.6375	2.9163	−0.7929	−1.2513	−1.5668	0.4416	29.0499
5.3023	0.8978	3.6417	3.0605	−0.7837	−1.2380	−1.5499	0.4436	21.0368
5.5221	0.6901	3.6471	3.2898	−0.7726	−1.2219	−1.5291	0.4461	12.5521
5.7957	0.4695	3.6508	3.5256	−0.7651	−1.2110	−1.5150	0.4478	7.3564
6.0919	0.2488	3.6523	3.7527	−0.7602	−1.2039	−1.5058	0.4490	4.3875
6.3960	0.0280	3.6511	3.9693	−0.7823	−1.2252	−1.5260	0.4498	2.6770
6.7152	−0.1878	3.6490	4.1772	−0.8000	−1.2537	−1.5609	0.4463	1.6416
7.0052	−0.3205	3.6547	4.3341	−0.8588	−1.3138	−1.6249	0.4270	1.0805
7.2287	−0.2881	3.6818	4.4115	−1.0999	−1.5535	−1.8627	0.3828	0.8094
7.3772	−0.1313	3.7227	4.4182	−1.5574	−2.0444	−2.3632	0.3225	0.7969
7.5055	−0.0681	3.7533	4.4776	−1.8772	−2.4389	−2.7869	0.2856	0.6976
8.8246	−0.1500	3.7471	4.5354	−1.7118	−2.2616	−2.6053	0.3004	0.6144
9.3863	−0.1013	3.7510	4.5019	−1.8034	−2.3575	−2.7029	0.2903	0.6616
9.6158	−0.0501	3.7545	4.4644	−1.9036	−2.4607	−2.8071	0.2798	0.7189
9.7582	0.0042	3.7574	4.4215	−2.0124	−2.5704	−2.9168	0.2691	0.7909
9.8616	0.0631	3.7593	4.3702	−2.1373	−2.6966	−3.0441	0.2583	0.8864

Table A.58: Evolutionary tracks including internal structure constants and gyration radii for 1.20 $M_\odot$ pre-MS rotating models.

$\log(age)$	$\log(L/L_\odot)$	$\log(T_{\rm eff})$	$\log(g)$	$\log(k_2)$	$\log(k_3)$	$\log(k_4)$	β	P(d)
2.2057	2.0500	3.5915	1.7861	−0.9051	−1.3926	−1.7333	0.4194	424.6815
3.5812	1.8326	3.6078	2.0686	−0.8663	−1.3531	−1.6928	0.4264	229.2039
4.0771	1.6122	3.6219	2.3452	−0.8354	−1.3110	−1.6414	0.4326	124.8186
4.4756	1.3922	3.6338	2.6133	−0.8107	−1.2764	−1.5983	0.4377	68.9621
5.0170	1.1828	3.6436	2.8618	−0.7919	−1.2497	−1.5646	0.4417	39.6330
5.2409	1.0534	3.6488	3.0121	−0.7826	−1.2362	−1.5474	0.4438	28.3102
5.4593	0.8507	3.6555	3.2415	−0.7711	−1.2196	−1.5260	0.4463	17.8688
5.7370	0.6303	3.6609	3.4829	−0.7627	−1.2074	−1.5102	0.4482	143.5963
6.0381	0.4097	3.6642	3.7182	−0.7574	−1.1997	−1.5002	0.4495	5.7218
6.3520	0.1893	3.6656	3.9443	−0.7887	−1.2344	−1.5359	0.4495	3.4040
6.6610	0.0039	3.6683	4.1414	−0.8106	−1.2668	−1.5767	0.4406	2.1021
6.9160	−0.0635	3.6824	4.2659	−0.9267	−1.3800	−1.6904	0.4115	1.4929
7.0985	0.0288	3.7136	4.2982	−1.2884	−1.7511	−2.0622	0.3564	1.3872
7.2113	0.2190	3.7495	4.2516	−1.8553	−2.3809	−2.7140	0.2872	1.5409
7.2855	0.3622	3.7797	4.2291	−2.3236	−2.9605	−3.3458	0.2350	1.6211
7.3695	0.2210	3.7872	4.4005	−2.1380	−2.8050	−3.2134	0.2534	1.1006
8.6320	0.2392	3.7907	4.3966	−2.1607	−2.8371	−3.2535	0.2469	1.1109
9.0903	0.2804	3.7925	4.3625	−2.2443	−2.9306	−3.3535	0.2384	1.1996
9.2849	0.3179	3.7936	4.3291	−2.3245	−3.0162	−3.4426	0.2312	1.2934
9.4012	0.3502	3.7938	4.2975	−2.3999	−3.0936	−3.5220	0.2253	1.3892

Table A.59: Evolutionary tracks including internal structure constants and gyration radii for 1.40 $M_\odot$ pre-MS rotating models.

$\log(age)$	$\log(L/L_\odot)$	$\log(T_{\rm eff})$	$\log(g)$	$\log(k_2)$	$\log(k_3)$	$\log(k_4)$	β	P(d)
2.1323	2.1806	3.5921	1.7248	−0.8965	−1.3808	−1.7186	0.4211	576.4682
3.5220	1.9642	3.6091	2.0089	−0.8605	−1.3451	−1.6828	0.4275	309.1253
4.0205	1.7440	3.6239	2.2886	−0.8318	−1.3058	−1.6348	0.4333	166.8086
4.4214	1.5239	3.6370	2.5608	−0.8086	−1.2733	−1.5944	0.4381	91.1295
4.9443	1.3132	3.6478	2.8150	−0.7909	−1.2480	−1.5623	0.4419	54.9553
5.1904	1.1831	3.6538	2.9689	−0.7817	−1.2349	−1.5455	0.4439	38.6001
5.4006	0.9906	3.6613	3.1919	−0.7707	−1.2190	−1.5251	0.4464	23.1380
5.6805	0.7702	3.6682	3.4399	−0.7616	−1.2058	−1.5080	0.4484	13.1016
5.9848	0.5497	3.6731	3.6803	−0.7703	−1.2114	−1.5110	0.4497	7.5571
6.3031	0.3352	3.6769	3.9101	−0.7915	−1.2408	−1.5443	0.4481	4.4688
6.5892	0.1854	3.6837	4.0872	−0.8295	−1.2843	−1.5941	0.4343	2.9828
6.8197	0.1621	3.7020	4.1840	−1.0086	−1.4598	−1.7683	0.3967	2.3925
6.9734	0.2938	3.7325	4.1740	−1.4736	−1.9496	−2.2645	0.3327	2.4469
7.0625	0.5040	3.7643	4.0910	−2.1031	−2.6698	−3.0205	0.2596	2.9570
7.1153	0.6474	3.7907	4.0535	−2.5659	−3.2715	−3.7095	0.2119	3.2213
7.1547	0.6918	3.8123	4.1037	−2.7712	−3.5774	−4.1033	0.1940	1.2118
7.2101	0.5148	3.8146	4.2911	−2.4228	−3.2123	−3.7252	0.2224	0.8261
7.6373	0.5395	3.8272	4.3181	−2.4716	−3.2913	−3.8389	0.2137	0.7513
8.7997	0.5847	3.8282	4.2767	−2.5756	−3.4018	−3.9555	0.2061	0.8174
9.0831	0.6249	3.8253	4.2244	−2.6721	−3.4946	−4.0454	0.1999	0.9199

Table A.60: Evolutionary tracks including internal structure constants and gyration radii for 1.60 $M_\odot$ pre-MS rotating models.

$\log(age)$	$\log(L/L_\odot)$	$\log(T_{\rm eff})$	$\log(g)$	$\log(k_2)$	$\log(k_3)$	$\log(k_4)$	β	P(d)
2.1002	2.2922	3.5923	1.6718	−0.8886	−1.3700	−1.7052	0.4227	751.3150
3.4763	2.0756	3.6099	1.9587	−0.8545	−1.3369	−1.6726	0.4286	399.4509
3.9753	1.8555	3.6254	2.2409	−0.8277	−1.3002	−1.6278	0.4341	213.8915
4.3781	1.6352	3.6392	2.5166	−0.8059	−1.2697	−1.5897	0.4386	115.7731
4.8830	1.4240	3.6510	2.7749	−0.7892	−1.2457	−1.5594	0.4422	66.1559
5.1509	1.2912	3.6576	2.9343	−0.7804	−1.2330	−1.5431	0.4441	45.8636
5.3645	1.0987	3.6662	3.1611	−0.7696	−1.2175	−1.5232	0.4465	27.2455
5.6481	0.8783	3.6742	3.4138	−0.7604	−1.2041	−1.5059	0.4485	15.2610
5.9567	0.6580	3.6804	3.6590	−0.7833	−1.2259	−1.5259	0.4497	8.6997
6.2655	0.4605	3.6861	3.8794	−0.7997	−1.2530	−1.5596	0.4455	5.2548
6.5309	0.3455	3.6961	4.0348	−0.8614	−1.3159	−1.6266	0.4255	3.6840
6.7367	0.3676	3.7173	4.0974	−1.1258	−1.5787	−1.8868	0.3784	3.1931
6.8635	0.5413	3.7468	4.0415	−1.7012	−2.2049	−2.5301	0.3056	3.6272
6.9325	0.7436	3.7746	3.9504	−2.3140	−2.9402	−3.3269	0.2373	4.4675
6.9739	0.8672	3.7985	3.9223	−2.7081	−3.4693	−3.9607	0.1989	4.7633
7.0174	0.9592	3.8409	4.0066	−2.9108	−3.7724	−4.3565	0.1807	1.6475
7.0698	0.7790	3.8465	4.2112	−2.5849	−3.4476	−4.0341	0.2059	1.0508
7.3246	0.7998	3.8752	4.3062	−2.5483	−3.4106	−4.0034	0.2068	0.8450
8.6418	0.8390	3.8730	4.2578	−2.6420	−3.5048	−4.0973	0.2007	0.9443
8.9205	0.8723	3.8622	4.1808	−2.7430	−3.6021	−4.1920	0.1939	1.1237

Table A.61: Evolutionary tracks including internal structure constants and gyration radii for 1.80 $M_\odot$ pre-MS rotating models.

$\log(age)$	$\log(L/L_\odot)$	$\log(T_{\rm eff})$	$\log(g)$	$\log(k_2)$	$\log(k_3)$	$\log(k_4)$	β	P(d)
2.0317	2.3900	3.5923	1.6251	−0.8814	−1.3599	−1.6927	0.4241	949.2004
3.4300	2.1747	3.6102	1.9120	−0.8505	−1.3309	−1.6648	0.4296	503.5350
3.9316	1.9546	3.6262	2.1962	−0.8253	−1.2964	−1.6227	0.4347	268.0285
4.3362	1.7343	3.6407	2.4744	−0.8048	−1.2676	−1.5868	0.4390	147.7201
4.8189	1.5228	3.6533	2.7364	−0.7889	−1.2448	−1.5579	0.4424	80.8777
5.1154	1.3870	3.6606	2.9016	−0.7803	−1.2325	−1.5421	0.4443	55.3229
5.3261	1.1992	3.6698	3.1261	−0.7703	−1.2179	−1.5234	0.4465	33.0263
5.6121	0.9787	3.6789	3.3831	−0.7610	−1.2045	−1.5061	0.4486	18.3103
5.9226	0.7604	3.6862	3.6311	−0.7888	−1.2339	−1.5349	0.4493	10.3685
6.2167	0.5827	3.6935	3.8378	−0.8056	−1.2604	−1.5688	0.4422	6.4576
6.4661	0.4952	3.7057	3.9743	−0.9005	−1.3529	−1.6623	0.4167	4.7246
6.6513	0.5552	3.7282	4.0042	−1.2460	−1.7042	−2.0133	0.3611	4.4122
6.7565	0.7579	3.7560	3.9126	−1.8855	−2.4222	−2.7619	0.2827	5.4401
6.8131	0.9334	3.7808	3.8363	−2.4318	−3.1094	−3.5378	0.2242	6.4795
6.8481	1.0436	3.8044	3.8243	−2.7590	−3.5523	−4.0812	0.1935	3.0541
6.9033	1.1866	3.8838	4.0004	−2.8906	−3.7532	−4.3419	0.1818	1.9216
6.9491	1.0012	3.8867	4.1988	−2.5687	−3.4343	−4.0268	0.2068	1.2262
7.0841	1.0342	3.9232	4.3128	−2.5230	−3.3817	−3.9742	0.2089	0.9490
8.4410	1.0475	3.9168	4.2741	−2.5811	−3.4396	−4.0317	0.2053	1.0376
8.7523	1.0797	3.9027	4.1844	−2.6910	−3.5450	−4.1344	0.1977	1.2712

Table A.62: Evolutionary tracks including internal structure constants and gyration radii for 2.00 $M_\odot$ pre-MS rotating models.

$\log(age)$	$\log(L/L_\odot)$	$\log(T_{\rm eff})$	$\log(g)$	$\log(k_2)$	$\log(k_3)$	$\log(k_4)$	β	P(d)
2.0185	2.4769	3.5923	1.5840	−0.8747	−1.3507	−1.6813	0.4255	1168.4883
3.3981	2.2597	3.6105	1.8738	−0.8454	−1.3238	−1.6560	0.4306	614.6632
3.8988	2.0397	3.6269	2.1595	−0.8217	−1.2914	−1.6164	0.4354	325.5618
4.3040	1.8196	3.6419	2.4397	−0.8024	−1.2642	−1.5825	0.4395	176.2027
4.7736	1.6077	3.6552	2.7046	−0.7874	−1.2427	−1.5551	0.4427	95.8040
5.0849	1.4711	3.6630	2.8726	−0.7793	−1.2309	−1.5401	0.4445	65.1218
5.2918	1.2885	3.6726	3.0937	−0.7699	−1.2173	−1.5226	0.4465	39.1713
5.5798	1.0679	3.6826	3.3544	−0.7695	−1.2124	−1.5137	0.4485	21.5269
5.8864	0.8566	3.6910	3.5995	−0.7917	−1.2397	−1.5426	0.4484	12.2672
6.1673	0.6970	3.6995	3.7933	−0.8134	−1.2682	−1.5774	0.4383	7.8664
6.4031	0.6354	3.7135	3.9108	−0.9436	−1.3946	−1.7036	0.4068	6.0091
6.5681	0.7320	3.7365	3.9061	−1.3766	−1.8468	−2.1600	0.3431	6.0737
6.6549	0.9438	3.7624	3.7979	−2.0332	−2.6138	−2.9784	0.2650	7.7830
6.7040	1.0935	3.7854	3.7403	−2.5060	−3.2267	−3.6942	0.2159	8.8803
6.7433	1.2232	3.8211	3.7562	−2.8186	−3.6488	−4.2169	0.1876	3.8951
6.7999	1.3839	3.9211	3.9969	−2.8615	−3.7217	−4.3100	0.1839	2.2108
6.8417	1.1955	3.9226	4.1926	−2.5382	−3.4019	−3.9937	0.2093	1.4163
6.9501	1.2416	3.9637	4.3117	−2.5057	−3.3644	−3.9570	0.2107	1.0795
8.2686	1.2306	3.9537	4.2826	−2.5309	−3.3880	−3.9796	0.2094	1.1551
8.6019	1.2619	3.9377	4.1869	−2.6413	−3.4941	−4.0831	0.2015	1.4361

Table A.63: Evolutionary tracks including internal structure constants and gyration radii for 2.30 $M_\odot$ pre-MS rotating models.

$\log(age)$	$\log(L/L_\odot)$	$\log(T_{\rm eff})$	$\log(g)$	$\log(k_2)$	$\log(k_3)$	$\log(k_4)$	β	P(d)
1.9530	2.5895	3.5920	1.5307	−0.8654	−1.3379	−1.6654	0.4273	1535.9376
3.3487	2.3735	3.6105	1.8209	−0.8391	−1.3149	−1.6447	0.4319	804.8569
3.8515	2.1534	3.6274	2.1086	−0.8175	−1.2852	−1.6085	0.4363	423.5857
4.2584	1.9334	3.6431	2.3912	−0.7997	−1.2601	−1.5771	0.4401	245.9360
4.7098	1.7206	3.6572	2.6606	−0.7858	−1.2401	−1.5516	0.4431	132.3521
5.0456	1.5813	3.6657	2.8340	−0.7780	−1.2289	−1.5373	0.4447	88.8182
5.2497	1.4034	3.6759	3.0528	−0.7695	−1.2165	−1.5214	0.4466	53.6905
5.5396	1.1841	3.6871	3.3168	−0.7888	−1.2333	−1.5351	0.4484	29.2647
5.8327	0.9894	3.6966	3.5495	−0.7983	−1.2516	−1.5582	0.4461	17.1459
6.0968	0.8553	3.7068	3.7245	−0.8358	−1.2904	−1.6007	0.4309	11.4714
6.3127	0.8337	3.7227	3.8099	−1.0430	−1.4933	−1.8011	0.3895	9.4310
6.4465	0.9849	3.7457	3.7506	−1.6049	−2.1093	−2.4364	0.3145	10.8041
6.5140	1.1726	3.7689	3.6556	−2.1891	−2.8304	−3.2403	0.2468	13.4393
6.5557	1.2961	3.7920	3.6243	−2.5609	−3.3224	−3.8355	0.2096	14.4406
6.6097	1.4856	3.8666	3.7359	−2.8053	−3.6408	−4.2184	0.1881	4.8152
6.6602	1.6386	3.9679	3.9887	−2.8199	−3.6747	−4.2620	0.1871	2.6882
6.6986	1.4493	3.9690	4.1835	−2.4971	−3.3556	−3.9456	0.2127	1.7233
6.7910	1.4991	4.0132	4.3111	−2.4715	−3.3260	−3.9170	0.2143	1.2866
8.0666	1.4717	3.9997	4.2844	−2.4749	−3.3265	−3.9162	0.2144	1.3714
8.4264	1.5060	3.9824	4.1803	−2.5972	−3.4446	−4.0317	0.2058	1.7382

Table A.64: Evolutionary tracks including internal structure constants and gyration radii for 2.50 $M_\odot$ pre-MS rotating models.

$\log(age)$	$\log(L/L_\odot)$	$\log(T_{\rm eff})$	$\log(g)$	$\log(k_2)$	$\log(k_3)$	$\log(k_4)$	β	P(d)
1.9521	2.6566	3.5917	1.4988	−0.8600	−1.3304	−1.6559	0.4285	1808.2412
3.3254	2.4396	3.6106	1.7913	−0.8356	−1.3096	−1.6379	0.4327	941.1419
3.8272	2.2193	3.6277	2.0801	−0.8152	−1.2816	−1.6038	0.4369	493.4489
4.2342	1.9992	3.6437	2.3641	−0.7983	−1.2578	−1.5740	0.4404	282.2677
4.6792	1.7858	3.6583	2.6359	−0.7850	−1.2387	−1.5496	0.4433	151.0266
5.0223	1.6468	3.6672	2.8105	−0.7777	−1.2280	−1.5360	0.4449	101.0726
5.2223	1.4734	3.6776	3.0254	−0.7697	−1.2165	−1.5211	0.4466	61.6494
5.5088	1.2585	3.6893	3.2873	−0.7928	−1.2394	−1.5423	0.4481	33.7647
5.7927	1.0747	3.6993	3.5114	−0.7996	−1.2541	−1.5619	0.4441	20.1694
6.0474	0.9555	3.7104	3.6751	−0.8546	−1.3093	−1.6205	0.4255	13.8508
6.2503	0.9605	3.7273	3.7374	−1.1244	−1.5792	−1.8876	0.3774	12.0036
6.3654	1.1365	3.7499	3.6518	−1.7346	−2.2717	−2.6154	0.2982	14.6115
6.4261	1.2994	3.7718	3.5765	−2.2534	−2.9295	−3.3686	0.2393	17.3706
6.4650	1.4128	3.7960	3.5613	−2.5717	−3.3506	−3.8833	0.2081	8.3556
6.5268	1.6354	3.8922	3.7239	−2.7823	−3.6163	−4.1935	0.1899	5.5043
6.5747	1.7864	3.9932	3.9777	−2.7878	−3.6402	−4.2258	0.1889	3.0656
6.6119	1.6030	3.9966	4.1757	−2.4794	−3.3358	−3.9245	0.2144	1.9599
6.6966	1.6529	4.0414	4.3055	−2.4515	−3.3034	−3.8926	0.2161	1.4560
7.9400	1.6134	4.0264	4.2852	−2.4383	−3.2866	−3.8743	0.2176	1.5276
8.3206	1.6498	4.0088	4.1775	−2.5638	−3.4082	−3.9936	0.2085	1.9531

Table A.65: Evolutionary tracks including internal structure constants and gyration radii for 2.80 $M_\odot$ pre-MS rotating models.

$\log(age)$	$\log(L/L_\odot)$	$\log(T_{\rm eff})$	$\log(g)$	$\log(k_2)$	$\log(k_3)$	$\log(k_4)$	β	P(d)
1.9056	2.7462	3.5912	1.4564	−0.8527	−1.3201	−1.6430	0.4300	2252.5721
3.2870	2.5301	3.6104	1.7492	−0.8304	−1.3021	−1.6284	0.4338	1169.2586
3.7904	2.3099	3.6279	2.0394	−0.8117	−1.2765	−1.5972	0.4376	610.0330
4.1987	2.0899	3.6443	2.3252	−0.7960	−1.2543	−1.5694	0.4409	325.4700
4.6323	1.8757	3.6595	2.6000	−0.7836	−1.2364	−1.5465	0.4436	172.9414
4.9913	1.7348	3.6689	2.7787	−0.7766	−1.2263	−1.5336	0.4451	114.6401
5.1865	1.5669	3.6795	2.9890	−0.7856	−1.2317	−1.5358	0.4467	70.6773
5.4628	1.3629	3.6917	3.2416	−0.7941	−1.2444	−1.5494	0.4470	39.5334
5.7347	1.1946	3.7026	3.4535	−0.8073	−1.2639	−1.5744	0.4401	24.2912
5.9764	1.0987	3.7149	3.5988	−0.8957	−1.3487	−1.6593	0.4155	17.3976
6.1564	1.1486	3.7327	3.6201	−1.2699	−1.7393	−2.0525	0.3566	16.5658
6.2486	1.3335	3.7543	3.5217	−1.8838	−2.4722	−2.8481	0.2793	20.7653
6.3028	1.4665	3.7759	3.4750	−2.3124	−3.0306	−3.5096	0.2322	23.1223
6.3517	1.6119	3.8192	3.5039	−2.6144	−3.4234	−3.9872	0.2037	10.6403
6.4118	1.8380	3.9269	3.7090	−2.7493	−3.5834	−4.1610	0.1924	6.5744
6.4569	1.9838	4.0273	3.9652	−2.7464	−3.5973	−4.1820	0.1919	3.6427
6.4929	1.8070	4.0333	4.1666	−2.4494	−3.3046	−3.8925	0.2171	2.2982
6.5740	1.8462	4.0777	4.3055	−2.4121	−3.2623	−3.8507	0.2201	1.6749
7.8072	1.8062	4.0611	4.2795	−2.4022	−3.2486	−3.8353	0.2214	1.7795
8.1921	1.8455	4.0433	4.1683	−2.5287	−3.3706	−3.9546	0.2118	2.2916

Table A.66: Evolutionary tracks including internal structure constants and gyration radii for 3.00 $M_\odot$ pre-MS rotating models.

$\log(age)$	$\log(L/L_\odot)$	$\log(T_{\rm eff})$	$\log(g)$	$\log(k_2)$	$\log(k_3)$	$\log(k_4)$	β	P(d)
1.9034	2.7887	3.5922	1.4478	−0.8479	−1.3133	−1.6345	0.4310	2475.3068
3.2856	2.5717	3.6113	1.7411	−0.8256	−1.2956	−1.6203	0.4347	1282.9376
3.7896	2.3518	3.6290	2.0318	−0.8082	−1.2716	−1.5910	0.4382	667.7505
4.1984	2.1317	3.6456	2.3182	−0.7934	−1.2507	−1.5648	0.4414	696.7648
4.6462	1.9185	3.6609	2.5928	−0.7817	−1.2338	−1.5432	0.4439	370.2940
4.9804	1.7809	3.6703	2.7680	−0.7752	−1.2244	−1.5311	0.4453	247.3825
5.1829	1.6096	3.6815	2.9841	−0.7991	−1.2471	−1.5518	0.4467	150.4165
5.4530	1.4153	3.6938	3.2273	−0.8002	−1.2554	−1.5637	0.4456	85.9270
5.7160	1.2617	3.7052	3.4266	−0.8164	−1.2734	−1.5854	0.4353	54.3120
5.9463	1.1917	3.7186	3.5503	−0.9531	−1.4043	−1.7134	0.4035	40.8592
6.1007	1.2878	3.7373	3.5289	−1.4341	−1.9316	−2.2570	0.3351	42.9183
6.1788	1.4573	3.7581	3.4428	−1.9899	−2.6178	−3.0229	0.2658	52.3348
6.2283	1.5745	3.7807	3.4159	−2.3527	−3.0955	−3.6008	0.2272	55.6678
6.2870	1.7556	3.8472	3.5022	−2.6141	−3.4244	−3.9910	0.2034	11.5912
6.3440	1.9760	3.9566	3.7197	−2.7296	−3.5620	−4.1391	0.1935	6.9958
6.3869	2.1047	4.0538	3.9800	−2.7206	−3.5669	−4.1499	0.1946	3.8432
6.4223	1.9122	4.0531	4.1706	−2.4073	−3.2559	−3.8410	0.2207	2.4864
6.5050	1.9455	4.0975	4.3149	−2.3618	−3.2065	−3.7925	0.2246	1.7920
7.7772	1.9254	4.0804	4.2667	−2.3861	−3.2277	−3.8118	0.2230	1.9992
8.1315	1.9665	4.0628	4.1549	−2.5145	−3.3516	−3.9332	0.2132	2.5780

Table A.67: Evolutionary tracks including internal structure constants and gyration radii for 3.30 $M_\odot$ pre-MS rotating models.

$\log(age)$	$\log(L/L_\odot)$	$\log(T_{\rm eff})$	$\log(g)$	$\log(k_2)$	$\log(k_3)$	$\log(k_4)$	β	P(d)
1.8938	2.8555	3.5922	1.4222	−0.8409	−1.3036	−1.6225	0.4324	2911.4436
3.2678	2.6397	3.6117	1.7161	−0.8217	−1.2896	−1.6124	0.4356	1503.5155
3.7716	2.4197	3.6295	2.0075	−0.8057	−1.2674	−1.5854	0.4389	780.3129
4.1815	2.1995	3.6465	2.2955	−0.7920	−1.2481	−1.5610	0.4418	414.8457
4.6323	1.9863	3.6622	2.5714	−0.7811	−1.2323	−1.5409	0.4442	219.8156
4.9584	1.8510	3.6718	2.7452	−0.7751	−1.2236	−1.5298	0.4455	147.3705
5.1843	1.6650	3.6844	2.9818	−0.8031	−1.2558	−1.5629	0.4460	85.4953
5.4451	1.4878	3.6969	3.2089	−0.8029	−1.2611	−1.5729	0.4414	50.7125
5.6940	1.3609	3.7092	3.3849	−0.8506	−1.3046	−1.6163	0.4240	33.8290
5.8988	1.3469	3.7245	3.4601	−1.1143	−1.5739	−1.8842	0.3776	28.4581
6.0132	1.4941	3.7438	3.3902	−1.6766	−2.2333	−2.5913	0.3022	33.4241
6.0790	1.6240	3.7642	3.3421	−2.1215	−2.8089	−3.2661	0.2499	37.3272
6.1270	1.7368	3.7934	3.3466	−2.4152	−3.1941	−3.7379	0.2200	19.0505
6.1975	1.9683	3.8941	3.5181	−2.6150	−3.4280	−3.9976	0.2030	12.5351
6.2496	2.1727	4.0034	3.7510	−2.7013	−3.5343	−4.1121	0.1952	7.3110
6.2904	2.2594	4.0917	4.0182	−2.6665	−3.5118	−4.0947	0.2003	3.9642
6.3272	2.0450	4.0794	4.1836	−2.3423	−3.1819	−3.7637	0.2268	2.7210
6.4179	2.0667	4.1209	4.3286	−2.2766	−3.1130	−3.6957	0.2318	1.9579
7.7750	2.0934	4.1050	4.2380	−2.3714	−3.2074	−3.7889	0.2242	2.4055
8.0655	2.1364	4.0880	4.1265	−2.5037	−3.3353	−3.9146	0.2143	3.0991

Table A.68: Evolutionary tracks including internal structure constants and gyration radii for 3.50 $M_\odot$ pre-MS rotating models.

$\log(age)$	$\log(L/L_\odot)$	$\log(T_{\rm eff})$	$\log(g)$	$\log(k_2)$	$\log(k_3)$	$\log(k_4)$	β	P(d)
1.8942	2.8885	3.5931	1.4185	−0.8366	−1.2975	−1.6150	0.4333	3130.6572
3.2701	2.6728	3.6126	1.7122	−0.8183	−1.2846	−1.6062	0.4363	1615.5427
3.7746	2.4528	3.6305	2.0040	−0.8032	−1.2638	−1.5806	0.4394	855.5534
4.1847	2.2328	3.6476	2.2923	−0.7904	−1.2455	−1.5576	0.4422	443.1973
4.6550	2.0202	3.6635	2.5683	−0.7800	−1.2305	−1.5385	0.4444	234.8054
4.9485	1.8908	3.6728	2.7350	−0.7907	−1.2384	−1.5439	0.4456	159.9802
5.1847	1.7015	3.6862	2.9781	−0.8045	−1.2611	−1.5708	0.4447	91.4479
5.4390	1.5371	3.6989	3.1931	−0.8111	−1.2697	−1.5831	0.4371	55.7637
5.6778	1.4326	3.7119	3.3498	−0.9010	−1.3531	−1.6633	0.4132	38.8834
5.8583	1.4639	3.7282	3.3835	−1.2703	−1.7493	−2.0664	0.3563	35.9841
5.9537	1.6122	3.7474	3.3120	−1.8123	−2.4122	−2.7997	0.2856	42.4146
6.0140	1.7236	3.7689	3.2867	−2.1871	−2.9042	−3.3901	0.2428	44.9584
6.0744	1.8725	3.8195	3.3409	−2.4621	−3.2558	−3.8148	0.2159	20.3535
6.1409	2.1033	3.9257	3.5351	−2.6223	−3.4367	−4.0074	0.2027	12.9209
6.1899	2.2928	4.0332	3.7759	−2.6859	−3.5187	−4.0961	0.1965	7.4077
6.2301	2.3403	4.1126	4.0464	−2.6139	−3.4604	−4.0435	0.2054	3.9906
6.2790	2.1580	4.1052	4.1994	−2.3305	−3.1631	−3.7420	0.2280	2.8161
6.4094	2.1572	4.1370	4.3277	−2.2531	−3.0855	−3.6663	0.2345	2.1040
7.7687	2.1974	4.1198	4.2187	−2.3720	−3.2044	−3.7841	0.2247	2.6962
8.0256	2.2413	4.1031	4.1075	−2.5060	−3.3337	−3.9114	0.2148	3.4725

Table A.69: Evolutionary tracks including internal structure constants and gyration radii for 3.80 $M_\odot$ pre-MS rotating models.

$\log(age)$	$\log(L/L_\odot)$	$\log(T_{\rm eff})$	$\log(g)$	$\log(k_2)$	$\log(k_3)$	$\log(k_4)$	β	P(d)
1.9054	2.9327	3.5945	1.4155	−0.8308	−1.2893	−1.6047	0.4345	3445.7255
3.2773	2.7170	3.6140	1.7094	−0.8139	−1.2781	−1.5978	0.4373	1775.2237
3.7821	2.4968	3.6321	2.0017	−0.8001	−1.2590	−1.5743	0.4401	925.9825
4.1930	2.2770	3.6493	2.2906	−0.7883	−1.2421	−1.5531	0.4427	476.1602
4.6969	2.0649	3.6654	2.5671	−0.7787	−1.2283	−1.5353	0.4447	252.0162
4.9571	1.9271	3.6756	2.7455	−0.8060	−1.2584	−1.5659	0.4454	167.1360
5.1897	1.7531	3.6890	2.9732	−0.8082	−1.2688	−1.5825	0.4411	98.9836
5.4330	1.6126	3.7020	3.1659	−0.8409	−1.2978	−1.6114	0.4268	63.5288
5.6506	1.5563	3.7165	3.2801	−1.0388	−1.4964	−1.8065	0.3892	48.8534
5.7873	1.6508	3.7336	3.2542	−1.5250	−2.0606	−2.4064	0.3214	51.8491
5.8664	1.7689	3.7530	3.2134	−1.9685	−2.6302	−3.0654	0.2659	56.9526
5.9202	1.8639	3.7773	3.2157	−2.2556	−3.0099	−3.5324	0.2347	56.6513
5.9984	2.0695	3.8640	3.3574	−2.4850	−3.2836	−3.8463	0.2140	21.4146
6.0594	2.2938	3.9727	3.5682	−2.6195	−3.4373	−4.0090	0.2023	13.1239
6.1048	2.4582	4.0767	3.8199	−2.6476	−3.4808	−4.0571	0.1989	7.3557
6.1446	2.4330	4.1369	4.0862	−2.4957	−3.3423	−3.9244	0.2143	4.0024
6.2009	2.3463	4.1477	4.2167	−2.3331	−3.1613	−3.7378	0.2272	2.9728
7.0148	2.2965	4.1588	4.3108	−2.2356	−3.0664	−3.6456	0.2362	2.3999
7.7592	2.3438	4.1400	4.1880	−2.3730	−3.2017	−3.7788	0.2251	3.1741
7.9728	2.3885	4.1235	4.0772	−2.5085	−3.3323	−3.9075	0.2151	4.0869

A.4 Rotating binary models: rotating stars in binary systems

Pre-main sequence evolutionary tracks for rotationally and tidally distorted stellar models are given in Tables (A.70) to (A.92). Same header as in tables of Appendix (A.1).

Table A.70: Evolutionary tracks including internal structure constants and gyration radii for 0.09 $M_\odot$ pre-MS rotationally and tidally distorted models.

$\log(age)$	$\log(L/L_\odot)$	$\log(T_{\rm eff})$	$\log(g)$	$\log(k_2)$	$\log(k_3)$	$\log(k_4)$	β	P(d)
2.8237	−0.1259	3.3938	2.0492	−1.2621	−1.8411	−2.2588	0.3593	45.1551
4.1938	−0.3507	3.4064	2.3239	−1.1683	−1.7256	−2.1163	0.3720	25.7335
4.7042	−0.5700	3.4255	2.6198	−1.1046	−1.6397	−2.0106	0.3830	13.8068
5.1314	−0.7898	3.4424	2.9077	−1.0325	−1.5516	−1.9082	0.3953	7.5905
5.5208	−1.0101	3.4554	3.1808	−0.9551	−1.4590	−1.8045	0.4087	4.3317
6.1513	−1.2132	3.4651	3.4235	−0.9185	−1.4073	−1.7429	0.4161	2.5735
6.3844	−1.3524	3.4708	3.5864	−0.9004	−1.3823	−1.7124	0.4201	1.8065
6.5657	−1.5553	3.4781	3.8198	−0.8711	−1.3456	−1.6694	0.4260	1.0883
6.8140	−1.7761	3.4844	4.0676	−0.8403	−1.3061	−1.6235	0.4322	0.6358
7.0892	−1.9967	3.4890	4.3092	−0.8347	−1.2923	−1.6031	0.4346	0.3709
7.3908	−2.2172	3.4914	4.5427	−0.8228	−1.2764	−1.5828	0.4377	0.2213
7.7000	−2.4377	3.4925	4.7715	−0.8156	−1.2645	−1.5670	0.4402	0.1334
8.0223	−2.6581	3.4911	4.9904	−0.7912	−1.2347	−1.5328	0.4461	0.0835
8.3414	−2.8792	3.4836	5.1848	−0.7540	−1.1888	−1.4805	0.4546	0.0559
8.6259	−3.1017	3.4636	5.3305	−0.7267	−1.1536	−1.4390	0.4614	0.0415
8.8533	−3.3250	3.4269	5.4088	−0.7162	−1.1391	−1.4212	0.4643	0.0352
9.2264	−3.5330	3.3846	5.4487	−0.7120	−1.1331	−1.4136	0.4656	0.0324
11.5704	−3.3642	3.4259	5.4455	−0.7160	−1.1386	−1.4204	0.4647	0.0325
11.8711	−3.1295	3.4714	5.3924	−0.7300	−1.1575	−1.4434	0.4614	0.0362
12.0479	−2.9040	3.4880	5.2309	−0.7701	−1.2089	−1.5030	0.4520	0.0501

Table A.71: Evolutionary tracks including internal structure constants and gyration radii for 0.10 $M_\odot$ pre-MS rotationally and tidally distorted models.

$\log(age)$	$\log(L/L_\odot)$	$\log(T_{\rm eff})$	$\log(g)$	$\log(k_2)$	$\log(k_3)$	$\log(k_4)$	β	P(d)
3.8575	−0.6246	3.4386	2.7779	−1.0687	−1.5934	−1.9603	0.3913	7.0589
5.1685	−0.8496	3.4530	3.0610	−0.9862	−1.4993	−1.8522	0.4039	3.9281
5.6886	−1.0661	3.4640	3.3229	−0.9293	−1.4260	−1.7678	0.4145	2.2710
6.3043	−1.2310	3.4707	3.5165	−0.9075	−1.3937	−1.7277	0.4196	1.4968
6.4465	−1.3944	3.4765	3.7053	−0.8874	−1.3670	−1.6952	0.4241	0.9944
6.6870	−1.6149	3.4831	3.9557	−0.8562	−1.3284	−1.6506	0.4307	0.5809
6.9605	−1.8357	3.4885	4.2028	−0.8438	−1.3073	−1.6231	0.4345	0.3383
7.2588	−2.0562	3.4918	4.4426	−0.8388	−1.2976	−1.6083	0.4373	0.2001
7.5672	−2.2767	3.4932	4.6765	−0.8352	−1.2907	−1.5981	0.4396	0.1201
7.8848	−2.4971	3.4929	4.9047	−0.8280	−1.2802	−1.5845	0.4430	0.0737
8.2133	−2.7175	3.4893	5.1190	−0.8010	−1.2474	−1.5471	0.4503	0.0474
8.5435	−2.9381	3.4777	5.2999	−0.7660	−1.2033	−1.4962	0.4594	0.0330
8.8665	−3.1583	3.4517	5.4212	−0.7474	−1.1782	−1.4659	0.4650	0.0259
10.7498	−3.2794	3.4314	5.4643	−0.7441	−1.1733	−1.4594	0.4664	0.0237
11.6318	−3.0482	3.4735	5.4005	−0.7616	−1.1969	−1.4881	0.4619	0.0269
11.9080	−2.8234	3.4877	5.2285	−0.8046	−1.2518	−1.5515	0.4513	0.0378
12.1991	−2.7565	3.4878	5.1583	−0.8192	−1.2704	−1.5728	0.4474	0.0433
12.3579	−2.7468	3.4846	5.1349	−0.8230	−1.2776	−1.5831	0.4461	0.0454
12.4620	−2.7177	3.4908	5.1300	−0.8194	−1.2758	−1.5839	0.4464	0.0459
12.5354	−2.6781	3.5079	5.1591	−0.8113	−1.2673	−1.5764	0.4481	0.0433

Table A.72: Evolutionary tracks including internal structure constants and gyration radii for 0.20 $M_\odot$ pre-MS rotationally and tidally distorted models.

$\log(age)$	$\log(L/L_\odot)$	$\log(T_{\rm eff})$	$\log(g)$	$\log(k_2)$	$\log(k_3)$	$\log(k_4)$	β	P(d)
2.9189	0.4129	3.5112	2.3322	−1.0162	−1.5437	−1.9205	0.3994	18.1258
4.2594	0.1903	3.5131	2.5628	−0.9768	−1.5020	−1.8741	0.4065	11.0536
4.7341	−0.0306	3.5134	2.7862	−0.9479	−1.4634	−1.8266	0.4122	6.8182
5.1111	−0.2514	3.5122	3.0044	−0.9229	−1.4303	−1.7866	0.4174	4.2508
5.5372	−0.4638	3.5098	3.2098	−0.8982	−1.3977	−1.7475	0.4226	2.7307
6.0300	−0.6445	3.5076	3.3843	−0.8781	−1.3702	−1.7141	0.4271	1.8779
6.1812	−0.8206	3.5067	3.5593	−0.8598	−1.3443	−1.6818	0.4315	1.2889
6.4222	−1.0410	3.5068	3.7846	−0.8433	−1.3199	−1.6500	0.4361	0.7921
6.7061	−1.2614	3.5070	4.0118	−0.8306	−1.3015	−1.6263	0.4400	0.4845
7.0202	−1.4814	3.5085	4.2460	−0.8254	−1.2921	−1.6129	0.4429	0.2918
7.3488	−1.7017	3.5106	4.4858	−0.8270	−1.2915	−1.6096	0.4449	0.1738
7.6802	−1.9222	3.5120	4.7261	−0.8352	−1.2998	−1.6169	0.4460	0.1037
8.0170	−2.1423	3.5101	4.9635	−0.8571	−1.3259	−1.6451	0.4453	0.0634
8.2895	−2.2766	3.5077	5.1045	−0.8725	−1.3449	−1.6663	0.4443	0.0474
10.8892	−2.2628	3.5074	5.0814	−0.8610	−1.3305	−1.6498	0.4458	0.0494
11.3759	−2.2495	3.5061	5.0590	−0.8537	−1.3215	−1.6398	0.4468	0.0518
11.5951	−2.2484	3.5049	5.0519	−0.8489	−1.3157	−1.6333	0.4476	0.0526
11.7365	−2.2471	3.5041	5.0461	−0.8443	−1.3101	−1.6271	0.4484	0.0534
11.8400	−2.2450	3.5037	5.0412	−0.8399	−1.3047	−1.6212	0.4492	0.0540
11.9212	−2.2419	3.5038	5.0373	−0.8357	−1.2997	−1.6156	0.4499	0.0546

Table A.73: Evolutionary tracks including internal structure constants and gyration radii for 0.30 $M_\odot$ pre-MS rotationally and tidally distorted models.

$\log(age)$	$\log(L/L_\odot)$	$\log(T_{\rm eff})$	$\log(g)$	$\log(k_2)$	$\log(k_3)$	$\log(k_4)$	β	P(d)
2.9991	0.7007	3.5499	2.3715	−0.9398	−1.4440	−1.8014	0.4130	26.4759
4.2725	0.4736	3.5538	2.6140	−0.8993	−1.4005	−1.7536	0.4203	15.6993
4.7451	0.2532	3.5560	2.8437	−0.8747	−1.3666	−1.7113	0.4255	9.49136
5.1406	0.0342	3.5566	3.0666	−0.8570	−1.3421	−1.6809	0.4293	5.7997
5.7343	−0.1494	3.5562	3.2496	−0.8441	−1.3244	−1.6591	0.4322	3.8687
5.8795	−0.3113	3.5547	3.4066	−0.8322	−1.3081	−1.6391	0.4349	2.7359
6.0964	−0.5321	3.5511	3.6148	−0.8176	−1.2874	−1.6132	0.4384	1.7293
6.3540	−0.7527	3.5465	3.8197	−0.8052	−1.2693	−1.5899	0.4417	1.1012
6.6404	−0.9735	3.5416	4.0240	−0.7958	−1.2552	−1.5713	0.4444	0.7014
6.9446	−1.1938	3.5366	4.2281	−0.7886	−1.2446	−1.5574	0.4469	0.4471
7.2691	−1.4139	3.5339	4.4422	−0.7852	−1.2386	−1.5488	0.4489	0.2787
7.6090	−1.6340	3.5339	4.6688	−0.7852	−1.2373	−1.5458	0.4504	0.1691
7.9741	−1.8525	3.5349	4.9004	−0.8068	−1.2586	−1.5664	0.4515	0.1017
10.1773	−1.9260	3.5342	4.9768	−0.7917	−1.2442	−1.5522	0.4520	0.0867
10.8841	−1.9132	3.5335	4.9595	−0.7893	−1.2411	−1.5487	0.4523	0.0899
11.1377	−1.9125	3.5330	4.9563	−0.7879	−1.2392	−1.5464	0.4525	0.0906
11.2946	−1.9109	3.5327	4.9536	−0.7865	−1.2374	−1.5443	0.4528	0.0913
11.4080	−1.9085	3.5328	4.9513	−0.7851	−1.2357	−1.5423	0.4530	0.0918
11.4964	−1.9050	3.5332	4.9494	−0.7839	−1.2340	−1.5404	0.4533	0.0923
11.5687	−1.9002	3.5341	4.9480	−0.7827	−1.2325	−1.5385	0.4535	0.0926

Table A.74: Evolutionary tracks including internal structure constants and gyration radii for 0.40 $M_\odot$ pre-MS rotationally and tidally distorted models.

$\log(age)$	$\log(L/L_\odot)$	$\log(T_{\rm eff})$	$\log(g)$	$\log(k_2)$	$\log(k_3)$	$\log(k_4)$	β	P(d)
2.7435	1.0500	3.5654	2.2076	−0.9409	−1.4447	−1.8012	0.4125	51.3876
4.0373	0.8262	3.5735	2.4630	−0.8901	−1.3884	−1.7392	0.4217	29.8287
4.5151	0.6054	3.5785	2.7043	−0.8570	−1.3427	−1.6827	0.4285	17.6704
4.9019	0.3855	3.5816	2.9368	−0.8356	−1.3127	−1.6450	0.4330	10.5805
5.5125	0.1825	3.5828	3.1454	−0.8226	−1.2943	−1.6217	0.4360	6.6456
5.6805	0.0473	3.5829	3.2817	−0.8153	−1.2841	−1.6089	0.4376	4.8997
5.8918	−0.1736	3.5818	3.4994	−0.8039	−1.2682	−1.5892	0.4403	3.0121
6.1435	−0.3944	3.5787	3.7093	−0.7934	−1.2532	−1.5702	0.4429	1.8860
6.4205	−0.6153	3.5738	3.9123	−0.7846	−1.2401	−1.5532	0.4452	1.1992
6.7153	−0.8359	3.5681	4.1123	−0.7769	−1.2289	−1.5385	0.4474	0.7678
7.0205	−1.0565	3.5619	4.3107	−0.7710	−1.2202	−1.5271	0.4494	0.4935
7.3374	−1.2769	3.5564	4.5123	−0.7872	−1.2342	−1.5391	0.4509	0.3146
7.6850	−1.4961	3.5543	4.7274	−0.8064	−1.2623	−1.5715	0.4501	0.1934
8.1892	−1.6996	3.5555	4.9433	−0.8078	−1.2703	−1.5859	0.4457	0.1180
10.2530	−1.6659	3.5546	4.9048	−0.8128	−1.2743	−1.5880	0.4478	0.1297
10.6338	−1.6425	3.5566	4.8903	−0.8365	−1.2984	−1.6133	0.4410	0.1314
10.8530	−1.6130	3.5593	4.8728	−0.8722	−1.3322	−1.6472	0.4322	0.1335
10.9986	−1.5763	3.5627	4.8512	−0.9238	−1.3809	−1.6956	0.4216	0.1363
11.1025	−1.5315	3.5669	4.8248	−0.9924	−1.4456	−1.7599	0.4094	0.1402
11.1818	−1.4758	3.5722	4.7918	−1.0878	−1.5347	−1.8480	0.3954	0.1457

Table A.75: Evolutionary tracks including internal structure constants and gyration radii for 0.50 $M_\odot$ pre-MS rotationally and tidally distorted models.

$\log(age)$	$\log(L/L_\odot)$	$\log(T_{\rm eff})$	$\log(g)$	$\log(k_2)$	$\log(k_3)$	$\log(k_4)$	β	P(d)
2.8043	1.1429	3.5814	2.2749	−0.9077	−1.3993	−1.7454	0.4189	56.8642
4.1207	0.9200	3.5899	2.5311	−0.8627	−1.3503	−1.6919	0.4271	32.7623
4.6013	0.6996	3.5958	2.7752	−0.8331	−1.3091	−1.6406	0.4333	19.2189
5.0336	0.4840	3.5993	3.0055	−0.8142	−1.2823	−1.6068	0.4373	11.5313
5.5287	0.3132	3.6008	3.1828	−0.8043	−1.2682	−1.5888	0.4396	7.7535
5.6844	0.1457	3.6013	3.3527	−0.7968	−1.2574	−1.5751	0.4413	5.2909
5.9266	−0.0751	3.6004	3.5706	−0.7881	−1.2452	−1.5597	0.4434	3.2407
6.1995	−0.2958	3.5975	3.7810	−0.7801	−1.2338	−1.5452	0.4454	2.0196
6.4874	−0.5167	3.5925	3.9831	−0.7731	−1.2234	−1.5318	0.4472	1.2828
6.7859	−0.7374	3.5862	4.1805	−0.7670	−1.2145	−1.5201	0.4490	0.8237
7.0934	−0.9581	3.5797	4.3767	−0.7849	−1.2303	−1.5338	0.4505	0.5301
7.4232	−1.1774	3.5744	4.5775	−0.8024	−1.2575	−1.5660	0.4489	0.3344
7.7716	−1.3490	3.5760	4.7607	−0.8403	−1.2993	−1.6132	0.4344	0.2122
8.8744	−1.4442	3.5760	4.8599	−0.8596	−1.3147	−1.6276	0.4306	0.1680
10.2363	−1.3985	3.5792	4.8269	−0.8771	−1.3338	−1.6476	0.4233	0.1779
10.5400	−1.3582	3.5836	4.8046	−0.9309	−1.3864	−1.6997	0.4136	0.1829
10.7142	−1.3122	3.5888	4.7798	−0.9982	−1.4520	−1.7647	0.4028	0.1885
10.8325	−1.2591	3.5948	4.7515	−1.0788	−1.5298	−1.8416	0.3910	0.1955
10.9204	−1.1964	3.6019	4.7180	−1.1747	−1.6215	−1.9326	0.3779	0.2045
10.9886	−1.1209	3.6104	4.6772	−1.3009	−1.7423	−2.0525	0.3635	0.2168

Table A.76: Evolutionary tracks including internal structure constants and gyration radii for 0.60 $M_\odot$ pre-MS rotationally and tidally distorted models.

$\log(age)$	$\log(L/L_\odot)$	$\log(T_{\rm eff})$	$\log(g)$	$\log(k_2)$	$\log(k_3)$	$\log(k_4)$	β	P(d)
2.8468	1.2415	3.5917	2.2964	−0.8899	−1.3748	−1.7149	0.4224	66.1500
4.1572	1.0187	3.6011	2.5561	−0.8486	−1.3303	−1.6666	0.4300	37.6799
4.6398	0.7983	3.6079	2.8037	−0.8207	−1.2912	−1.6178	0.4359	21.8893
5.2428	0.5895	3.6122	3.0302	−0.8030	−1.2660	−1.5859	0.4397	13.2328
5.4810	0.4483	3.6141	3.1792	−0.7948	−1.2543	−1.5709	0.4415	9.4747
5.6841	0.2446	3.6154	3.3885	−0.7863	−1.2419	−1.5551	0.4435	5.9097
5.9435	0.0239	3.6149	3.6077	−0.7790	−1.2317	−1.5421	0.4452	3.6018
6.2272	−0.1969	3.6123	3.8192	−0.7726	−1.2224	−1.5302	0.4468	2.2339
6.5211	−0.4178	3.6075	4.0221	−0.7669	−1.2140	−1.5193	0.4484	1.4132
6.8205	−0.6386	3.6010	4.2181	−0.7740	−1.2182	−1.5211	0.4498	0.9083
7.1350	−0.8586	3.5946	4.4138	−0.7968	−1.2476	−1.5531	0.4495	0.5806
7.4682	−1.0453	3.5934	4.5987	−0.8274	−1.2857	−1.5984	0.4379	0.3681
7.7702	−1.1039	3.6072	4.7177	−0.9832	−1.4392	−1.7513	0.4031	0.2560
9.0494	−1.1610	3.6069	4.7759	−0.9867	−1.4438	−1.7547	0.4020	0.2228
10.0570	−1.1134	3.6122	4.7491	−1.0337	−1.4909	−1.8021	0.3937	0.2325
10.3437	−1.0635	3.6186	4.7249	−1.1017	−1.5588	−1.8702	0.3837	0.2404
10.5146	−1.0054	3.6259	4.6966	−1.1807	−1.6361	−1.9473	0.3724	0.2501
10.6305	−0.9393	3.6341	4.6634	−1.2795	−1.7325	−2.0435	0.3601	0.2627
10.7160	−0.8626	3.6430	4.6228	−1.4025	−1.8525	−2.1635	0.3467	0.2797
10.7815	−0.7718	3.6529	4.5716	−1.5589	−2.0039	−2.3144	0.3323	0.3045

Table A.77: Evolutionary tracks including internal structure constants and gyration radii for 0.70 $M_\odot$ pre-MS rotationally and tidally distorted models.

$\log(age)$	$\log(L/L_\odot)$	$\log(T_{\rm eff})$	$\log(g)$	$\log(k_2)$	$\log(k_3)$	$\log(k_4)$	β	P(d)
2.7548	1.3909	3.5961	2.2311	−0.8890	−1.3730	−1.7120	0.4225	89.9212
4.0822	1.1689	3.6068	2.4953	−0.8479	−1.3291	−1.6648	0.4300	50.6539
4.5671	0.9486	3.6151	2.7488	−0.8188	−1.2885	−1.6143	0.4361	29.0568
5.1358	0.7384	3.6208	2.9821	−0.7992	−1.2606	−1.5790	0.4403	17.3146
5.4153	0.5942	3.6237	3.1379	−0.7898	−1.2472	−1.5618	0.4424	12.2145
5.6114	0.3997	3.6261	3.3423	−0.7810	−1.2343	−1.5453	0.4444	7.7053
5.8726	0.1791	3.6268	3.5663	−0.7740	−1.2243	−1.5325	0.4460	4.6402
6.1582	−0.0416	3.6253	3.7818	−0.7684	−1.2163	−1.5222	0.4474	2.8474
6.4548	−0.2625	3.6217	3.9890	−0.7634	−1.2090	−1.5128	0.4488	1.7809
6.7552	−0.4832	3.6159	4.1877	−0.7850	−1.2294	−1.5316	0.4499	1.1353
7.0766	−0.7023	3.6101	4.3850	−0.7995	−1.2536	−1.5613	0.4471	0.7165
7.3873	−0.8488	3.6133	4.5467	−0.8577	−1.3149	−1.6274	0.4287	0.4692
7.6430	−0.8380	3.6365	4.6324	−1.0946	−1.5516	−1.8626	0.3849	0.3432
7.9230	−0.8784	3.6480	4.7225	−1.2337	−1.7086	−2.0239	0.3691	0.2643
9.7060	−0.8484	3.6477	4.6904	−1.1980	−1.6669	−1.9804	0.3687	0.2864
10.0616	−0.7977	3.6542	4.6661	−1.2679	−1.7372	−2.0512	0.3595	0.2971
10.2580	−0.7376	3.6621	4.6378	−1.3519	−1.8202	−2.1341	0.3490	0.3103
10.3943	−0.6636	3.6718	4.6027	−1.4538	−1.9189	−2.2323	0.3370	0.3282
10.4910	−0.5779	3.6821	4.5585	−1.5838	−2.0447	−2.3578	0.3240	0.3532
10.5632	−0.4769	3.6918	4.4955	−1.7622	−2.2176	−2.5305	0.3092	0.4033

Table A.78: Evolutionary tracks including internal structure constants and gyration radii for 0.80 $M_\odot$ pre-MS rotationally and tidally distorted models.

$\log(age)$	$\log(L/L_\odot)$	$\log(T_{\rm eff})$	$\log(g)$	$\log(k_2)$	$\log(k_3)$	$\log(k_4)$	β	P(d)
2.6879	1.5166	3.5989	2.1745	−0.8873	−1.3703	−1.7083	0.4229	117.4304
4.0214	1.2954	3.6108	2.4425	−0.8470	−1.3277	−1.6628	0.4301	65.5005
4.5081	1.0750	3.6203	2.7007	−0.8177	−1.2870	−1.6124	0.4362	37.1561
5.0396	0.8646	3.6272	2.9389	−0.7972	−1.2578	−1.5755	0.4406	21.9107
5.3622	0.7163	3.6309	3.1023	−0.7867	−1.2428	−1.5562	0.4429	15.2039
5.5562	0.5266	3.6343	3.3059	−0.7773	−1.2291	−1.5386	0.4450	9.6108
5.8204	0.3061	3.6363	3.5348	−0.7701	−1.2187	−1.5252	0.4467	5.7220
6.1087	0.0852	3.6359	3.7547	−0.7648	−1.2111	−1.5155	0.4480	3.4733
6.4070	−0.1356	3.6332	3.9651	−0.7604	−1.2047	−1.5073	0.4491	2.1540
6.7111	−0.3562	3.6284	4.1674	−0.7896	−1.2355	−1.5380	0.4497	1.3581
7.0362	−0.5643	3.6250	4.3633	−0.8081	−1.2648	−1.5748	0.4433	0.8493
7.3205	−0.6633	3.6338	4.4996	−0.9065	−1.3623	−1.6744	0.4173	0.5770
7.5379	−0.5894	3.6660	4.5578	−1.2196	−1.6823	−1.9945	0.3665	0.4408
7.7440	−0.5743	3.6928	4.6517	−1.4391	−1.9393	−2.2640	0.3417	0.3423
9.3869	−0.5946	3.6858	4.6456	−1.3554	−1.8452	−2.1660	0.3473	0.3366
9.8110	−0.5433	3.6926	4.6213	−1.4249	−1.9147	−2.2356	0.3386	0.3544
10.0218	−0.4852	3.6998	4.5917	−1.5086	−1.9974	−2.3181	0.3286	0.3774
10.1643	−0.4165	3.7073	4.5524	−1.6202	−2.1084	−2.4294	0.3167	0.4104
10.2736	−0.3309	3.7147	4.4959	−1.7694	−2.2536	−2.5740	0.3022	0.4631
10.3560	−0.2264	3.7206	4.4142	−1.9770	−2.4536	−2.7728	0.2859	0.5520

Table A.79: Evolutionary tracks including internal structure constants and gyration radii for 0.90 $M_\odot$ pre-MS rotationally and tidally distorted models.

$\log(age)$	$\log(L/L_\odot)$	$\log(T_{\rm eff})$	$\log(g)$	$\log(k_2)$	$\log(k_3)$	$\log(k_4)$	β	P(d)
2.6419	1.6241	3.6009	2.1260	−0.8848	−1.3667	−1.7036	0.4234	148.2934
3.9726	1.4034	3.6137	2.3973	−0.8466	−1.3267	−1.6611	0.4303	81.9669
4.4602	1.1831	3.6242	2.6592	−0.8180	−1.2869	−1.6118	0.4363	46.0751
4.9662	0.9720	3.6321	2.9021	−0.7970	−1.2572	−1.5743	0.4407	26.8779
5.3175	0.8219	3.6366	3.0703	−0.7859	−1.2412	−1.5539	0.4432	18.4579
5.5093	0.6363	3.6408	3.2729	−0.7760	−1.2268	−1.5354	0.4454	11.6986
5.7760	0.4159	3.6439	3.5062	−0.7683	−1.2156	−1.5209	0.4472	6.8970
6.0673	0.1952	3.6448	3.7307	−0.7631	−1.2081	−1.5113	0.4484	4.1403
6.3678	−0.0256	3.6429	3.9449	−0.7638	−1.2066	−1.5080	0.4494	2.5432
6.6767	−0.2460	3.6392	4.1507	−0.7913	−1.2393	−1.5426	0.4491	1.5843
6.9948	−0.4327	3.6389	4.3374	−0.8206	−1.2783	−1.5898	0.4384	0.9980
7.2556	−0.4841	3.6539	4.4508	−0.9632	−1.4173	−1.7285	0.4051	0.7009
7.4417	−0.3624	3.6939	4.4909	−1.3316	−1.7998	−2.1132	0.3508	0.5787
7.6043	−0.2931	3.7284	4.5598	−1.6701	−2.1998	−2.5358	0.3129	0.4970
9.0539	−0.3642	3.7196	4.5964	−1.5183	−2.0357	−2.3668	0.3258	0.4594
9.5757	−0.3144	3.7248	4.5672	−1.5980	−2.1165	−2.4478	0.3162	0.4896
9.8030	−0.2599	3.7300	4.5330	−1.6913	−2.2106	−2.5421	0.3057	0.5276
9.9488	−0.1987	3.7348	4.4906	−1.8055	−2.3263	−2.6586	0.2940	0.5789
10.0574	−0.1270	3.7389	4.4352	−1.9437	−2.4622	−2.7938	0.2810	0.6537
10.1523	−0.0295	3.7418	4.3487	−2.1427	−2.6516	−2.9802	0.2655	0.7909

Table A.80: Evolutionary tracks including internal structure constants and gyration radii for 1.00 $M_\odot$ pre-MS rotationally and tidally distorted models.

$\log(age)$	$\log(L/L_\odot)$	$\log(T_{\rm eff})$	$\log(g)$	$\log(k_2)$	$\log(k_3)$	$\log(k_4)$	β	P(d)
2.2954	1.8910	3.5901	1.8618	−0.9140	−1.4048	−1.7486	0.4177	295.0759
3.6548	1.6729	3.6056	2.1410	−0.8718	−1.3609	−1.7026	0.4253	160.6325
4.1462	1.4528	3.6185	2.4122	−0.8387	−1.3158	−1.6475	0.4319	88.7067
4.5433	1.2324	3.6292	2.6758	−0.8122	−1.2787	−1.6015	0.4374	49.5897
5.1020	1.0252	3.6375	2.9163	−0.7929	−1.2513	−1.5668	0.4416	29.0489
5.3023	0.8978	3.6417	3.0605	−0.7837	−1.2380	−1.5499	0.4436	21.0367
5.5221	0.6901	3.6471	3.2898	−0.7726	−1.2219	−1.5291	0.4461	12.5520
5.7957	0.4695	3.6508	3.5256	−0.7651	−1.2110	−1.5150	0.4478	7.3564
6.0919	0.2488	3.6523	3.7527	−0.7602	−1.2039	−1.5058	0.4490	4.3874
6.3960	0.0280	3.6511	3.9694	−0.7823	−1.2252	−1.5260	0.4498	2.6770
6.7152	−0.1878	3.6490	4.1772	−0.8000	−1.2537	−1.5609	0.4463	1.6416
7.0052	−0.3205	3.6547	4.3341	−0.8588	−1.3138	−1.6249	0.4270	1.0805
7.2287	−0.2881	3.6818	4.4115	−1.0999	−1.5535	−1.8627	0.3828	0.8094
7.3772	−0.1313	3.7227	4.4182	−1.5574	−2.0444	−2.3632	0.3225	0.7969
7.5055	−0.0681	3.7533	4.4776	−1.8772	−2.4389	−2.7869	0.2856	0.6976
8.8246	−0.1500	3.7471	4.5354	−1.7118	−2.2616	−2.6053	0.3004	0.6144
9.3863	−0.1013	3.7510	4.5019	−1.8034	−2.3575	−2.7029	0.2903	0.6616
9.6158	−0.0501	3.7545	4.4644	−1.9036	−2.4607	−2.8071	0.2798	0.7189
9.7582	0.0042	3.7574	4.4215	−2.0124	−2.5704	−2.9168	0.2691	0.7909
9.8616	0.0631	3.7593	4.3702	−2.1373	−2.6966	−3.0441	0.2583	0.8864

Table A.81: Evolutionary tracks including internal structure constants and gyration radii for 1.20 $M_\odot$ pre-MS rotationally and tidally distorted models.

$\log(age)$	$\log(L/L_\odot)$	$\log(T_{\rm eff})$	$\log(g)$	$\log(k_2)$	$\log(k_3)$	$\log(k_4)$	β	P(d)
2.2057	2.0500	3.5915	1.7875	−0.9050	−1.3925	−1.7332	0.4194	424.6592
3.5812	1.8326	3.6078	2.0692	−0.8662	−1.3531	−1.6928	0.4264	229.1930
4.0771	1.6122	3.6219	2.3454	−0.8354	−1.3110	−1.6414	0.4326	124.8134
4.4756	1.3922	3.6338	2.6134	−0.8107	−1.2764	−1.5983	0.4377	68.9593
5.0170	1.1828	3.6436	2.8619	−0.7919	−1.2497	−1.5646	0.4417	39.6317
5.2409	1.0534	3.6488	3.0121	−0.7826	−1.2362	−1.5474	0.4438	28.3100
5.4593	0.8507	3.6555	3.2415	−0.7711	−1.2196	−1.5260	0.4463	17.8687
5.7370	0.6303	3.6609	3.4829	−0.7627	−1.2074	−1.5102	0.4482	143.5903
6.0381	0.4097	3.6642	3.7182	−0.7574	−1.1997	−1.5002	0.4495	5.7217
6.3520	0.1893	3.6656	3.9443	−0.7887	−1.2344	−1.5359	0.4495	3.4040
6.6610	0.0039	3.6683	4.1414	−0.8106	−1.2668	−1.5767	0.4406	2.1021
6.9160	−0.0635	3.6824	4.2659	−0.9267	−1.3800	−1.6904	0.4115	1.4929
7.0985	0.0288	3.7136	4.2982	−1.2884	−1.7512	−2.0622	0.3564	1.3872
7.2113	0.2190	3.7495	4.2516	−1.8554	−2.3809	−2.7140	0.2871	1.5409
7.2855	0.3622	3.7797	4.2291	−2.3236	−2.9605	−3.3458	0.2350	1.6211
7.3695	0.2210	3.7872	4.4005	−2.1380	−2.8050	−3.2134	0.2534	1.1006
8.6320	0.2392	3.7907	4.3966	−2.1607	−2.8371	−3.2535	0.2469	1.1109
9.0903	0.2804	3.7925	4.3625	−2.2443	−2.9306	−3.3535	0.2384	1.1996
9.2849	0.3179	3.7936	4.3291	−2.3245	−3.0162	−3.4426	0.2312	1.2934
9.4012	0.3502	3.7938	4.2975	−2.3999	−3.0936	−3.5220	0.2253	1.3892

Table A.82: Evolutionary tracks including internal structure constants and gyration radii for 1.40 $M_\odot$ pre-MS rotaionally and tidally distorted models.

$\log(age)$	$\log(L/L_\odot)$	$\log(T_{\rm eff})$	$\log(g)$	$\log(k_2)$	$\log(k_3)$	$\log(k_4)$	β	P(d)
2.1323	2.1806	3.5921	1.7262	−0.8964	−1.3807	−1.7185	0.4211	576.4316
3.5220	1.9642	3.6091	2.0094	−0.8605	−1.3451	−1.6827	0.4275	309.1122
4.0205	1.7440	3.6239	2.2888	−0.8318	−1.3058	−1.6348	0.4333	166.8013
4.4215	1.5239	3.6370	2.5609	−0.8086	−1.2733	−1.5944	0.4381	91.1255
4.9443	1.3132	3.6478	2.8151	−0.7909	−1.2480	−1.5623	0.4419	54.9532
5.1904	1.1831	3.6538	2.9689	−0.7817	−1.2349	−1.5455	0.4439	38.5998
5.4006	0.9906	3.6613	3.1919	−0.7707	−1.2190	−1.5251	0.4464	23.1379
5.6805	0.7702	3.6682	3.4399	−0.7616	−1.2058	−1.5080	0.4484	13.1016
5.9848	0.5497	3.6731	3.6803	−0.7703	−1.2114	−1.5110	0.4497	7.5571
6.3031	0.3352	3.6769	3.9101	−0.7915	−1.2408	−1.5443	0.4481	4.4688
6.5892	0.1854	3.6837	4.0872	−0.8295	−1.2843	−1.5941	0.4343	2.9828
6.8197	0.1621	3.7020	4.1840	−1.0086	−1.4598	−1.7684	0.3967	2.3925
6.9734	0.2938	3.7325	4.1740	−1.4736	−1.9496	−2.2645	0.3327	2.4469
7.0625	0.5040	3.7643	4.0910	−2.1031	−2.6698	−3.0206	0.2596	2.9570
7.1153	0.6474	3.7907	4.0535	−2.5659	−3.2715	−3.7095	0.2119	3.2213
7.1547	0.6918	3.8123	4.1037	−2.7712	−3.5774	−4.1033	0.1940	1.2118
7.2101	0.5148	3.8146	4.2911	−2.4228	−3.2122	−3.7252	0.2224	0.8260
7.6305	0.5394	3.8272	4.3181	−2.4714	−3.2911	−3.8387	0.2137	0.7514
8.7990	0.5845	3.8282	4.2768	−2.5745	−3.4007	−3.9545	0.2061	0.8173
9.0670	0.6225	3.8256	4.2280	−2.6682	−3.4914	−4.0427	0.2003	0.9120

Table A.83: Evolutionary tracks including internal structure constants and gyration radii for 1.60 $M_\odot$ pre-MS rotationally and tidally distorted models.

$\log(age)$	$\log(L/L_\odot)$	$\log(T_{\rm eff})$	$\log(g)$	$\log(k_2)$	$\log(k_3)$	$\log(k_4)$	β	P(d)
2.1002	2.2922	3.5923	1.6732	−0.8886	−1.3699	−1.7051	0.4227	751.2762
3.4764	2.0756	3.6099	1.9592	−0.8545	−1.3369	−1.6726	0.4286	399.4334
3.9753	1.8554	3.6254	2.2411	−0.8277	−1.3001	−1.6278	0.4341	213.8814
4.3781	1.6352	3.6392	2.5167	−0.8059	−1.2697	−1.5897	0.4386	115.7679
4.8831	1.4240	3.6510	2.7749	−0.7892	−1.2457	−1.5594	0.4422	66.1531
5.1509	1.2912	3.6576	2.9344	−0.7804	−1.2330	−1.5431	0.4441	45.8633
5.3645	1.0987	3.6662	3.1611	−0.7696	−1.2175	−1.5232	0.4465	27.2454
5.6481	0.8783	3.6742	3.4138	−0.7604	−1.2041	−1.5059	0.4485	15.2610
5.9567	0.6580	3.6804	3.6590	−0.7833	−1.2259	−1.5259	0.4497	8.6997
6.2655	0.4605	3.6861	3.8794	−0.7997	−1.2530	−1.5596	0.4455	5.2548
6.5309	0.3455	3.6961	4.0348	−0.8614	−1.3159	−1.6266	0.4255	3.6840
6.7367	0.3676	3.7173	4.0974	−1.1258	−1.5787	−1.8868	0.3784	3.1931
6.8635	0.5413	3.7468	4.0415	−1.7012	−2.2048	−2.5300	0.3056	3.6272
6.9325	0.7436	3.7746	3.9504	−2.3143	−2.9413	−3.3290	0.2373	4.4675
6.9739	0.8672	3.7985	3.9223	−2.7079	−3.4691	−3.9606	0.1989	4.7633
7.0172	0.9591	3.8407	4.0060	−2.9094	−3.7709	−4.3553	0.1807	1.6512
7.0697	0.7797	3.8466	4.2109	−2.5831	−3.4458	−4.0325	0.2059	1.0520
7.3239	0.7997	3.8752	4.3062	−2.5460	−3.4081	−4.0011	0.2068	0.8455
8.6388	0.8388	3.8730	4.2582	−2.6355	−3.4981	−4.0907	0.2007	0.9437
8.9114	0.8709	3.8624	4.1829	−2.7349	−3.5947	−4.1849	0.1941	1.1190

Table A.84: Evolutionary tracks including internal structure constants and gyration radii for 1.80 $M_\odot$ pre-MS rotationally and tidally distorted models.

$\log(age)$	$\log(L/L_\odot)$	$\log(T_{\rm eff})$	$\log(g)$	$\log(k_2)$	$\log(k_3)$	$\log(k_4)$	β	P(d)
2.0317	2.3899	3.5923	1.6265	−0.8813	−1.3598	−1.6926	0.4241	949.1508
3.4301	2.1747	3.6102	1.9125	−0.8504	−1.3308	−1.6647	0.4296	503.5106
3.9317	1.9546	3.6262	2.1964	−0.8253	−1.2964	−1.6227	0.4347	268.0157
4.3362	1.7343	3.6407	2.4745	−0.8048	−1.2675	−1.5868	0.4390	146.5798
4.8188	1.5228	3.6533	2.7363	−0.7889	−1.2449	−1.5579	0.4424	80.26500
5.1154	1.3870	3.6606	2.9016	−0.7804	−1.2325	−1.5421	0.4443	54.89937
5.3262	1.1990	3.6698	3.1263	−0.7702	−1.2179	−1.5234	0.4465	32.7635
5.6124	0.9786	3.6789	3.3833	−0.7610	−1.2045	−1.5061	0.4486	18.1614
5.9229	0.7602	3.6862	3.6313	−0.7879	−1.2329	−1.5339	0.4493	10.2853
6.2169	0.5826	3.6935	3.8379	−0.8052	−1.2593	−1.5670	0.4422	6.4066
6.4663	0.4952	3.7057	3.9744	−0.8987	−1.3512	−1.6610	0.4166	4.6881
6.6514	0.5554	3.7282	4.0042	−1.2479	−1.7080	−2.0182	0.3610	4.3790
6.7565	0.7582	3.7560	3.9126	−1.8867	−2.4254	−2.7658	0.2827	5.3997
6.8131	0.9335	3.7808	3.8363	−2.4339	−3.1143	−3.5434	0.2242	6.4306
6.8481	1.0436	3.8044	3.8243	−2.7612	−3.5580	−4.0886	0.1935	3.0542
6.9035	1.1867	3.8841	4.0016	−2.8935	−3.7596	−4.3500	0.1819	1.9166
6.9493	1.0004	3.8866	4.1993	−2.5705	−3.4400	−4.0345	0.2070	1.2249
7.0877	1.0317	3.9230	4.3147	−2.5227	−3.3860	−3.9811	0.2092	0.9446
8.4517	1.0483	3.9166	4.2724	−2.5853	−3.4483	−4.0427	0.2051	1.0415
8.7550	1.0799	3.9025	4.1836	−2.6946	−3.5531	−4.1446	0.1977	1.2734

Table A.85: Evolutionary tracks including internal structure constants and gyration radii for 2.00 $M_\odot$ pre-MS rotationally and tidally distorted models.

$\log(age)$	$\log(L/L_\odot)$	$\log(T_{\rm eff})$	$\log(g)$	$\log(k_2)$	$\log(k_3)$	$\log(k_4)$	β	P(d)
2.0185	2.4769	3.5923	1.5854	−0.8746	−1.3506	−1.6811	0.4255	1168.4132
3.3982	2.2597	3.6105	1.8743	−0.8454	−1.3238	−1.6559	0.4306	614.6425
3.8988	2.0397	3.6269	2.1597	−0.8217	−1.2914	−1.6164	0.4354	325.5443
4.3040	1.8195	3.6419	2.4398	−0.8024	−1.2642	−1.5825	0.4395	176.1942
4.7737	1.6077	3.6552	2.7047	−0.7874	−1.2427	−1.5551	0.4427	95.8000
5.0850	1.4711	3.6630	2.8726	−0.7793	−1.2309	−1.5401	0.4445	65.1214
5.2918	1.2885	3.6726	3.0938	−0.7699	−1.2173	−1.5226	0.4465	39.1710
5.5798	1.0679	3.6826	3.3544	−0.7695	−1.2124	−1.5137	0.4485	21.5268
5.8864	0.8566	3.6910	3.5995	−0.7917	−1.2397	−1.5426	0.4484	12.2672
6.1673	0.6970	3.6995	3.7933	−0.8134	−1.2682	−1.5774	0.4383	7.8664
6.4031	0.6354	3.7135	3.9108	−0.9436	−1.3946	−1.7037	0.4068	6.0091
6.5681	0.7320	3.7365	3.9061	−1.3766	−1.8468	−2.1600	0.3431	6.0737
6.6549	0.9438	3.7624	3.7979	−2.0329	−2.6130	−2.9772	0.2650	7.7830
6.7040	1.0934	3.7854	3.7404	−2.5067	−3.2285	−3.6972	0.2159	8.8800
6.7433	1.2232	3.8211	3.7562	−2.8191	−3.6500	−4.2184	0.1876	3.8955
6.7999	1.3839	3.9211	3.9969	−2.8620	−3.7231	−4.3119	0.1839	2.2110
6.8417	1.1955	3.9226	4.1926	−2.5386	−3.4031	−3.9954	0.2093	1.4164
6.9500	1.2416	3.9637	4.3117	−2.5062	−3.3655	−3.9585	0.2107	1.0796
8.2686	1.2306	3.9537	4.2826	−2.5314	−3.3890	−3.9811	0.2094	1.1552
8.6019	1.2619	3.9377	4.1869	−2.6434	−3.4973	−4.0868	0.2015	1.4362

Table A.86: Evolutionary tracks including internal structure constants and gyration radii for 2.30 $M_\odot$ pre-MS rotationally and tidally distorted models.

$\log(age)$	$\log(L/L_\odot)$	$\log(T_{\rm eff})$	$\log(g)$	$\log(k_2)$	$\log(k_3)$	$\log(k_4)$	β	P(d)
1.9530	2.5895	3.5920	1.5321	−0.8654	−1.3378	−1.6652	0.4274	1535.8403
3.3488	2.3735	3.6105	1.8214	−0.8391	−1.3149	−1.6447	0.4319	804.8123
3.8516	2.1534	3.6274	2.1088	−0.8175	−1.2852	−1.6085	0.4363	423.5659
4.2584	1.9333	3.6431	2.3913	−0.7997	−1.2601	−1.5771	0.4401	245.9235
4.7098	1.7206	3.6572	2.6606	−0.7858	−1.2401	−1.5516	0.4431	132.3465
5.0456	1.5813	3.6657	2.8340	−0.7780	−1.2289	−1.5373	0.4447	88.8174
5.2497	1.4034	3.6759	3.0528	−0.7695	−1.2165	−1.5214	0.4466	53.6902
5.5396	1.1841	3.6871	3.3168	−0.7888	−1.2333	−1.5351	0.4484	29.2646
5.8327	0.9894	3.6966	3.5495	−0.7983	−1.2516	−1.5582	0.4461	17.1458
6.0968	0.8553	3.7068	3.7245	−0.8358	−1.2904	−1.6007	0.4309	11.4714
6.3127	0.8337	3.7227	3.8099	−1.0430	−1.4934	−1.8011	0.3895	9.4310
6.4465	0.9849	3.7457	3.7506	−1.6049	−2.1093	−2.4364	0.3145	10.8042
6.5140	1.1726	3.7689	3.6556	−2.1891	−2.8304	−3.2404	0.2468	13.4394
6.5557	1.2962	3.7920	3.6243	−2.5610	−3.3225	−3.8357	0.2096	14.4406
6.6097	1.4856	3.8667	3.7359	−2.8054	−3.6408	−4.2183	0.1881	4.8148
6.6602	1.6386	3.9679	3.9887	−2.8188	−3.6737	−4.2608	0.1871	2.6880
6.6986	1.4493	3.9690	4.1835	−2.4970	−3.3554	−3.9454	0.2127	1.7232
6.7908	1.4996	4.0132	4.3108	−2.4714	−3.3259	−3.9170	0.2142	1.2874
8.0638	1.4714	3.9997	4.2848	−2.4746	−3.3264	−3.9160	0.2145	1.3712
8.4255	1.5057	3.9824	4.1808	−2.5935	−3.4407	−4.0276	0.2058	1.7372

Table A.87: Evolutionary tracks including internal structure constants and gyration radii for 2.50 $M_\odot$ pre-MS rotationally and tidally distorted models.

$\log(age)$	$\log(L/L_\odot)$	$\log(T_{\rm eff})$	$\log(g)$	$\log(k_2)$	$\log(k_3)$	$\log(k_4)$	β	P(d)
1.9521	2.6565	3.5917	1.5002	−0.8600	−1.3303	−1.6558	0.4285	1808.1513
3.3255	2.4395	3.6106	1.7919	−0.8356	−1.3096	−1.6379	0.4327	941.1054
3.8272	2.2193	3.6277	2.0803	−0.8152	−1.2816	−1.6038	0.4369	493.4222
4.2343	1.9992	3.6437	2.3642	−0.7983	−1.2578	−1.5740	0.4404	282.2535
4.6792	1.7858	3.6583	2.6359	−0.7850	−1.2387	−1.5496	0.4433	151.0203
5.0223	1.6468	3.6672	2.8105	−0.7777	−1.2280	−1.5360	0.4449	101.0719
5.2223	1.4734	3.6776	3.0254	−0.7697	−1.2165	−1.5211	0.4466	61.6492
5.5088	1.2585	3.6893	3.2873	−0.7928	−1.2394	−1.5423	0.4481	33.7646
5.7927	1.0747	3.6993	3.5115	−0.7996	−1.2541	−1.5619	0.4441	20.1694
6.0474	0.9555	3.7104	3.6751	−0.8546	−1.3093	−1.6205	0.4255	13.8508
6.2503	0.9605	3.7273	3.7374	−1.1244	−1.5792	−1.8876	0.3774	12.0036
6.3654	1.1365	3.7499	3.6518	−1.7346	−2.2717	−2.6154	0.2982	14.6116
6.4261	1.2994	3.7718	3.5765	−2.2535	−2.9295	−3.3686	0.2393	17.3707
6.4650	1.4128	3.7960	3.5613	−2.5717	−3.3506	−3.8833	0.2081	8.3554
6.5268	1.6354	3.8922	3.7238	−2.7823	−3.6163	−4.1935	0.1899	5.5309
6.5747	1.7864	3.9932	3.9777	−2.7878	−3.6401	−4.2258	0.1889	3.0804
6.6119	1.6030	3.9966	4.1757	−2.4836	−3.3406	−3.9297	0.2144	1.9692
6.6965	1.6529	4.0414	4.3054	−2.4519	−3.3037	−3.8929	0.2161	1.4630
7.9402	1.6134	4.0264	4.2851	−2.4406	−3.2892	−3.8771	0.2176	1.5344
8.3207	1.6498	4.0088	4.1775	−2.5651	−3.4093	−3.9946	0.2085	1.9621

Table A.88: Evolutionary tracks including internal structure constants and gyration radii for 2.80 $M_\odot$ pre-MS rotationally and tidally distorted models.

$\log(age)$	$\log(L/L_\odot)$	$\log(T_{\rm eff})$	$\log(g)$	$\log(k_2)$	$\log(k_3)$	$\log(k_4)$	β	P(d)
1.9056	2.7462	3.5912	1.4578	−0.8526	−1.3200	−1.6429	0.4300	2252.4325
3.2871	2.5301	3.6104	1.7497	−0.8304	−1.3021	−1.6284	0.4338	1169.2022
3.7904	2.3099	3.6279	2.0396	−0.8117	−1.2765	−1.5972	0.4376	609.9972
4.1987	2.0898	3.6443	2.3253	−0.7960	−1.2543	−1.5694	0.4409	325.4510
4.6324	1.8757	3.6595	2.6000	−0.7836	−1.2364	−1.5465	0.4436	172.9332
4.9913	1.7348	3.6689	2.7787	−0.7766	−1.2263	−1.5336	0.4451	114.6390
5.1865	1.5669	3.6795	2.9890	−0.7856	−1.2317	−1.5358	0.4467	70.6771
5.4628	1.3629	3.6917	3.2416	−0.7941	−1.2444	−1.5494	0.4470	39.5333
5.7347	1.1946	3.7026	3.4535	−0.8073	−1.2639	−1.5744	0.4401	24.2912
5.9765	1.0987	3.7149	3.5988	−0.8957	−1.3487	−1.6593	0.4155	17.3976
6.1564	1.1486	3.7327	3.6201	−1.2699	−1.7393	−2.0525	0.3566	16.5659
6.2486	1.3335	3.7543	3.5217	−1.8840	−2.4728	−2.8491	0.2793	20.7655
6.3028	1.4665	3.7759	3.4750	−2.3128	−3.0318	−3.5119	0.2322	23.1219
6.3517	1.6118	3.8192	3.5039	−2.6149	−3.4249	−3.9903	0.2037	10.6422
6.4118	1.8379	3.9269	3.7089	−2.7498	−3.5852	−4.1645	0.1924	6.5939
6.4569	1.9838	4.0273	3.9652	−2.7464	−3.5986	−4.1850	0.1919	3.6532
6.4929	1.8071	4.0333	4.1667	−2.4496	−3.3057	−3.8951	0.2171	2.3042
6.5740	1.8461	4.0776	4.3055	−2.4111	−3.2622	−3.8520	0.2201	1.6792
7.8086	1.8063	4.0611	4.2793	−2.3986	−3.2455	−3.8334	0.2214	1.7852
8.1925	1.8456	4.0433	4.1681	−2.5288	−3.3720	−3.9575	0.2118	2.2991

Table A.89: Evolutionary tracks including internal structure constants and gyration radii for 3.00 $M_\odot$ pre-MS rotationally and tidally distorted models.

$\log(age)$	$\log(L/L_\odot)$	$\log(T_{\rm eff})$	$\log(g)$	$\log(k_2)$	$\log(k_3)$	$\log(k_4)$	β	P(d)
1.9034	2.7887	3.5922	1.4491	−0.8479	−1.3132	−1.6345	0.4310	2475.2225
3.2857	2.5717	3.6113	1.7415	−0.8256	−1.2956	−1.6203	0.4347	1282.8697
3.7896	2.3517	3.6290	2.0320	−0.8082	−1.2716	−1.5910	0.4382	667.7444
4.1984	2.1317	3.6456	2.3183	−0.7934	−1.2507	−1.5648	0.4414	696.7314
4.6463	1.9185	3.6609	2.5928	−0.7817	−1.2338	−1.5432	0.4439	370.2808
4.9804	1.7809	3.6703	2.7680	−0.7752	−1.2244	−1.5311	0.4453	247.3808
5.1829	1.6096	3.6815	2.9841	−0.7991	−1.2471	−1.5518	0.4467	150.4159
5.4530	1.4153	3.6938	3.2273	−0.8002	−1.2554	−1.5637	0.4456	85.9267
5.7160	1.2617	3.7052	3.4266	−0.8164	−1.2734	−1.5854	0.4353	54.3118
5.9463	1.1917	3.7186	3.5503	−0.9531	−1.4043	−1.7134	0.4035	40.8592
6.1007	1.2878	3.7373	3.5289	−1.4341	−1.9316	−2.2570	0.3351	42.9184
6.1788	1.4573	3.7581	3.4428	−1.9899	−2.6178	−3.0229	0.2658	52.3350
6.2283	1.5745	3.7807	3.4159	−2.3527	−3.0955	−3.6008	0.2272	55.6678
6.2870	1.7556	3.8473	3.5022	−2.6141	−3.4244	−3.9910	0.2034	11.5861
6.3440	1.9760	3.9567	3.7197	−2.7296	−3.5620	−4.1391	0.1935	6.9928
6.3869	2.1047	4.0538	3.9800	−2.7206	−3.5669	−4.1499	0.1946	3.8415
6.4223	1.9122	4.0531	4.1706	−2.4060	−3.2544	−3.8394	0.2207	2.4850
6.5050	1.9456	4.0975	4.3149	−2.3609	−3.2055	−3.7914	0.2246	1.7912
7.7778	1.9255	4.0804	4.2666	−2.3824	−3.2234	−3.8072	0.2230	1.9986
8.1317	1.9666	4.0628	4.1548	−2.5133	−3.3503	−3.9318	0.2132	2.5770

Table A.90: Evolutionary tracks including internal structure constants and gyration radii for 3.30 $M_\odot$ pre-MS rotationally and tidally distorted models.

$\log(age)$	$\log(L/L_\odot)$	$\log(T_{\rm eff})$	$\log(g)$	$\log(k_2)$	$\log(k_3)$	$\log(k_4)$	β	P(d)
1.8938	2.8554	3.5922	1.4237	−0.8408	−1.3035	−1.6224	0.4324	2911.3270
3.2679	2.6396	3.6117	1.7166	−0.8217	−1.2895	−1.6124	0.4356	1503.4222
3.7716	2.4197	3.6296	2.0077	−0.8057	−1.2674	−1.5854	0.4389	780.2710
4.1815	2.1995	3.6465	2.2956	−0.7920	−1.2481	−1.5610	0.4418	414.8244
4.6324	1.9863	3.6622	2.5715	−0.7811	−1.2323	−1.5409	0.4442	219.7970
4.9584	1.8509	3.6718	2.7452	−0.7751	−1.2236	−1.5298	0.4455	147.3693
5.1843	1.6650	3.6844	2.9818	−0.8031	−1.2558	−1.5629	0.4460	85.4949
5.4451	1.4878	3.6969	3.2089	−0.8029	−1.2611	−1.5729	0.4414	50.7124
5.6940	1.3609	3.7092	3.3849	−0.8506	−1.3046	−1.6163	0.4240	33.8290
5.8988	1.3469	3.7245	3.4601	−1.1143	−1.5739	−1.8843	0.3776	28.4582
6.0132	1.4941	3.7438	3.3902	−1.6770	−2.2342	−2.5926	0.3022	33.4239
6.0790	1.6240	3.7642	3.3421	−2.1215	−2.8093	−3.2669	0.2499	37.3272
6.1270	1.7368	3.7934	3.3466	−2.4152	−3.1943	−3.7386	0.2200	19.0507
6.1975	1.9683	3.8941	3.5181	−2.6150	−3.4282	−3.9984	0.2030	12.5355
6.2496	2.1727	4.0034	3.7510	−2.7013	−3.5346	−4.1129	0.1952	7.3113
6.2904	2.2594	4.0917	4.0182	−2.6653	−3.5108	−4.0941	0.2003	3.9642
6.3271	2.0449	4.0793	4.1836	−2.3402	−3.1797	−3.7618	0.2268	2.7215
6.4178	2.0668	4.1210	4.3286	−2.2770	−3.1138	−3.6970	0.2318	1.9580
7.7741	2.0933	4.1050	4.2381	−2.3713	−3.2076	−3.7896	0.2242	2.4048
8.0652	2.1363	4.0880	4.1266	−2.5072	−3.3392	−3.9191	0.2143	3.0983

Table A.91: Evolutionary tracks including internal structure constants and gyration radii for 3.50 $M_\odot$ pre-MS rotationally and tidally distorted models.

$\log(age)$	$\log(L/L_\odot)$	$\log(T_{\rm eff})$	$\log(g)$	$\log(k_2)$	$\log(k_3)$	$\log(k_4)$	β	P(d)
1.8942	2.8884	3.5931	1.4199	−0.8365	−1.2974	−1.6149	0.4333	3130.5225
3.2702	2.6728	3.6126	1.7127	−0.8183	−1.2846	−1.6062	0.4363	1615.4709
3.7746	2.4527	3.6305	2.0042	−0.8032	−1.2638	−1.5806	0.4394	855.5131
4.1848	2.2328	3.6476	2.2923	−0.7904	−1.2455	−1.5576	0.4422	443.1757
4.6551	2.0202	3.6635	2.5683	−0.7800	−1.2305	−1.5385	0.4444	234.7947
4.9485	1.8908	3.6728	2.7350	−0.7907	−1.2384	−1.5439	0.4456	159.9791
5.1847	1.7015	3.6862	2.9781	−0.8045	−1.2611	−1.5708	0.4447	91.4475
5.4390	1.5371	3.6989	3.1931	−0.8111	−1.2697	−1.5831	0.4371	55.7635
5.6778	1.4326	3.7119	3.3498	−0.9010	−1.3531	−1.6633	0.4132	38.8833
5.8583	1.4639	3.7282	3.3835	−1.2717	−1.7510	−2.0681	0.3564	35.9837
5.9537	1.6122	3.7474	3.3120	−1.8132	−2.4125	−2.7989	0.2856	42.4147
6.0140	1.7237	3.7689	3.2867	−2.1890	−2.9064	−3.3925	0.2428	44.9576
6.0744	1.8722	3.8194	3.3408	−2.4637	−3.2576	−3.8164	0.2159	20.3521
6.1408	2.1031	3.9256	3.5349	−2.6240	−3.4389	−4.0098	0.2027	12.9209
6.1899	2.2927	4.0331	3.7756	−2.6878	−3.5210	−4.0987	0.1965	7.4084
6.2301	2.3406	4.1126	4.0461	−2.6123	−3.4589	−4.0420	0.2054	3.9914
6.2791	2.1594	4.1057	4.1999	−2.3354	−3.1690	−3.7483	0.2279	2.8118
6.4137	2.1573	4.1371	4.3278	−2.2564	−3.0896	−3.6708	0.2345	2.1027
7.7701	2.1976	4.1198	4.2183	−2.3735	−3.2064	−3.7863	0.2247	2.6976
8.0262	2.2415	4.1030	4.1071	−2.5108	−3.3393	−3.9174	0.2148	3.4743

Table A.92: Evolutionary tracks including internal structure constants and gyration radii for 3.80 $M_\odot$ pre-MS rotationally and tidally distorted models.

$\log(age)$	$\log(L/L_\odot)$	$\log(T_{\rm eff})$	$\log(g)$	$\log(k_2)$	$\log(k_3)$	$\log(k_4)$	β	P(d)
1.9054	2.9327	3.5945	1.4169	−0.8307	−1.2892	−1.6046	0.4345	3445.3990
3.2773	2.7170	3.6140	1.7099	−0.8139	−1.2781	−1.5978	0.4373	1775.1803
3.7821	2.4968	3.6321	2.0019	−0.8001	−1.2590	−1.5743	0.4401	925.9471
4.1930	2.2770	3.6493	2.2907	−0.7883	−1.2421	−1.5531	0.4427	476.1415
4.6970	2.0649	3.6654	2.5671	−0.7787	−1.2283	−1.5353	0.4447	252.0066
4.9571	1.9271	3.6756	2.7455	−0.8060	−1.2584	−1.5659	0.4454	167.1348
5.1897	1.7531	3.6890	2.9732	−0.8094	−1.2697	−1.5829	0.4411	98.9829
5.4330	1.6126	3.7020	3.1659	−0.8415	−1.2981	−1.6116	0.4268	63.5286
5.6506	1.5563	3.7165	3.2801	−1.0419	−1.4992	−1.8092	0.3892	48.8547
5.7873	1.6508	3.7336	3.2542	−1.5291	−2.0640	−2.4094	0.3214	51.8494
5.8664	1.7689	3.7530	3.2134	−1.9729	−2.6339	−3.0686	0.2659	56.9525
5.9202	1.8639	3.7773	3.2157	−2.2602	−3.0137	−3.5356	0.2347	56.6517
5.9985	2.0697	3.8641	3.3576	−2.4899	−3.2878	−3.8502	0.2140	21.4071
6.0594	2.2939	3.9728	3.5684	−2.6243	−3.4415	−4.0128	0.2023	13.1183
6.1048	2.4583	4.0767	3.8201	−2.6522	−3.4848	−4.0607	0.1989	7.3523
6.1446	2.4329	4.1369	4.0863	−2.5032	−3.3499	−3.9321	0.2143	4.0014
6.2010	2.3471	4.1481	4.2172	−2.3351	−3.1628	−3.7389	0.2271	2.9692
7.0301	2.2968	4.1586	4.3098	−2.2395	−3.0700	−3.6489	0.2361	2.4051
7.7615	2.3442	4.1398	4.1872	−2.3741	−3.2022	−3.7789	0.2251	3.1799
7.9739	2.3888	4.1233	4.0763	−2.5095	−3.3328	−3.9076	0.2151	4.0947

Appendix B

Published Papers

B.1 Theoretical values of the Rossby Number for low-mass, rotating pre-main sequence stars

N.R. Landin, L.T.S. Mendes and L.P.R. Vaz

published in the Proceedings of Magnetic Fields in the Universe: From Laboratory and Stars to Primordial Structures. AIP Conference Proceedings, Volume 784, p. 607-612 (2005).

My specific contribution to this paper:

1. By using the version of the `ATON` code described in Chap. (4), I generated stellar evolutionary models and obtained self consistent theoretical estimates for global convective turnover time τ_c and Rossby Number Ro for rotating pre-main sequence stars.

2. I created and analyzed the figures presented in the paper.

3. I also made a comparison between our results and the only work we found out in literature that reports these quantities for young rotating stars.

B.2 Non-gray rotating stellar models and the evolutionary history of the Orion Nebular Cluster

N.R. Landin, P. Ventura, F. D'Antona, L.T.S. Mendes and L.P.R. Vaz

accepted to be published at the Astronomy and Astrophysics main journal

My specific contribution to this paper:

1. By using the version of the `ATON` code described in Chap. (5), I computed new sets of pre-main sequence stellar evolutionary tracks.
2. For each star of our ONC sample, provided by Dr. K. Stassun, I estimate a mass and an age, for each of our sets of models by linearly interpolating between the two nearest tracks and studied how these estimatives varies with the mixing length parameter.
3. I analyzed the rotational properties of the ONC stars, studied the observational evidences of disk locking and looked for its trends with mass.
4. I made the comparison between the lithium abundances found with the models and those observed in young open clusters (Soderblom et al. 1993 and Garcia Lopez et al. 1994).
5. I created and analyzed the figures and tables presented in the paper.